UNIVERSITY OF CALIFORNIA SAN DIEGO

Development of micro-physiological multi-organ-on-chip platforms

A dissertation submitted in partial satisfaction of the
requirements for the degree Doctor of Philosophy

in

Bioengineering

by

Gaurav Agrawal

Committee in Charge:

Professor Shyni Varghese, Chair
Professor Ju Chen
Professor Michael Gilson
Professor Christian Metallo
Professor Yingxiao Wang

2018

The dissertation of Gaurav Agrawal is approved, and it is acceptable in quality and form for publication on microfilm and electronically:

Chair

University of California San Diego

2018

EPIGRAPH

……stand up eight"

"Fall down seven times……

- *Japanese Proverb*

TABLE OF CONTENTS

LIST OF FIGURES

ACKNOWLEDGMENTS

I would like to sincerely thank all of the individuals who have contributed tremendously towards the completion of my graduate degree. First and foremost, I would like to thank my parents, who have always instilled in me the importance of a strong education as foundational to career success. They have taught me the values of hard work, excellence, and perseverance, which has shown in my graduate work, and have always been there in the good times and tough times. I am grateful for the sacrifices and difficulties they endured in coming to this country to raise my sister and I.

I am equally thankful for my fiancé, Guneet Kaur, who has supported me at every point throughout graduate school, from transitioning from MS to the PhD, to long work hours on nights and weekends for experiments, to attempting to form a start-up based on the organ-on-chip technology, to founding Blue LINC on campus. I am extremely appreciative of her tolerance with my work and extra-curricular projects, and for sticking through the toughest times with me. She has helped me grow in numerous ways as an individual, and I feel lucky to have met her so many years ago and to be soon marrying her.

Next, I would like to thank my dissertation advisor, Shyni Varghese, for her support, mentorship, patience, and guidance. Without Shyni, I would have never done a Ph.D. She saw something in me, a curious, driven, and hard-working M.S. student, and gave me the opportunity to pursue further graduate studies. She has devoted many hours of her time to training me to think critically and analytically in order to be a stronger scientist. Shyni has always believed in me and given me the opportunity to work on interesting, higher-risk projects. I am particularly thankful that she understood my career interests early on, and allowed me to pursue opportunities in entrepreneurship and leadership outside of the lab.

I would also like to acknowledge those who have molded my scientific and engineering abilities throughout graduate school. Particularly, I would like to thank two former lab members, Aereas Aung, who was an incredible scientific mentor, and Han Liang Lim, who continued to work with me even after he graduated, and who has become a close friend and partner in brainstorming crazy business ideas. I would also thank the rest of my fellow lab mates, past and present, for their friendly and collaborative nature that made my graduate school experience a positive one.

Lastly, I would like to extend my gratitude to my professors, mentors, and colleagues who dedicated time and energy to help me learn and grow. I am particularly thankful for my mentors from NSF I-Corps, my first foray into entrepreneurship that lit the start-up fire in me. I am also thankful for my colleagues and mentors from Blue LINC, including my co-founders. These experiences helped me grow as a leader and entrepreneur, and allowed me to wear many hats which diversified my graduate school education. Although there were many challenges along the way, these experiences also made life very fun and interesting.

Chapter 1, in full, is currently being prepared for submission to publish the material. Gaurav Agrawal and Shyni Varghese, "Organs-on-Chips: Changing the Paradigm of Drug Development". The dissertation author is the primary investigator and author of this material.

Chapter 2, in full, is a re-print of material that has been published in the journal *Lab on a Chip*. Agrawal G*, Aung A*, Varghese S. Skeletal muscle-on-a-chip: an *in vitro* model to evaluate tissue formation and injury. *Lab on a Chip*. 2017; 17: 3447-3461. The dissertation author is the primary investigator and co-author of this material.

Chapter 3, in full, is currently being prepared for submission to publish the material. Gaurav Agrawal, Priya Nayak, Shyni Varghese, "Human induced-pluripotent stem cell-

derived myoblasts produce functional skeletal muscle microtissues: an hiPSC-organ-on-a-chip". The dissertation author is the primary investigator and lead author of this material.

Chapter 4, in full, is currently prepared and in submission for publication of the material. Gaurav Agrawal, Han Liang Lim, Shyni Varghese, "Multi-organ 'body-on-a-chip' platform as a model system to assess cancer drug efficacy and toxicity". The dissertation author is the primary investigator and a co-author of this material.

VITA

2013 – 2018	**University of California, San Diego** *Doctor of Philosophy in Bioengineering* GPA: 3.81 (on a 4.0 scale)
2009 – 2013	**University of California, Los Angeles** *Bachelor of Science in Bioengineering, Magna Cum Laude* GPA: 3.78 (on a 4.0 scale)

ACHIEVEMENTS AND HONORS

2018	Gordon Fellow Award
2018	Jacobs School of Engineering – Graduate Student Council Award
2018	UC San Diego Grad SLAM Finalist (TED-like research talk)
2016-2018	Ruth L. Kirschstein National Research Service Award
2016-2017	Gordon Scholar in Engineering Leadership
2016	Jacobs School of Engineering Research Expo – Best Poster Award
2016	OneStart Americas Bio-entrepreneurship Semi-Finalist
2015	NSF Innovation Corps (I-Corps) National Grant Recipient ($53000)
2013	B.S. awarded Magna Cum Laude, UCLA
2009 – 2013	UC Regents' Scholarship
2009 – 2013	UCLA Engineering Scholarship
2009 – 2013	Dean's Honors List
2009 – 2013	National Merit Scholarship

RESEARCH EXPERIENCE

Sep 2013 – Present	*Graduate Researcher* **Bio-Inspired Materials and Stem Cell Engineering Laboratory** **Thesis Advisor: Shyni Varghese, Ph.D** **Dissertation Topic:** "Development of micro-physiological multi-organ-on-chip platforms"
Jan 2011 – Jun 2013	*Undergraduate Researcher* **Wound Healing Research Group** **PI: Benjamin Wu, D.D.S., Ph.D**
Sep 2012 – Jun 2013	*Undergraduate Researcher*

Optofluidics Laboratory
PI: Eric Pei-Yu Chiou, Ph.D

JOURNAL PUBLICATIONS

2018 **Agrawal G,** Varghese S. Organs-on-Chips: Changing the Paradigm of Drug Development. *In Preparation.*

2018 **Agrawal G**, Nayak P, Varghese S. Human induced-pluripotent stem cell-derived myoblasts produce functional skeletal muscle microtissues: an hiPSC-organ-on-a-chip. *In Preparation.*

2018 **Agrawal G***, Lim HL*, Varghese S. Multi-organ 'body-on-a-chip' platform as a model system to assess cancer drug efficacy and toxicity. *In Submission.*

2017 **Agrawal G***, Aung A*, Varghese S. Skeletal muscle-on-a-chip: an *in vitro* model to evaluate tissue formation and injury. *Lab on a Chip*. 2017; 17: 3447-3461.

2015 Davey SK* Aung A*, **Agrawal G**, Lim HL, Kar M, Varghese S. Embedded 3D photopatterning of hydrogels with diverse and complex architectures for tissue engineering and disease models. *Tissue Eng: Part C*. 2015; 21(11): 1188-1196.

2015 Linsley C, Quach V, **Agrawal G**, Hartnett E, Wu B. Visible light and near infrared-responsive chromophores for drug delivery-on-demand applications. *Drug Delivery Translational Research*. 2015; 1(6): 611-624.

CONFERENCE PRESENTATIONS

2017 Lim HL, **Agrawal G,** Varghese S. "'You-on-a-chip': modular integrated organ-on-a-chip systems for cancer drug testing". Jacobs School Research Expo, UCSD, 2017.

2016 **Agrawal G**, Aung A, Theprungsirikul J, Varghese S. 3D Skeletal Muscle-on-a-Chip as an *In Vitro* Tool. Jacobs Research Expo, 2016. *(Best Poster Presentation Awardee)*

2013 **Agrawal G**, Bhullar I, Talati I, Vuong G, Chiou PY. Electric Field Programmed Deforming Catheter for Cardiac Ablation. UCLA Design Symposium, 2013.

LEADERSHIP AND ACTIVITIES

Nov 2015 – Present **Blue LINC Health**
Co-founder & President (March 2017-Present), VP ('16-'17)
- Founded an interdisciplinary medical innovation program at UC San Diego (www.bluelinc.ucsd.edu)

Sep 2016 – Jun 2017 **Gordon Engineering Leadership Program**
Graduate Gordon Scholar

Jan 2016 – Apr 2016 **OneStart Americas Life Sciences and Healthcare Accelerator**
Semifinalist Team

Jan 2015 – Dec 2015 **National Science Foundation Innovation Corps (NSF I-Corps)**
Entrepreneurial Lead (UCSD Site and National)

Sep 2013 – Jun 2015 **Bioengineering Graduate Society**
Vice President, External

TEACHING EXPERIENCE

Sep 2014 – Dec 2014 *Bioengineering 166A*, *Cell and Tissue Engineering*
UC San Diego

Jan 2014 – Mar 2014 *Chemistry 7L*, *General Chemistry Lab*
UC San Diego

Sep 2013 – Dec 2013 *Chemistry 4*, *Basic Chemistry Lab*
UC San Diego

WORK EXPERIENCE

Jun 2013 – Sep 2013 *Sensors Research and Development Intern*
Medtronic, Inc., Northridge, CA

Jul 2011 – Sep 2011 *Formulations Research and Development Intern*
Allergan, Inc., Irvine, CA

PROFESSIONAL MEMBERSHIPS

July 2017 – Present **Gordon Scholars Society**

April 2011 – Present **Tau Beta Pi, National Engineering Honor Society**

Sep 2009 – Jun 2013 **Regents' Scholars Society**

SKILLS, QUALIFICATIONS, AND INTERESTS

Software: MATLAB, LabVIEW, COMSOL, SolidWorks, AutoCAD
Microscopy (conventional and confocal)
Languages: English and Hindi
Hobbies include basketball, soccer, dance, violin, traveling, home brewing beer

ABSTRACT OF THE DISSERTATION

Development of micro-physiological multi-organ-on-chip platforms

by

Gaurav Agrawal

Doctor of Philosophy in Bioengineering

University of California, San Diego, 2018

Professor Shyni Varghese, Chair

Patients around the world who suffer from a host of debilitating conditions rely on medications for treatment. However, pharmaceutical researchers and drug developers face immense challenges to new drug discovery. Drug companies currently spend 10-15 years and upwards of $1 billion (USD) developing and testing a single new drug, and despite this, up to 90% of drug candidates ultimately fail to pass clinical trials and obtain FDA approval. A

significant reason for this failure is the inability of traditional pre-clinical testing systems, such as cell monolayers in multi-well plates and animal models such as mice, to accurately predict drug toxicity and efficacy in humans. Recent studies have focused on engineering functional, three-dimensional tissue analogs that better mimic native human physiology in an *in vitro* system. As next-generation pre-clinical drug screening platforms, these human tissue analogs may provide a more accurate indication of the likelihood of a drug's success or failure in humans, thus increasing the efficiency of drug development.

In this regard, organ-on-a-chip systems have shown great promise. In an organ-on-a-chip, engineered tissue constructs are housed in a microfluidic device in which nutrients are supplied and wastes are removed via the continuous perfusion of media, similar to the function of the blood vessel network in the human body. Due to their micro-scale size, these systems also minimize the amounts of reagents and drug compound required for testing, potentially reducing costs and circumventing supply limitations. Organs-on-chips for lung, gut, heart, and others have already been developed. Furthermore, in theory multiple individual organs-on-chips could be linked together to form a multi-organ "body-on-a-chip" system to recapitulate whole human physiology and study on- and off-target drug effects.

This dissertation is intended to contribute to the development of single- and multi-organ-on-a-chip systems in order to outline approaches to creating human tissue models *in vitro* and assess their feasibility in drug screening. Chapter 1 is a literature review of the current state of organ-on-a-chip research, past accomplishments, and future directions. In particular, I have highlighted how organs-on-chips may serve as valuable disease models by replicating human disease pathophysiology through the use of patient-specific cells, increasing the likelihood of researching and developing cures for rare diseases. In Chapter 2,

I have detailed the development of a novel micro-physiological 3D model of skeletal muscle in a microfluidics device. Interestingly, despite its key role in supporting motion, strength, and activity in everyday life, few prior advancements had been made in skeletal-muscle-on-a-chip platforms. In addition to creating aligned 3D muscle microtissues, we have characterized their formation under various physical cues, developed a method to quantify force generated by the muscle strip, and performed a proof-of-concept small molecule screen to demonstrate the effect of muscle injury on structure, morphology, and function. In Chapter 3, I have extended the previous study by utilizing human induced-pluripotent stem cells (hiPSCs) to create 3D muscle microtissues which mimic human muscle physiology. Further, by using microfluidics to apply a cyclical mechanical load to the tissues through pulsatile flow, thus increasing and decreasing fluid pressure to simulate a "massage-like" phenomenon, I have shown an upregulation in myogenic maturation of the hiPSC-based muscle tissues. This demonstrates an additional feature of microfluidics that, to our knowledge, has not previously been explored. Further, we have shown that the muscle tissues contract in response to the neurotransmitter acetylcholine, indicating their functional maturation. This is the first development of a skeletal-muscle-on-a-chip with hiPSCs, and in the future, this system may be used for personalized medicine and disease modeling. In Chapter 4, I have detailed the development of a multi-organ "body-on-a-chip" system by integrating together individual 3D organs-on-chips of liver, heart, skeletal muscle, and cancer. Multi-organ platforms enable organ-organ cross-talk, which can be critical in applications ranging from fundamental biological research to drug development. We have demonstrated the viability, structural maturation, and function of each tissue under integrated co-culture conditions. Further, we have performed a cancer drug screen using 5-Fluorouracil

and its pro-drug form, Tegafur, to illustrate liver metabolic activity and molecular cross-talk between organs that leads to cancer drug efficacy and off-target toxicity. This validates the value of a multi-organ system over individual organs-on-chips, where certain information may not manifest because there is no communication between tissues.

CHAPTER 1:

Organs-on-Chips: Changing the Paradigm of Drug Development

Gaurav Agrawal[1], Shyni Varghese[1,2*]

[1] Department of Bioengineering, University of California, San Diego, La Jolla, California, USA

[2] Department of Biomedical Engineering, Duke University, Durham, North Carolina, USA

1.1 Abstract

In recent years, a growing area of interest in pharmaceutical drug development has centered around creating physiologically-relevant models of human tissues. These systems may better predict the expected effect of a drug in a human, thus increasing the success rate of drugs that pass from pre-clinical trials on to clinical testing. The organ-on-a-chip (OOC) is an *in vitro* tool that combines microfabrication techniques with tissue engineering to create a micro-scale tissue model in a microfluidic system that mimics native tissue structure and function. Combined with recent advances in human cell sourcing, including stem-cell based technologies, OOCs can emulate human tissue physiology and recreate disease pathophysiology to serve as potentially valuable tools in drug screening, disease modeling, and individualized medicine. OOCs may address many of the limitations associated with cell and animal models, and hopefully will be able to reduce the reliance on animal testing and expedite the rate of drug development. Here, we will review recent advances regarding microfluidic OOC systems and discuss advantages and limitations of these platforms as compared to the current pre-clinical testing paradigm. Specifically, we will discuss the unmet need in drug development, and how microfluidics may unlock the key to solving some of these issues. Further, we will look deeply at the OOC models already developed, including lung, gut, liver, heart, skeletal muscle, and cancer, as well as disease models based on human induced-pluripotent stem cells. We will also assess advances in multi-organ systems that incorporate organ cross-talk. Finally, attention is given to the practical limitations and challenges of the OOC, the future outlook of this technology, and its promising potential impact in expediting research, development, and precision medicine.

1.2 Introduction

Pharmaceutical companies have been faced with extraordinary challenges due to the increased costs and reduced efficiency of drug development coupled with the low success rate of drug approval.[1, 2] In fact, it has been estimated that companies spend 10-15 years and between $1-3 billion developing a single drug candidate, yet face attrition and failure rates of up to 90% amongst the candidates that move on to clinical trials.[3] Further, studies have broken down the drug development cost distribution and found that 32% of the expense is spent on preclinical development and 63% is spent on clinical trials (53% on Phase II trials on to new-drug launch). Therefore, the majority of the cost lies in late-stage clinical trials. By this point, the drug developer may have already spent hundreds of millions of dollars, and failure of the drug candidate can result in catastrophic losses and opportunity costs in terms of sunken monetary cost, time, and resources. It is believed that drug attrition can largely be attributed to the poor predictive power of existing pre-clinical testing models, which include cell- and animal-based systems from which results often fail to translate to humans in clinical trials. Therefore, physiologically-relevant human-based models that recapitulate the structure and function of native tissues and organs could potentially be better predictors of drug toxicity and efficacy in humans.[4, 5] In fact, such platforms may more accurately select the candidates likely to succeed in clinical trials to proceed down the development pipeline while discarding those likely to fail, increasing the overall efficiency and success rate in drug development.

Engineered cell and tissue models have shown promise in addressing this unmet need. Advances in cell culture and cell sourcing, as well as microfabrication techniques, have led to recent breakthrough micro-tissue and micro-organ *in vitro* platforms for performing pre-clinical assays. These systems have allowed researchers to spatially-control cell placement

and tissue growth and temporally-control the application of various chemical, electrical, or mechanical cues with high-precision.[6, 7] Within this has been the advent of novel microfluidic organ-on-a-chip (OOC) platforms, which enable the simulation of human organs within a low-cost, reproducible, and controlled *in vitro* environment. By incorporating various physicochemical cues, OOCs have the potential to reconstitute organ-level functions at the micro-tissue level. Over the last decade, functional OOC models of lung, liver, heart, gut, skeletal muscle, bone, brain, kidney, skin, and cancer have been developed. Further, human-sourced cells, including induced-pluripotent stem cell technology, have recently been shown to maintain the healthy or diseased phenotype of the original host, and can enable the development of inexpensive, scalable, human-relevant OOC disease models for drug development and personalized medicine.[3] Finally, exploiting the microfluidics aspect of these systems can allow researchers to combine multiple OOCs into a single recirculating system, creating an *in vitro* representation of an entire human being. Several groups have begun integrating OOCs to develop multi-organ systems capable of evaluating both drug toxicity and efficacy.[8]

In this review, we provide a perspective on the promising opportunity afforded by the OOC platforms currently under development. First, we will discuss the unmet need in drug development, and how OOCs and microfluidics can help solve this issue. Next, we will talk about various technologies that have recently been developed to contribute to OOCs. We will also discuss advancements in OOC development for several of the organs mentioned previously. Finally, we will address the practical challenges and future outlook for this exciting technology to revolutionize research in the therapeutic discovery industry.

1.3 The Unmet Need

Drug development requires extensive and exhaustive preclinical discovery and testing, largely dictated by FDA requirements, before a compound is approved to move to clinical testing in humans. It can be reasoned that the inefficiency of today's drug development process is in part due to insufficient pre-clinical models which fail to accurately select the most promising candidates to move to more lengthy and expensive clinical trials. Modern preclinical screening methods employ both *in vitro* cell-based systems and *in vivo* animal models. Conventional *in vitro* systems include two-dimensional (2D) layers of cells plated on plastic culture dishes or simple three-dimensional (3D) cellular models. The 2D cell culture systems are largely employed as quick, inexpensive, high-throughput screens to assess target binding efficiency, toxicology, and compound hit rate for hundreds to thousands of compound iterations. While these are critical and necessary for initial discovery and development, they are far too simplistic in nature to reflect the mechanisms and conditions that occur in a native physiological environment.[9-11] More advanced 2D systems that spatially-confine cells in various geometries or incorporate multiple cell types, still fail to represent the complexity of native tissue. To address this, 3D cellular models were developed to improve the resemblance to *in vivo* tissue. These models use various techniques to spatially-organize cells into a 3D structure, creating a physiological microenvironment in which cell-cell and cell-extracellular matrix interactions lead to polarization, zonation, and activation of biochemical pathways.[12] To develop 3D models, cells may be encapsulated in a cell-compatible hydrogel, seeded onto a biomaterial scaffold, or clustered into a spheroid form, effectively creating a micro-scale organoid.[13-15] Efforts have been taken to modulate the biochemical and mechanical microenvironment by varying cell packing density or

material stiffness, and to incorporate relevant support cell types including stromal cells. In fact, 3D models have been proven to better capture signaling pathways and drug responsiveness than comparable 2D cell monolayer systems.[16-18] However, these also have substantial limitations, including variability between samples, biochemical gradients due to transport constraints, and difficulty in quantifying cellular activity from different areas of the tissue or functionally-analyzing inputs and outputs from the encapsulated cells. Further, these 3D systems are still simple and lack standard multi-scale tissue architecture, vasculature indigenous to all tissues in the body, and immune cells that circulate in the bloodstream. Additionally, the 3D cultures are typically maintained in static conditions, lacking most mechanical stimuli such as tension, compression, and shear that native tissues commonly experience due to voluntary and involuntary activities. These physiological stimuli may include the stretch experienced by lung epithelial cells during breathing, the cyclic peristaltic motions experienced by intestinal cells, and flow-induced shear of endothelial cells that line various tissues. Therefore, these 3D tissue models still fail to reconstitute organ-level function with fidelity, creating an ongoing need for higher-complexity 3D tissue models in order to increase their predictive power as drug screening systems and reverse the current exceedingly low success rate of drug candidates.

Following *in vitro* studies, *in vivo* preclinical studies in animal models must be passed for a drug to proceed to clinical trials. While animal models, such as mice, dogs, and monkeys, replicate tissue- and organ-level function, and enable systemic multi-organ analysis, these are fundamentally flawed because of the inherent differences between animal and human species, such as metabolic processes, bioavailability, biochemical signaling pathways, and protein or transcription factor binding sites, among others. For example,

differences in ventricular repolarization, contractile function, and calcium handling makes animals poor models to screen for cardiac toxicity.[19] In fact, despite certain known inter-species differences in cardiac activity, an apparent cardiotoxicity seen in animals may erroneously screen out a potentially curative new medication. Such false-positive and false-negatives play a major role in eliminating promising compounds on the basis of risk and profitability rather than pursuing a potential breakthrough that will improve clinical outcomes.[20] Alternatively, positive outcomes observed in animal studies that have led to clinical testing in humans has led to situations where the treatment was ineffective or harmful to the patient. Additionally, animals are costly, require large facilities to house and care, take weeks to breed and develop, and are inherently variable from one another just like each human is unique as well. A large amount of compound is required to dose an animal as well, leading to increased costs and short supplies. Extended dosing periods, on the order of weeks, and dosing schedules irrelevant to humans, put strain on researchers using animal models for early compound selection.[21, 22] Further, there are ethical issues associated with putting drug compounds with unknown consequences into animals, and extensive controls are required to ensure that neither these animals nor their byproducts enter into the environment of the outside world. Taken together, while animal models are critical to the current state of drug development, there are major flaws to accurately, efficiently, and economically predict drug toxicity and efficacy in humans.

Micro-physiological *in vitro* platforms, such as the OOC, have the potential to combine human-sourced cells with 3D tissue culture techniques within a microfluidic platform that incorporates flow to mimic vascular delivery. Supporting technologies can be implemented to externally-apply mechanical stimuli and integrate sensors to quantify

electrical, mechanical, and chemical activity of the contained micro-scale tissues. Therefore, OOCs may overcome many of the aforementioned limitations of 2D and 3D tissue systems as well as animal models to accurately model human physiology and predict drug activity as expected in a human.

1.4 How do microfluidic devices enhance tissue and organ models?

OOCs are microfluidic devices, or "biochips", that can compartmentalize various tissue-specific cell types into micro-sized chambers and culture these cells over an extended period of time.[23] Over time, these cells assemble into simplified models that emulate the structure and function of their organ-level counterparts. These bioreactors can sustain either 2D or 3D cultures of cells by using fluidics to perfuse a continuous stream of nutrients while constantly removing wastes and metabolic byproducts, essentially mimicking the core function of blood vessels in the human body, albeit without the cellular components of the vascular network themselves (Fig. 1.1). Providing a constant concentration of amino acids and proteins creates a physiological environment that circumvents the mass transport issues commonly-associated with static culture. Further, in micro-scale fluidic channels at low flow rates, viscous forces dominate and flow is laminar, creating chemical gradients that can be used to study cell migration, tissue formation, cell differentiation, activation of signaling pathways, axon outgrowths, and neurotoxin response.[24-27] Additionally, microfluidics allows the incorporation of fluid shear stress, which can be modulated by flow rate or device design. Flow-induced shear stress can be maximized, with direct contact of the flow to the cells, or minimized, by protecting the cells from flow using hydrogels, structural barriers, or additional channels. Further, using fluid flow and pressure, a variety of mechanical

perturbations can be cyclically applied to the tissues including stretch, compression, and pulsatile flow.[28, 29] Various channels and micro-chambers can be designed to independently control nutrient administration to distinct cell types while maintaining cellular cross-talk. The outflow, or eluent, from the device can be obtained and analyzed to study absorption, drug uptake, metabolism, and secretion. In the future, microfluidics may be useful in studying interactions of tissues with immune cells and blood, or in investigating cancer metastasis from a primary tissue to a secondary site. Therefore, microfluidics can allow more precise control over various experimental parameters and can increase the number of assays performed in a single sample.

The majority of microfluidics and 'lab-on-a-chip' devices have been built using poly(dimethylsiloxane) (PDMS), a silicone elastomer material that is favorable for a variety of reasons. PDMS has no known toxic effects on cells or tissues, it is optically-transparent which makes it amenable to microscopy and imaging-based analysis, it is permeable to gases such as oxygen and carbon dioxide, it can be patterned with high resolution using soft lithography techniques, it is easy to mold into a size and shape of choice, and it is relatively inexpensive.[30] Thus, it can be designed to have multiple channels for fluid flow routed to a variety of chambers and connected to one another in any manner desired.

1.5 Cell sourcing for *in vitro* tissue modeling

Drug development and screening has historically utilized a variety of cell sources – commercially-available cell lines, primary animal cells, primary human cells, and stem cells – each of which has been used in OOC development. Each cell type has its own benefits and drawbacks. For example, cell lines are immortalized human- or animal-derived tissue-

specific cells that are cost-effective, easy to use, unlimited in supply, can be passaged indefinitely, and bypass ethical concerns of primary cells or animal models.[31] Additionally, and perhaps most importantly, cell lines provide a pure population of cells, ensuring consistent samples and reproducible experimental results. However, since cell lines have been genetically-manipulated in order to be immortalized, it is uncertain how their phenotype, genetic make-up, function, differentiation ability, and responsiveness to drugs or other stimuli changes over time. Further, many cell lines were developed 40-50 years ago, and serial passaging of cell lines may lead to additional variations that would create heterogeneities between cultures over time.[32] Although immortalized cell lines have been the primary driver of research over the last 50 years due to their ease of use, cell lines are less than ideal cell sources.

Primary animal cells, such as those from mice, are easy to obtain through established cell isolation protocols. In fact, robust protocols for the isolation of mouse myoblasts, hepatocytes, alveolar cells, keratinocytes, dermal cells, and neonatal rat cardiomyocytes, amongst many others, have already been developed and are commonly employed.[33-37] Small animals such as mice and rats can be easily bred to generate a large supply of organs and tissues for cell isolation. Unfortunately, the principal drawback of primary animal cells is the lack of relevance to humans, therefore drug screens on animal cells may fail to predict drug effect in the human body. Further, each animal from which cells are sourced is unique from the next, adding inconsistencies to experiments.

Primary human cells are more attractive cell sources, namely due to their relevance to adult humans and biological representation of the tissue of interest. However, primary cells, such as those of blood cells, hepatocytes, pancreatic islets, and muscle cells, must be

isolated from humans or, in some cases, cadavers.[38] Thus, these cells have supply constraints, and require extensive procedures to obtain and maintain the cells. Further, since cells are obtained from various donors, their function and phenotype lacks consistency from batch to batch, making experimental reproducibility an issue. Certain cells, such as contracting cardiomyocytes, pose greater hurdles to isolation since they must be harvested either from myocardial biopsies following open-heart surgery or from a patient's heart in a narrow window after a patient's death in the period after the heart can no longer be used as a transplant and before it completely ceases functioning and loses viability.[39] Disease modeling with primary human cells is restricted by limited donor tissue availability and genetic variation between donor tissues.

Human stem cells, consisting of embryonic stem cells (ESCs) and induced-pluripotent stem cells (iPSCs) are additional cell sources for *in vitro* modeling. These stem cells are pluripotent, meaning they can be efficiently differentiated into any of the three germ layers – mesoderm, endoderm, ectoderm – before further differentiation to a tissue-specific lineage. Further, as pluripotent cells, they can be expanded infinitely, circumventing supply issues associated with primary cells. Also, these are human-sourced cells, thus preserving relevance to human physiology and function. Researchers have been able to use genome-editing techniques, such as CRISPR/Cas9, to induce mutations in stem cells to model a human disease, avoiding ethical problems and species variation.[40] However, embryonic stem cells are harvested from early-stage embryos, which can be ethically-challenging and faces limited availability. Further, ESCs serve as poor cell sources for personalized medicine since the exact disease-causing genetic mutation in the patient may remain unknown for CRIPSR/Cas9-based genetic modification. On the other hand, iPSCs have immense potential

to accurately-model human disease on a patient-specific level. The iPSCs are generated from adult somatic cells, such as peripheral blood mononuclear cells, that are genetically-reprogrammed back to pluripotency.[41, 42] Therefore, these cells can be obtained from a patient at any time, have no ethical issues associated with harvesting embryos, and retain the pathological phenotype for patient-specific disease modeling. For example, iPSCs from a patient with Duchenne muscular dystrophy (DMD), a genetic X-linked condition that impedes normal formation of the dystrophin protein and inhibits motion, activity, muscle growth, can be differentiated into skeletal muscle myoblasts and subsequently used to model the DMD of that specific patient.[43] These cells can then be used to screen for the optimal therapeutic regiments that would upregulate dystrophin formation, prevent further muscle damage, or restore muscle strength and contractile capability on an individual patient-level. Combined with the organ-on-a-chip, these could serve as valuable cell sources for drug development or personalized medicine tailored to each patient.

1.6 Organ-on-a-chip: state of development

Interest in the development of OOC technology for drug development, human tissue modeling, and exploratory research applications has surged over the past several years. OOC tissue models have been developed for the majority of the key organs and tissues in the human body. In this section, we will detail the recent key advances in OOC models of lung, gut, heart, liver, skeletal muscle, and cancer tissues, and highlight challenges yet to be overcome.

Lung-on-a-chip

Recapitulating lung function is critical to understanding how inhaled drugs, gases, irritants, or particulate matter reach the bloodstream and affect both alveolar tissue and downstream organs. Individuals are exposed to harmful compounds in the air breathe these in on a daily basis, thus organotypic lung models would be useful to study the effect of pathogens and pollutants on the lungs.[44, 45] Porous membranes for the development of an air-liquid interface that permits gas exchange between the media and the air were utilized to model lung tissue. Here, human lung epithelial cells would be grown to confluency on one side of the membrane and exposed to air on the other side, leading to differentiation of the cells into a pseudostratified columnar epithelium.[46] The first microfluidic lung model contained ultra-thin PDMS membranes that mimic alveolar structures aimed at maximizing the efficiency of gas transfer into the medium to provide levels of oxygen and carbon dioxide that mimics that of the native lung.[47] However, this model does not incorporate breathing, which enhances the transport of gas, fluid, nutrients, nanoparticles, and other factors across the alveolar-vascular barrier and which would therefore more accurately reflect the physiological relevance of an *in vitro* lung.

To address this, Ingber and colleagues recreated the alveolar epithelial-vascular barrier by co-culturing the alveolar epithelial A549 cell line and human pulmonary microvascular endothelial cells on opposite sides of a fibronectin-coated porous membrane within a microfluidic device that incorporated cyclic mechanical strains of the cell-laden porous membrane to mimic the physiology of a breathing lung (Fig. 1.2).[29] The system is composed of two micro-channels separated by a thin, porous membrane on which the cells are attached and cultured. As media is pumped through the channel containing endothelial cells, while the endothelial layer is separated by the porous membrane, fluid shear stress is

selectively applied to the vascular layer similar to blood flow through the pulmonary microvasculature. Additionally, a computerized vacuum pump is connected to two empty micro-chambers located adjacent to but separate from the cell-laden micro-channels. Cyclically-applying a vacuum to the two side micro-chambers mechanically-stretches the porous membrane between 5-15% strain every 5 seconds, simulating normal inspiration and expiration that stretches and relaxes the alveolar-capillary interface during physiological-breathing. Under air-liquid interface culture, surfactant production by alveolar epithelial cells increased and stabilized the thin liquid layer. Further, the capabilities of the lung-on-a-chip to reproduce complex organ-level functions was demonstrated by simulating pulmonary inflammation. Introduction of tumor necrosis factor-α (TNF-α), a potent pro-inflammatory factor, into the alveolar microchannel led to activation of the as evident in the upregulation of intercellular adhesion molecule-1 (ICAM-1), a leukocyte adhesion molecule. As a result, neutrophils introduced into the "blood" micro-channel firmly adhered to the activated endothelium and eventually transmigrated across the porous membrane onto the surface of the alveolar epithelium, effectively replicating the features of pulmonary inflammation. Similarly, bacteria introduction to the alveolar side of the lung-on-chip led to migration of neutrophils and phagocytosis of the bacteria. Finally, in nano-toxicology studies, it was found that mechanical strain augments the toxic response of the lung to nanoparticles and increases nanoparticle uptake into the blood vessel. In a separate study, interleukin-2 (IL-2) was introduced to the lung-on-a-chip to reproduce drug toxicity-induced pulmonary edema.[48] In fact, it was shown that the mechanical stretch due to breathing plays a critical role in vascular permeability and leakage that leads to fluid secretion in edema, a finding uniquely found from the breathing lung-on-a-chip. The edema disease model was used to identify new potential

therapeutics to prevent intercellular gap formation and pulmonary leakage that can be life-threatening. Finally, barrier permeability and drug response in the lung-on-a-chip was found to be similar in magnitude to that of a whole *ex vivo* mouse lung, confirming the utility of the lung-on-a-chip as a predictive drug screening tool. The tool was further developed in later studies to support a columnar, pseudostratified, mucociliary bronchiolar epithelium that showed toxicity to interleukin-13 as seen in asthmatics.[49] A pulmonary disease model of COPD was developed to demonstrate inflammatory exacerbation in response to pathogenic stimuli, and suppression of inflammation after treatment with an experimental anti-inflammatory drug. The same lung-on-a-chip COPD model was utilized to analyze the effect of smoking on the pathophysiology of human bronchiolar epithelium.[50] Whole smoke, from both conventional and electronic cigarettes, when delivered to the bronchiolar epithelial chamber while "breathing" was induced, caused toxicities including decreased cilia beating and increased IL-8 secretion, demonstrating smoke-induced injury response *in vitro*. This tool is valuable in evaluating healthy and disease-specific responses of the human lung to inhaled smoke or other aerosols or particulate matter. Ultimately, these studies demonstrate the versatility of the human lung-on-a-chip platform in modeling human tissue and disease pathophysiology and evaluating drug response on a molecular, cellular, and tissue-level.

Gut-on-a-Chip

Similar to the lung-on-a-chip, simulating physiological function of the gut is critical to understanding how ingested foods, drugs, and liquids are digested, absorbed, and transported to the bloodstream for use by the body. With respect to drug development, the small intestine is a barrier responsible for the selective re-absorption of orally-administered

medications, which affects dosage requirements and bioavailability. Further, the gut is one of the first tissues that a nutrient, drug, or chemical interacts with upon ingestion. Therefore, physiological modeling of the gastrointestinal tract would permit studies of gastric inflammation, host-microbe interplay, and therapeutic discovery for diseases affecting the gastrointestinal tract such as Crohn's disease. Currently, animal models pose challenges to sufficiently predicting drug absorption, oral bioavailability, and intestinal metabolism in humans.[51] While *in vitro* models using Caco-2 cells cultured on Transwell inserts to create epithelial monolayers or hydrogel scaffolds to create 3D intestinal villi have been used to study gut absorption and drug permeability, these systems fail to recapitulate the complex tissue-specific structural and functional properties of the human intestine.[52-54] Microfluidic-based gut microdevices utilizing a semi-permeable membrane on which to culture a monolayer of Caco-2 cells were used to evaluate permeability coefficients of various molecules.[55, 56] However, a major factor missing in the aforementioned models is a mechanical peristaltic motion that the native gut experiences.

Ingber and colleagues built a functional gut-on-a-chip platform where Caco-2 cells are cultured on a thin permeable PDMS membrane within a microfluidic device that permits cyclic mechanical strains to mimic peristalsis, similar to the previously-discussed lung-on-a-chip system (Fig 1.3).[57] It was also shown that, as compared to static culture in a Transwell insert, the intestinal epithelial layer in the gut-on-a-chip with peristaltic motion had enhanced cell polarity, intestinal villi formation, barrier integrity, and upregulation of metabolizing enzymes such as CYP3A4.[58] As a critical component of the human gut is presence and co-existence with a microbial community, the gut-on-a-chip was co-cultured with a known

intestinal microbe, *Lactobacillus rhamnosus*, and remained viable and functional for several days.

In a separate study, the gut-on-a-chip was used to develop a disease model of human intestinal inflammation.[59] Under peristalsis, the gut-on-a-chip permitted long-term co-culture with known commensal probiotic microbes of the gut microbiome with intestinal epithelial cells. Further, the structure and function of intestinal pathophysiology, such as villi destruction and epithelial inflammatory processes, were recapitulated in response to pathogenic bacteria, such as *E. coli*. Similar to animal and human studies, it was demonstrated that probiotics and antibiotics can suppress tissue injury due to the pathogenic bacteria. Further, inflammation stimulated epithelial cells to produce pro-inflammatory cytokines that cause injury to villi and compromise barrier integrity. When peristalsis was halted, mimicking gastric conditions in patients with ileus or inflammatory bowel disease, bacterial overgrowth was activated. Thus, the gut-on-a-chip was proven to model intestinal inflammation, decouple various contributions to pathophysiology, and identify potential therapeutics in the form of inflammatory suppressors in this *in vitro* system. The gut-on-a-chip was also used to analyze infection, replication, and production of human enterovirus, a common virus that can lead to meningitis, bronchitis, pneumonia, myocarditis, and diabetes.[60] Given that analysis of enterovirus infection is challenging in animals due to variability between virus receptors in animals and humans, this study demonstrates a suitable *in vitro* model for investigating the pathophysiology of enterovirus infection. The gut-on-a-chip was further used to mimic intestinal injury due to acute exposure to radiation.[61] In the device, radiation exposure led to increased generation of reactive oxygen species, cell death, villi destruction, decrease in barrier permeability, and DNA fragmentation. Administration

of a prophylactic radio-protective drug, dimethyloxaloylglycine, prevented the radiation-induced injury responses (Fig 1.4). Finally, to position the gut-on-a-chip as a system to support human-related research and drug development, primary human intestinal cells isolated from tissue biopsies were used to form an intestinal monolayer comprised of villi-like projections and exhibiting multi-lineage differentiation.[62] The gut-on-a-chip has significant potential as a research tool to study metabolism, nutrition, infection, inflammation, disease pathophysiology, and drug development. Incorporation of patient-specific hiPSC-derived cells will expand its scope to a wider host of disease states and applications in personalized medicine.

Liver-on-a-chip

The liver is the principal organ involved in nutrient drug metabolism, a key constituent in determining a drug's bioavailability in the bloodstream, and a necessary tissue for toxicological studies. In fact, drug-induced liver toxicity and injury is one of the primary reasons for delays or failures in clinical trials, and animal models often fail to predict clinical response.[63] As a disease model, a human relevant liver-on-a-chip could accelerate research to find a treatment for acute hepatitis B, a viral infection that attacks the liver and only affects humans and chimpanzees. One of the key challenges in *in vitro* modeling of the liver remains the sheer complexity of liver tissue, which is composed of a wide variety of cells, such as hepatocytes, Kupffer cells, fibroblasts, and endothelial cells, with functions that vary with hepatic zonation and architectural arrangement. Since this results in spatiotemporal variation in drug metabolism and clearance, a physiological liver model would be a valuable tool in drug development. With respect to *in vitro* liver models, cellular zonation and formation of

nutrient gradient has been achieved using liver spheroids; however, this lacks fluid flow and the complexity of integrating various cell types.[64] Further, the liver is one of the most highly perfused organs of the body, and shear stress exerted by high rate of blood flow on hepatocytes has been shown to regulate gene expression.[65]

To address this, Powers, et al., developed a perfusable 3D liver tissue platform that exerted a physiological fluid shear stress onto liver spheroids and remained viable for 2 weeks.[66] More recently, Bhise and colleagues developed a liver-on-a-chip using bioprinted HepG2/C3A spheroids for drug toxicity studies (Fig. 1.5).[67] The production of proteins by the liver, including albumin, ceruloplasmin, transferrin, and A1AT was quantified over 1 month of culture, indicating long-term viability of the samples. Administration of acetaminophen, a drug known to cause liver toxicity, led to liver injury as evident by decreased biomarker secretion and metabolic activity. Bavli, et al. developed a liver-on-a-chip incorporated with sensors and oxygen-reactive micro-probes to monitor mitochondrial respiration and measure glucose and lactate levels.[68] In fact, cellular adaptation to mitochondrial damage was assessed by noting a shift from the oxidative to glycolytic pathway following exposure to rotenone and troglitazone, confirming the utility of the liver-on-a-chip to assess chemical toxicity even when no obvious effects on the cell or tissue viability are observed. Additionally, in the liver, bile canaliculi form between radially-arranged hepatocytes and excrete bile, while contains metabolic products generated by hepatocytes. To recreate this, Nakao et al. developed a device to recreate the structure of the hepatic cord using rat primary hepatocytes arranged in two aligned lines, ultimately forming bile canaliculi.[69] This demonstrates that biomimicry of tissue-specific architecture can result in the formation of functional tissue components.

Liver-on-a-chip disease models have also been developed. Using rat primary hepatocytes, Lee et al. modeled alcohol-induced liver disease by exposing liver spheroids to ethanol and observing decreased cell viability and impaired albumin secretion as compared to control samples, as well as fibrotic tissue build-up similar to what is seen *in vivo*.[70] The injury was partially-reversed upon supplying fresh, alcohol-free media to the liver tissues. Looking forward, hiPSC-based liver-on-a-chip models could open the door for patient-specific or disease-specific *in vitro* models. Recently, Schepers and colleagues demonstrated differentiation, viability, and sustained albumin secretion of iPS-derived hepatocyte aggregates encapsulated in a polyethylene glycol diacrylate (PEGDA) hydrogel and loaded onto a microfluidic chip.[71] As cells are sourced from an increasingly diverse population, such iPSC-derived models will be valuable tools in drug development and disease modeling that is relevant to human tissue function and pathophysiology.

Heart-on-a-chip

The heart is a critical organ responsible for pumping blood throughout the body, providing nutrients and oxygen to tissues while carrying away wastes, metabolites, and damaging toxins. Cardiovascular disease is amongst the leading cause of death in the world, and cardiac toxicity is the main cause of drug failures and withdrawals in phase I clinical trials.[72] Animal models have been shown to be poor models to evaluate cardiotoxicity due to innate species-based differences in heart rate, contraction, and calcium handling. Therefore, OOC models that mimic human cardiac function could be valuable tools in human-relevant drug screening. The design of heart-on-a-chip systems should emulate the structure of native cardiac tissue, including anisotropic alignment of cardiomyocytes and 3D laminar tissue

morphology. Further, incorporation of electrical stimulation, supporting cell types, and real-time readouts of contraction frequency, force amplitude, electrophysiology, and calcium flux. Several recent *in vitro* models of cardiac tissues have been formed using hESC-derived cardiomyocytes or neonatal rat cardiomyocytes encapsulated in a collagen-based or fibrin-based extracellular matrix, supported by two support structures, in which tissue structure and function has been characterized.[73-76] However, incorporation of engineered cardiac microtissues within a microfluidic device would enable simulation of fluid shear stresses and allow for future integration with other OOC devices to evaluate drug response on a systemic level.

Agarwal et al. described one of the first heart-on-a-chip platforms in which a microfluidic device houses an array of muscular thin films: monolayers of neonatal rat cardiomyocytes seeded on thin cantilever layers of soft elastomers that deflect during systolic contraction (Fig. 1.6).[77, 78] This deflection was quantified to calculate contractile stresses generated by the cardiac tissues. Anisotropic cardiac microtissues were composed of aligned cells expressing cardiac proteins like sarcomeric actinin. Electrodes were incorporated for electric field stimulation of the tissues. Further, the administration of isoproterenol correctly predicted a dose-dependent increase in contractility of the cardiac tissues, elucidating the heart-on-chip's role as a potential drug screening platform. Recently, Aung et al. demonstrated the development of three-dimensional heart-on-a-chip device composed of neonatal mouse cardiomyocytes encapsulated in the gelatin-derived hydrogel and viable for multiple weeks.[79] The microfluidic device was composed of a multi-layered hydrogel, including a polyacrylamide (PAm) layer on the bottom surface. Contractile stresses transduced to the PAm were measured by monitoring the elastic deformations of the PAm

and fitting these into the appropriate constitutive model for a linear elastic isotropic material. Further, changes in contractile properties were assessed for the positive inotropic agent epinephrine.

Recent progress in the establishment of robust cardiac differentiation protocols has led to the development of hiPSC-based cardiac heart-on-chip platforms. Mathur et al. used hiPSC-derived cardiomyocytes to create 3D cardiac microtissues with aligned tissue structures that remain viable and functional over several weeks.[80] Further, spontaneous cardiac contraction was characterized by analyzing beating frequency and electrophysiology via fluorescent calcium transients; however, contractile force was not quantified in this system. Contractile response to four pharmacological agents – isoproterenol, verapamil, metoprolol, and E4031 – resulted in IC50/EC50 values consistent with clinical values for adult human tissues, demonstrating the utility of the heart-on-chip to predict drug response. In another study, Marsano et al. used hiPSC-cardiomyocytes to form a 3D cardiac heart-on-a-chip platform that incorporates a pneumatic actuation system to induce homogeneous uniaxial cyclic strains to the tissue constructs.[81] It was demonstrated that mechanical strain increased cell viability, expression of cardiac markers troponin T and connexin-43, electromechanical coupling, synchronous contraction, contractile amplitude, and contraction velocity. Kit Parker and colleagues further developed the muscular thin film heart-on-a-chip to develop a cardiac disease model of the mitochondrial cardiomyopathy known as Barth syndrome from hiPSC donors.[82] The heart-on-a-chip was used to elucidate the pathophysiology of Barth syndrome in an *in vitro* platform, including structural, functional, and metabolic abnormalities of these tissues compared to controls. These included sarcomeric irregularities, low contractile stresses, and high levels of reactive oxygen species. The

platform was also used to assess new potential therapies for patient's suffering from Barth syndrome. Undoubtedly, future iterations of the heart-on-a-chip will continue to use patient-specific hiPSC-derived cardiomyocytes to study disease pathophysiology and screen for new drug therapies, especially for rare genetic conditions for which animal models are lesser developed or understood.

Skeletal Muscle-on-a-Chip

As the largest organ of our body by mass at 40-45%, skeletal muscle is responsible for supporting motion and activity that enhances quality of life for every human on earth. Additionally, skeletal muscle is injured in many ways – trauma, atrophy, or genetically-linked dystrophy. Skeletal muscle inflammation can lead to muscle weakness and long-term motion impairment. Therefore, human physiologically-relevant microfluidic skeletal muscle-on-a-chip platforms could be valuable tools in disease modeling and drug development. A host of animal models exist, including *mdx* mice to model Duchenne muscular dystrophy; however, animals are not ideal for studying drug discovery or cell transplantation as related to humans. A variety of 3D *in vitro* models of skeletal muscle have been developed over the last several years, typically involving the encapsulation of immortalized mouse myoblasts or primary mouse muscle cells in a collagen-based or fibrin-based hydrogel suspended between two support pillars to induce tissue alignment.[83-87] Asada and colleagues demonstrated sarcomere alignment and force generation of C2C12-based 3D skeletal muscle tissues optogenetically-controlled to contract.[87] Bursac and colleagues used neonatal rat myogenic cells to create macroscale 3D muscle tissue strips that are disrupted when exposed to cardiotoxin.[83] In a separate study using human primary myogenic cells, tissues were shown to contract in

response to electrical and chemical stimuli, while displaying hypertrophy or toxic myopathy in response to various drugs similar to clinical expectations.[88] These studies were recently extended to human relevance using hiPSC-derived myogenic cells.[89] In fact, skeletal muscle tissues have been cultured on free-standing PDMS substrates to create biological robots that move when the muscle contracts upon electrical stimulation.[90]

Within microfluidic skeletal muscle-on-a-chip systems, fewer advancements have been made. Anene-Nzelu et al. created a microfluidic system to culture and differentiate C2C12-based skeletal muscle tissues.[91] The synergistic effect of fluid shear stress parallel to topographical microgrooves led to efficient differentiation of muscle tissues, elongation of nuclei, and nuclear alignment (Fig. 1.7). Shimizu et al. developed a microfluidic skeletal muscle-on-a-chip with C2C12 cells encapsulated in a collagen hydrogel that compacts over the course of tissue culture.[92] Muscle tissue function was verified by observing twitch and tetanic contractions in response to increasing frequencies of electrical stimulation. In a separate study, a skeletal muscle disease model was developed by using dexamethasone to induce skeletal muscle atrophy.[93] As expected, skeletal muscle damage was observed in the form of fewer myotubes and lower contractile force, which was reversed by treatment with insulin-like growth factor (IGF-I), demonstrating the use of this platform as a drug screening platform. Ultimately, few advancements have been made in skeletal muscle-on-a-chip systems. Given the need for advanced, physiologically-relevant platforms, and rise in iPSC technology, skeletal muscle-on-a-chip platforms will serve as valuable tools in modeling rare diseases such as Duchenne muscular dystrophy to expedite the discovery of new therapeutics.

Cancer-on-a-Chip

With cancer rates rising due to an aging population and increasing environmental and health risk factors, microphysiological tumor models are needed to expedite drug discovery and development. Recreating the cancer microenvironment, including the tumor, stroma, and vascular network to reproduce how cancer cells interact with one another, other cell types, matrix proteins, and various chemical or biological stimuli would permit studies of tumor formation, proliferation, or death. In drug development, mouse models, including human xenografts in immunocompromised mice and humanized mice, serve as valuable and necessary tools because they capture the complexity of the tumor microenvironment in a living "whole-body" system. However, aside from the high-cost of animal studies, analysis at discrete steps requires sacrificing the animal, and obtaining quantitative mechanistic results poses serious challenges. Most importantly, the inability of these results to translate to humans has necessitated *in vitro* models, including OOCs. Many groups have worked to reproduce cancer *in vitro* by developing 3D models of solid tumors using cell lines, along with co-culture with support cells, incorporation of extracellular matrix, and spatiotemporal introduction of chemical factors.[94] However, the application of 3D tumor models to cancer-on-a-chip could provide a systematic approach to studying cancer by incorporating flow and shear stress, creating increasingly-complex microenvironments to simulate native cancer tissue (such as breast tissue niche in addition to breast cancer cells), modeling cancer metastasis to a secondary site, testing drug efficacy, and developing a personalized medicine model from biopsied tumor tissue.

Several cancer-on-a-chip devices have been developed to provide insight into tumor growth, cancer cell metastasis, drug penetration, drug specificity, and drug efficacy.[95-99] For example, Kim et al. developed a cancer-on-a-chip platform composed of 3D tumor spheroids

cultured under perfusion within a microfluidics device.[100] Recently, Aung et al. described a tumor-on-chip platform in which a morphogen-gradient due to fluid flow results in the formation of an endothelial barrier that mimics the blood vessel-tumor microenvironment, and further assessed the utility of the system for drug screening by administering doxorubicin.[101] Hughes and colleagues detailed the formation of a cancer-on-a-chip composed of 3D microtumors infiltrated and supported by perfusable vascular networks.[102] These vascularized tumors were shown to respond to standard cancer therapies, including taxol and estradiol. Further, this system permits investigation of drugs that specifically target the tumor vasculature, including linifanib, which by disrupting angiogenesis and vascular stability could reduce nutrient supply to the tumor and help lead to successful treatment. This same system was scaled up to permit analysis of 12 independent samples for higher-throughput analysis, critical for economical drug screening.[103] Marturano-Kruik et al. developed a complex OOC breast cancer metastasis model by creating a bone perivascular niche composed of a bone matrix, endothelial cells, bone marrow stem cells, and metastatic breast cancer cells to investigate cancer infiltration and colonization into bone tissue.[104] In fact, under perfusion in the microfluidic chip, perivascular cells formed a dense vascular network that mediates cancer migration and reduces cancer cell proliferation, indicating the importance of mechanobiological cues to accurately recreate a tumor microenvironment. One key hurdle in cancer-on-a-chip systems is cell sourcing, where the majority of previously-described platforms utilize easy-to-use cell lines of questionable identity and relevance to humans. Although cancer biopsy tissue is in limited supply and is comprised of cells of varying genetic identity, these cells would serve as valuable systems for individualized medicine in determining the optimal drug regiments from one patient to the next.

Multi-organ-on-a-Chip

The human body is a highly-interconnected system of organs and tissues that communicate with one another via soluble factors through an extensive vascular network. In the case of a medication, the drug typically follows a linear path after ingestion, where it is broken down in the stomach, reabsorbed by the intestinal lining, metabolized by the liver, and then pumped to the rest of the body by the heart, eventually reaching both the target tissue and off-target tissues. Metabolism in the body may alter a drug's molecular structure or bioavailability, thus its effect may deviate from its original expected outcome. Therefore, recreating physiological organ-organ cross-talk is essential to holistically understanding drug response. Additionally, while a drug may be efficacious to the diseased target tissue, it may also cause unexpected, potentially-fatal off-target toxicities. In fact, drug-induced toxicities, primarily cardiotoxicity and hepatotoxicity, account for up to 30% of drug attrition phase I clinical trials.[105] Certain gold-standard treatments for cancer malignancies are known to cause severe cardiotoxicities; however, due to their effectiveness in managing cancer progression, cardiac function is managed with beta blockers and ACE inhibitors. For example, the anthracycline doxorubicin directly causes apoptosis of cardiac myocytes due to a severe increase in oxidative stress, leading to issues ranging from minor arrhythmias to congestive heart failure. To combat doxorubicin-induced cardiotoxicity in breast cancer patients, dexrazoxane is co-administered as cardioprotective agent that reduces the presence of toxic superoxide radicals through iron chelation.[106] Such co-dependent interactions are typically investigated in animals because they are difficult to model and predict in conventional *in vitro* cell culture. In addition to this, pharmacokinetics and associated processes such as

ADME (absorption, distribution, excretion, and metabolism) must be modeled and studied in a whole living organism. However, as discussed previously, animal studies have high costs and ethical issues, and moreover often fail to translate to clinical trials due to inherent differences between the two species. Therefore, while individual organs-on-chips have been shown to effectively model the structure and function of native tissues and their chemical, physical, and mechanical microenvironments, a multi-organ 'body-on-a-chip' system that integrates individual organs into a single platform with a unified "vascular network" represented by microfluidic channels may facilitate a more complete, physiological approach to drug delivery and uptake.

Several different multi-organ approaches have been explored in recent years. The Shuler research group developed a modular, gravity flow-driven platform to independently develop intestinal tract and liver tissues in 3D constructs before integrating them together for 14 days of co-culture, maintaining barrier function of the GI tissue and metabolic rates and protein production of the liver tissue.[107] They further developed a pumpless device with chambers for up to 13 organs, including barrier (skin, GI tract, lung) and non-barrier (heart, liver, kidney, muscle, brain, bone marrow, spleen, pancreas, adrenal glands, fat) type tissues.[108] In a proof-of-concept with five tissues, high cell viability was observed after 7 days of culture. Loskill et al. recently described a Lego-like plug-and-play organ-on-a-chip system to enable individual culture of OOCs and subsequent connection together to create a multi-organ platform with a single flow-through of media rather than recirculation.[109] In a two-organ system containing two heart-on-chip devices, the integrated system yielded high viability and cardiac function over time. Griffith and colleagues describe a re-usable microfluidic platform powered by a pneumatically-driven pump for the co-culture of up to

10 tissue constructs and demonstrate cellular viability and function over a three-week period.[110]

Multi-organ platforms have also been developed to evaluate drug toxicities and organ cross-talk. A multi-organ pumpless microfluidic system containing 3D hydrogel cultures of liver, colon cancer, and bone marrow in independent chambers was developed and shown to reproduce the metabolism of a cancer pro-drug, Tegafur, by the liver to 5-fluorouracil and subsequent death of cancer cells.[8] Zhang et al. described the development of an automated OOC system with integrated physical, biochemical, and optical sensors for *in situ* real-time analysis, and performed various drug tests to demonstrate electrochemical sensing of parameters such as albumin secretion, CK-MB secretion, temperature, pH, and oxygen levels.[111] Ma et al. developed a multi-organ 3D system of liver and glioblastoma tissues and showed that cells within the 3D culture were more resistant to cancer therapeutics than their 2D equivalents.[112] Hickman and colleagues showed the viability and function of a four-organ system (heart, liver, skeletal muscle, and brain), and also used the system to demonstrate that the pharmacological toxicities of five different drugs to each tissue was in general accordance with published human and animal data.[113] Most recently, Atala and colleagues have demonstrated inter-organ interactions of a three-chip system consisting of liver, heart, and lung OOCs, and observed drug responses that rely on tissue cross-talk such as bleomycin-induced secretion of lung inflammatory factors which drove cardiac cell death and reduction in contractile function (Fig. 1.9).[114] Therefore, multi-organ-on-a-chip systems offer the potential to mimic the *in vivo* paradigm in order to serve as predictive tools that inform drug development from multiple angles.

1.7 What limitations do microfluidics devices present?

Despite its obvious benefits, microfluidics-based OOC devices have drawbacks that will need to be overcome. First, PDMS has its limitations. As a hydrophobic material, a known drawback to PDMS is its ability to absorb hydrophobic molecules, including drug compounds which are often hydrophobic.[115, 116] Therefore, as drug screening platforms, PDMS-based microfluidic devices are not ideal for all toxicity and efficacy studies. For example, if a drug is retained within the PDMS upon infusion into the device, the actual concentration of drug delivered to the cells in the device will be lower than expected, thus the results cannot be readily accepted. Further studies would be necessary to determine how much of the drug is absorbed by the PDMS under acellular conditions in order to adjust the administered concentration accordingly. Additional materials have also been explored for OOCs, such as polystyrene and polycarbonate, which do not absorb molecules. However, these tend to be costly and cannot be readily molded into any shape.[117]

There are additional shortcomings to microfluidics technology as well. As mentioned previously, PDMS-based microfluidic devices are fabricated through soft lithography and replica molding, where each device is created by casting un-polymerized PDMS onto a silicon wafer.[118] This requires extensive labor to initially cast, cure, and remove the patterned PDMS substrate before bonding it to glass to create the device. Depending on the intricacies of the device design, there may be additional fabrication procedures along the way, such as incorporating a porous membrane or pre-forming hydrogels.[29, 79] This can lead to long manufacturing times and higher development costs. Most devices are single-use as re-sterilization can be a challenge, especially after cells and tissues have been cultured inside. Additionally, microfluidics devices are powered by syringe pumps, peristaltic pumps, or

microfluidic controllers. Each instrument occupies a significant amount of space and can only power a finite number of samples. Transporting OOCs with specialized equipment, inputs, and outputs could be difficult and may not be feasible without compromising tissue integrity. With respect to simulating physiological conditions, fluidic-based mechanical stimulation is not sufficient for all tissue types. For example, cardiac and skeletal muscle applications require the incorporation of electrodes to stimulate the active contraction of the tissues.[74, 88] Further, the effect of various physical factors, such as surface topography and roughness, can become amplified at the micro-scale and could cause turbulent flow or spatially-heterogeneous flow distribution if not carefully designed. At the micro-scale, there may be a limit to the level of tissue complexity that can be achieved. For example, the feature size, including the height and width, of PDMS-based devices is entirely dependent on the resolution of the original silicon wafer, with a height maximizing around 100μm. Therefore, the formation of certain tissue architectures, such as a blood vessel with a lumen to allow for blood flow or multi-layered cell stacks to re-create various tissue architectures, could be hindered by the dimensions permitted by the device. Lastly, integration of multiple organs-on-chips will face challenges due to the various specialized media conditions required for the maintenance of different cell types. While cell lines are often resistant to media fluctuations, as OOCs move towards hiPSC-based tissues sensitive to specific media formulations, a new universal media, or "blood substitute", will be required to sustain their structure and function.

1.8 Supporting Technologies to Enhance OOCs

Adjacent technologies, such as 3D printing, offer an alternative strategy that could help overcome some of the limitations associated with microfluidics. 3D bioprinting involves

creating organ-like constructs layer-by-layer using different biomaterials. Various 3D printing "inks" have been developed to either encapsulate cells, such as gelatin methacrylate, or create sacrificial layers, such as Pluronic-F127 or carbohydrate glass.[119] In fact, Kolesky et. al., recently used 3D printing to print three cell inks: a silicone elastomer to create the microfluidic housing for the tissue-engineered sample, a cell-laden hydrogel of fibroblasts, and an acellular Pluronic F127-based sacrificial network, which was removed and subsequently seeded with endothelial cells that lined the walls to form a perfusable vasculature (Fig. 1.10).[120] In a follow-up study the authors again married microfluidics and 3D printing to demonstrate the formation of a thick vasculature that, when perfused with relevant growth factors, induced the differentiation of human mesenchymal stem cells seeded in the surrounding regions to an osteogenic lineage.[121] Further, the tissue-engineered construct was sustained under constant perfusion for over 6 weeks. Therefore, 3D printing technologies can incorporate the continuous flow aspect of microfluidics within a versatile, user-friendly, and programmable and automated system. Layer-based printing also allow for the incorporation of additional electrical, mechanical, and biological components. Lind et. al. demonstrated the 3D bioprinting of cardiac microphysiological devices printed with six different biomaterial inks, including one to build a strain gauge sensor directly into the device to automatically quantify contractile stresses generated by the cardiac micro-tissues.[122] As 3D bioprinting research continues to burgeon, printers with higher resolution and new inks with versatile, biocompatible material properties will continue to be developed.[123]

1.9 Conclusion

By mimicking human tissue physiology, including tissue architecture and function, and the native micro-environmental cues, organs-on-chip (OOCs) provide an attractive alternative platform for drug development. OOCs capable of accurately predicting the human physiological response to drugs could supplement current *in vitro* studies and greatly reduce the number of animal studies performed. By de-risking each compound, OOCs would remove drug candidates most likely to fail in humans, thus allowing pharmaceutical researchers to efficiently allocate time and resources to the highest-value indications and ultimately increase the rate of success of new drugs candidates. OOCs also provide a platform for application to disease modeling and personalized medicine. When combined with human cell sources, such as hiPSC which maintain the genetic identity of the original donor, OOCs can be a powerful, transformative research tool to understand disease pathophysiology and elucidate therapeutic targets. Further, OOCs can provide accurate and cost-effective models to enable drug discovery for rare, under-studied diseases, offering hope for patients suffering from conditions with no cure in sight. Integrating multiple human-based OOCs together into one unified platform sharing a single circulatory network could ultimately emulate a whole human *in vitro*, enabling the simultaneous study of drug efficacy and toxicities. Up to this point, the clinical significance and drug-screening translatability of OOCs has yet to be proven; however, as OOC model complexity increases and drug validation studies continue, we anticipate OOCs to bridge the wide expanse between pre-clinical and clinical development.

1.10 Acknowledgments

Chapter 1, in full, is currently being prepared for submission to publish the material. Gaurav Agrawal and Shyni Varghese, “Organs-on-Chips: Changing the Paradigm of Drug Development”. The dissertation author is the primary investigator and author of this material.

1.11 Figures

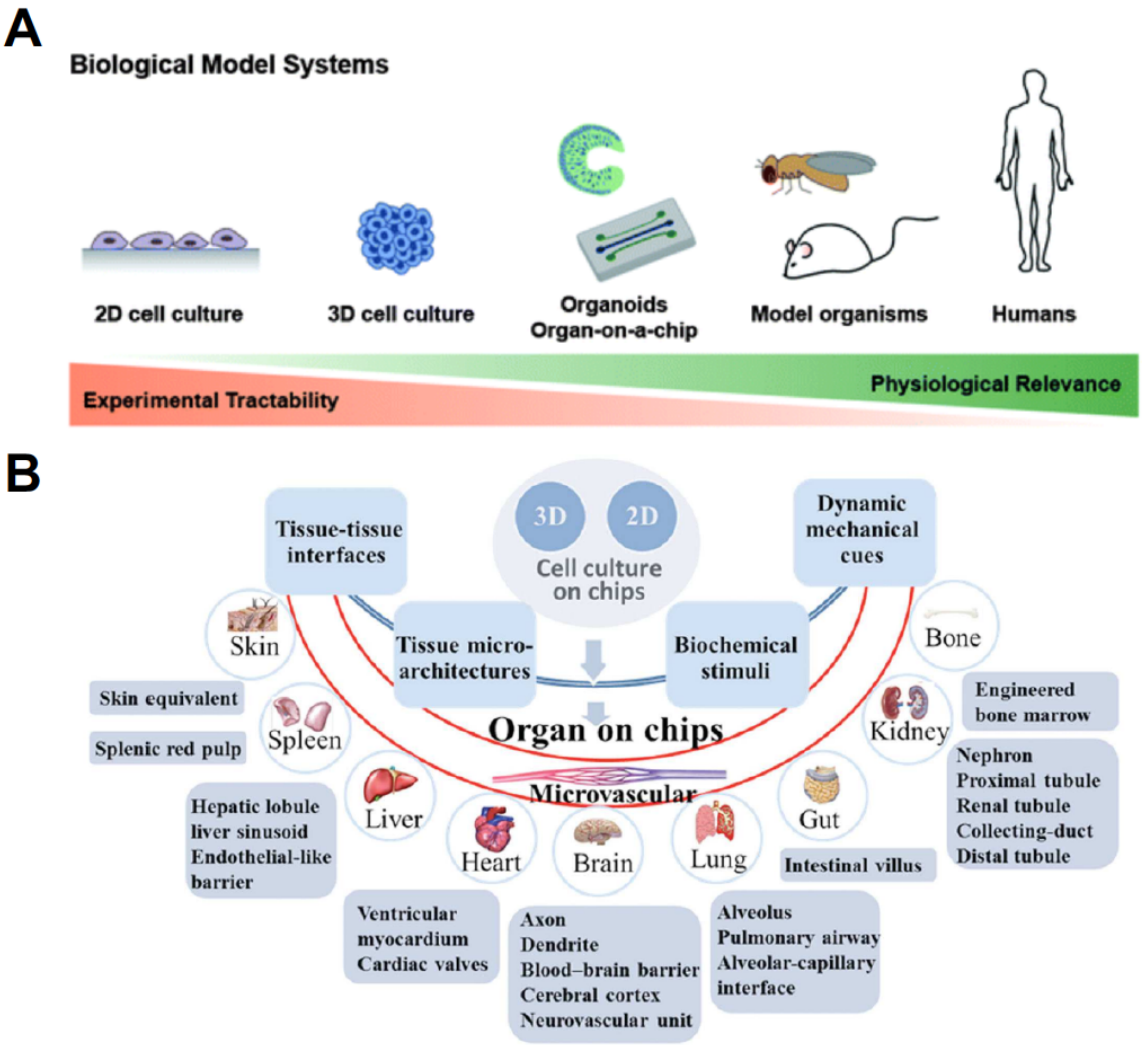

Figure 1.1: Organ-on-a-Chip systems

(A) Various biological model systems, ranging from 2D cell culture to humans. Organs-on-chips form a bridge between cell culture and whole organisms, and may better predict drug response in humans. Reprinted from Jackson, et al.[124] (B) Organs-on-chips incorporate various physiological aspects to recreate complex cell and tissue microenvironments and simulate various functional organs. Reprinted from Zheng, et al.[125]

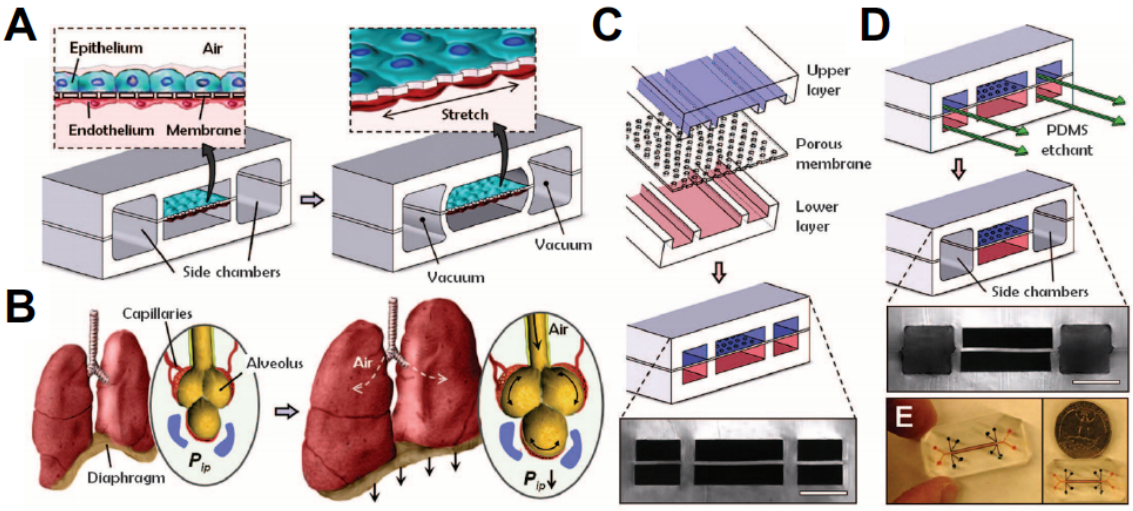

Figure 1.2: Lung-on-a-chip model system

(A) Porous membrane coated with epithelial cells on one side and endothelial cells on the other side, adjacent to empty chambers. Applying a vacuum generates a mechanical strain to stretch the cell-laden membrane. (B) Natural lung expansion process during breathing, recreated in the lung-on-a-chip. (C) Two PDMS components are bonded to a porous membrane, which is later etched away on the side channels to create vacuum chambers (D). Reprinted from Huh, et al.[29]

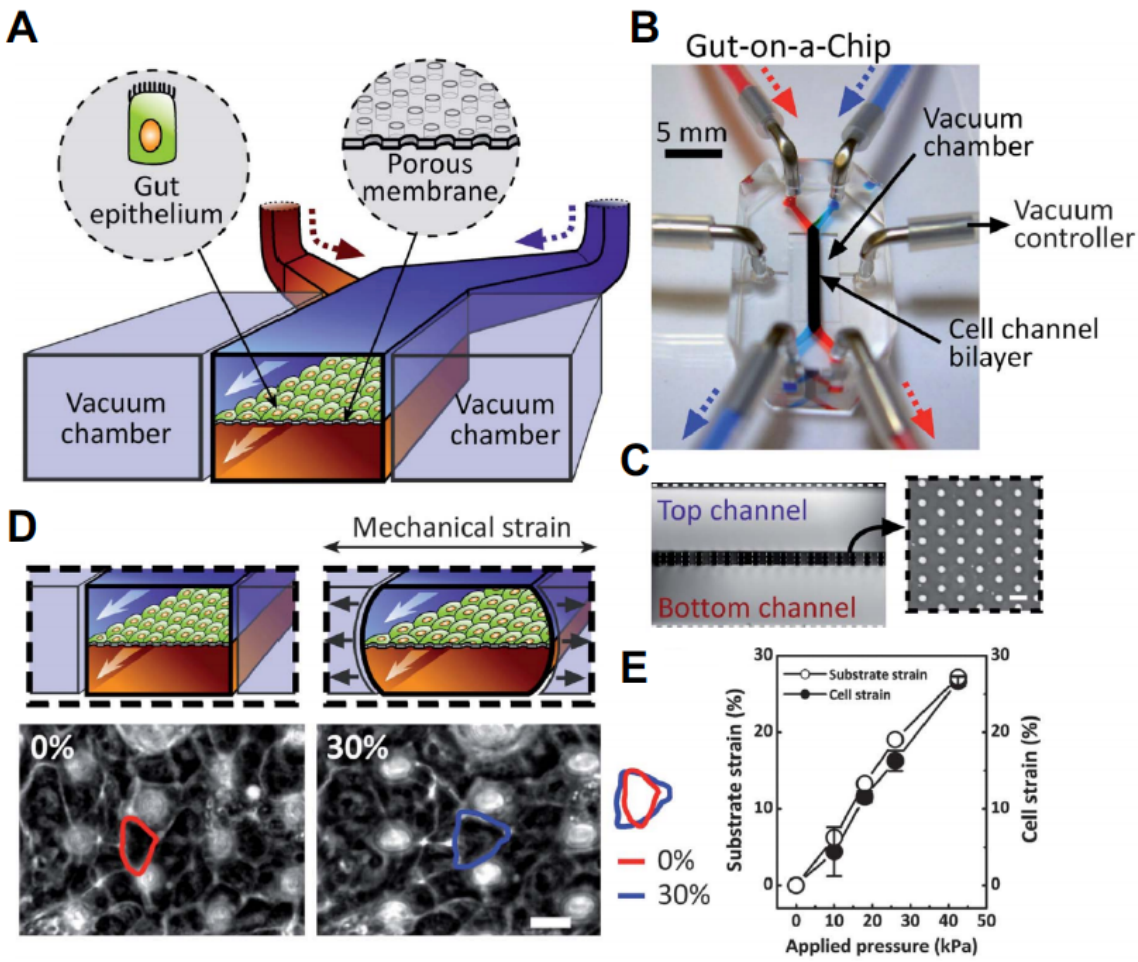

Figure 1.3: Gut-on-a-chip model system

(A) Schematic depicting the gut-on-a-chip with a porous membrane coated with epithelial cells on one side adjacent to two empty chambers. (B) Picture of the gut-on-a-chip showing the various flow paths for media or vacuum. (C) Photo of the cross-sectional view of the device, with the porous membrane horizontally-across the center. (D) Applying a vacuum generates a mechanical strain to stretch the cell-laden membrane up to 30%, mimicking peristalsis. (E) Quantification of strain in the porous membrane versus strain in the gut epithelial cells. Reprinted from Kim, et al.[57]

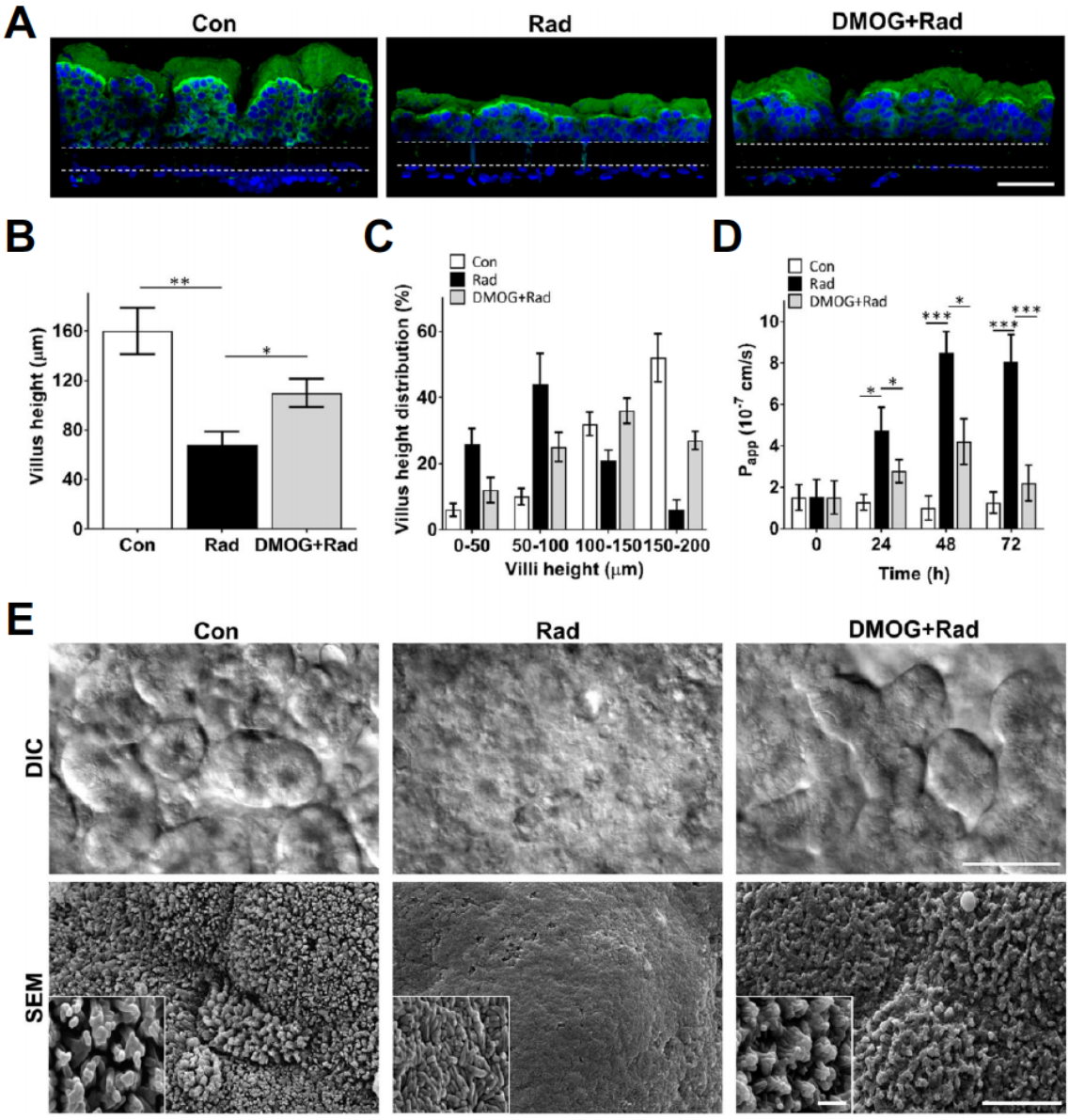

Figure 1.4: Gut-on-a-chip mimics intestinal injury due to radiation

(A) Intestinal villi are destroyed by radiation but protected by prophylactic administration of DMOG, a radio-protective drug. Changes in (B) villi height, (C) villus height distribution, (D) and apparent paracellular permeability before and after exposure to radiation and/or DMOG protection. (E) DIC and SEM micrograph images of villi under these same conditions. Reprinted from Jalili-Firoozinezhad, et al.[61]

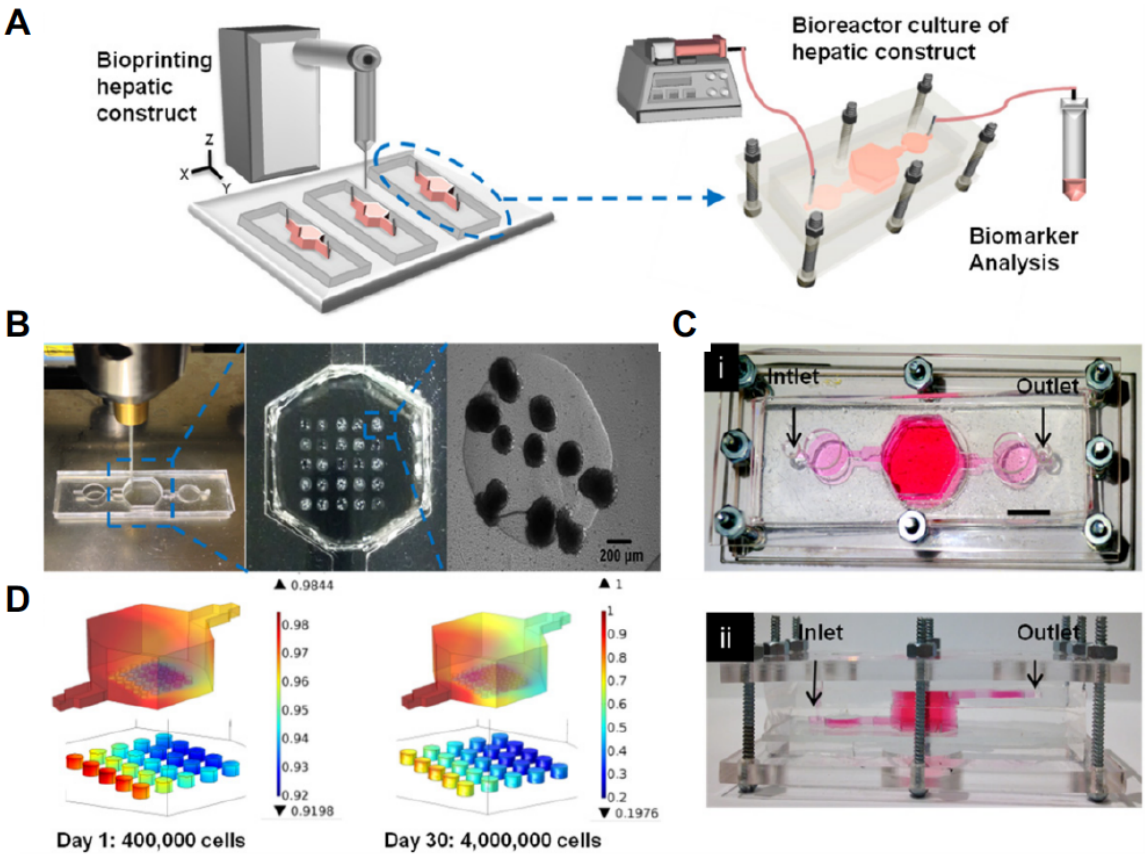

Figure 1.5: Liver-on-a-chip developed via bioprinting

(A) Schematic of hepatic bioprinted microfluidic device with biomarker analysis of secreted elutant. (B) Photo of bioprinting, demonstrating formation of multiple independent constructs per device. Each construct consists of hepatic spheroids. (C) Top-view and side-view of complete device with media perfused. (D) Model of oxygen concentration gradient at day 1 and day 30 of culture. Reprinted from Bhise, et al.[67]

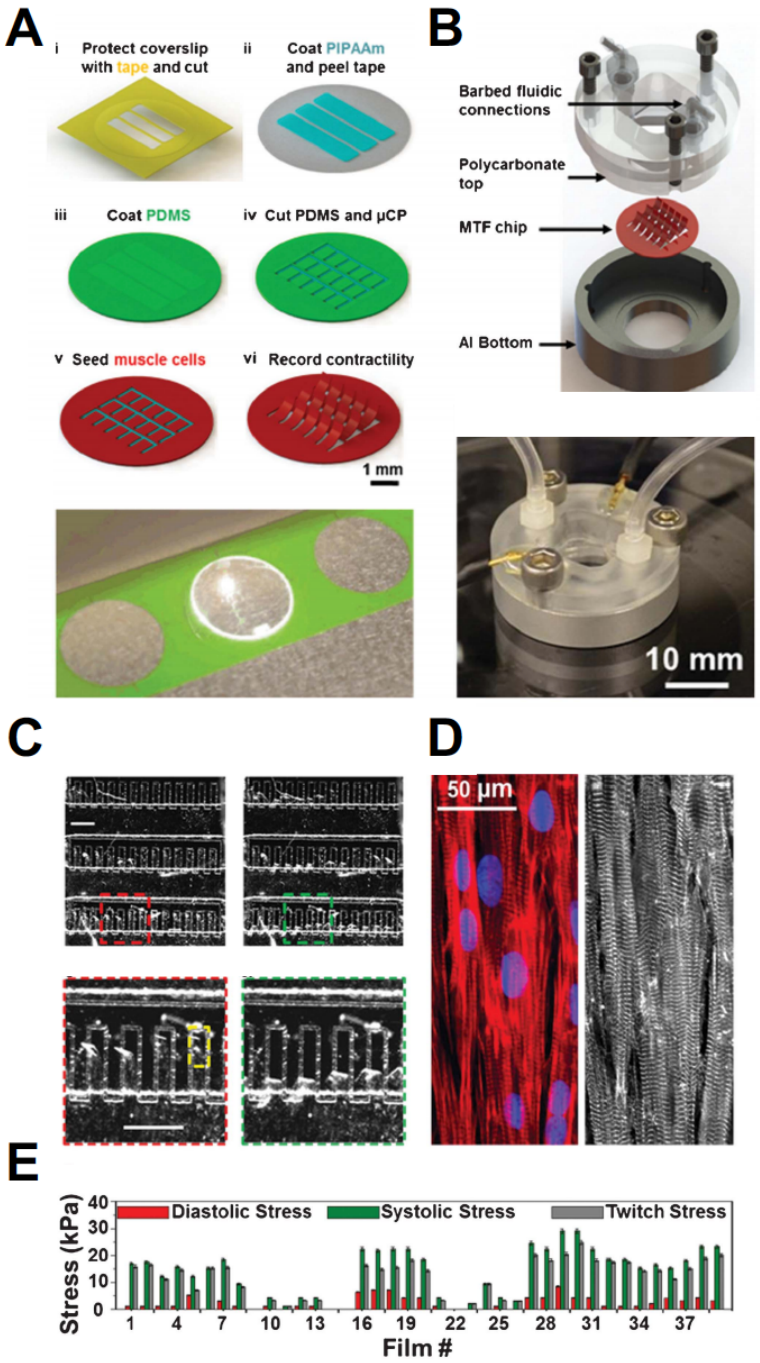

Figure 1.6: Heart-on-a-chip model system

(A) Procedure for forming muscular thin film (MTF). (B) Integration of the MTF into a microfluidic device. (C) Array of cardiac MTFs and displacement of MTFs during systolic and diastolic contraction. (D) IF staining of actin filaments with nuclei (left), and α-actinin (right). (E) Quantification of stresses from one chip for 40 MTF samples. Reprinted from Agarwal, et al.[78]

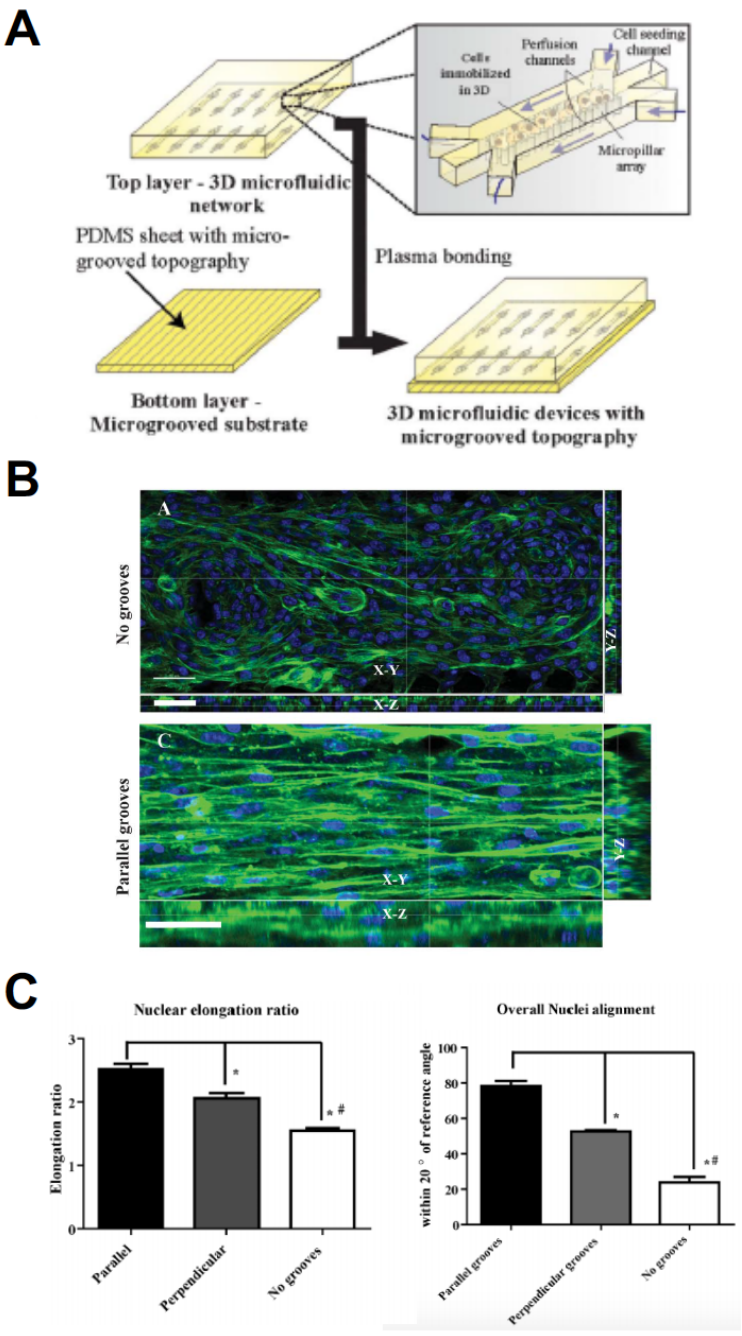

Figure 1.7: Skeletal muscle-on-a-chip model system

(A) Schematic of microfluidic device with micro-grooved topography to promote cell alignment. (B) IF staining of actin filaments with nuclei on patterned and un-patterned substrates (C) Quantification of nuclear elongation ratio and nuclear alignment. Reprinted from Anene-Nzelu, et al.[91]

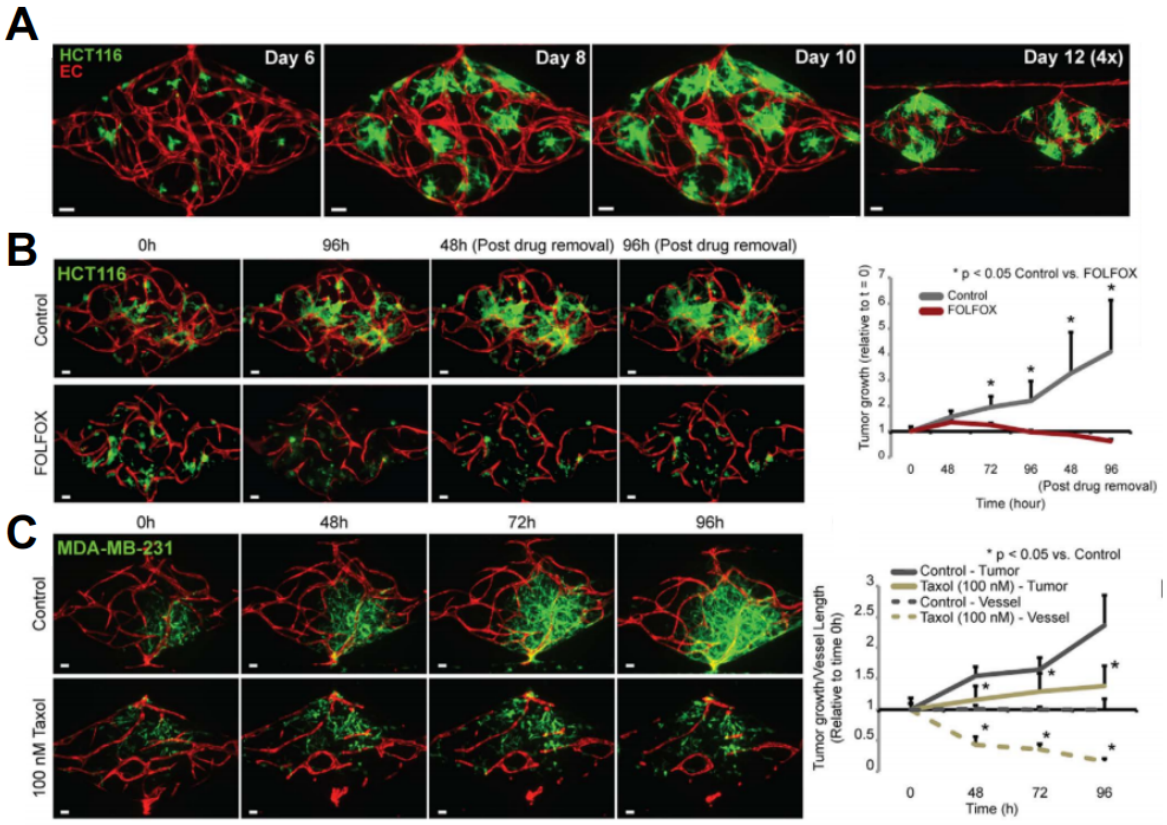

Figure 1.8: Highly-vascularized cancer-on-a-chip subjected to standard-of-care treatments

(A) Vasculature (red) and micro-tumors (green) are cultured for 12 days, leading to tumor growth under normal conditions. (B) Drug screen of FOLFOX (combination of 5-FU, Leucovorin, and Oxaliplatin) versus no-drug control demonstrates suppression of tumor growth in response to drug as compared to control conditions. (C) Drug screen of Taxol versus no-drug control illustrates suppression of tumor growth in response to drug as compared to control. Reprinted from Sobrino, et al.[102]

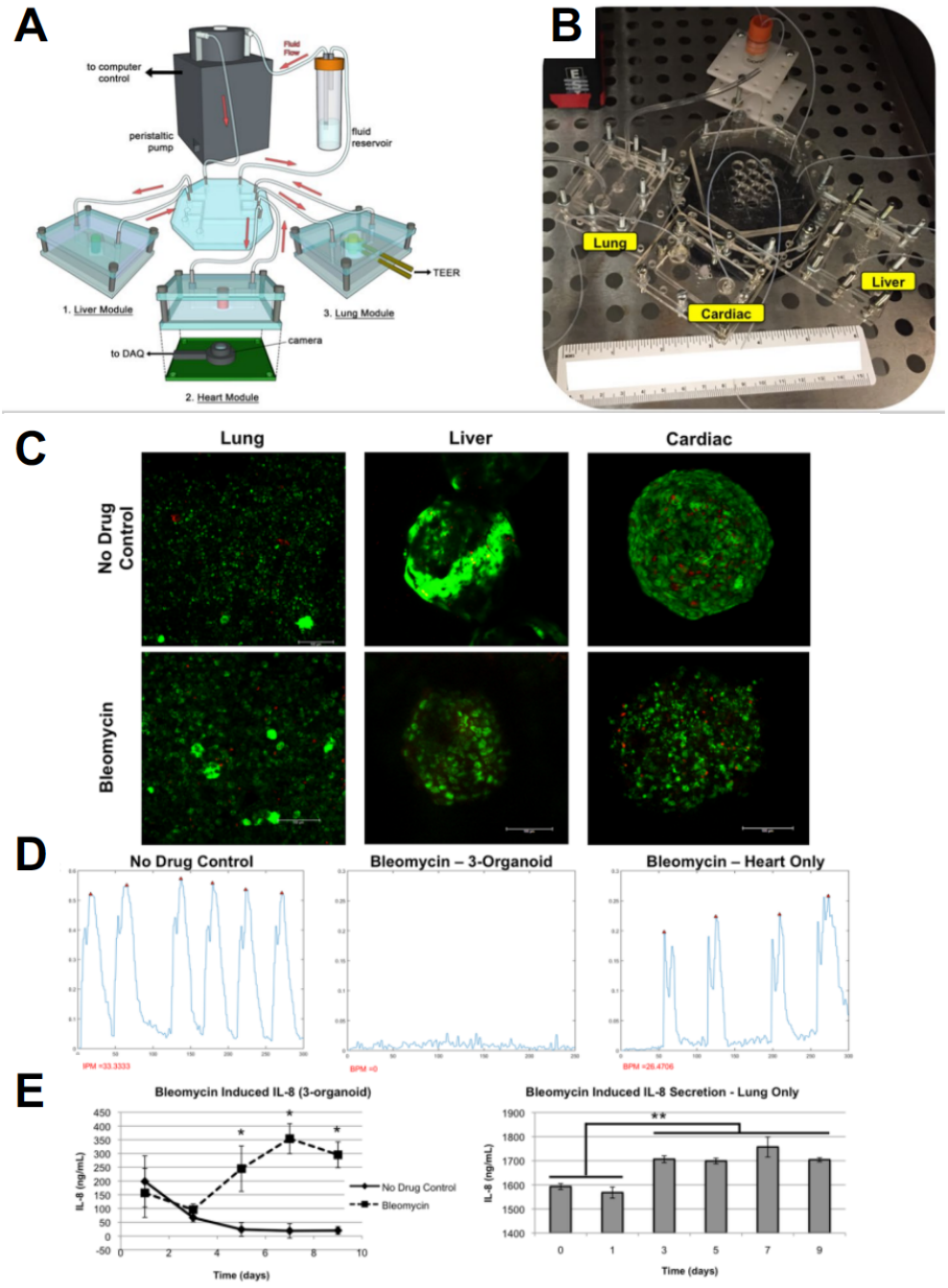

Figure 1.9: Multi-organ-on-chip system consisting of liver, heart, and lung models

(A) Schematic of setup and (B) photo of actual multi-organ system. (C) Live/dead cell viability following bleomycin administration. (D) Bleomycin-induced cardiac toxicity as indicated by drop in cardiac activity due to secretion of lung inflammatory factors. (E) Bleomycin causes secretion of IL-8 in the integrated multi-organ system as well as in a standalone, individual lung-on-chip. Reprinted from Skardal, et al.[114]

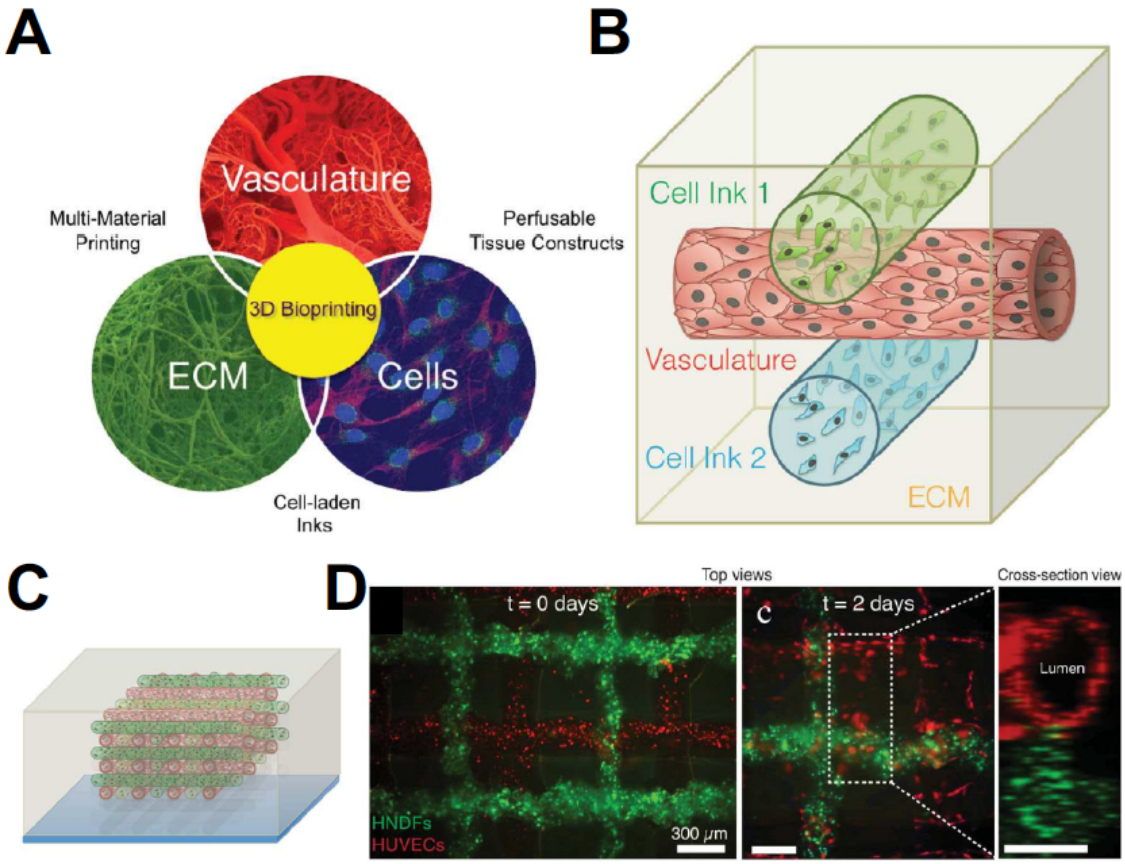

Figure 1.10: 3D bioprinting to create multi-material constructs

(A) Schematic depiction of capability of 3D bioprinters to create perfusable tissue constructs using multiple cell-laden and acellular inks. (B) Printing of vasculature, cells, and ECM proteins creates discrete subunits that contribute to the tissue engineered construct. (C) Illustration of multi-layered 3D printed construct containing two cell inks, one for fibroblasts (green) and one for endothelial cells (red). (D) IF images of the multi-material print demonstrate the formation of a vascular lumen. Reprinted from Kolesky, et al.[120]

1.12 References

1. S. M. Paul, D. S. Mytelka, C. T. Dunwiddie, C. C. Persinger, B. H. Munos, S. R. Lindborg and A. L. Schacht, *Nat Rev Drug Discov*, 2010, **9**, 203-214.

2. J. W. Scannell, A. Blanckley, H. Boldon and B. Warrington, *Nat Rev Drug Discov*, 2012, **11**, 191-200.

3. A. Mathur, P. Loskill, S. Hong, J. Y. Lee, S. G. Marcus, L. Dumont, B. R. Conklin, H. Willenbring, L. P. Lee and K. E. Healy, *Stem Cell Res Ther*, 2013, **4**.

4. I. Kola and J. Landis, *Nat Rev Drug Discov*, 2004, **3**, 711-715.

5. J. Bowes, A. J. Brown, J. Hamon, W. Jarolimek, A. Sridhar, G. Waldron and S. Whitebread, *Nat Rev Drug Discov*, 2012, **11**, 909-922.

6. E. R. Shamir and A. J. Ewald, *Nat Rev Mol Cell Bio*, 2014, **15**, 647-664.

7. S. N. Bhatia and D. E. Ingber, *Nature biotechnology*, 2014, **32**, 760-772.

8. J. H. Sung and M. L. Shuler, *Lab on a chip*, 2009, **9**, 1385-1394.

9. R. Greek and A. Menache, *Int J Med Sci*, 2013, **10**, 206-221.

10. F. Pampaloni, E. G. Reynaud and E. H. K. Stelzer, *Nat Rev Mol Cell Bio*, 2007, **8**, 839-845.

11. R. Edmondson, J. J. Broglie, A. F. Adcock and L. J. Yang, *Assay Drug Dev Techn*, 2014, **12**, 207-218.

12. D. Antoni, H. Burckel, E. Josset and G. Noel, *Int J Mol Sci*, 2015, **16**, 5517-5527.

13. F. J. O'Brien, *Mater Today*, 2011, **14**, 88-95.

14. G. D. Nicodemus and S. J. Bryant, *Tissue Eng Pt B-Rev*, 2008, **14**, 149-165.

15. E. Fennema, N. Rivron, J. Rouwkema, C. van Blitterswijk and J. de Boer, *Trends Biotechnol*, 2013, **31**, 108-115.

16. R. Mroue and M. J. Bissell, *Methods Mol Biol*, 2013, **945**, 221-250.

17. E. Cukierman, R. Pankov, D. R. Stevens and K. M. Yamada, *Science*, 2001, **294**, 1708-1712.

18. A. Riedl, M. Schlederer, K. Pudelko, M. Stadler, S. Walter, D. Unterleuthner, C. Unger, N. Kramer, M. Hengstschlager, L. Kenner, D. Pfeiffer, G. Krupitza and H. Dolznig, *J Cell Sci*, 2017, **130**, 203-218.

19. G. Gintant, P. T. Sager and N. Stockbridge, *Nat Rev Drug Discov*, 2016, **15**, 457-471.

20. A. Jekunen, *Drug Des Devel Ther*, 2014, **8**, 2009-2016.

21. R. Vassar, *Nature Medicine*, 2011, **17**, 932-933.

22. P. Pound, S. Ebrahim, P. Sandercock, M. B. Bracken, I. Roberts and R. Grp, *Brit Med J*, 2004, **328**, 514-517.

23. A. D. van der Meer and A. van den Berg, *Integr Biol (Camb)*, 2012, **4**, 461-470.

24. H. V. Prentice-Mott, C. H. Chang, L. Mahadevan, T. J. Mitchison, D. Irimia and J. V. Shah, *Proceedings of the National Academy of Sciences of the United States of America*, 2013, **110**, 21006-21011.

25. E. Cimetta, C. Cannizzaro, R. James, T. Biechele, R. T. Moon, N. Elvassore and G. Vunjak-Novakovic, *Lab on a chip*, 2010, **10**, 3277-3283.

26. R. R. Xiao, W. J. Zeng, Y. T. Li, W. Zou, L. Wang, X. F. Pei, M. Xie and W. H. Huang, *Anal Chem*, 2013, **85**, 7842-7850.

27. A. Seidi, H. Kaji, N. Annabi, S. Ostrovidov, M. Ramalingam and A. Khademhosseini, *Biomicrofluidics*, 2011, **5**, 22214.

28. S. H. Park, W. Y. Sim, B. H. Min, S. S. Yang, A. Khademhosseini and D. L. Kaplan, *PloS one*, 2012, **7**, e46689.

29. D. Huh, B. Matthews, A. Mammoto, A. Montoya-Zavala, H. Y. Hsin and D. E. Ingber, *Science*, 2010, **328**, 1662-1669.

30. M. C. Belanger and Y. Marois, *J Biomed Mater Res*, 2001, **58**, 467-477.

31. G. Kaur and J. M. Dufour, *Spermatogenesis*, 2012, **2**, 1-5.

32. J. P. Gillet, S. Varma and M. M. Gottesman, *J Natl Cancer Inst*, 2013, **105**, 452-458.

33. T. A. Rando and H. M. Blau, *The Journal of cell biology*, 1994, **125**, 1275-1287.

34. M. Severgnini, J. Sherman, A. Sehgal, N. K. Jayaprakash, J. Aubin, G. Wang, L. Zhang, C. G. Peng, K. Yucius, J. Butler and K. Fitzgerald, *Cytotechnology*, 2012, **64**, 187-195.

35. W. E. Louch, K. A. Sheehan and B. M. Wolska, *J Mol Cell Cardiol*, 2011, **51**, 288-298.

36. M. Corti, A. R. Brody and J. H. Harrison, *Am J Respir Cell Mol Biol*, 1996, **14**, 309-315.

37. U. Lichti, J. Anders and S. H. Yuspa, *Nature protocols*, 2008, **3**, 799-810.

38. R. A. Coleman, *ISRN Pharm*, 2011, **2011**, 806789.

39. E. Dick, D. Rajamohan, J. Ronksley and C. Denning, *Biochem Soc Trans*, 2010, **38**, 1037-1045.

40. Z. Zhang, Y. Zhang, F. Gao, S. Han, K. S. Cheah, H. F. Tse and Q. Lian, *Mol Ther Nucleic Acids*, 2017, **9**, 230-241.

41. K. Takahashi and S. Yamanaka, *Cell*, 2006, **126**, 663-676.

42. Y. Shi, H. Inoue, J. C. Wu and S. Yamanaka, *Nat Rev Drug Discov*, 2017, **16**, 115-130.

43. E. Shoji, H. Sakurai, T. Nishino, T. Nakahata, T. Heike, T. Awaya, N. Fujii, Y. Manabe, M. Matsuo and A. Sehara-Fujisawa, *Scientific reports*, 2015, **5**, 12831.

44. L. Boublil, E. Assemat, M. C. Borot, S. Boland, L. Martinon, J. Sciare and A. Baeza-Squiban, *Toxicol In Vitro*, 2013, **27**, 533-542.

45. O. Escaffre, V. Borisevich, L. A. Vergara, J. W. Wen, D. Long and B. Rockx, *J Gen Virol*, 2016, **97**, 1077-1086.

46. P. H. Karp, T. O. Moninger, S. P. Weber, T. S. Nesselhauf, J. L. Launspach, J. Zabner and M. J. Welsh, *Methods Mol Biol*, 2002, **188**, 115-137.

47. T. Kniazeva, J. C. Hsiao, J. L. Charest and J. T. Borenstein, *Biomedical microdevices*, 2011, **13**, 315-323.

48. D. Huh, D. C. Leslie, B. D. Matthews, J. P. Fraser, S. Jurek, G. A. Hamilton, K. S. Thorneloe, M. A. McAlexander and D. E. Ingber, *Sci Transl Med*, 2012, **4**, 159ra147.

49. K. H. Benam, R. Villenave, C. Lucchesi, A. Varone, C. Hubeau, H. H. Lee, S. E. Alves, M. Salmon, T. C. Ferrante, J. C. Weaver, A. Bahinski, G. A. Hamilton and D. E. Ingber, *Nature methods*, 2016, **13**, 151-157.

50. K. H. Benam, R. Novak, J. Nawroth, M. Hirano-Kobayashi, T. C. Ferrante, Y. Choe, R. Prantil-Baun, J. C. Weaver, A. Bahinski, K. K. Parker and D. E. Ingber, *Cell Syst*, 2016, **3**, 456-466 e454.

51. X. Cao, S. T. Gibbs, L. Fang, H. A. Miller, C. P. Landowski, H. C. Shin, H. Lennernas, Y. Zhong, G. L. Amidon, L. X. Yu and D. Sun, *Pharm Res*, 2006, **23**, 1675-1686.

52. I. Hubatsch, E. G. Ragnarsson and P. Artursson, *Nature protocols*, 2007, **2**, 2111-2119.

53. J. Yu, S. Peng, D. Luo and J. C. March, *Biotechnology and bioengineering*, 2012, **109**, 2173-2178.

54. J. H. Sung, J. Yu, D. Luo, M. L. Shuler and J. C. March, *Lab on a chip*, 2011, **11**, 389-392.

55. H. Kimura, T. Yamamoto, H. Sakai, Y. Sakai and T. Fujii, *Lab on a chip*, 2008, **8**, 741-746.

56. Y. Imura, Y. Asano, K. Sato and E. Yoshimura, *Anal Sci*, 2009, **25**, 1403-1407.

57. H. J. Kim, D. Huh, G. Hamilton and D. E. Ingber, *Lab on a chip*, 2012, **12**, 2165-2174.

58. H. J. Kim and D. E. Ingber, *Integr Biol (Camb)*, 2013, **5**, 1130-1140.

59. H. J. Kim, H. Li, J. J. Collins and D. E. Ingber, *Proceedings of the National Academy of Sciences of the United States of America*, 2016, **113**, E7-15.

60. R. Villenave, S. Q. Wales, T. Hamkins-Indik, E. Papafragkou, J. C. Weaver, T. C. Ferrante, A. Bahinski, C. A. Elkins, M. Kulka and D. E. Ingber, *PloS one*, 2017, **12**, e0169412.

61. S. Jalili-Firoozinezhad, R. Prantil-Baun, A. Jiang, R. Potla, T. Mammoto, J. C. Weaver, T. C. Ferrante, H. J. Kim, J. M. S. Cabral, O. Levy and D. E. Ingber, *Cell Death Dis*, 2018, **9**, 223.

62. M. Kasendra, A. Tovaglieri, A. Sontheimer-Phelps, S. Jalili-Firoozinezhad, A. Bein, A. Chalkiadaki, W. Scholl, C. Zhang, H. Rickner, C. A. Richmond, H. Li, D. T. Breault and D. E. Ingber, *Scientific reports*, 2018, **8**, 2871.

63. V. J. Navarro and J. R. Senior, *N Engl J Med*, 2006, **354**, 731-739.

64. W. J. McCarty, O. B. Usta and M. L. Yarmush, *Scientific reports*, 2016, **6**, 26868.

65. T. Torii, M. Miyazawa and I. Koyama, *Transplant Proc*, 2005, **37**, 4575-4578.

66. M. J. Powers, K. Domansky, M. R. Kaazempur-Mofrad, A. Kalezi, A. Capitano, A. Upadhyaya, P. Kurzawski, K. E. Wack, D. B. Stolz, R. Kamm and L. G. Griffith, *Biotechnology and bioengineering*, 2002, **78**, 257-269.

67. N. S. Bhise, V. Manoharan, S. Massa, A. Tamayol, M. Ghaderi, M. Miscuglio, Q. Lang, Y. Shrike Zhang, S. R. Shin, G. Calzone, N. Annabi, T. D. Shupe, C. E. Bishop, A. Atala, M. R. Dokmeci and A. Khademhosseini, *Biofabrication*, 2016, **8**, 014101.

68. D. Bavli, S. Prill, E. Ezra, G. Levy, M. Cohen, M. Vinken, J. Vanfleteren, M. Jaeger and Y. Nahmias, *Proceedings of the National Academy of Sciences of the United States of America*, 2016, **113**, E2231-2240.

69. Y. Nakao, H. Kimura, Y. Sakai and T. Fujii, *Biomicrofluidics*, 2011, **5**, 22212.

70. J. Lee, B. Choi, Y. No da, G. Lee, S. R. Lee, H. Oh and S. H. Lee, *Integr Biol (Camb)*, 2016, **8**, 302-308.

71. A. Schepers, C. Li, A. Chhabra, B. T. Seney and S. Bhatia, *Lab on a chip*, 2016, **16**, 2644-2653.

72. I. J. Onakpoya, C. J. Heneghan and J. K. Aronson, *BMC Med*, 2016, **14**, 10.

73. T. Boudou, W. R. Legant, A. Mu, M. A. Borochin, N. Thavandiran, M. Radisic, P. W. Zandstra, J. A. Epstein, K. B. Margulies and C. S. Chen, *Tissue engineering. Part A*, 2012, **18**, 910-919.

74. N. Thavandiran, N. Dubois, A. Mikryukov, S. Masse, B. Beca, C. A. Simmons, V. S. Deshpande, J. P. McGarry, C. S. Chen, K. Nanthakumar, G. M. Keller, M. Radisic and P. W. Zandstra, *Proceedings of the National Academy of Sciences of the United States of America*, 2013, **110**, E4698-4707.

75. A. Hansen, A. Eder, M. Bonstrup, M. Flato, M. Mewe, S. Schaaf, B. Aksehirlioglu, A. P. Schwoerer, J. Uebeler and T. Eschenhagen, *Circulation research*, 2010, **107**, 35-44.

76. V. Y. Sidorov, P. C. Samson, T. N. Sidorova, J. M. Davidson, C. C. Lim and J. P. Wikswo, *Acta biomaterialia*, 2017, **48**, 68-78.

77. A. Grosberg, P. W. Alford, M. L. McCain and K. K. Parker, *Lab on a chip*, 2011, **11**, 4165-4173.

78. A. Agarwal, J. A. Goss, A. Cho, M. L. McCain and K. K. Parker, *Lab on a chip*, 2013, **13**, 3599-3608.

79. A. Aung, I. S. Bhullar, J. Theprungsirikul, S. K. Davey, H. L. Lim, Y. J. Chiu, X. Ma, S. Dewan, Y. H. Lo, A. McCulloch and S. Varghese, *Lab on a chip*, 2016, **16**, 153-162.

80. A. Mathur, P. Loskill, K. Shao, N. Huebsch, S. Hong, S. G. Marcus, N. Marks, M. Mandegar, B. R. Conklin, L. P. Lee and K. E. Healy, *Scientific reports*, 2015, **5**, 8883.

81. A. Marsano, C. Conficconi, M. Lemme, P. Occhetta, E. Gaudiello, E. Votta, G. Cerino, A. Redaelli and M. Rasponi, *Lab on a chip*, 2016, **16**, 599-610.

82. G. Wang, M. L. McCain, L. Yang, A. He, F. S. Pasqualini, A. Agarwal, H. Yuan, D. Jiang, D. Zhang, L. Zangi, J. Geva, A. E. Roberts, Q. Ma, J. Ding, J. Chen, D. Z. Wang, K. Li, J. Wang, R. J. Wanders, W. Kulik, F. M. Vaz, M. A. Laflamme, C. E. Murry, K. R. Chien, R. I. Kelley, G. M. Church, K. K. Parker and W. T. Pu, *Nat Med*, 2014, **20**, 616-623.

83. M. Juhas, G. C. Engelmayr, Jr., A. N. Fontanella, G. M. Palmer and N. Bursac, *Proceedings of the National Academy of Sciences of the United States of America*, 2014, **111**, 5508-5513.

84. G. Moon du, G. Christ, J. D. Stitzel, A. Atala and J. J. Yoo, *Tissue engineering. Part A*, 2008, **14**, 473-482.

85. D. Neal, M. S. Sakar, L. L. Ong and H. Harry Asada, *Lab on a chip*, 2014, **14**, 1907-1916.

86. Y. C. Huang, R. G. Dennis, L. Larkin and K. Baar, *Journal of applied physiology*, 2005, **98**, 706-713.

87. M. S. Sakar, D. Neal, T. Boudou, M. A. Borochin, Y. Li, R. Weiss, R. D. Kamm, C. S. Chen and H. H. Asada, *Lab on a chip*, 2012, **12**, 4976-4985.

88. L. Madden, M. Juhas, W. E. Kraus, G. A. Truskey and N. Bursac, *eLife*, 2015, **4**, e04885.

89. L. Rao, Y. Qian, A. Khodabukus, T. Ribar and N. Bursac, *Nature communications*, 2018, **9**, 126.

90. C. Cvetkovic, R. Raman, V. Chan, B. J. Williams, M. Tolish, P. Bajaj, M. S. Sakar, H. H. Asada, M. T. Saif and R. Bashir, *Proceedings of the National Academy of Sciences of the United States of America*, 2014, **111**, 10125-10130.

91. C. G. Anene-Nzelu, K. Y. Peh, A. Fraiszudeen, Y. H. Kuan, S. H. Ng, Y. C. Toh, H. L. Leo and H. Yu, *Lab on a chip*, 2013, **13**, 4124-4133.

92. K. Shimizu, H. Araki, K. Sakata, W. Tonomura, M. Hashida and S. Konishi, *Journal of bioscience and bioengineering*, 2015, **119**, 212-216.

93. K. Shimizu, R. Genma, Y. Gotou, S. Nagasaka and H. Honda, *Bioengineering (Basel)*, 2017, **4**.

94. M. E. Katt, A. L. Placone, A. D. Wong, Z. S. Xu and P. C. Searson, *Front Bioeng Biotechnol*, 2016, **4**, 12.

95. I. K. Zervantonakis, S. K. Hughes-Alford, J. L. Charest, J. S. Condeelis, F. B. Gertler and R. D. Kamm, *Proceedings of the National Academy of Sciences of the United States of America*, 2012, **109**, 13515-13520.

96. C. L. Walsh, B. M. Babin, R. W. Kasinskas, J. A. Foster, M. J. McGarry and N. S. Forbes, *Lab on a chip*, 2009, **9**, 545-554.

97. A. Y. Hsiao, Y. S. Torisawa, Y. C. Tung, S. Sud, R. S. Taichman, K. J. Pienta and S. Takayama, *Biomaterials*, 2009, **30**, 3020-3027.

98. S. Bersini, J. S. Jeon, G. Dubini, C. Arrigoni, S. Chung, J. L. Charest, M. Moretti and R. D. Kamm, *Biomaterials*, 2014, **35**, 2454-2461.

99. A. Albanese, A. K. Lam, E. A. Sykes, J. V. Rocheleau and W. C. Chan, *Nature communications*, 2013, **4**, 2718.

100. T. Kim, I. Doh and Y. H. Cho, *Biomicrofluidics*, 2012, **6**, 34107.

101. A. Aung, J. Theprungsirikul, H. L. Lim and S. Varghese, *Lab on a chip*, 2016, **16**, 1886-1898.

102. A. Sobrino, D. T. Phan, R. Datta, X. Wang, S. J. Hachey, M. Romero-Lopez, E. Gratton, A. P. Lee, S. C. George and C. C. Hughes, *Scientific reports*, 2016, **6**, 31589.

103. D. T. T. Phan, X. Wang, B. M. Craver, A. Sobrino, D. Zhao, J. C. Chen, L. Y. N. Lee, S. C. George, A. P. Lee and C. C. W. Hughes, *Lab on a chip*, 2017, **17**, 511-520.

104. A. Marturano-Kruik, M. M. Nava, K. Yeager, A. Chramiec, L. Hao, S. Robinson, E. Guo, M. T. Raimondi and G. Vunjak-Novakovic, *Proceedings of the National Academy of Sciences of the United States of America*, 2018, **115**, 1256-1261.

105. N. Ferri, P. Siegl, A. Corsini, J. Herrmann, A. Lerman and R. Benghozi, *Pharmacol Therapeut*, 2013, **138**, 470-484.

106. T. M. Suter and M. S. Ewer, *European Heart Journal*, 2013, **34**, 1102-+.

107. M. B. Esch, H. Ueno, D. R. Applegate and M. L. Shuler, *Lab on a chip*, 2016, **16**, 2719-2729.

108. P. G. Miller and M. L. Shuler, *Biotechnology and bioengineering*, 2016, **113**, 2213-2227.

109. P. Loskill, S. G. Marcus, A. Mathur, W. M. Reese and K. E. Healy, *PloS one*, 2015, **10**.

110. C. D. Edington, W. L. K. Chen, E. Geishecker, T. Kassis, L. R. Soenksen, B. M. Bhushan, D. Freake, J. Kirschner, C. Maass, N. Tsamandouras, J. Valdez, C. D. Cook, T. Parent, S. Snyder, J. J. Yu, E. Suter, M. Shockley, J. Velazquez, J. J. Velazquez, L. Stockdale, J. P. Papps, I. Lee, N. Vann, M. Gamboa, M. E. LaBarge, Z. Zhong, X. Wang, L. A. Boyer, D. A. Lauffenburger, R. L. Carrier, C. Communal, S. R. Tannenbaum, C. L. Stokes, D. J. Hughes, G. Rohatgi, D. L. Trumper, M. Cirit and L. G. Griffith, *Scientific reports*, 2018, **8**.

111. Y. S. Zhang, J. Aleman, S. R. Shin, T. Kilic, D. Kim, S. A. M. Shaegh, S. Massa, R. Riahi, S. Chae, N. Hu, H. Avci, W. Zhang, A. Silvestri, A. S. Nezhad, A. Manbohi, F. De Ferrari, A. Polini, G. Calzone, N. Shaikh, P. Alerasool, E. Budina, J. Kang, N. Bhise, J. Ribas, A. Pourmand, A. Skardal, T. Shupe, C. E. Bishop, M. R. Dokmeci, A. Atala and A. Khademhosseini, *Proceedings of the National Academy of Sciences of the United States of America*, 2017, **114**, E2293-E2302.

112. L. Ma, J. Barker, C. C. Zhou, W. Li, J. Zhang, B. Y. Lin, G. Foltz, J. Kublbeck and P. Honkakoski, *Biomaterials*, 2012, **33**, 4353-4361.

113. C. Oleaga, C. Bernabini, A. S. T. Smith, B. Srinivasan, M. Jackson, W. McLamb, V. Platt, R. Bridges, Y. Q. Cai, N. Santhanam, B. Berry, S. Najjar, N. Akanda, X. F. Guo, C. Martin, G. Ekman, M. B. Esch, J. Langer, G. Ouedraogo, J. Cotovio, L. Breton, M. L. Shuler and J. J. Hickman, *Scientific reports*, 2016, **6**.

114. A. Skardal, S. V. Murphy, M. Devarasetty, I. Mead, H. W. Kang, Y. J. Seol, Y. S. Zhang, S. R. Shin, L. Zhao, J. Aleman, A. R. Hall, T. D. Shupe, A. Kleensang, M.

R. Dokmeci, S. J. Lee, J. D. Jackson, J. J. Yoo, T. Hartung, A. Khademhosseini, S. Soker, C. E. Bishop and A. Atala, *Scientific reports*, 2017, **7**.

115. J. D. Wang, N. J. Douville, S. Takayama and M. ElSayed, *Ann Biomed Eng*, 2012, **40**, 1862-1873.

116. M. W. Toepke and D. J. Beebe, *Lab on a chip*, 2006, **6**, 1484-1486.

117. S. Halldorsson, E. Lucumi, R. Gomez-Sjoberg and R. M. T. Fleming, *Biosens Bioelectron*, 2015, **63**, 218-231.

118. Y. Xia and G. M. Whitesides, *Angew Chem Int Ed Engl*, 1998, **37**, 550-575.

119. J. S. Miller, K. R. Stevens, M. T. Yang, B. M. Baker, D. H. Nguyen, D. M. Cohen, E. Toro, A. A. Chen, P. A. Galie, X. Yu, R. Chaturvedi, S. N. Bhatia and C. S. Chen, *Nat Mater*, 2012, **11**, 768-774.

120. D. B. Kolesky, R. L. Truby, A. S. Gladman, T. A. Busbee, K. A. Homan and J. A. Lewis, *Adv Mater*, 2014, **26**, 3124-3130.

121. D. B. Kolesky, K. A. Homan, M. A. Skylar-Scott and J. A. Lewis, *Proceedings of the National Academy of Sciences of the United States of America*, 2016, **113**, 3179-3184.

122. J. U. Lind, T. A. Busbee, A. D. Valentine, F. S. Pasqualini, H. Yuan, M. Yadid, S. J. Park, A. Kotikian, A. P. Nesmith, P. H. Campbell, J. J. Vlassak, J. A. Lewis and K. K. Parker, *Nat Mater*, 2017, **16**, 303-308.

123. H. G. Yi, H. Lee and D. W. Cho, *Bioengineering (Basel)*, 2017, **4**.

124. E. L. Jackson and H. Lu, *Integr Biol-Uk*, 2016, **8**, 672-683.

125. F. Y. Zheng, F. F. Fu, Y. Cheng, C. Y. Wang, Y. J. Zhao and Z. Z. Gu, *Small*, 2016, **12**, 2253-2282.

CHAPTER 2:

Skeletal muscle-on-a-chip: an *in vitro* model to evaluate tissue formation and injury

Gaurav Agrawal[1†], Aereas Aung [1†], Shyni Varghese[1,2*]

[1] Department of Bioengineering, University of California, San Diego, La Jolla, California, USA

[2] Department of Biomedical Engineering, Duke University, Durham, North Carolina, USA

2.1 Abstract

Engineered skeletal muscle tissues can be used for *in vitro* studies that require physiologically relevant models of native tissues. Herein, we describe the development of a three-dimensional (3D) skeletal muscle tissue that recapitulates the architectural and structural complexities of muscle within a microfluidic device. Using a 3D photo-patterning approach, we spatially confined a cell-laden gelatin network around two bio-inert hydrogel pillars, which induce uniaxial alignment of the cells and serve as anchoring sites for the encapsulated cells and muscle tissues as they form and mature. We have characterized the tissue morphology and strain profile during differentiation of the cells and skeletal muscle tissue formation by using a combination of fluorescence microscopy and computational tools. The time-dependent strain profile suggests the existence of individual cells within the gelatin matrix, which differentiated to form a multinucleated skeletal muscle tissue bundle as a function of culture time. We have also developed a method to calculate the passive tension generated by the engineered muscle tissue bundles suspended between two pillars. Finally, as a proof-of-concept we have examined the applicability of the skeletal muscle-on-chip system as a screening platform. We studied the dose-dependent effect of cardiotoxin on the engineered muscle tissue architecture and its subsequent effect on the passive tension. This simple yet effective tool can be appealing for studies that necessitate the analysis of skeletal muscle structure and function, including preclinical drug discovery and development.

2.2 Introduction

The development of technological platforms that generate three-dimensional (3D) organoids recapitulating the structural and biological features of native tissues has led to promising *in vitro* systems for studying tissue morphogenesis and function. A number of studies have demonstrated the potential application of these tools in preclinical drug discovery.[1-7] Further, such technologies may expedite the development of patient-specific disease models and advance personalized treatment regiments.

Current research in this area has focused on the development of a number of organ- and tissue-on-chip platforms ranging from traditional monolayer cultures to multicellular three dimensional organoids.[8] Organs-on-chips, which contain engineered microtissues that capture the physiological complexity of the native tissues within a continuous perfusion device, can be developed in a reproducible and cost-effective manner. These microphysiological systems also have the potential to supplement preclinical animal studies during drug discovery and development in order to improve the translatability of the drugs to the clinic.[9, 10] In fact, functional organs-on-chips simulating the lungs, gut, heart, and blood-brain barrier already have been developed.[11-19]

Engineered skeletal muscle tissue models are currently being developed. Skeletal muscle is the largest organ (by mass) of the human body, comprising approximately 40% of the mass of healthy individuals.[20] Skeletal muscle fibers contain sarcomeres that contract in unison to generate the forces that provides motion and activity to daily life. Major areas of health concern are skeletal muscle wasting, which can be attributed to a variety of factors including genetic conditions, autoimmune diseases, lack of use during aging or disability, space travel, and injury from sports, trauma, or tumor excision.[21-23] These conditions, if left

untreated, can lead to significantly impaired strength and mobility. *Ex vivo* skeletal muscle models that emulate the structural organization, functional capabilities, and regenerative potential of native muscle could provide new tools for screening both drug and cell or tissue-based therapies.

Pioneering efforts by Vandenbergh and colleagues established the first *in vitro* functional 3D muscle tissues in a dish, in which the authors have shown the formation of cylindrical muscle bundles from primary rodent myoblasts.[24] Further studies have assessed the biological and contractile properties of engineered muscle constructs during formation and in response to various mechanical, electrical, and optical stimuli.[25-33] Previous efforts to calculate the mechanical stresses generated by muscle cells have employed various tools and methods including force transducers, movements of bright spots on myotubes, displacements of muscular thin films (MTFs), or traction force microscopy.[34-36] Although engineered skeletal muscle models have been extensively developed and studied, there exist fewer advancements in skeletal muscle-on-chip platforms.[37, 38] Tissue-on-chip microfluidic platforms utilize continuous perfusion, thereby circumventing mass transport limitations associated with stagnant cell cultures. Continuous perfusion also allows temporal variations in drug concentrations to mimic physiological conditions in the human body. Furthermore, such microfluidic systems minimize the usage of reagents and compounds.

Herein, we describe the development of a skeletal muscle-on-a-chip platform and its application in studying skeletal muscle tissue morphogenesis, maturation, and cardiotoxin-induced changes in engineered muscle tissue architecture and passive tension. Specifically, we have used a 3D photopatterning technology to create anchoring hydrogel structures and cell-laden hydrogel constructs. This approach has allowed us to spatially-organize the cells

within a hydrogel network around the anchoring pillars to form uniaxially-aligned, densely-packed 3D cylindrical muscle tissues that reflect the structure of native skeletal muscle. Furthermore, we have quantified the strain patterns generated by the encapsulated cells as they differentiate to form a multinucleated tissue bundle in real time. We have also developed a method to quantify the passive tension of the muscle tissue bundle using finite element modeling. Finally, we have performed a proof-of-concept study to demonstrate toxin-induced changes in tissue architecture and passive tension, illustrating the potential utility of this platform as a screening platform.

2.3 Materials and Methods

Cell culture

The C2C12 mouse murine myoblast cell line was obtained from ATCC. The cells were cultured in growth medium (GM), composed of Dulbecco's Modified Eagle's high glucose medium (Hyclone) supplemented with 10% fetal bovine serum (FBS, Gibco) and 1% penicillin/streptomycin (Gibco). The cells were grown to 70% confluency and passaged prior to usage in the experiments.

Synthesis of gelatin methacrylate (GelMA)

Gelatin methacrylate (GelMA) was synthesized as described previously.[39, 40] Briefly, 10g of bovine skin gelatin (Sigma Aldrich, St. Louis, MO, USA) was dissolved in 100 mL of PBS, and heated to 60°C while stirring for an hour until the gelatin fully dissolved. The temperature was lowered to 50°C, after which 8 mL of methacrylic anhydride (MA; Sigma Aldrich, Cat. No. 276685) was added dropwise to the gelatin solution, which was then stirred vigorously for 1 hour. The solution was diluted with 200 mL of warm PBS, dialyzed against MilliQ ultrapure water using 12-14 kDa cutoff dialysis tubing (Spectrum Laboratories, Rancho Dominguez, CA, USA) for seven days at 40°C, changing water three times per day, to remove unreacted methacrylic anhydride and contaminants from the solution. The dialyzed GelMA solution was then flash frozen in liquid nitrogen and lyophilized in a freeze dryer for 4 days, and stored at -20°C.

Synthesis of lithium phenyl-2,4,6-trimethylbenzoylphosphinate (LAP)

The photoinitiator, LAP, was synthesized as described elsewhere.[41] In brief, 2,4,6-trimethylbenzoyl chloride was added drop-by-drop to an equal molar solution of dimethyl phenylphosphonite under argon while stirring at room temperature. After 18 hours, the temperature was set to 50°C, after which excess lithium bromide with 2-butanone was added to the reaction mixture. This resulted in the formation of a white precipitate within 10 minutes, after which the temperature was reduced to room temperature for 4 hours. The solution was filtered to isolate the precipitate, then washed three times using 2-butanone to ensure complete removal of excess lithium bromide. The product was dried using a vacuum to remove excess 2-butanone, yielding LAP in crystal form.

Fabrication of silicon mold

Micropatterned silicon wafers were fabricated as described previously.[19] Briefly, the microfluidic channels and chamber design was photolithographically defined using NR9-1500PY negative photoresist (Futurrex, Frankling, NJ, USA) on a 4-inch diameter silicon wafer. The Si wafer was etched using a deep reactive ion etching (DRIE) process, in which SF6 gas was flowed at 100 sccm for 11 seconds of reaction time, followed by a passivation cycle when C4F8 gas was flowed at 80 sccm for 7 seconds. An etching depth of 75μm was achieved using an etch rate of 0.7μm per cycle. Next, the NR9-1500PY photoresist was removed by immersing in acetone for 4 hours before rinsing with methanol, isopropanol, and deionized water. The Si mold was blown dry with compressed nitrogen gas and silanized by vapor deposition of trichlorosilane (TCI Inc, Portland, OR, USA) to allow PDMS casting and removal.

Formation of PAm hydrogels on glass

To tether the PAm hydrogels within the microfluidic device, glass coverslips were chemically-methacrylated as described previously,[42, 43] Briefly, round glass coverslips (12mm round, #1 thickness, Fisher) and rectangular glass coverslips (24mm x 50mm, #1 thickness, Fisher) were rinsed with 100% ethanol for 15 minutes. After aspiration of the ethanol, the glass was treated with a methacrylate solution composed of 97.7% (v/v) of ethanol, 0.3% (v/v) glacial acetic acid, and 2% (v/v) 3-(trimethoxysilyl)propyl methacrylate (Sigma Aldrich) for 5 minutes, then washed with pure ethanol twice with gentle shaking. The ethanol was aspirated off, and the glass coverslips were dried at 60°C for 2 hours prior to use.

A polyacrylamide (PAm) precursor solution composed of 5% (wt/v) acrylamide (UltraPure Acrylamide, ThermoFisher Scientific), 0.225% (wt/v) *N,N'*-methylenebis(acrylamide) (Sigma Aldrich), and 0.12% (wt/v) ammonium persulfate (APS, Sigma Aldrich) in phosphate buffered saline (PBS) was first made. Fluorescent far red particles of 0.2μm (ThermoFisher Scientific) were added to the precursor solution at a 1:100 dilution. Prior to polymerization, 0.6μL of a 10% (wt/v) *N,N,N',N'*-tetramethylethylenediamine (TEMED, Sigma Aldrich) in PBS was added to the precursor solution. After quickly mixing, 6μL of the solution was dropped onto the center of a methacrylated 24 x 50mm coverslip and subsequently covered with a non-methacrylated 12mm round coverslip to make a PAm hydrogel of that shape and size. This process was repeated with a non-methacrylated square coverslip and a methacrylated 12mm round coverslip. After a polymerization time of 30 minutes, the samples were immersed in DI water prior to gently removing the non-methacrylated glass by cleaving it off with a razorblade. The result was a set of PAm hydrogels tethered to the 24mm x 50mm glass rectangles and

another set tethered to 12mm circular glass, which would form the bottom and top surfaces of the microfluidic device, respectively (Fig. 2.2A).

Fabrication of microfluidics device

To keep the PAm hydrogels hydrated, 6μL of DI water was dropped onto the circular region of the microfabricated silicon wafer before covering it with the PAm-tethered 12mm round coverslip, facedown. Polydimethylsiloxane (PDMS, Sylgard 184, Dow Corning) was prepared by vigorously mixing together base and curing agent in a 10:1 ratio by mass, then degassed in a vacuum chamber to remove bubbles. The PDMS was gently casted onto the silicon wafer containing the PAm hydrogel, then baked at 37°C overnight to cure the PDMS (Fig. 2.2B). The PDMS mold, with the PAm hydrogel attached, was then removed from the wafer, and 0.5mm diameter holes were punched at the two ends to provide an inlet and outlet paths for perfusion. Finally, the PDMS was irreversibly bonded to the PAm-tethered rectangular coverglass after UV-ozone treatment and subsequent baking at 37°C overnight, resulting in PAm hydrogels on the top and bottom of the central chamber of the microfluidic device (Fig. 2.2C). PBS was perfused into the device to equilibrate the hydrogels prior to use.

Pillar formation

To form the PAm pillars, we employed a 3D photopatterning method described previously.[42] First, a precursor solution composed of 5% Am and 0.225% BisAm in PBS was prepared. The photoinitiator, LAP, was added at a concentration of 2mM, and the solution was perfused into the device. A transparency photomask with circular patterns of varying sizes (100μm, 200μm, 300μm) and inter-pillar distances (500μm, 1000μm, and 1500μm) was

obtained, and the pattern of choice was mounted onto the stage of a fluorescence microscope, centered over an open spot in the lens turret. The device was positioned on top of the pattern of the photomask, exposed to collimated UV light of approximately 365 ± 40nm excitation wavelength for 1 minute. The regions of the hydrogel precursor solution exposed to the UV light polymerized, resulting in circular pillars (Fig. 2.1A-C). Unreacted solution was removed by repeatedly washing with PBS. Thus, the complete device was constructed with top and bottom PAm hydrogel layers and PAm hydrogel pillars sandwiched between as anchors for the muscle tissues. The device was sterilized under UV light for 30 minutes prior to cell encapsulation.

Encapsulation of cells in GelMA around PAm pillars

A 7% (wt/v) GelMA solution in PBS was prepared by dissolving the GelMA powder in PBS at 60°C for 30 minutes. This solution was syringe filtered with 0.22μm to remove contaminants and insoluble components. C2C12 cells were mixed into the GelMA solution at a cell density of 12.5 million cells/mL before adding 0.01% ascorbic acid (Sigma Aldrich), a free-radical scavenger, and 2mM LAP, a photoinitiator.

The cell-laden hydrogel solution was injected into the fluidics device with a syringe. A transparency photomask containing a capsule pattern was placed onto the fluorescence microscope as described previously. The device was mounted on the photomask and manually positioned to locate two pillars within the capsule shape using the microscope eyepiece under brightfield illumination. This region was exposed to UV light for 12-15 seconds to photopolymerize the GelMA solution containing the C2C12 cells (Fig. 2.1D-E). This process was repeated several times within one device to obtain up to 10 samples.

Unreacted monomer solution and cells were washed away with sterile PBS. Thus, the 3D skeletal muscle-on-a-chip with cells patterned between and around anchoring pillars was created.

The samples were cultured in growth media for 24 hours, then switched to differentiation media, composed of Dulbecco's Modified Eagle's high glucose medium (Hyclone) supplemented with 2% horse serum (HS, Omega Scientific) and 2% penicillin/streptomycin (Gibco), to induce cell differentiation and fusion. Media was supplied to the cells within the device through a syringe pump (Harvard Apparatus) at a constant flow rate of 40μL/hour in an incubator set at 37°C and 10% CO_2. This flow rate was used based on our previous study which showed that, for samples in our device, a steady-state concentration can be achieved within 1000 seconds at a flow rate of 40μL/hour.[43]

Immunofluorescence staining of muscle tissues

The tissues were washed with PBS three times, fixed with 4% paraformaldehyde (PFA, Sigma Aldrich) solution for 15 minutes at room temperature, followed by several PBS washes to remove excess PFA. Next, a blocking buffer composed of 3% bovine serum albumin (BSA, Sigma Aldrich) and 0.5% Triton-X 100 (Fisher Scientific) was added and incubated for 1 hour in 4°C to prevent non-specific binding of antibodies. Mouse monoclonal antibody for myosin heavy chain (MF20, Developmental Studies Hybridoma Bank) was diluted 1:100 in blocking buffer and perfused into the device overnight at 4°C. The primary antibody was removed with several PBS washes. A solution containing the following was prepared: AlexaFluor 488 goat anti-mouse secondary antibody (Cat. No. A-11001, ThermoFisher Scientific) diluted 1:100 in blocking buffer, rhodamine-conjugated phalloidin

(Cat. No. R415, ThermoFisher Scientific) diluted 1:100 in blocking buffer, and Hoechst 33342 dye (Cat. No. H3570, ThermoFisher Scientific) diluted to 1x in blocking buffer. The muscle strips were incubated in this solution overnight at 4°C, then washed away with excess PBS prior to imaging. For cytoskeletal F-actin staining, fixed tissues were incubated in Phalloidin 488 (ThermoFisher), diluted 1:250 in blocking buffer, along with Hoechst 33342 dye diluted to 1x in blocking buffer, for 3 hours, then washed extensively with PBS prior to imaging.

Microscopy for imaging acellular samples and staining samples

A laser scanning confocal microscope (Olympus FV1000) was used to obtain Z-stack images of acellular 3D samples of the PAm hydrogel layers, PAm pillars, and patterned GelMA hydrogels. Each component was doped with 1% (v/v) 200nm fluorescent microspheres that emit at various wavelengths, including yellow-green (505/515nm), orange (540/560nm), and dark red (660/680nm). Samples were imaged at 10x magnification, with a z-step size of 1.0μm.

A spinning disk confocal microscope (Perkin Elmer Ultraview) was used for Z-stack imaging of tissues stained for myosin heavy chain (green), F-actin (red), and nuclei (blue). Samples were imaged with a 40x oil immersion objective lens, with a z-step size of 0.5μm. Single layer images of fluorescent particles for quantification of bead displacements and subsequent strains were also captured with the spinning disk confocal.

A Keyence BZ-X710 fluorescence microscope was used to obtain videos of acellular samples under perfusion at varying flow rates (40μL/hr, 100μL/hr, 400μL/hr) to ensure that the GelMA hydrogel and PAm pillars were attached to the top and bottom PAm hydrogel

layers. To improve visualization, the fluid was doped with far-red (200 nm; magenta color) particles. Samples were imaged at 10x and 20x objective lens.

Quantification of alignment score and fusion index

Z-stack images obtained from the confocal microscope were processed in ImageJ (NIH) for quantification. Alignment score was assessed as the deviation of multinucleated myotubes with three or more nuclei from the major axis. The major axis for each sample was drawn as the line connecting the centroids of the two pillars. The angular deviation was noted from ImageJ in 10° intervals and plotted as a histogram. Fusion index was calculated as the number of nuclei within multinucleated myotubes containing three or more nuclei out of the total number of nuclei within the sample, as a percentage.[44] A grid was overlayed on a merged stack of MF20 staining and nuclei counterstain, helping to facilitate the analysis. As a note, the tissue on the outer rims of the pillars was not considered in these calculations as the tissue in these regions is not unidirectionally-aligned and functions primarily to anchor the engineered microtissue in place. Data is presented as mean ± standard deviation, and the comparison between the groups was carried out by using one-way ANOVA with Tukey's multiple comparison test, where P-values < 0.1 were considered statistically significant. For both alignment and fusion, n = 3-5 samples per group from 3 different chips were used. Data is presented using GraphPad Prism software.

Calculation of elastic modulus of PAm hydrogel

PAm hydrogels with a radius and height of 3.5 and 3 mm, respectively, were fabricated and incubated in PBS overnight to reach equilibrium prior to compression tests.[45]

The tests were performed on an Instron 3342 Universal Testing System equipped with Model 2519-104 force transducer. The maximum force load was set to 250 N and the samples were compressed at a rate of 0.3 mm/min. The Young's modulus was determined by calculating the slope of a linear region of stress–strain curve.

Quantification of strains

Fluorescent particles embedded within the PAm hydrogels were imaged using a confocal microscope at days 0, 2, 4, 8, and 12. The 2D images of the fluorescent particles embedded in the PAm hydrogels was recorded before C2C12 encapsulation (reference state) and at various post-encapsulation time points, up to 12 days (deformed state). The deformation of the PAm hydrogel surface was calculated by analyzing the 2D bead displacement using particle image velocimetry (PIV) to compare the reference state images to the deformed state images, yielding a displacement vector field, u and v. The corresponding strains were calculated using infinitesimal strain approximation given by $\boldsymbol{\varepsilon}_{ij} = 1/2 * (u_{ij} + v_{ji})$. The mean of the absolute value of the individual components of the strain tensor was calculated at different x-positions to examine the changes in the cell-generated forces as a function of culture time.

Comparison of empirical strain distribution with theoretical strain distribution

A finite element model of a cylinder with a height of 70μm and diameter of 100μm tethered to a rectangular prism of length 350μm was created using COMSOL Version 4.2. Here, the cylindrical structure and the rectangular prism was used to model the hydrogel pillar and the underlying PAm hydrogel, respectively. A displacement boundary condition

was applied at the periphery of the cylinder along the x-axis while a symmetric condition was imposed at the top surface of the cylinder. The rectangular prism was tethered in all directions at the bottom surface while all other surfaces were considered stress free. These boundary conditions were used to generate a theoretical strain field resulting from the cylindrical structure being displaced 5μm along the x-axis. This displacement value was equal to the average displacement of three samples found experimentally by comparing the reference state images to the deformed state images. The theoretical strain field from FEM model was compared to the strain field resulting from the displacement field obtained via PIV.

Calculation of passive tension

The tissue samples were cultured for 12 days prior to analyzing the displacement of the pillars to which they are tethered. The values for the pillar displacement determined experimentally from individual microtissues were used as the displacement boundary conditions within the COMSOL based finite element model described previously. Here, the resultant stress tensor component, τ_{xz}, was integrated under the pillar area and multiplied by 2 to approximate the passive tension existing within the muscle fiber.

Assessing pillar bending

To assess the potential bending of the PAm pillars, finite element analysis was carried out on the domain depicted in Figure 2.13A. A traction boundary condition was applied to the surface of the pillar in the x-direction to simulate the contractile forces generated by the cells. Stress values of 0, 115, 230, and 450 Pa were used, which corresponds to passive tensions of 0, 5, 10, and 20 μN over the lateral surface area of the pillar. These passive

tensions were used in the FEA because they span the entire range of the tension generated by the muscle tissues (Fig. 2.13E). Boundary conditions applied on the upper and lower surfaces were obtained from FEM analysis of pillar displacements. The displacements of the pillar in the *x*-direction were plotted to examine the presence of bending.

Cardiotoxin –induced structural disruption of the engineered tissue

As a proof-of-concept validation of the potential application of the skeletal-muscle-on-a-chip platform as a screening molecule, we have examined cardiotoxin-induced changes of the engineered skeletal muscle tissue. To this end, day 12 engineered muscle tissue strips were exposed to cardiotoxin from Naja mossambica mossambica (Sigma, C9759) at concentrations of 0 μM, 0.1 μM, and 0.5 μM diluted in differentiation medium (2% horse serum in DMEM). The compound was supplied to the tissues in the microfluidic chip under continuous flow at 40 μL/hr. Structural changes of the tissue were examined after 24 hours of cardiotoxin administration, where samples were fixed with PFA and stained for F-actin and nuclei. Changes in passive tension were assessed over a 3-day period of cardiotoxin administration. The passive tension was quantified every 24 hours for 3-days by analyzing the displacement of the left and right pillar as compared to the reference day 0 pillar positions in COMSOL, as described previously. Data is presented as mean ± standard deviation, where n = 4-5 samples per group from 3 different chips. Data is presented using GraphPad Prism software.

2.4 Results

Device Fabrication and Characterization

To develop aligned 3D skeletal muscle tissues and calculate the strain profile and passive tension within the tissue, we created a microfluidic device containing a central chamber with multiple hydrogel structures. Specifically, a cell-laden gelatin network, confined around two PAm pillars, was sandwiched between two PAm hydrogel layers. The acellular PAm hydrogel structures were designed to serve different functions: (1) PAm hydrogel pillars acted as anchoring sites, which induce uniaxial alignment of the cells/tissues, (2) top and bottom hydrogel layers spatially confined cell-laden gelatin networks and underwent quantifiable elastic deformations necessary to quantify the cell and tissue generated strains and forces.

Figure 2.1 and Figure 2.2 illustrate the device fabrication and subsequent cell encapsulation procedures. Following the initial fabrication of the device, we used a previously described 3D photo-patterning method to generate PAm hydrogel pillars between the top and bottom PAm hydrogel planar layers (Fig. 2.1A-C, Fig. 2.3A).[42] With all the necessary components in place, we next used the same photo-patterning technique to form a cell-laden gelatin methacrylate (GelMA) hydrogel around the PAm pillars (Fig. 2.1D-E). While any shape can be patterned, we found the capsule shape to be most optimal in order to position cells between and around the anchoring pillars. To depict this setup, an acellular sample was constructed, with each hydrogel containing 200 nm diameter fluorescent particles of different colors. Using a confocal microscope, the sample was imaged to visualize these structures within the device. The side view, represented by the X-Z projection, clearly shows the PAm hydrogel pillars in green and the GelMA hydrogel capsule in red placed between

the planar PAm hydrogel layers in violet (Fig. 2.4A). The X-Y projections, depicting a top view at different Z planes (Fig. 2.4B), and a 3D rendering of each component along with a 3D representation of the composite structure (Fig. 2.4C), are also shown. The thicknesses of the middle layer (comprised of PAm pillars and GelMA hydrogel) and the planar hydrogels on the top and bottom were measured to be approximately 70 and 40μm, respectively.

To ensure that the GelMA hydrogel and PAm pillars were fixed in place, acellular samples were analyzed to show that these hydrogel structures would not detach from the top and bottom PAm hydrogel layers in response to flow. Evidence that the GelMA hydrogel and PAm pillars are attached to the PAm hydrogel layer can be clearly observed in Supplementary Videos 1-5 (data not shown). As seen from Supplementary Videos 1-3, in all flow conditions, the GelMA hydrogel and PAm pillars remain stationary and do not dislodge, even at the highest flow rate of 400μL/hr, which is ten times the flow rate that was used during muscle tissue culture. Supplementary Videos 4 and 5 further demonstrate the strong adhesion of the GelMA hydrogel and PAm pillars to the underlying PAm hydrogel. Supplementary Video 4, which displays the GelMA structure and PAm pillar at position Z2 (see Figure 2.4A), clearly shows the fluid flowing around the periphery of the GelMA hydrogel under perfusion. No such fluid flow is observed at the interface of the GelMA-PAm hydrogels (Supplementary video 5, which shows the interface between the underlying PAm hydrogel layer and both the GelMA hydrogel and PAm pillar at position Z3; see Figure 2.4A). The absence of fluid flow at the GelMA-PAm hydrogel layer interface further suggests that the hydrogel layers are adhered to each other strongly.

Formation of 3D skeletal muscle micro tissues

Skeletal muscle microtissues were formed using C2C12 murine myoblasts encapsulated in a GelMA hydrogel, where gelatin is a collagen-derived matrix with inherent cell adhesive sites. Using photo-polymerization, the cells were encapsulated within a GelMA hydrogel surrounding the two PAm pillars and sandwiched between two acellular polyacrylamide hydrogel layers. Up to ten of these structures were formed within one microfluidic chip, spatially separated from one another by a minimum of 800μm in all directions. Following the initial encapsulation, the chip was perfused with PBS to wash away un-encapsulated cells and un-reacted reagents. The cells were cultured in growth medium for 24 hours to equilibrate with the new environment, and then maintained in low-serum differentiation medium for the remainder of the culture to induce differentiation, cell fusion, and the formation of multinucleated myotubes. The cell-laden GelMA hydrogel was monitored for tissue formation and remodeling for up to 12 days (Fig. 2.5A). Brightfield images at various time points in Figure 2.5A show that cell-cell attachment and alignment were evident by day 2, formation of a dense microtissue by day 5, and further compaction of the muscle tissue strip by day 12.

To assess the need for the PAm hydrogel pillars-induced uniaxial cell alignment on skeletal muscle tissue formation, cell-laden GelMA hydrogels of identical geometries were fabricated within the device without the pillar support and compared against those cultured under identical conditions but in presence of pillars (Fig. 2.3B). By day 5, cells cultured in the absence of pillars collapsed inwards into a ball of cells while those cultured in presence of pillars formed intact, aligned muscle strips. Thus, due to cell-mediated degradation of the GelMA hydrogel and contraction of the myoblasts, the anchoring function of the pillars was necessary to generate muscle tissue strips.

Effect of pillar diameter and inter-pillar distance on microtissue formation

Having established that 3D skeletal muscle microtissues can be successfully generated within a microfluidic device, we next evaluated the effect of varying the pillar diameters and inter-pillar distances on tissue differentiation and maturation. To do so, we quantified two well-known characteristics of multinucleated myotubes, fusion index and alignment score, at day 12 of the culture. The selected region of the engineered organoid outlined by the "box" in Figure 2.6A, hereafter termed as characteristic tissue volume, was used to calculate fusion index and alignment score. Note that the figure only shows a single slice of the tissues but the analyses was performed for the entire 3D tissue.

First, the inter-pillar distance was kept constant at 500μm while the pillar diameters were varied at 100μm, 200μm, and 300μm. The aspect ratios of the resulting characteristic tissue volumes were 1:5, 2:5, and 3:5. In the second set of experiments, the pillar diameter was fixed at 100μm, while the inter-pillar distances were varied at 500μm, 1000μm, and 1500μm. The aspect ratios of the resulting characteristic tissue volumes were 1:5, 1:10, and 1:15. Together the experiments allowed us to determine the effect of aspect ratio on tissue formation. Initial observations suggested that groups with an aspect ratio of 1:10 and 1:15 were found to be more susceptible to rupture, while groups with an aspect ratio of 2:5 and 3:5 remodeled and compacted the GelMA hydrogel to a lesser degree compared to those in 1:5 aspect ratio.

Samples were cultured for 12 days and immunostained for myosin heavy chain, a marker for differentiated muscle cells, and counterstained for the nuclei. The presence of cells expressing myosin heavy chain and containing multiple nuclei indicated the formation of

multinucleated myotubes. As seen in Figure 2.7A over 90% of myotubes in the groups with aspect ratios 1:5, 1:10, and 1:15 were aligned within 10° of the major axis, and almost 100% were within 20°. On the other hand, for the groups with aspect ratios of 2:5 and 3:5, there was a significantly larger variation in alignment relative to the major axis, with some myotubes having up to 60-70° deviation from the major axis, indicating more random orientation and less alignment. Furthermore, from Figure 2.7B, the fusion indices for the groups with aspect ratios of 1:15, 1:10, 2:5, and 3:5 were in the range of 14-15%, while that of the 1:5 group was approximately 32%. The fusion index for the group with an aspect ratio of 1:5 is more than two-folds greater than that of the other groups. The corresponding images for all aspect ratios are shown in Fig. 2.6B. Together the data suggests that the microtissues with an aspect ratio of 1:5 had the highest efficiency for myotube formation, thus we utilized the tissues with this ratio for all further analyses.

Characterization of muscle tissue morphology and differentiation

Engineered muscle tissue strips with the aspect ratio of 1:5 were further characterized. Samples cultured for 12 days were stained for myosin heavy chain, F-actin (to assess cytoskeletal alignment and cellular organization within the microtissue), and the nuclei. Images of a representative z-slice obtained from a spinning disk confocal microscope show multiple horizontally-aligned multinucleated myotubes parallel to one another within each organoid, suggesting the formation of muscle tissue bundles (Fig. 2.4B). Further, the unidirectional alignment of all cells along the major axis throughout the microtissue, including those not expressing myosin heavy chain, was clearly seen in images of F-actin staining. Y-Z cross-sectional images of myotubes and nuclei illustrate a three-dimensional,

cylindrical muscle bundle densely packed with several myotubes of approximately 10-15μm in diameter, with nuclei dotting the periphery (Fig. 2.4C). This closely resembles the fascicular morphology of native skeletal muscle tissue.[46] The corresponding high-magnification image clearly depicts elongated nuclei that are primarily present on the periphery of the myotubes, as indicated by the white triangles (Fig. 2.4D). These hallmarks of skeletal muscle tissue provide further confidence that our engineered muscle organoids mimic several structural features of native skeletal muscle.

Calculation of Strains During Tissue Morphogenesis

We next examined the strains that are exhibited by the C2C12 cells as they differentiate, organize, and fuse to form multinucleated myotubes and 3D tissues. Since the GelMA degrades and remodels with tissue formation, the stress transduced to the underlying PAm hydrogel layer was used for the strain calculations. We examined the deformation of the PAm planar hydrogel and quantified the 2-dimensional strain field ($\varepsilon_{xx}, \varepsilon_{yy}, \varepsilon_{xy}$) as a function of culture time (days 2, 4, 8, and 12). The strains are shown within a mask of the perimeter of the microtissue (dotted lines in Fig. 2.8A) to illustrate their precise location. While the strains ε_{xx} were present throughout the tissue early in tissue formation (at days 2 and 4), as the cells differentiate, fuse, and remodel the surrounding matrix to form a muscle strip, the strains were localized to the pillars, yielding almost no deformation in the region between the pillars (Fig. 2.8A). A similar trend was also evident in $\varepsilon_{yy}$and ε_{xy}directions (Fig. 2.9A, 2.10A). Time-dependent immunofluorescence staining further corroborated these strain patterns. At day 4, most cells remain as undifferentiated single cells, while at day 12,

cells have fused to form a continuous 3D tissue composed of several multinucleated myotubes (Fig. 2.11).

Furthermore, we quantified the strain magnitudes along the tissue length by binning several x-positions over the length of the tissue to confirm the strain pattern in Fig. 2.8A. As evidenced in Figure 2.8B, by day 12, the strain magnitudes of ε_{xx} were highest at the pillars and minimal elsewhere throughout the construct area. Furthermore, the magnitudes of ε_{xx}were approximately two-fold greater than those of ε_{yy} and ε_{xy}, indicating that the strain in the x-direction is dominant (Supp. Fig. 2.9B, 2.10B). Considering also the cylindrical geometry of the muscle bundle from Figure 2.5C, these results could be attributed to the muscle strip detaching from the underlying hydrogel layer after day 4 and forming a tense hanging rope as the cells fuse to each other to form multi-nucleated tubes and remodel the GelMA. The formation of such a tissue rope anchored to the PAm pillars resulted in the localization of cellular forces around the two PAm pillars.

We also examined the displacement of the pillars at day 2 and day 12 of tissue development. Figure 2.8C shows confocal images of the fluorescent particles embedded in the PAm hydrogel underneath the muscle strip, overlaying day 0 (green) with either day 2 (red, left) or day 12 (red, right). The circles are the rims of the PAm pillars, which are highlighted by the presence of fluorescent beads. Note that there are no beads visible within the outline of the pillars due to imaging constraints. At day 2, when the tissue was nascent, the beads appeared as yellow, indicating a strong overlap of green (day 0) and red beads (day 2), which in turn suggested no noticeable pillar displacement. On the contrary, at day 12, there was a distinct shift and measureable inward displacement of the beads compared to day 0, indicating that the cellular forces exerted by the fused muscle strip shifted the pillars.

Calculation of Passive Tension

Since the cells were simply pulling the pillars inwards along the major axis without rotations, we used finite element analysis to calculate the passive tensile forces generated by the microtissues. We compared the experimentally determined strain field on the top surface of the PAm hydrogel layer with that of a theoretical strain field resulting from purely displacing the PAm pillars along a single dimension. The experimentally determined elastic modulus of the PAm hydrogels, 11.85 ± 1.31 kPa, was used in determining the theoretical strain field (Fig. 2.12). The theoretical strain field was obtained using finite element analysis where the depiction of the domain with a simulated displacement of a single pillar is given in Figure 2.13A. The resultant displacement field of the PAm pillar (on the PAm hydrogel layer) is shown as a heat map in Figure 2.13B. The comparison of the experimentally determined strains with those from the theoretical calculations is given in Figure 2.13C. Note that the region of the heat map immediately around the pillars, given by a dark red and blue circular shape, was error due to a poor signal-to-noise ratio. However, outside of this region, there was a strong overlap in the patterns of the strain fields for ε_{xx}, ε_{yy}, and ε_{xy}. This pattern suggested that the muscle tissue strip displaces the PAm pillars towards the center of the microtissues and the resultant force could be obtained using the loading configuration that was simulated using the finite element model. To this end, we first generated the shear stresses, τ_{xz}, resulting from the engineered muscle strip at a single pillar with displacement arrows overlaid (Fig. 2.13D). The summation of these stresses over the area of each pillar yielded the passive tension. Figure 2.13E presents a distribution of the passive tension of over 30 engineered skeletal muscle microtissues (6-8 different chips), where the mean tension is

8.16μN ± 3.41μN. As a result, the system developed in this study can be used to engineer mature skeletal muscle tissue mimics as well as quantify passive tension generated by the tissue.

Cardiotoxin –induced disruption of the engineered tissue

To assess the potential application of the skeletal muscle-on-a-chip platform as a screening tool, we performed a proof-of-concept study to evaluate cardiotoxin-induced structural changes of the engineered tissue and the accompanying changes in the passive tension. Cardiotoxin (CTX) is a toxin found in snake venom that is known to prompt myotube depolarization and disrupt the muscle cytoskeleton and is commonly used in experiments to induce skeletal muscle injury in animal models. We evaluated the response of the engineered muscle microtissues to CTX by applying 0 μM (control), 0.1 μM, or 0.5 μM CTX to day 12 muscle samples. As seen in Figure 2.14, our results show a dose-dependent response to cardiotoxin. After 24 hours of exposure to CTX, the control samples and samples exposed to 0.1 μM had an intact or mostly-intact cytoskeleton, respectively; however, those exposed to 0.5 μM cardiotoxin exhibited a severely disrupted and fragmented cytoskeleton and architecture (Figure 2.14A). The changes in passive tension for these three groups reflects the cardiotoxin-induced structural damages of the engineered tissue. The passive tension of the control samples remains constant over a 3-day experimental period, whereas the tissues exposed to 0.1 μM cardiotoxin incurred a gradual decrease in passive tension and 0.5 μM samples incur a sharp and immediate drop in tension (Figure 2.14B). Most of the samples exposed to 0.5 μM cardioxin showed a complete cytoskeletal rupture of the tissues by the end of the 3-day experimental period. This proof-of-concept study highlights the practical

application of our platform by assessing both the tissue structural changes and the associated changes in passive tension in response to a small molecule.

2.5 Discussion

Organ-on-a-chip systems have been touted as the next generation of *in vitro* tissue-specific models for studying tissue development and disease causation, and for use in drug discovery and development. Such systems have many advantages as a perfusion system surpasses the limitations associated with static 3D cultures as it continuously provides fresh nutrients and removes wastes and metabolic byproducts, while minimizing the usage of reagents and compounds. Further, current organ-on-a-chip platforms have been able to mimic the native cellular and tissue responses to various mechanical or chemical perturbations.[11, 12, 34] In this study, we have utilized a previously described 3D photo-patterning technology to additively form acellular and cell-laden hydrogel structures to generate skeletal muscle tissues within a microfluidics device.[42]

The immunofluorescence images show that the engineered tissues displayed the hallmarks of skeletal muscle tissue – cylindrical fascicular morphology, multinucleated myotubes, nuclei elongation, and nuclei on myotube periphery. The GelMA hydrogel used to encapsulate the cells facilitated the formation of multinucleated myotubes to create 3D tissues. GelMA, which supports initial attachment of cells to the surrounding biomaterial via inherent cell-adhesive sites, further promotes cell fusion as it actively degrades and remodels in the presence of cells. These properties of GelMA support multinucleated myotube formation, cellular alignment, and matrix remodeling to form a compact muscle tissue bundle.

Moreover, we have developed a method to calculate the passive tension generated by the muscle tissue bundle based on the real-time strain profile. Since the cell-mediated degradation of the GelMA hydrogel results in a change in its material properties over time, it

is inaccurate to utilize traction stress measurements from GelMA to quantify the contractile stresses and strains associated with the engineered tissue. Hence, we used a "far-field" approach in which we used stress transduction from the cell-laden GelMA to the underlying PAm hydrogel.[19] The PAm is a bioinert, non-degrading material that exhibits constant linear elastic material properties throughout the course of the experiments. The deformation of PAm hydrogels due to the contractile stresses generated by the cells embedded within the GelMA layer was quantified by tracking the fluorescent particles in real-time. The material deformations allowed us to calculate the strain patterns of the developing tissue as a function of time to evaluate muscle tissue formation and, subsequently, obtain the passive tensile forces.

An inherent limitation of far field measurements is the decay of stresses as a function of distance between the stress-generating cells and the underlying elastic material ("sensor") under deformation. To minimize the effect of decay on stress transduction, only the fluorescent particles on the surface of the PAm layer immediately adjacent to the cell-laden GelMA hydrogel were imaged during data acquisition. Furthermore, cell-laden GelMA hydrogels were packed with high cell density to ensure the presence of cells throughout the structure. The degradation of the GelMA hydrogel with culture time could have an effect on the strain profile; however, the degradation-mediated changes in the strain profile will be negligible as the encapsulated myoblasts fuse to form multinucleated muscle tissues suspended by the PAm pillars. The strain profile gathered at the later culture time is mostly due to the PAm pillar displacement which is caused by the muscle tissues pulling inwards.

We first showed that our engineered muscle bundle forms a three-dimensional free-hanging rope-like structure by comparing the immunofluorescence images from Figure 2.5B-

C with the strain distribution heat map from Figure 2.8B. Noting the cylindrical morphology of the muscle strip, along with the day 12 strain profile indicating that the strains are localized entirely at the pillars, we deduced that the engineered muscle has released from the hydrogel surfaces and stays as a suspended rope-like structure. As a result, the tensile force could be calculated directly from the pillar displacement. The displacement of the pillars formed the boundary conditions for the finite element model of a linearly elastic isotropic material to determine the stresses generated at each pillar, which summed to yield the value of the tension. Since the top and bottom PAm hydrogels were of similar thickness and rigidity, the displacement of the pillar was considered to be uniform and thus only the fluorescent particles in the bottom PAm layer were tracked. Further, the significant distance of 800μm between each engineered tissue ensured that the measured displacements belonged only to the respective sample, and that the deformation of the PAm surface due to one muscle tissue would have negligible effects on the readouts of the adjacent samples. In fact, the value for the mean tension, 8.16μN, is similar to the average static tension of 10.8μN found by Sakar, et al., in their engineered muscle microtissues.[29]

We performed bending analysis along the length of the pillar shaft to evaluate the bending of the pillars caused by the tension generated by the microtissues. By applying a load perpendicular to the shaft, our analyses show bending of the pillars, where the amount of bending increases with increasing tension applied (Fig. 2.15). Since all displacements were measured in presence of fluid flow any bending of the pillars observed could be due to the suspended microtissues and hence should not have any effect on the passive tension calculations. Moreover, the bending does not disrupt the force transmitted from the PAm pillars to the PAm hydrogel layers.

As we alluded to earlier, organs-on-chips are being developed to address limitations of current preclinical drug development studies. Our proof-of-concept cardiotoxin study demonstrates the versatility of our platform to not only examine changes in muscle tissue structure and morphology, but also the effect of a small molecule on the tension within a muscle strip. In our case, we have evaluated the changes in passive tension with respect to cardiotoxin concentration over the entire culture time. As expected, a lower concentration of the toxin had less effect on muscle structure and tension than the higher concentration. This initial study lays the foundation for future studies in which, upon incorporation of electrical or optical stimulation to induce active contraction of the muscle strips, we can further quantify the reduction in force generation capability in response to drug or small molecule toxicity. Further studies can also incorporate inflammatory cues to examine the effect of inflammation on skeletal muscle formation and function.

Taken together, the PAm hydrogel layers, the degradable nature of GelMA, and the PAm support pillars allowed for the remodeling of the extracellular matrix and the alignment and fusion of single cells into multinucleated myotubes to form compact skeletal muscle tissue bundles. In addition to serving as a "force sensor", the PAm hydrogel layers on the top and bottom of the device performed two critical functions. First, PAm is a bioinert hydrogel that prevents cell attachment, thus cells are spatially confined and prevented from attaching to any region outside the patterned space. Secondly, the PAm hydrogel allows for GelMA and PAm to entangle with its meshwork during gelation. Due to the molecular miscibility of monomers, the GelMA and acrylamide monomers diffuse into the PAm hydrogel network, and subsequently create physical entanglements with the underlying PAm. This not only maintains the structural integrity of the cell-laden GelMA hydrogels, but also supports

attachment of the PAm pillars to the polyacrylamide hydrogel layers on the top and bottom surfaces of the central chamber of the device following photo-polymerization. This PAm-layer-PAm-pillar attachment was critical to the successful quantification of the passive tension generated by the tissues.

The strength of our platform is the ability to quantify tension during tissue culture in real-time without destroying the engineered muscle tissues. Also, the design described in this study yields three-dimensional (3D) muscle strips. Our platform is amenable to both light and fluorescence microscopy. This sets up our system for future studies, where we can incorporate electrical or optical stimulation to induce the active contraction of the tissues and measure the twitch and tetanic forces that are generated. One could also envision varying the mechanical properties of the pillars and hydrogels to mimic the mechanical properties of the extracellular environment. For example, we can modify the stiffness of the pillars to force these tissues to contract against larger or smaller loads, and thus measure the fatigue induced by working the muscle. However, our system also has some limitations. For example, length-tension relationships are typically determined by shortening or lengthening the construct. As our skeletal muscle construct is engineered in a closed system, it cannot be accessed by any micromanipulators and as such cannot be shortened or lengthened, making it difficult to measure the length-tension relationship.

2.6 Conclusion

In summary, we have created a 3D skeletal muscle-on-a-chip platform and described a method to calculate the passive tension generated by the engineered muscle tissues. Our approach utilizes the tissue anchoring sites, which induce uniaxial alignment, to obtain the strain profile and force measurements. We have demonstrated that the multi-layered hydrogel system supports tissue growth for long-term cultures and we have also characterized the resulting tissue structure and morphology. Our proof-of-concept toxicity study illustrates the ability of this platform to recapitulate expected changes in the skeletal muscle tissue structure and function in response to application of a small molecule. Further, the skeletal muscle-on-a-chip detailed here provides a platform to study stimuli-induced changes in cell fusion and myotube size and relate this to the associated functional force measurements. Moving forward, using both healthy and disease-specific human induced pluripotent stem cells (hiPSCs), such as those with Duchenne's muscular dystrophy (DMD), will allow us to build human- and patient-specific skeletal muscle platforms that improve upon the complexity of existing *in vitro* disease models.[47] Ultimately, we hope to investigate the effects of novel pharmaceutical and cell-based therapeutics on the structure and function of human skeletal muscle tissues from both toxicity and efficacy standpoints.

2.7 Acknowledgments

The authors acknowledge that this study was supported by the California Institute for Regenerative Medicine (CIRM) under grant number RT3-07907. In particular, I would like to thank Jomkuan Theprungsirikul for her help with creating microfluidic devices and encapsulating cells during the course of the study. Also, I would like to thank Dr. Aereas Aung for his skills in computational analysis to determine strains and forces.

Chapter 2, in full, is a re-print of material that has been published in the journal *Lab on a Chip*. Agrawal G*, Aung A*, Varghese S. Skeletal muscle-on-a-chip: an *in vitro* model to evaluate tissue formation and injury. *Lab on a Chip*. 2017; 17: 3447-3461. The dissertation author is the primary investigator and co-author of this material.

2.8 Figures

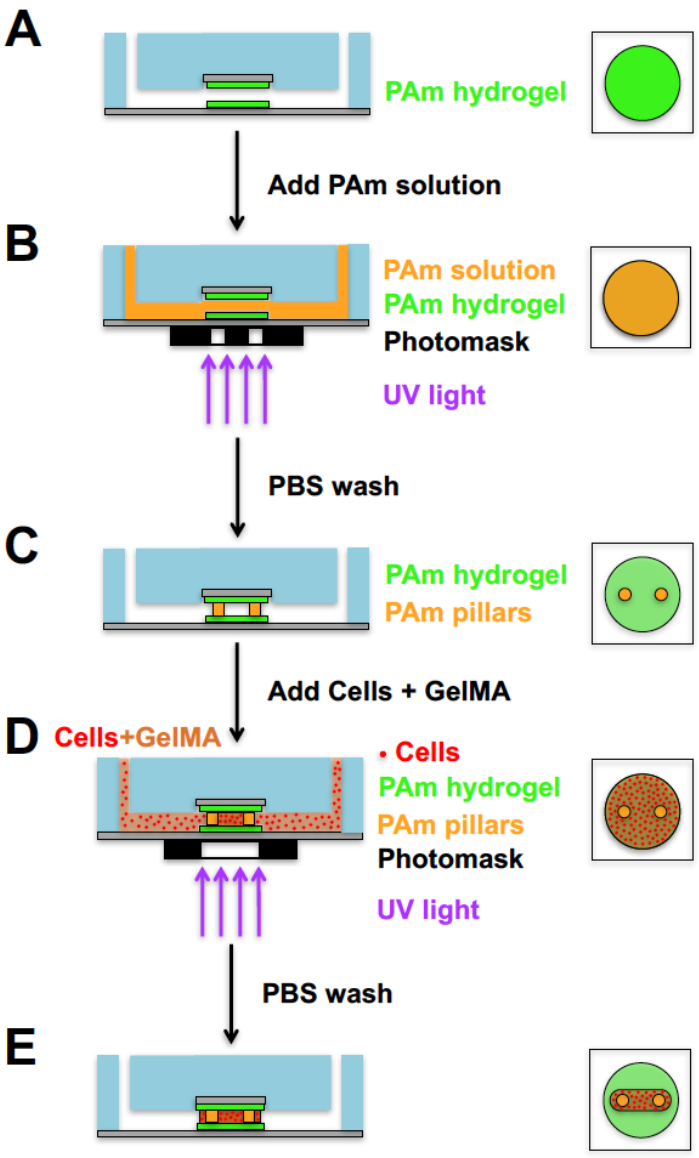

Figure 2.1: 3D photopatterning of support pillars and encapsulation of cells.

(Left: Side view of full device; Right: Top view of central chamber) (A-B) To create support pillars, the bonded microfluidic chip was infused with acrylamide (Am) solution containing photoinitiator and was photopolymerized using a collimated UV light and a transparency photomask containing 100 µm diameter circle patterns. (C-D) After washing with PBS, a precursor solution composed of cells, GelMA, and photoinitiator was polymerized around the pillars using the same method as before, except with a capsule-shaped pattern. (E) PBS solution was used to wash the samples, and the device was perfused with maintenance media by using a syringe pump.

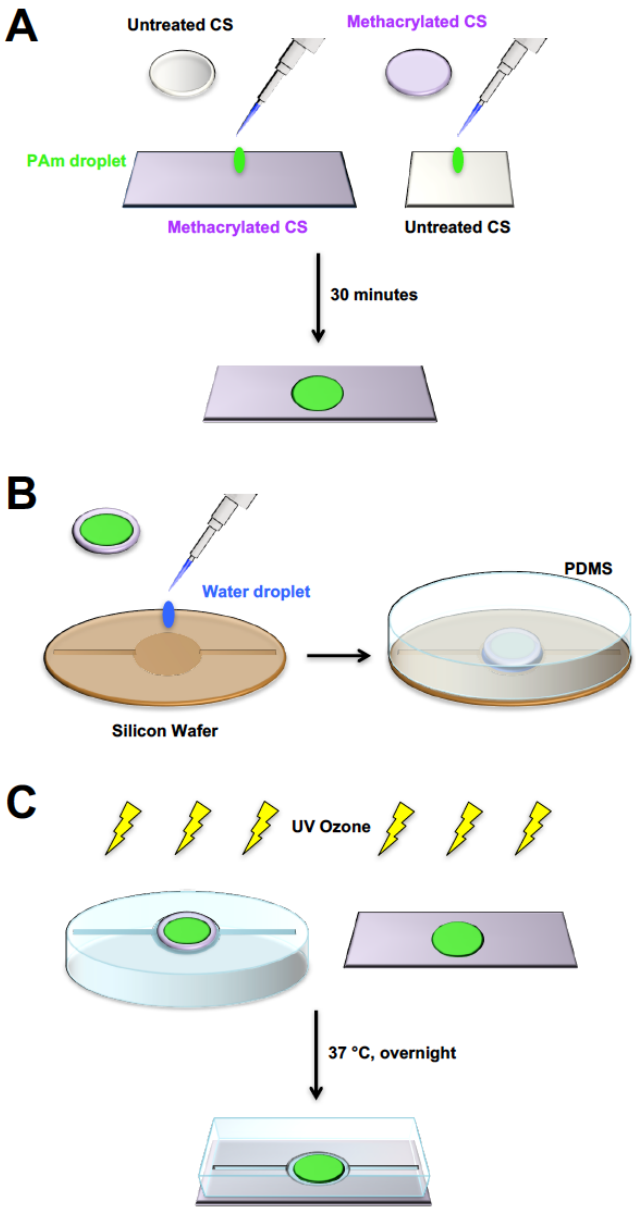

Figure 2.2: Schematic of fabrication of microfluidic device

(A) Acrylamide (Am) precursor solution was placed between non-functionalized and methacrylated coverslips. After gelation, the non-functionalized coverslip was cleaved off, yielding PAm hydrogel-tethered coverslips. (B) A droplet of water was deposited onto the central chamber pattern of a silicon wafer prior to placing a PAm hydrogel-tethered circular coverslip on top. Uncured PDMS was gently poured onto the construct and cured at 37°C overnight. (C) The PDMS mold attached to the PAm hydrogel-tethered coverslip was removed and bonded overnight to the rectangular PAm hydrogel-tethered coverslips following UV/Ozone treatment.

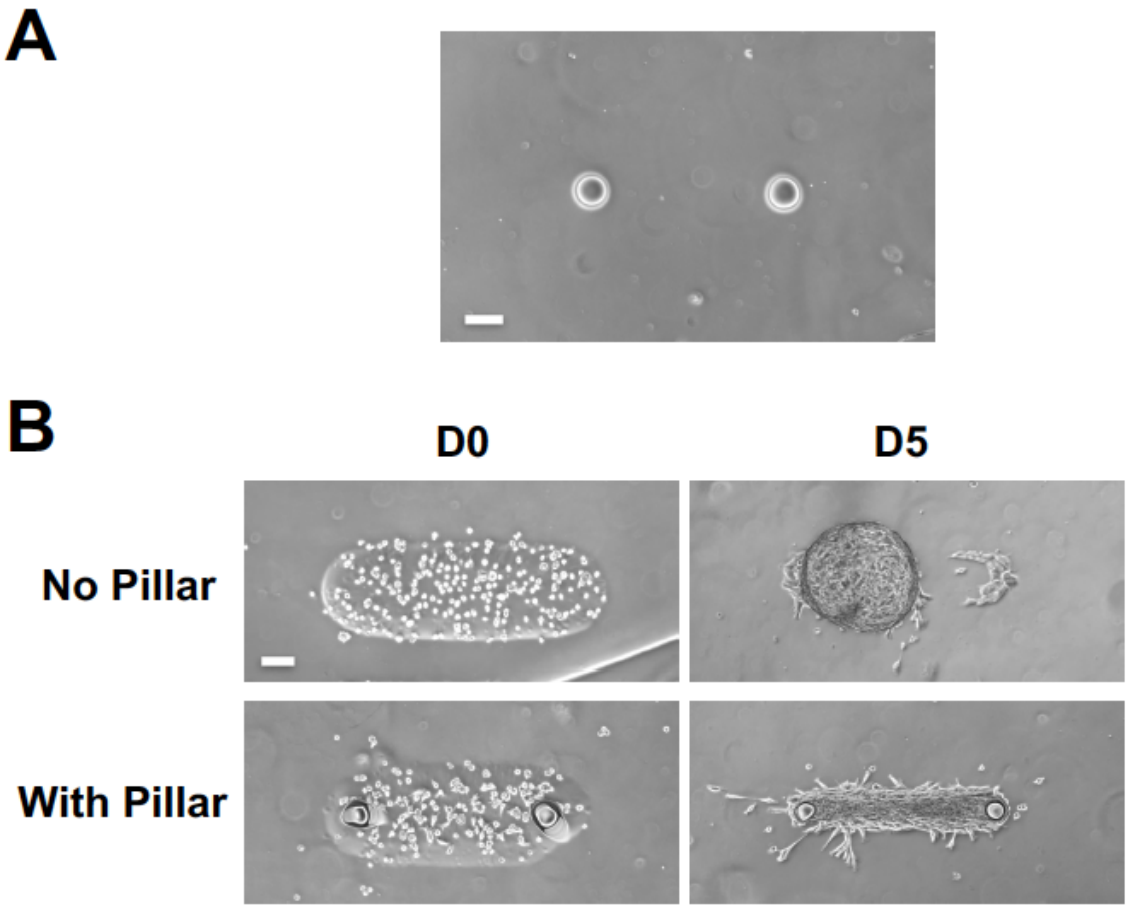

Figure 2.3: Pillar-induced cellular alignment.

(A) Acrylamide (Am) was photopolymerized to create circular pillars that attach to the bottom and top PAm planar hydrogels in the central chamber of the device. The diameter of these hydrogel pillars was pre-determined by patterns created in a transparency photomask. (B) With no support pillars, the tissue compacts from all directions and forms a sphere. With support pillars in place, the tissue compacts around these anchor points and the cells align unidirectionally, forming a tissue that represents a muscle bundle. All scale bars: 100 μm.

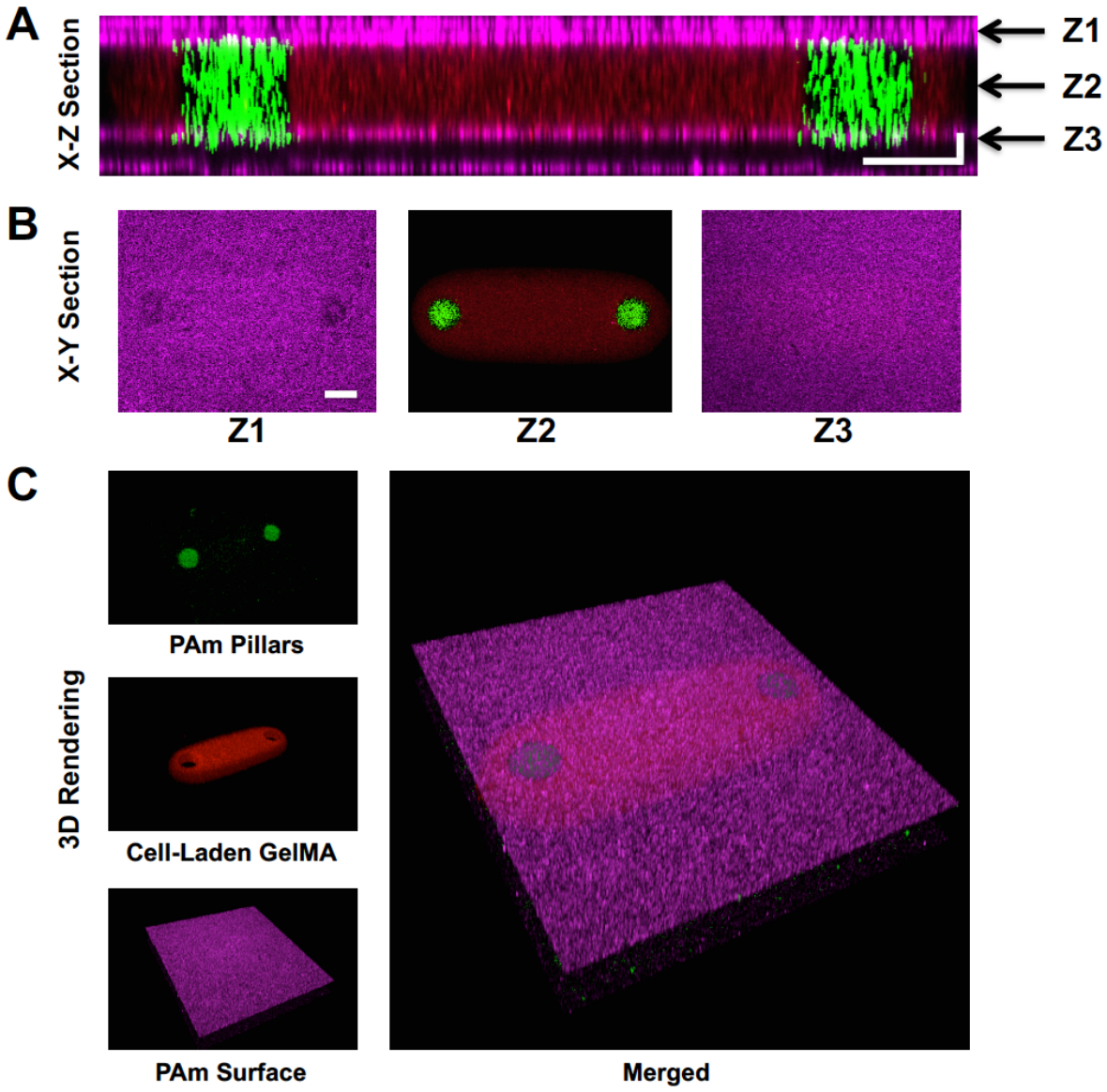

Figure 2.4: Characterization of various hydrogel structures within flow chamber.

Z-stack images of the hydrogels, loaded with fluorescent microparticles, were obtained using a laser scanning confocal microscope (Green: PAm pillars; Red: GelMA hydrogel; Magenta: PAm planar hydrogels). (A) X-Z cross-section and (B) X-Y planes at the specified Z locations are shown. (C) 3D renderings of each component and the composite structure are shown. Scale bars: (A) Horizontal: 100 µm; Vertical: 30 µm; (B) 100 µm.

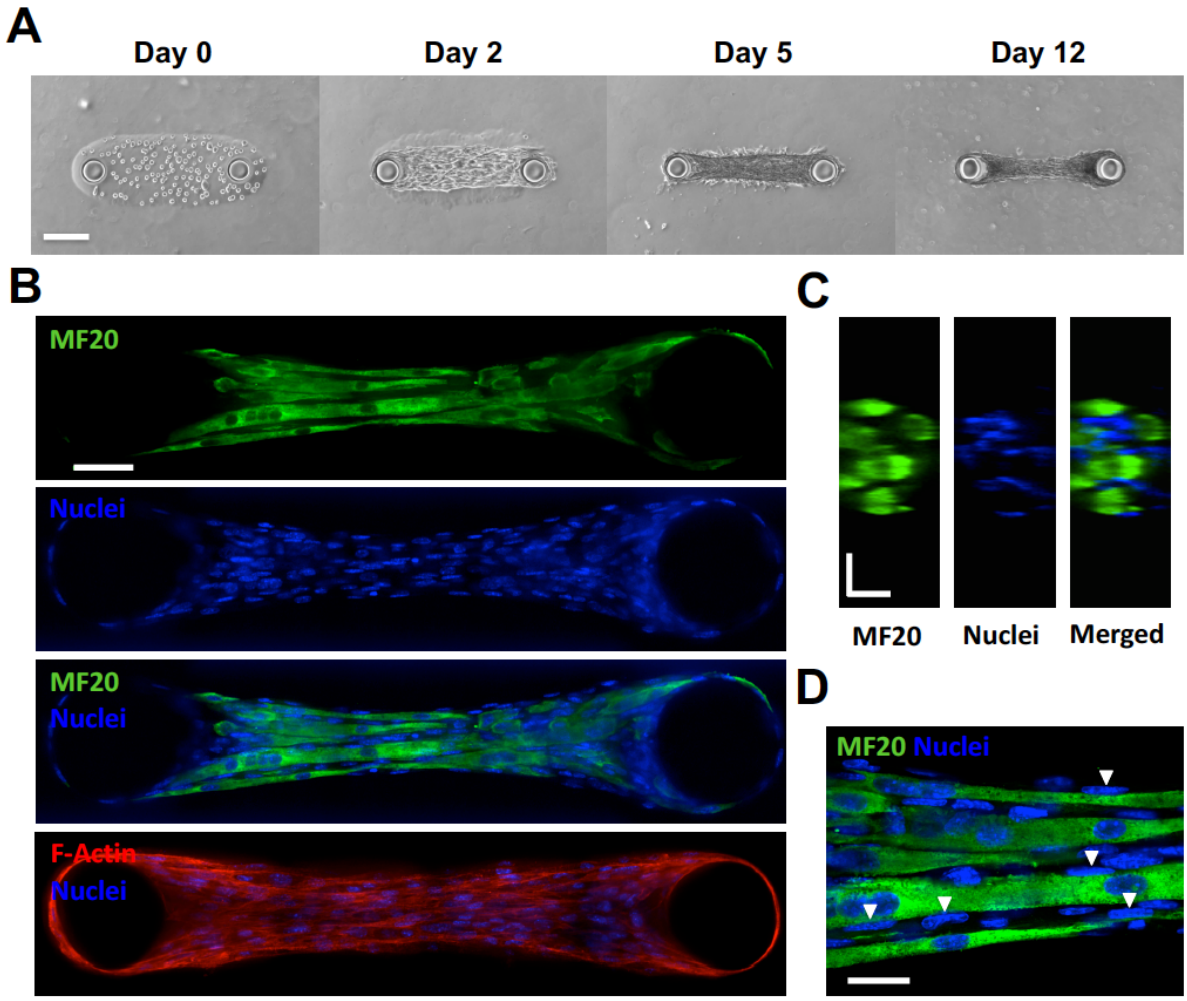

Figure 2.5: Muscle tissue growth and characterization.

(A) Brightfield images depict cell growth, attachment, and hydrogel compaction as a function of days in culture. (B) Immunofluorescent staining images taken from a spinning disk confocal microscope of day 12 samples for myosin heavy chain (MF20) (green), nuclei (blue), and the merged composite. This result suggests a highly matured muscle tissue composed of several multinucleated myotubes. F-actin staining (red) depicts cytoskeletal alignment (Bottom). (C) Y-Z confocal sections of a microtissue stained for MF20 (green) and nuclei (blue) illustrate the three-dimensional, cylindrical morphology and fascicular structure of the engineered muscle tissue. (D) High magnification (100X) images of MF20 and nuclei depict the arrangement of nuclei on the periphery of myotubes (white arrows). Scale bars: (A) 150 µm; (B) 50 µm; (C) and (D) 20 µm.

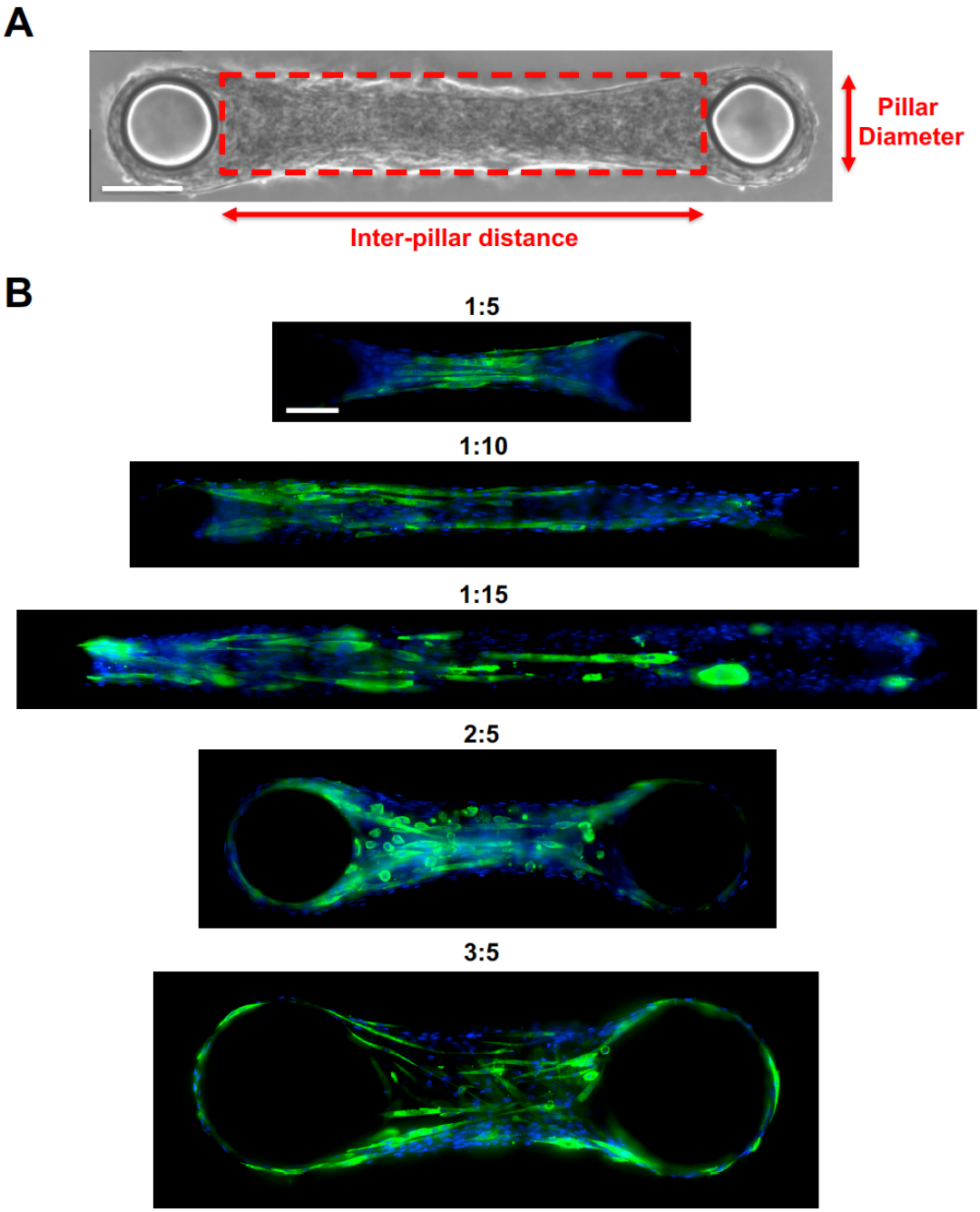

Figure 2.6: Varying the aspect ratio of the characteristic tissue volume.

(A) Brightfield image of microtissue overlaid with a red box to illustrate the pillar diameter and inter-pillar distance. The resulting aspect ratios included 1:5, 1:10, 1:15, 2:5, and 3:5. (B) Immunofluorescence staining images of myosin heavy chain (green) and nuclei (blue) for each tissue variation visually illustrates that the 1:5 sample has optimal alignment and fusion. All scale bars: 100 μm.

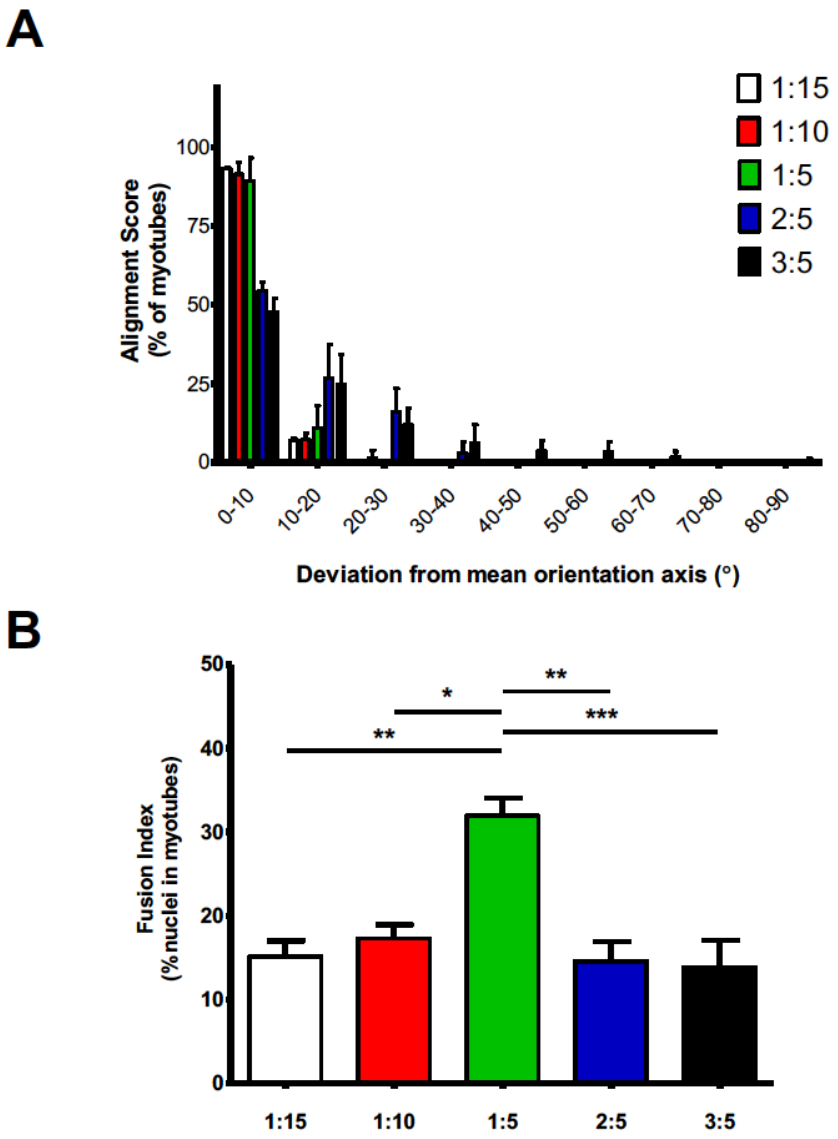

Figure 2.7: Myotube alignment and muscle cell fusion.

(A) Alignment score showing the deviation of the longitudinal myotube axis from the mean orientation axis for 5 experimental groups (1:15, 1:10, 1:5, 2:5, and 3:5) after 12 days of culture. Values are calculated as a percent of total myotubes per sample. 3-5 samples from 3 different chips were used per group. For each group, the plot illustrates the mean value along with standard deviation. (B) Fusion indices, calculated as the percentage of the total number of nuclei within myotubes relative to the total number of nuclei in the sample, for each experimental group, analyzed from confocal z-stacks of immunofluorescence staining for myosin heavy chain (MF20) and nuclei counterstain. 2000 nuclei from 3-5 samples examined from 3 different chips were used for each group. The plot shows the mean value alone with standard deviation. One-way ANOVA with Tukey's multiple comparison test was used to assess statistical significance (*$p < 0.1$, **$p < 0.01$, ***$p < 0.001$).

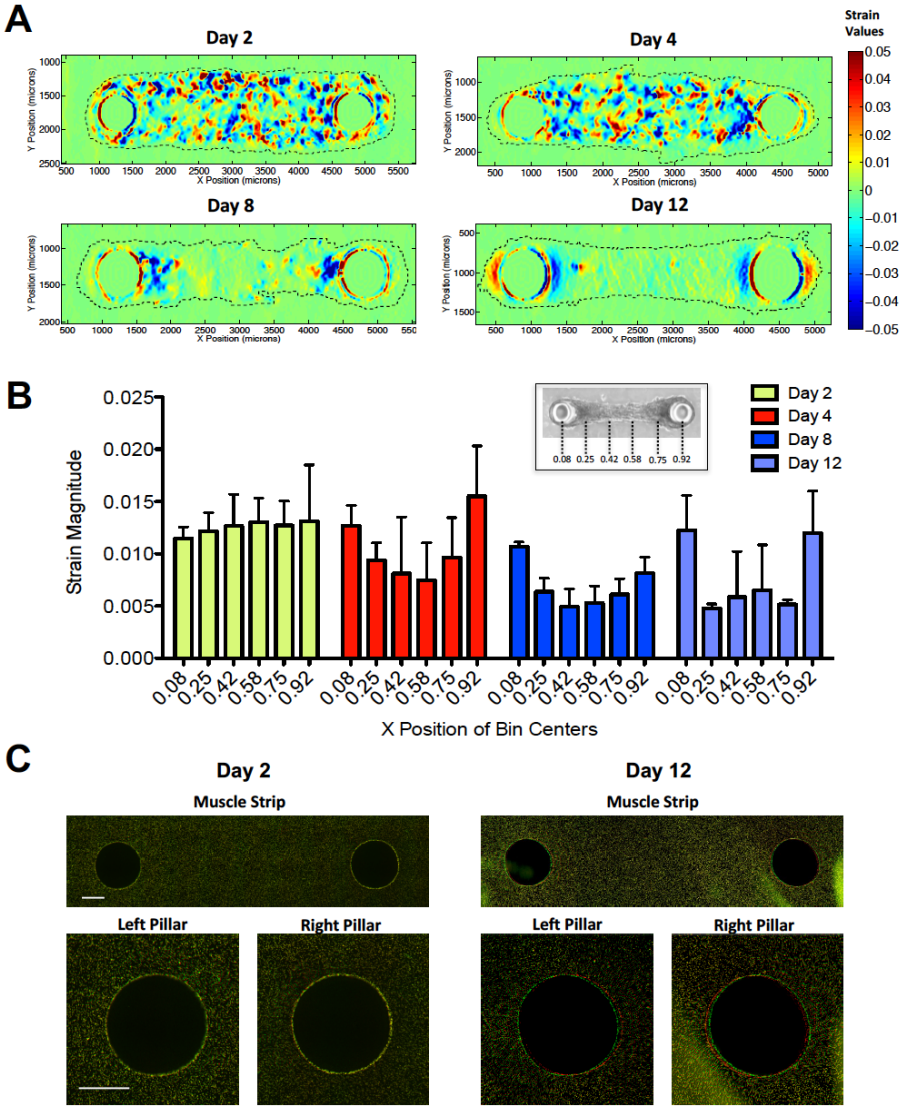

Figure 2.8: Quantification of cell generated strains on the PAm hydrogel with culture time.

(A) Heat map of tensile strain values, ε_{xx}, calculated from the deformations observed on the PAm hydrogel layer at culture days 2, 4, 8, and 12. The dotted lines display the contour of the cell-laden GelMA hydrogel. Negative and positive values indicate contraction and extension of the hydrogel. (B) Bar graph of binned values of ε_{xx} along the long axis of cell-laden GelMA hydrogel. The locations of the bin centers are indicated in the x-axis of the plot and are shown pictorially in the inset containing the Brightfield image of the microtissue. (C) An overlay of X-Y confocal sections of fluorescent particles embedded in the PAm hydrogel surface at Day 0 (green) and Day 2 (red) in the left panel and at Day 0 (green) and Day 12 (red) in the right panel. The lack of overlap between green and red beads in the right panel indicates the inward shift of the two pillars at Day 12 suggesting the contraction of the microtissue. Scale bars: 50µm.

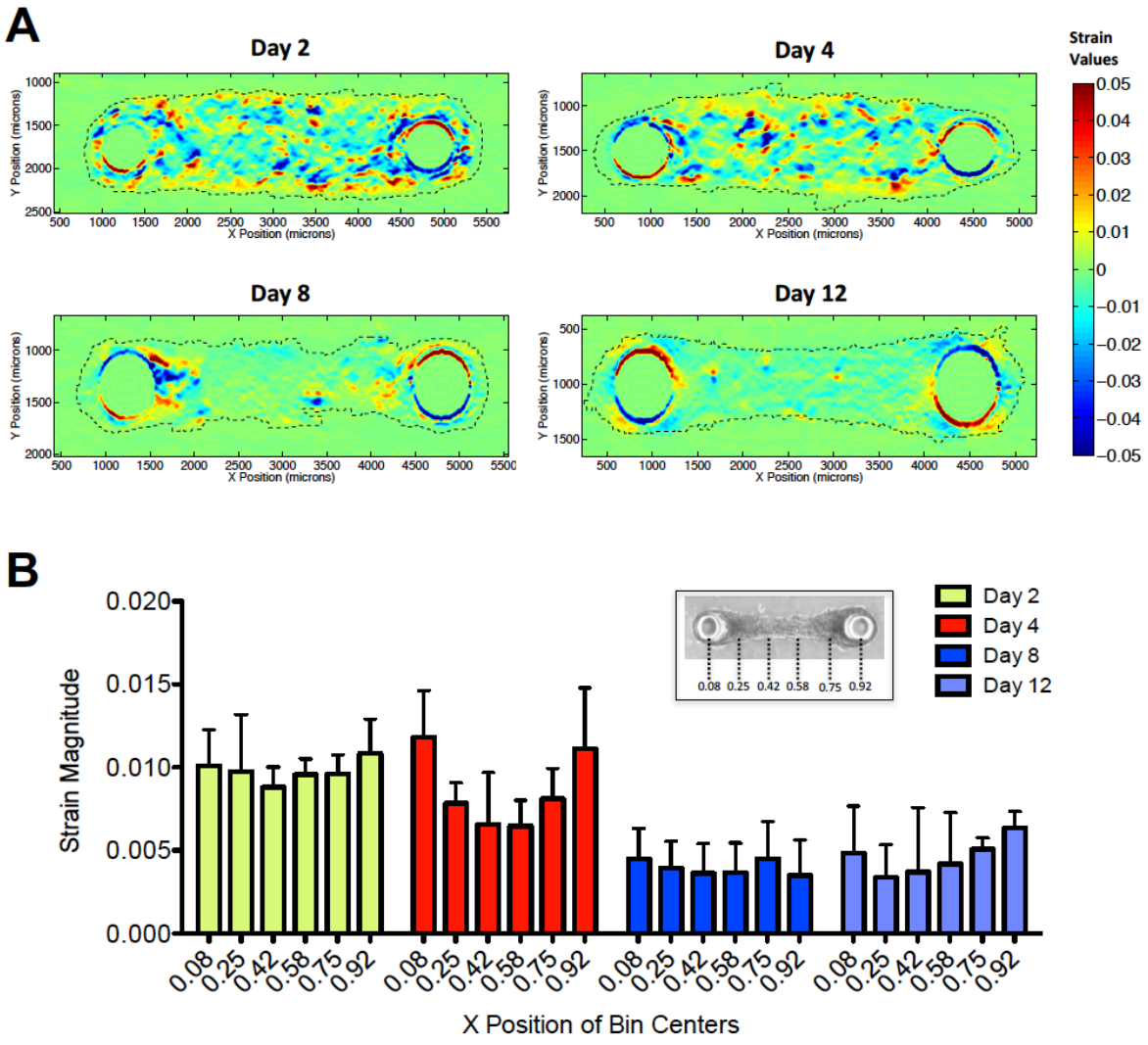

Figure 2.9: Strain calculations, ε_{yy}.

(A) Strains in the y-direction are calculated from the displacements measured in the PAm hydrogel layer by the cells as they pull on its surface. The strains are shown within the contour of the tissue sample (indicated by a dotted red line) as it matures over time. The strains are calculated with respect to the reference state of the sample at day 0. (B) Quantification of strain magnitude for ε_{yy} at x-positions binned across the long axis of the tissue as shown in the inset at days 2, 4, 8, and 12 in culture. At least 4 different samples were used to generate the plot.

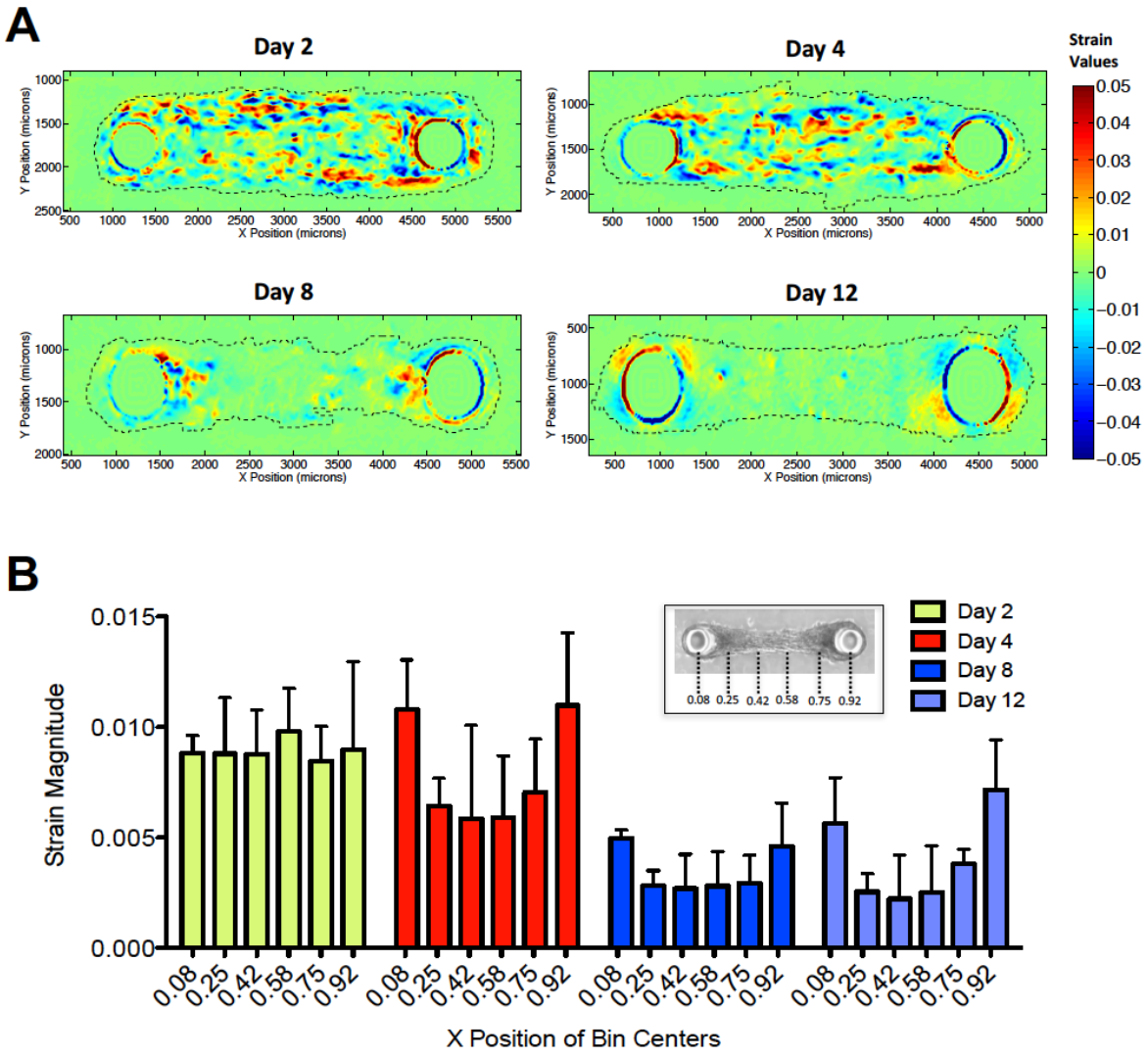

Figure 2.10: Strain calculations, ε_{xy}.

(A) Shear strains are calculated from the displacements measured in the PAm hydrogel layer by the cells as they pull on its surface. The strains are shown within the contour of the tissue sample (indicated by a dotted red line) as it matures over time. The strains are calculated with respect to the reference state of the sample at day 0. (B) Quantification of strain magnitude for ε_{xy} at x-positions binned across the long axis of the tissue as shown in the inset at days 2, 4, 8, and 12 in culture. At least 4 different samples were used to generate the plot.

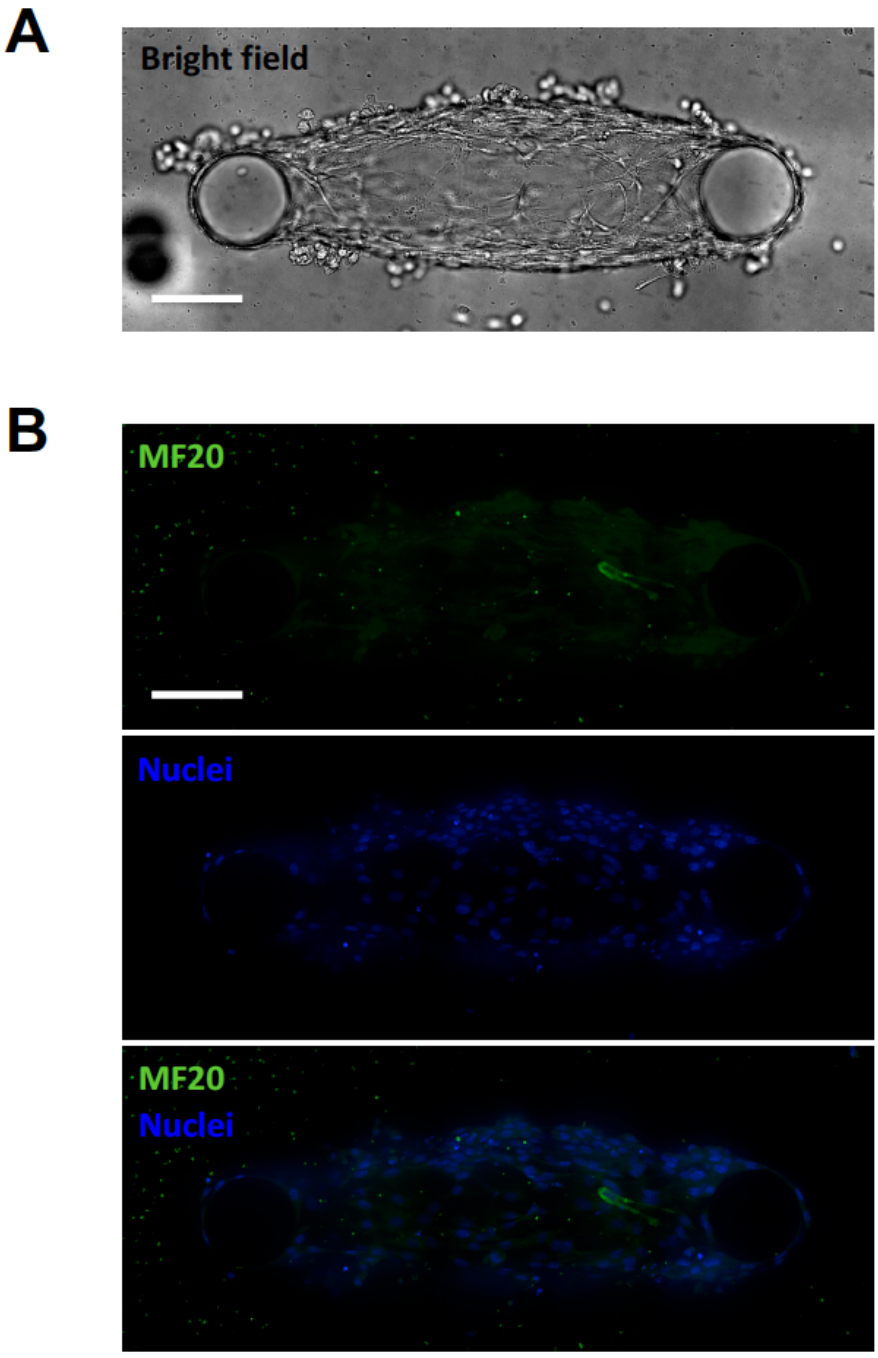

Figure 2.11: Day 4 muscle tissues.

(A) Brightfield and (B) immunofluorescence staining images of samples fixed at day 4. Merged image of myosin heavy chain (MF20) (green) and nuclei (blue) counterstain shows no myotube formation. All scale bars: 100 μm.

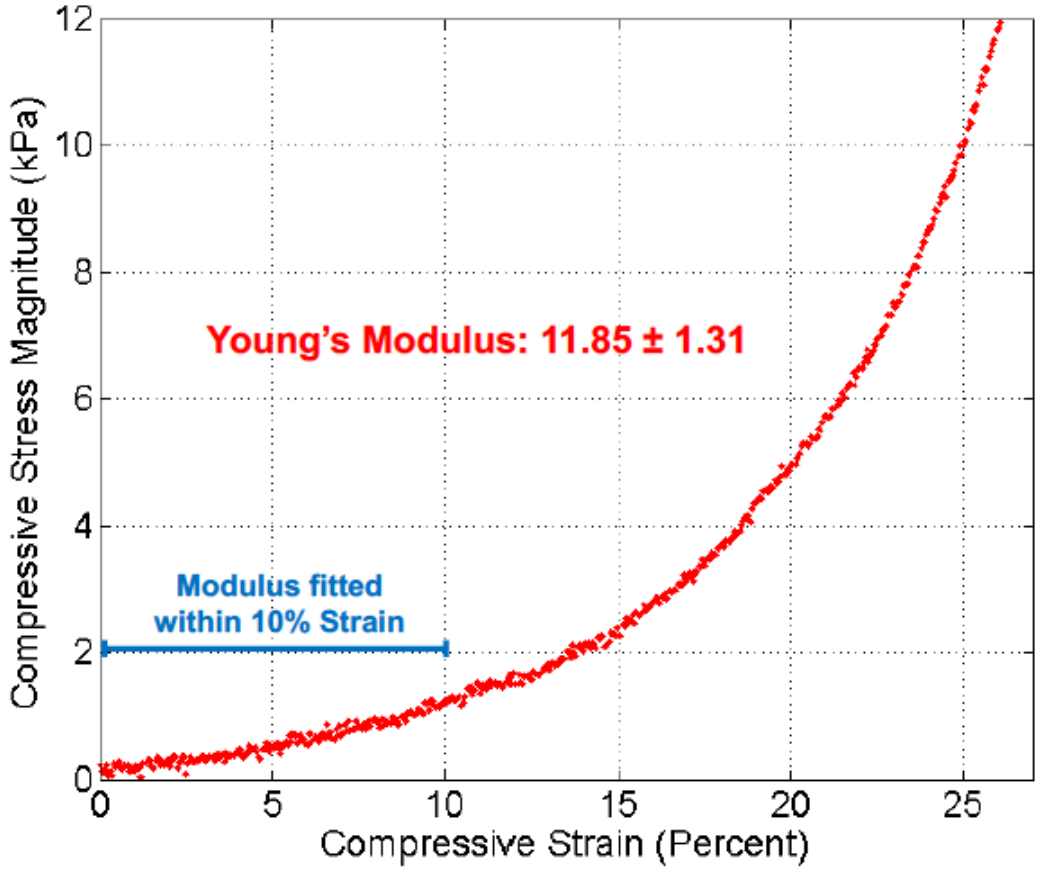

Figure 2.12: Stress-strain curve of the PAm hydrogel.

A representative stress-strain curve of a PAm hydrogel under compressive loading. The x- and y-axis denotes the compressive strain and stress, respectively. The stress-strain curve within the 10% strain region (indicated by the blue line) was linearly fitted to obtain the Young's modulus which was determined to be 11.85 ± 1.31 kPa.

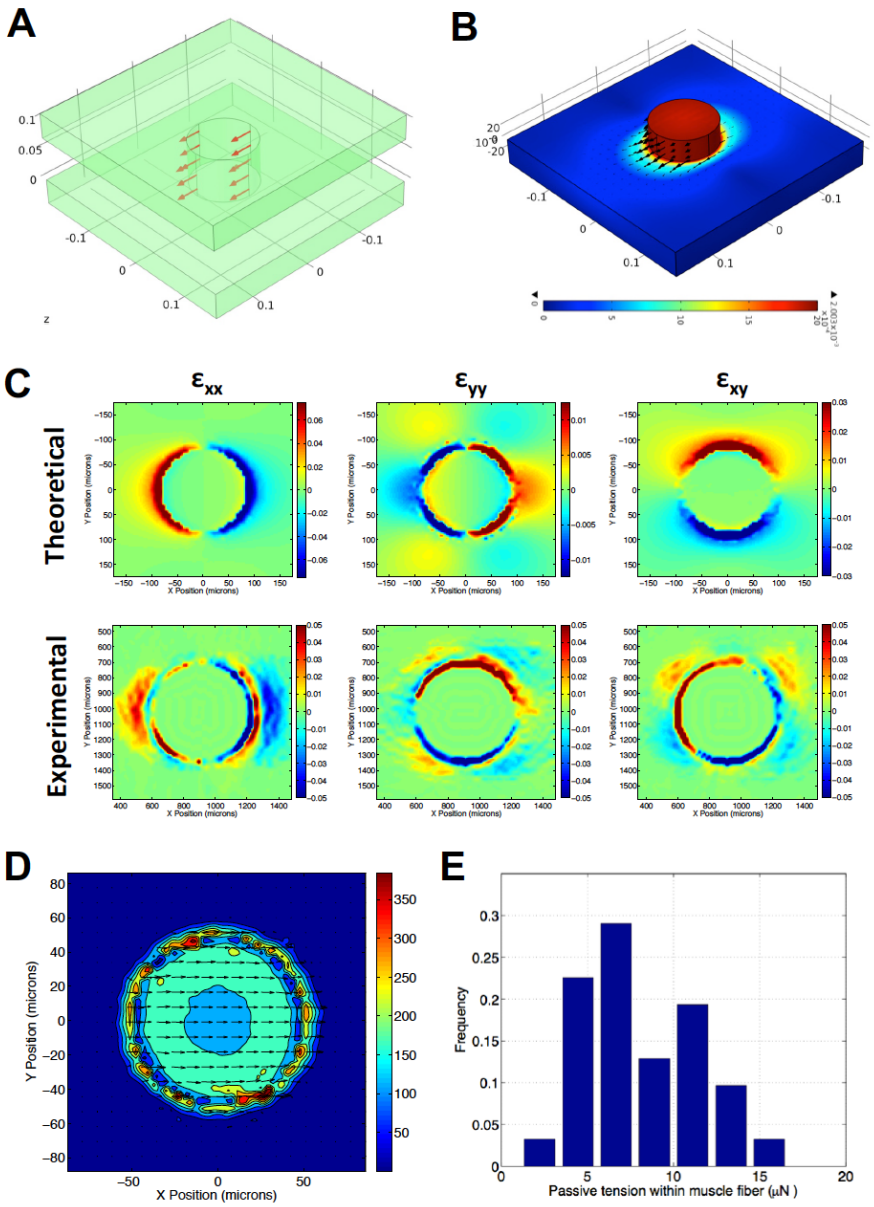

Figure 2.13: Quantification of passive tension generated by the engineered muscle using COMSOL.

(A) 3D rendering of the finite element domain used for simulating the deformations in the PAm hydrogel caused by pillar displacement. (B) The magnitude of the displacement vectors shown as a heat map on the finite element domain. (C) The strain values for $\varepsilon_{xx}, \varepsilon_{yy}$, and ε_{xy} on the surface of the PAm hydrogels obtained from finite element simulations (theoretical, top row) and empirically (experimental, bottom row). (D) Stress tensor component, τ_{xz}, and traction stress vector obtained from the finite element simulations shown as a heat map and vector field, respectively. (E) Histogram showing the distribution of the magnitudes of passive tension generated by 30 microtissues.

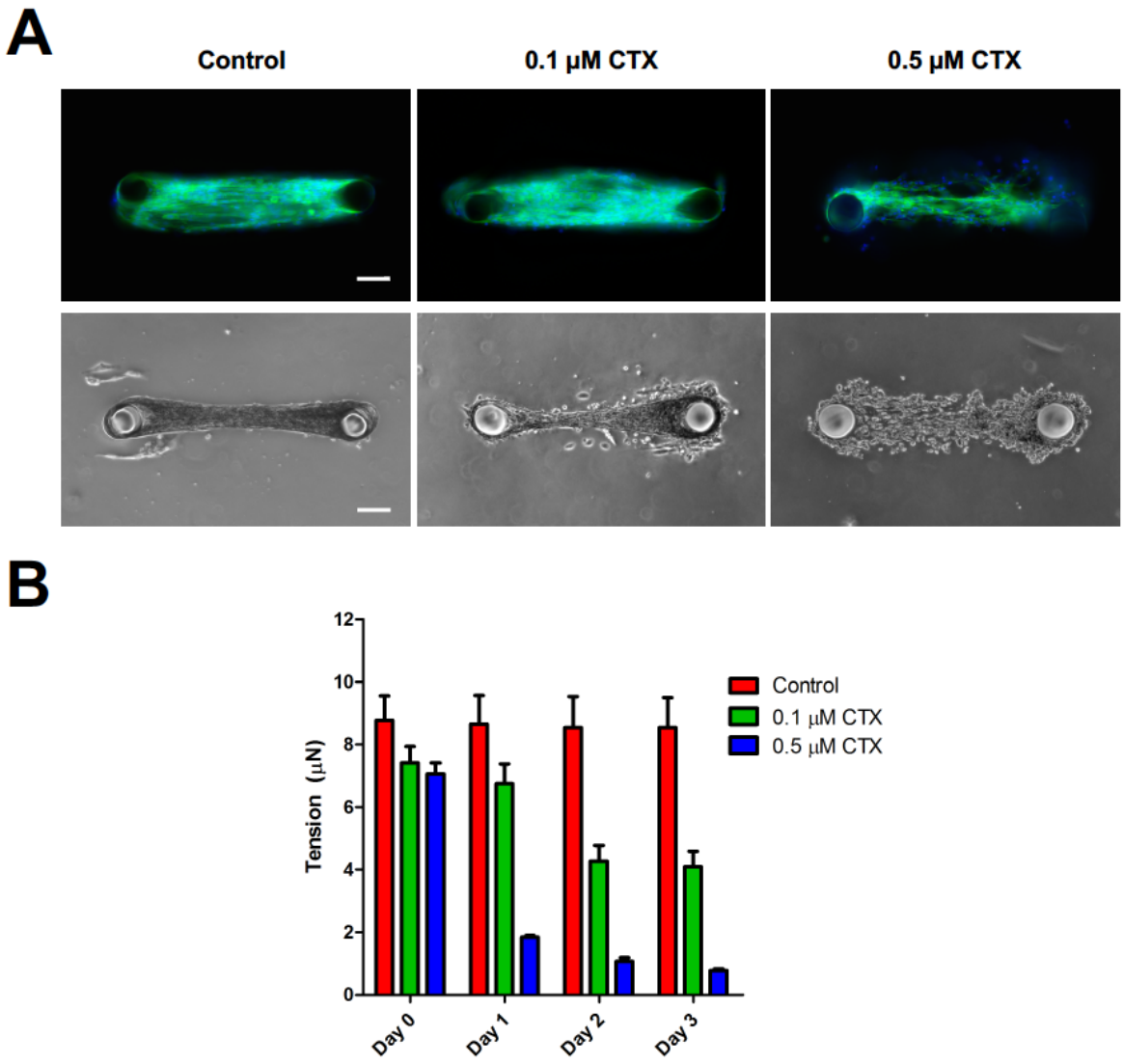

Figure 2.14: Dose-dependent response of engineered muscle strips to cardiotoxin (CTX).

(A) F-actin and brightfield images of muscle strips subjected to 0 μM, 0.1 μM, and 0.5 μM CTX for 24 hours. (B) CTX administration results in a dose-dependent drop in passive tension due to cytoskeletal disruption.

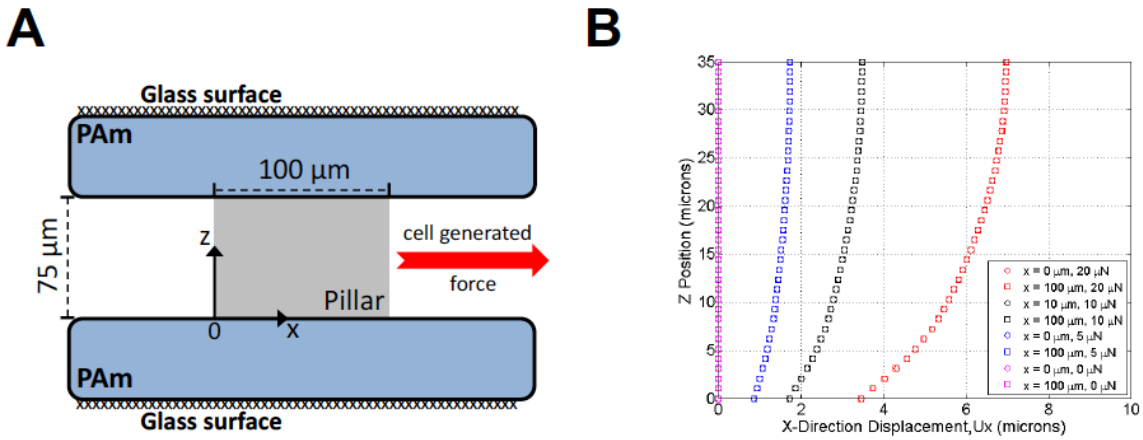

Figure 2.15: Analysis of pillar bending.

(A) Diagram showing the XZ cross-section of the finite element domain bisecting the center of the PAm pillar. The red arrow indicates the direction of the traction stress boundary condition caused by cell generated forces. (B) The displacement of the pillar in the X-direction (Ux) along Z positions on the left (x = 0 µm) and right (x = 100 µm) side of the pillar region under passive tensions of 0, 5, 10, and 20 µN. Note the axis origin at the bottom left corner of the pillar region.

2.9 References

1. D. Loessner, K. S. Stok, M. P. Lutolf, D. W. Hutmacher, J. A. Clements and S. C. Rizzi, *Biomaterials*, 2010, **31**, 8494-8506.

2. H. Karlsson, M. Fryknas, R. Larsson and P. Nygren, *Experimental cell research*, 2012, **318**, 1577-1585.

3. H. K. Dhiman, A. R. Ray and A. K. Panda, *Biomaterials*, 2005, **26**, 979-986.

4. A. S. Kienhuis, H. M. Wortelboer, J. C. Hoflack, E. J. Moonen, J. C. Kleinjans, B. van Ommen, J. H. van Delft and R. H. Stierum, *Drug metabolism and disposition: the biological fate of chemicals*, 2006, **34**, 2083-2090.

5. A. A. Chen, D. K. Thomas, L. L. Ong, R. E. Schwartz, T. R. Golub and S. N. Bhatia, *Proceedings of the National Academy of Sciences of the United States of America*, 2011, **108**, 11842-11847.

6. A. Hansen, A. Eder, M. Bonstrup, M. Flato, M. Mewe, S. Schaaf, B. Aksehirlioglu, A. P. Schwoerer, J. Uebeler and T. Eschenhagen, *Circulation research*, 2010, **107**, 35-44.

7. N. Thavandiran, N. Dubois, A. Mikryukov, S. Masse, B. Beca, C. A. Simmons, V. S. Deshpande, J. P. McGarry, C. S. Chen, K. Nanthakumar, G. M. Keller, M. Radisic and P. W. Zandstra, *Proceedings of the National Academy of Sciences of the United States of America*, 2013, **110**, E4698-4707.

8. K. H. Benam, S. Dauth, B. Hassell, A. Herland, A. Jain, K. J. Jang, K. Karalis, H. J. Kim, L. MacQueen, R. Mahmoodian, S. Musah, Y. S. Torisawa, A. D. van der Meer, R. Villenave, M. Yadid, K. K. Parker and D. E. Ingber, *Annual review of pathology*, 2015, **10**, 195-262.

9. A. K. Capulli, K. Tian, N. Mehandru, A. Bukhta, S. F. Choudhury, M. Suchyta and K. K. Parker, *Lab on a chip*, 2014, **14**, 3181-3186.

10. S. N. Bhatia and D. E. Ingber, *Nature biotechnology*, 2014, **32**, 760-772.

11. D. Huh, B. Matthews, A. Mammoto, A. Montoya-Zavala, H. Y. Hsin and D. E. Ingber, *Science*, 2010, **328**, 1662-1669.

12. H. J. Kim, D. Huh, G. Hamilton and D. E. Ingber, *Lab on a chip*, 2012, **12**, 2165-2174.

13. H. J. Kim, H. Li, J. J. Collins and D. E. Ingber, *Proceedings of the National Academy of Sciences of the United States of America*, 2016, **113**, E7-15.

14. A. Agarwal, J. A. Goss, A. Cho, M. L. McCain and K. K. Parker, *Lab on a chip*, 2013, **13**, 3599-3608.

15. A. Grosberg, P. W. Alford, M. L. McCain and K. K. Parker, *Lab on a chip*, 2011, **11**, 4165-4173.

16. J. A. Brown, V. Pensabene, D. A. Markov, V. Allwardt, M. D. Neely, M. Shi, C. M. Britt, O. S. Hoilett, Q. Yang, B. M. Brewer, P. C. Samson, L. J. McCawley, J. M. May, D. J. Webb, D. Li, A. B. Bowman, R. S. Reiserer and J. P. Wikswo, *Biomicrofluidics*, 2015, **9**, 054124.

17. A. Herland, A. D. van der Meer, E. A. FitzGerald, T. E. Park, J. J. Sleeboom and D. E. Ingber, *PloS one*, 2016, **11**, e0150360.

18. A. Mathur, P. Loskill, K. Shao, N. Huebsch, S. Hong, S. G. Marcus, N. Marks, M. Mandegar, B. R. Conklin, L. P. Lee and K. E. Healy, *Scientific reports*, 2015, **5**, 8883.

19. A. Aung, I. S. Bhullar, J. Theprungsirikul, S. K. Davey, H. L. Lim, Y. J. Chiu, X. Ma, S. Dewan, Y. H. Lo, A. McCulloch and S. Varghese, *Lab on a chip*, 2016, **16**, 153-162.

20. I. Janssen, S. B. Heymsfield, Z. Wang and R. Ross, *J Appl Physiol*, 2000, **89**, 81-88.

21. I. Janssen, S. B. Heymsfield and R. Ross, *JAGS*, 2002, **50**, 889-896.

22. H. H. Vandenburgh, J. Chromiak, J. Shansky, M. Del Tatto and J. Lemaire, *FASEB*, 1999, **13**, 1031-1038.

23. R. H. Fitts, S. W. Trappe, D. L. Costill, P. M. Gallagher, A. C. Creer, P. A. Colloton, J. R. Peters, J. G. Romatowski, J. L. Bain and D. A. Riley, *The Journal of physiology*, 2010, **588**, 3567-3592.

24. J. Shansky, J. Chromiak, M. Del Tatto and H. H. Vandenburgh, *In Vitro Cell Dev. Biol.*, 1997, **33**, 659-661.

25. C. A. Powell, B. L. Smiley, J. Mills and H. H. Vandenburgh, *American journal of physiology. Cell physiology*, 2002, **283**, C1557-1565.

26. R. G. Dennis and P. E. Kosnik, *In Vitro Cell Dev. Biol.*, 2000, **36**, 327-335.

27. Y. C. Huang, R. G. Dennis, L. Larkin and K. Baar, *Journal of applied physiology*, 2005, **98**, 706-713.

28. G. Moon du, G. Christ, J. D. Stitzel, A. Atala and J. J. Yoo, *Tissue engineering. Part A*, 2008, **14**, 473-482.

29. M. S. Sakar, D. Neal, T. Boudou, M. A. Borochin, Y. Li, R. Weiss, R. D. Kamm, C. S. Chen and H. H. Asada, *Lab on a chip*, 2012, **12**, 4976-4985.

30. L. Madden, M. Juhas, W. E. Kraus, G. A. Truskey and N. Bursac, *eLife*, 2015, **4**, e04885.

31. D. Neal, M. S. Sakar, L. L. Ong and H. Harry Asada, *Lab on a chip*, 2014, **14**, 1907-1916.

32. C. Cvetkovic, R. Raman, V. Chan, B. J. Williams, M. Tolish, P. Bajaj, M. S. Sakar, H. H. Asada, M. T. Saif and R. Bashir, *Proceedings of the National Academy of Sciences of the United States of America*, 2014, **111**, 10125-10130.

33. P. Heher, B. Maleiner, J. Pruller, A. H. Teuschl, J. Kollmitzer, X. Monforte, S. Wolbank, H. Redl, D. Runzler and C. Fuchs, *Acta biomaterialia*, 2015, **24**, 251-265.

34. A. P. Nesmith, A. Agarwal, M. L. McCain and K. K. Parker, *Lab on a chip*, 2014, **14**, 3925-3936.

35. C. Mann and D. Leckband, *Cellular and Molecular Bioengineering*, 2010, **3**, 40-49.

36. A. P. Nesmith, M. A. Wagner, F. S. Pasqualini, B. B. O'Connor, M. J. Pincus, P. R. August and K. K. Parker, *The Journal of cell biology*, 2016, **215**, 47-56.

37. K. Shimizu, H. Araki, K. Sakata, W. Tonomura, M. Hashida and S. Konishi, *Journal of bioscience and bioengineering*, 2015, **119**, 212-216.

38. C. G. Anene-Nzelu, K. Y. Peh, A. Fraiszudeen, Y. H. Kuan, S. H. Ng, Y. C. Toh, H. L. Leo and H. Yu, *Lab on a chip*, 2013, **13**, 4124-4133.

39. J. W. Nichol, S. T. Koshy, H. Bae, C. M. Hwang, S. Yamanlar and A. Khademhosseini, *Biomaterials*, 2010, **31**, 5536-5544.

40. H. Kang, Y. R. Shih, Y. Hwang, C. Wen, V. Rao, T. Seo and S. Varghese, *Acta biomaterialia*, 2014, **10**, 4961-4970.

41. T. Majima and W. Schnabel, *Macromol. Chem.*, 1991, **192**, 2307-2315.

42. S. K. Davey, A. Aung, G. Agrawal, H. L. Lim, M. Kar and S. Varghese, *Tissue engineering. Part C, Methods*, 2015, **21**, 1188-1196.

43. A. Aung, J. Theprungsirikul, H. L. Lim and S. Varghese, *Lab on a chip*, 2016, **16**, 1886-1898.

44. N. Sangaj, P. Kyriakakis, D. Yang, C. W. Chang, G. Arya and S. Varghese, *Biomacromolecules*, 2010, **11**, 3294-3300.

45. C. Zhang, A. Aung, L. Liao and S. Varghese, *Soft matter*, 2009, **5**, 3831.

46. R. L. Lieber, *Skeletal muscle structure, function and plasticity: the physiological basis of rehabilitation*, Lippincott Williams & Wilkins, 2002.

47. E. Shoji, H. Sakurai, T. Nishino, T. Nakahata, T. Heike, T. Awaya, N. Fujii, Y. Manabe, M. Matsuo and A. Sehara-Fujisawa, *Scientific reports*, 2015, **5**, 12831.

CHAPTER 3:

Human induced-pluripotent stem cell-derived myoblasts produce functional skeletal muscle microtissues: an hiPSC-organ-on-a-chip

Gaurav Agrawal[1], Priya Nayak [1], Shyni Varghese[1,2*]

[1] Department of Bioengineering, University of California, San Diego, La Jolla, California, USA

[2] Department of Orthopaedic Surgery, Duke University, Durham, North Carolina, USA

***** To whom correspondence may be addressed: svarghese@ucsd.edu

3.1 Abstract

Micro-engineered human skeletal muscle tissues that accurately recreate native tissue morphology and function would be valuable *in vitro* models for pre-clinical research. Recent advances in microfluidic organ-on-a-chip technologies have shown promise in replicating tissue-specific function and capturing disease pathophysiology. By incorporating microfluidics, organs-on-chips recreate the continuous fluid flow that supplies cells with nutrients similar to blood in our bodies. Further, these platforms have shown promise in recapitulating tissue architecture and function, and can be mechanically- and chemically-perturbed to mimic *in vivo* conditions with high-fidelity. Here, we describe the development of a three-dimensional (3D) skeletal muscle tissue, formed entirely from human induced-pluripotent stem cell-derived myogenic progenitors, in a microfluidic device – the hiPSC-skeletal-muscle-on-a-chip (hiPSC-SMOC). Using a novel light-based protein-patterning approach, we have spatially-confined hiPSC-derived myogenic precursors around two anti-fouling hydrogel pillars that function to induce unidirectional tissue alignment and guide tissue formation. We have characterized tissue morphology by using imaging tools to assess the expression of myogenic markers, MF20, desmin, myogenin, and Pax7. Further, we have used the microfluidic aspect of our device to administer a cyclical mechanical stimulation via pulsatile fluid flow. We have found that increased frequency of mechanical loading leads to increased expression of myogenin, a late-stage myogenic marker. Further, we have demonstrated hiPSC-SMOC muscle microtissue functionality by observing its response to acetylcholine, the neurotransmitter released by motor neurons at the neuromuscular junction. The unique union of microfluidics with hiPSC-muscle tissues has allowed us to explore new methods of promoting the maturation and function of skeletal muscle tissues. A hiPSC-

SMOC utilizing patient-specific cells could be a powerful tool in recreating the physiology of a healthy or diseased patient, including those with uncommon genetic disorders. Thus, a 3D hiPSC-SMOC provides a human-based tissue alternative to standard two-dimensional (2D) cell culture systems and mouse-based animal systems, which until today remain the paradigm models for pre-clinical studies of skeletal muscle, including drug discovery and disease modeling.

3.2 Introduction

Understanding and studying the interactions between cells and their microenvironment that lead to the formation of matured tissues requires the availability of platforms that recreate the physiological complexities of human tissues. Recent advances in tissue engineering have focused on the formation of three-dimensional (3D) tissue analogs. These capture inherent cell-cell and cell-ECM interactions while also recreating relevant tissue functions. Thus, 3D tissue analogs are attractive alternatives to traditional cell monolayers which fail to mimic the complexity of human tissues. In fact, the development of complex 3D *in vitro* tissue systems is of paramount importance for human disease modeling and drug discovery to avoid the need for animal studies, which are costly, inefficient, and fundamentally non-human and thus lack relevance to human studies.[1]

In this regard, organ-on-chip models that mimic tissue-specific function have arisen as promising technologies for preclinical toxicity and efficacy screening.[2, 3] These low cost, *in vitro* systems bring a higher complexity to tissues than standard cell culture. Organs-on-chips provide nutrients and remove cellular wastes through constant fluid flow similar to blood in the body. Additionally, they allow for cellular compartmentalization to incorporate various cell types. Finally, tissues in organs-on-chips can be stimulated in various methods, whether that be mechanical, electrical, or optical, to replicate the various cues a native tissue may experience. Thus far, functional organs-on-chips simulating the lungs, gut, heart, and blood-brain barrier already have been developed. [4-12]

Interestingly, the majority of the current organ-on-a-chip studies utilize cell lines or animal-derived cells arranged in two-dimensional sheets, thus lacking clear relevance to human physiology. The development of 3D human organ-on-chip platforms may further

advance the field and could capture the physiological complexity of native tissues. Further, few recent studies have utilized human cell sources, such as primary human cells from biopsies or induced-pluripotent stem cells (hiPSCs) generated from adult human cells.[11, 13-15] While biopsy-derived cells maintain the phenotype of the original patient, they are limited in number and difficult to obtain. On the other hand, hiPSCs are obtained from any patient by reprogramming adult somatic cells back to a pluripotent, embryonic-like state.[16, 17] These hiPSCs can be terminally-differentiated to a somatic cell that replicates the genetic make-up and phenotype representative of the cell's final function. Thus, hiPSCs could be taken from healthy or diseased patients to create human-specific and disease-specific models. Combined with the organ-on-a-chip, these could serve as valuable cell sources for drug development or personalized medicine tailored to each patient.

Implementing hiPSCs-derived cells in *in vitro* models of skeletal muscle would be instrumental in fundamental biological research as well as drug development. Skeletal muscle comprises about 40% of the mass of an adult human, making it the most abundant tissue in the body, and is responsible for the motion and strength that allows us to live healthy and fulfilling lives. Skeletal muscle damage can be caused by tears from trauma or surgery, atrophy from lack of use as in age-related sarcopenia, or dystrophy which results from genetic defects.[18-21] Particularly in the case of genetically-based disorders, which may include Duchenne and Becker muscular dystrophies, patients suffer from progressive muscle degeneration, loss of power and motion, and eventually respiratory and cardiac failure that causes death. There are currently no cures available, and palliative care includes physical therapy, steroids, and pain medications. Given the lack of treatment options and the difficulty in developing clinically-relevant models for the development of new therapies, hiPSC-based

model systems that can recreate the structural, morphological, and functional aspects of skeletal muscle, along with its disease-state, could be powerful tools.

Recent advancements have been made in developing 3D human tissue models of skeletal muscle using cells from hiPSCs. Rao and colleagues have used transient over-expression of hiPSCs with the myogenic transcription factor, Pax7, to develop functional 3D skeletal muscle bundles that form multinucleated myofibers and actively contract in response to electrical and chemical stimulation.[22] Maffioletti, et al., used hiPSC from patients with Duchenne, limb-girdle, and congenital muscular dystrophies to create 3D artificial muscle tissues that recapitulated the pathological characteristics of these respective diseases with high-fidelity.[23] To this point, hiPSC-based skeletal muscle models have yet to be integrated with microfluidic organ-on-a-chip systems. Instead, skeletal-muscle-on-chip platforms have been recently created using the C2C12 mouse myoblast cell line.[24-26] Further, given the recent progress in creating hiPSC-based 3D tissue mimics, we have yet to understand how mechanical stimuli can enhance hiPSC differentiation and maturation. Previous studies using primary human myoblasts have shown that cyclic stretch of engineered muscle strips leads to myofiber hypertrophy and a stronger contractile response.[27-29] It is important to elucidate mechanical factors that may contribute to the maturation of hiPSC-muscle tissue in order to develop models that better mimic adult human muscle tissue. Taken together, the use of hiPSC-derived myoblasts in a 3D organ-on-chip platform that develops matured skeletal muscle tissues that recapitulate the structural organization and functional capabilities of native muscle could be valuable in screening for both drug-based and cell-based therapies.

Here, we describe the development of a 3D skeletal muscle-on-a-chip system with microtissues formed entirely from hiPSC-derived myogenic progenitors, to our knowledge

the first of its kind. Using chemically-mediated differentiation, we have developed myogenic progenitors from hiPSCs before seeding the cells into a microfluidic device via a novel protein photo-patterning method. We have demonstrated the formation of aligned skeletal muscle microtissues after 8 days of culture, where the tissues express myogenic markers including myosin heavy chain, desmin, myogenin, Pax7, and sarcomeric α-actinin. Further, we have utilized microfluidics to apply cyclical mechanical stimulation to the microtissues via pulsatile fluid flow, and have observed increased expression of the late-stage myogenic maturation marker, myogenin, in response to mechanical loading. Finally, we have demonstrated that the microtissues have reached functional maturity by showing tissue contraction in response to the neurotransmitter acetylcholine. Such hiPSC-based platforms could be useful as clinically-relevant models for drug screening and disease modeling. Further, these could be linked together with other organ-on-a-chip systems such as liver, heart, and cancer, to incorporate tissue-tissue cross-talk and study drug effect on a more systemic level.

3.3 Materials and Methods

Cell culture of human induced pluripotent stem cells

Human induced-pluripotent stem cell (hiPSC) line L-εPCCC3 was generously provided by Dr. Inder Verma from the Salk Institute. Cells were initially thawed and plated at low confluency on Matrigel (Corning)-coated 6-well plates, and maintained in mTeSR-1 stem cell media (Stem Cell Technologies), a feeder-free maintenance media. The hiPSCs were passaged using ReLeSR (Stem Cell Technologies) cell dissociation solution at 70% confluency a minimal of three times prior to differentiating into myogenic precursors, to ensure the cells retained pluripotency prior to differentiation.

Differentiation of hiPSC to myogenic precursors

Human iPSC colonies were dissociated with Versene (Gibco) and plated as single cells on a Matrigel-coated 12-well plate in mTeSR-1 with Thiazovivin (Selleck Chemicals). At approximately 35% confluency, media was switched to DMEM/F12 supplemented with Insulin-Transferrin-Selenium (Sigma-Aldrich), 3μM CHIR99021 (Selleck Chemicals), and 0.5μM LDN193189 (Miltenyi Biotec). On day 3, 20ng/mL FGF-2 (R&D Systems) was added to the previous media for 3 more days. After day 6, media was swapped to DMEM/F12 supplemented with 10ng/mL HGF, 2ng/mL IGF-1, 20ng/mL FGF-2, and 0.5μM LDN193189 (Miltenyi Biotec). On day 8, media was swapped to DMEM/F12 supplemented with 15% knockout serum replacement (KOSR, Gibco) and 2ng/mL IGF-1. On day 12, media was swapped to DMEM/F12 supplemented with 15% knockout serum replacement (KOSR, Gibco), 10ng/mL HGF, and 2ng/mL IGF-1. Media changes were daily up to day 12, then every other day after that up to day 30.

Cells were then passaged after reaching day 30. Cells were pre-treated with 2uM TZV for 2 hours prior to passaging, then detached with TrypLE Express by incubating cells for five minutes at 37°C. Cells were re-plated in a modified medium consisting of DMEM/F12, 20%KOSR, 1% non-essential amino acids, 1% Glutamax, 1% antibiotics, and 2.5ng/mL FGF. Each well of differentiated cells was passaged to 3 wells. Upon reaching 70-80% confluency, cells were switched to differentiation medium composed of DMEM/F12, 1% NEAA, 1% Glutamax, 1% antibiotics, and 1% ITS supplement.

Synthesis of gelatin methacrylate (GelMA)

The synthesis of gelatin methacrylate (GelMA) followed a protocol described previously.[30, 31] Briefly, 10g of bovine gelatin (Sigma Aldrich) was dissolved in 100 mL of PBS and heated to 60°C for 60 minutes, with stirring, until the gelatin was fully dissolved. Next, the temperature was reduced to 50°C, and 8 mL of methacrylic anhydride (Sigma Aldrich) was added drop-by-drop to the dissolved gelatin. The solution was then stirred at a high speed for 60 minutes. PBS was warmed and added to the mixed solution, which was dialyzed against Milli-Q ultrapure water using a 12-14 kDa cutoff dialysis tubing (Spectrum Laboratories) for seven days at 40°C, changing water three times per day. This was meant to remove contaminants, excess small molecules, and unreacted methacrylic anhydride from the solution. Lastly, the dialyzed GelMA solution was then flash frozen in liquid nitrogen and lyophilized in a freeze dryer for 4 days until it became a lightweight white cake-like solid, and stored at -20°C until use.

Synthesis of lithium phenyl-2,4,6-trimethylbenzoylphosphinate (LAP) photoinitiator

The photoinitiator used in this study, LAP, was synthesized as described elsewhere.[32] Briefly, 2,4,6-trimethylbenzoyl chloride (Sigma Aldrich) was added dropwise to an equal molar solution of dimethyl phenylphosphonite (Sigma Aldrich) under argon, while stirring at 25°C. The temperature was changed to 50°C after 18 hours of reaction time, and 4M excess lithium bromide (Sigma Aldrich) with 2-butanone was added to the reaction mixture. A white precipitate was formed within 10 minutes, after which the temperature was reduced to 25°C for 4 hours. The precipitate was isolated via filtration, then washed three times using 2-butanone to ensure complete removal of excess lithium bromide. The excess 2-butanone was removed by drying the product under vacuum, yielding LAP as a white crystalline powder.

Fabrication of silicon mold

Micro-patterned silicon wafers were fabricated as described previously.[12] Briefly, a photomask of the desired microfluidic device design was developed in AutoCAD and printed by CAD/Art Services, Inc. Next, a 5-inch diameter silicon wafer was spun-coat with NR9-1500PY negative photoresist (Futurrex). The microfluidic design was lithographically-defined via UV light. The Si wafer was etched using the deep reactive ion etching (DRIE) process, which entails flowing SF6 gas at 100 sccm for 11 seconds of reaction time, followed by flowing C4F8 gas at 80 sccm for a 7-second passivation cycle. An etching depth of 75μm was achieved using an etch rate of 0.7μm per cycle. After etching, the photoresist was removed by immersing the silicon wafer in acetone for 4 hours before rinsing with methanol, isopropanol, and deionized water. Finally, the Si mold was dried with compressed nitrogen gas and silanized by vapor deposition of trichlorosilane (TCI Inc.) to allow casting and removal of PDMS.

Methacrylation of Glass Coverslips

To tether polyacrylamide (PAm) hydrogels within the microfluidic device, cover-glass was chemically-methacrylated as described previously.[31, 33] Briefly, round glass coverslips (12mm round, #1 thickness, Fisher) and rectangular glass coverslips (24mm x 50mm, #1 thickness, Fisher) were washed with 200 proof ethanol for 15 minutes, then treated with a methacrylate solution composed of 97.7% (v/v) of ethanol, 0.3% (v/v) glacial acetic acid, and 2% (v/v) 3-(trimethoxysilyl)propyl methacrylate (Sigma Aldrich) for 5 minutes. The glass was washed several times with 200 proof ethanol under agitation, then dried under heat at 60°C for 2 hours prior to use.

Fabrication of microfluidics device with PAm hydrogel layers

The hiPSC-MOC was created in a device that contained a flat PAm hydrogel layer on the top and bottom of the central chamber of the microfluidic device as described previously, with slight modifications.[26] To create the hydrogels, a polyacrylamide (PAm) precursor solution composed of 5% (wt/v) acrylamide (UltraPure Acrylamide, ThermoFisher Scientific), 0.225% (wt/v) *N,N'*-methylenebis(acrylamide) (Sigma Aldrich), and 0.12% (wt/v) ammonium persulfate (APS, Sigma Aldrich) in phosphate buffered saline (PBS) was made. For imaging purposes, 200nm fluorescent far red microparticles (ThermoFisher Scientific) were added to the precursor solution at a 1:100 dilution. Quickly, 0.6µL of a 10% (wt/v) *N,N,N',N'*-tetramethylethylenediamine (TEMED, Sigma Aldrich) in PBS was mixed into the precursor solution. Immediately, 3µL of the solution was dropped onto the center of a methacrylated 24 x 50mm coverslip and covered with a non-methacrylated 12mm round

coverslip to create a 12mm round PAm hydrogel layer. A similar process was followed to make an equal PAm hydrogel layer on a 12mm round coverglass, in which 2.5μL of PAm solution was dropped onto a non-methacrylated 24 x 50mm coverglass and covered with a methacrylated 12mm round coverglass. After 30 minutes to allow for polymerization, the samples were immersed in DI water before cleaving off the non-methacrylated glass with a razor blade, leaving behind a 12mm round PAm hydrogel tethered to the 24 x 50mm rectangular coverglass and 12mm round coverglass. These would form the bottom and top surfaces of the microfluidic device.

To create the device, 5μL of DI water was dropped onto the circular central chamber of the micropatterned silicon wafer, before covering it with the 12mm round PAm-tethered coverglass (facedown), to keep the PAm hydrated throughout the fabrication process. Next, polydimethylsiloxane (PDMS) (Sylgard 184, Dow Corning) was prepared by mixing base and curing agent together in a 10:1 ratio by mass for 5 minutes. After bubbles were removed by vacuum, the PDMS was cast onto the micropatterned silicon wafer containing 12mm round glass with PAm hydrogel, then baked at 60°C for 2 hours to cure the PDMS. The PDMS was separated from the silicon wafer with the 12mm round glass and PAm hydrogel still attached. To provide access points for inlet and outlet tubing, 1.0mm round holes were punched into the PDMS at the two ends of the microfluidics pattern. Next, the PDMS was bonded to the PAm-tethered rectangular glass after treating both surfaces with UV-Ozone for 5 minutes, fixing the two components together, and baking at 60°C for at least 2 hours. This resulted in a microfluidics device, in which the central chamber is flanked by PAm hydrogels on the top and bottom surfaces of the device. DI water was perfused into the device after

bonding, to hydrate the hydrogels. Prior to use, PBS was perfused into the device to allow the PAm hydrogels to equilibrate.

Formation of PAm pillars for skeletal muscle-on-a-chip

To create uniaxially-aligned skeletal muscle microtissues, anchoring pillars were first formed in the microfluidic device, as described previously.[26] Briefly, a precursor solution composed of 5% acrylamide, 0.225% bis-acrylamide, and 2mM LAP in PBS was prepared and perfused into the device. A transparency photomask with an array of circular patterns of 125μm diameter and 500μm pillar-to-pillar distance was placed onto the microscope stage, and the central chamber of the microfluidic device was centered over the pattern. The device was exposed to UV light for 80 seconds to initiate photo-polymerization, resulting in circular hydrogel pillars sandwiched between the bottom and top PAm hydrogel layers within the device. Unreacted monomer solution wash washed away with repeated PBS washes, and the device was sterilized under UV light for 2 hours prior to encapsulation of cells.

Acellular pre-patterning of GelMA matrix

Due to their inherent sensitivity to abnormal environmental conditions, myogenic precursors were seeded onto a protein-patterned surface rather than encapsulation directly into a hydrogel matrix. To do this, we utilized free-radical initiated photopolymerization to create a geometrically-defined coating of GelMA onto the PAm hydrogel layer at the bottom of the microfluidics device. A 4.5% (wt/v) GelMA solution in PBS was prepared by dissolving the GelMA precipitate in PBS for 30 mins at 60°C. The solution was sterilized by syringe filtration with a 0.22μm filter to remove contaminants and any insoluble components.

Also, 0.01% ascorbic acid (Sigma Aldrich), a free-radical quencher, and 2mM LAP, a photoinitiator, were added to prepare the GelMA solution for photo-polymerization.

The acellular hydrogel solution was infused into the microfluidic device using a syringe. A transparency photomask containing an array of capsule patterns (300μm-by-1000μm ellipses) was placed on the fluorescence microscope, and the device containing the hydrogel solution was manually positioned using the microscope eyepiece under brightfield illumination to locate two pillars within the capsule pattern. This region was then exposed to collimated UV light (365nm ± 40nm excitation wavelength) for 15 seconds to photopolymerize the GelMA solution into a capsule shape. This process was repeated several times to obtain up to 10 samples within each device. Unreacted monomer solution was washed away with several sterile PBS washes, resulting in GelMA hydrogels of extremely low stiffness strategically-positioned around two PAm pillars. The device was connected to a syringe pump (Harvard Apparatus) and supplied basic cellular growth media, consisting of Dulbecco's Modified Eagle high-glucose medium (Hyclone) supplemented with 10% fetal bovine serum (Gibco) and 5% penicillin-streptomycin (Gibco), overnight at a constant flow rate of 40μL/hr in an incubator set to 37°C and 10% CO_2. These settings were chosen based on previous studies.[12, 26, 33] Due to the low rigidity of the GelMA hydrogel and heat from the incubator, the majority of polymerized GelMA was washed away overnight, leaving behind only the GelMA that had polymerized to form an inter-penetrating network at the PAm interface, forming a thin protein-coated surface for cell attachment.

Seeding of hiPSC-myogenic precursors into device

One day after GelMA protein-patterning, a cell suspension composed of myogenic precursors at a cell density of 20 million cells/mL in hiPSC-muscle growth media consisting of 20% knockout serum replacement (Gibco), 1% Glutamax (Gibco), 1% non-essential amino acids (Gibco), 2.5ng/mL basic fibroblast growth factor (bFGF, Sigma), and 1% penicillin-streptomycin (Gibco) in Dulbecco's Modified Eagle medium: nutrient mixture F/12 (DMEM/F12; Gibco) supplemented with 2μM Thiazovivin was prepared and perfused into the microfluidic device containing PAm hydrogel pillars and GelMA protein pattern. The cell-infused device was placed in an incubator at 37°C and 10% CO_2 for 30 minutes to allow sufficient time for cell attachment. Unattached cells were washed away with a sterile PBS wash and a media wash, resulting in hiPSC-myogenic precursors attached to the PAm via a GelMA cell-adhesive coating, arranged as a 2D layer of cells in a capsule shape surrounding the two PAm hydrogel pillars. Samples were cultured in hiPSC-muscle growth media for the first 24 hours, then switched over to hiPSC-muscle differentiation media composed of 2% horse serum (Omega Scientific), 1% insulin-transferrin-selenium supplement (ITS, Sigma), 1% Glutamax (Gibco), 1% non-essential amino acids (Gibco), and 1% antibiotic-antimycotic (Gibco) in Dulbecco's Modified Eagle medium: nutrient mixture F/12 (DMEM/F12; Gibco) for the remaining 7 days of tissue culture to induce cell differentiation and fusion. Media was supplied through a syringe pump at constant flow rate of 40μL/hr. The hiPSC-SMOC was cultured in an incubator at 37°C and 10% CO_2 for the duration of the experiment.

Immunofluorescence staining of microtissues

To visualize expression of tissue-specific proteins post-integration, hiPSC-SMOC tissues were stained for representative muscle-specific markers. At the end of culture,

samples were washed with PBS three times, fixed with 4% paraformaldehyde (PFA, Sigma Aldrich) for 15 minutes at room temperature, then washed again with PBS to remove excess PFA. A blocking buffer was prepared, composed of 3% bovine serum albumin (BSA, Sigma Aldrich) and 0.5% Triton-X 100 (Fisher Scientific), and added to the samples for 1 hour in 4°C, to prevent non-specific binding of antibodies. Next, primary antibodies were diluted in blocking buffer and added to the samples overnight at 4°C. The tissues were stained for myosin heavy chain (MF20 mouse monoclonal, Developmental Studies Hybridoma Bank), desmin (rabbit polyclonal, Abcam), Paired box protein Pax-7 (Pax7 mouse monoclonal, Developmental Studies Hybridoma Bank), myogenin (MyoG mouse monoclonal, Developmental Studies Hybridoma Bank), and sarcomeric α-actinin (SAA mouse monoclonal, Sigma Aldrich). After 24 hours, stains were washed away with several PBS washes. Next, a solution consisting of fluorescently-labeled secondary antibody diluted 1:100 in blocking buffer along with Hoechst 33342 dye diluted to 1x to view nuclei, was added to the samples overnight at 4°C, then washed away with excess PBS prior to imaging. The secondary antibodies included AlexaFluor 488 goat anti-rabbit secondary antibody (ThermoFisher Scientific) and AlexaFluor 568 goat anti-mouse secondary antibody (ThermoFisher Scientific). Samples were imaged with a spinning disk confocal microscope (Perkin Elmer UltraView) at 40x magnification.

Flow-induced mechanical stimulation of hiPSC-SMOC tissues

Microfluidics flow actuation via pulsed flow was used to apply a mechanical force to the skeletal muscle microtissues. A cyclical load that applies a shear stress to the tissue was applied to the muscle tissue by programming a pulsatile flow pattern in lieu of standard

laminar flow. For pulsatile flow, media was supplied at a flow rate of 100mL/hr for 1 second, then stopped for 30 seconds, and repeated for 20 minutes (40 total pulse cycles). When pulsatile flow was not in effect, standard laminar flow at a rate of 40μL/hr was used. The three different experimental conditions were control, long-interval pulse flow, and short-interval pulse flow. In the control, no pulsatile flow was applied. In the long-interval pulse flow, pulsatile flow was applied for 20 minutes every 6 hours. In the short-interval pulse flow, pulsatile flow was applied for 20 minutes every 2 hours. Thus, an increased number of loading cycles was applied in short-interval pulse as compared to the long-interval pulse condition. In total, pulsatile flow was applied for 3 days from day 1 to day 4 before further characterization and analysis of the tissues.

Computational-modeling of pulsatile flow and tissue-stresses

The system was modeled using COMSOL Multiphysics version 4.2. Given that cells comprising the tissue span the entire height of the chamber, the tissue was assumed to be uniform along its height in the z-direction. Thus, the system was modeled as a combination of fluid dynamics (fluid flow) and solid mechanics (tissue) under 2D planar conditions. The geometry of the chamber was defined as a rectangular prism of dimensions 12mm x 10mm x 0.070mm (length x width x height). The geometry of the tissue was drawn in AutoCAD to mimic the geometry of an hiPSC-SMOC microtissue at day 8, with a height of 0.070mm. The muscle tissue was modeled as a Neo-Hookean hyperelastic material, with material constants based on those previously-determined of muscle fibers. We defined the material to have a density of 1000kg/m^3, bulk modulus of 2.48 x 10^{10} dyn/cm^2, a Poisson's Ratio of 0.45, a Young's Modulus of 24.7 kPa, Lame constant μ of 714000 N/m^2, and Lame constant λ of

179000 N/m^2.[34-36] The PAm hydrogel pillars were modeled as linearly elastic isotropic materials with a density of 1000kg/m^3, a Poisson's Ratio of 0.45, and a Young's Modulus of 11.85 kPa. Laminar flow rates of 40 μL/hr and 100 mL/hr were input, with a no-slip boundary conditions. Heat maps representing flow velocity, pressure, fluid shear stress, and stress tensors in x, y, and xy were obtained.

Acetylcholine-mediated microtissue contraction

To assess functionality of the hiPSC-SMOC microtissues, the neurotransmitter acetylcholine was supplied to the tissues to simulate standard conditions at the neuromuscular junction in the human body. Acetylcholine chloride (Sigma Aldrich) was diluted in hiPSC-muscle differentiation media at 10mM based on similar studies, and supplied to day 8 tissues via a syringe pump.[22, 37] Light microscopy images were taken before and after supplementation of acetylcholine at 30 second intervals for 5 minutes, then stitched together.

Quantification of MyoG score and nuclear elongation ratio

MyoG score was quantified based on immunofluorescence images of samples stained for MyoG in order to assess the maturation of skeletal muscle microtissues. MyoG score was defined as the number of cell nuclei stained positive for MyoG divided by the total number of nuclei, as a percentage. Nuclear elongation was defined as the aspect ratio of the major axis to the minor axis of each nucleus, as described previously.[38] For both parameters, a minimum of four samples from independent experiments were analyzed. Data is presented as mean ± standard deviation, and the comparison between the groups was carried out by

using one-way ANOVA with Tukey's multiple comparison test, where P-values < 0.1 were considered statistically significant. Data is presented using GraphPad Prism software.

3.4 Results

Differentiation and characterization of hiPSC-myogenic progenitors

To develop a functional, human-specific skeletal muscle-on-a-chip platform, we first differentiated human induced-pluripotent stem cells to myogenic progenitor cells. A previously developed protocol by Chal, et al., was used, with slight modifications in the derivation process.[39] The hiPS cells were cultured as single cells and committed to the paraxial mesoderm via the GSK3β inhibitor CHIR99021, Insulin-Transferrin-Selenium, and LDN193189. Next, various growth factors were used over a 25-day period to induce the cells to myogenic lineage. Specifically, mesoderm-committed cells were cultured in serum-free conditions containing IGF-1, HGF, and FGF-2 growth factors. Immunofluorescence staining for various muscle-specific markers was performed to assess differentiation. By day 25, cells expressed the early myogenic marker MYF5 and satellite cell marker PAX7, and by day 35, cells expressed the late myogenic markers myogenin and MF20 for fast muscle fibers, as well as the cytoskeletal protein dystrophin (Figure 3.1). As cells elongated and fused into multinucleated myotubes, cells aligned next to one another. Thus, we showed that we can obtain a primarily early-stage myogenic population expressing MYF5+/PAX7-/MYOG-/MF20- and further differentiate this to a later stage myogenic population expressing MYF5+/PAX7+/MYOG+/MF20+. In culture, it was also observed that many cells detached from the culture plate or died over time if cultured for extended periods of time. Therefore, for the hiPSC-SMOC, we utilized cells that were primarily classified as early-stage cells in order to maintain their differentiation capacity and maximize cell viability during 3D tissue formation in the microfluidics chamber.

Device Fabrication and Characterization

To develop aligned 3D skeletal muscle tissues from hiPSC-myogenic progenitors, we developed a microfluidics device containing a central chamber with multiple hydrogel structures. A key component was the use of polyacrylamide for two purposes: (1) hydrogel pillars as anchoring structures to induce unidirectional tissue alignment and thus, promote myogenesis, and (2) bio-inert hydrogel on the top and bottom of the device to prevent cell attachment and thus promote 3D tissue formation over time.

This project builds on the skeletal muscle-on-a-chip described in Chapter 2, with notable differences. Specifically, in the original platform, C2C12 mouse myoblasts were encapsulated in the device directly in gelatin methacrylate, owing to its cell-adhesive and degradable nature that made it amenable to cell-mediated matrix remodeling to form a 3D muscle tissue. However, it was observed during experimentation that when the same procedure was followed using the hiPSC-myogenic progenitors, the majority of the cells did not survive (Figure 3.2A). This was evident by the absence of cell spreading and cell-cell attachment within the GelMA construct. We hypothesized that, given that the hiPSC-myogenic progenitors are derived from pluripotent stem cells, these cells remain extremely sensitive to unnatural or harsh environmental conditions. It is possible that impurities or small molecules in the GelMA precursor solution were toxic to the hiPSC-myogenic precursors, and led to their eventual death. Therefore, we explored other methods of seeding sensitive hiPSC-myogenic precursors without direct cell encapsulation into a protein matrix.

We theorized that GelMA could still be used as a material on which cells may be seeded, similar to protein patterning methods utilizing fibronectin or laminin that have been described elsewhere.[40] GelMA is an appropriate material owing to the fact that, as a derivative

of collagen, it inherently carries cell-adhesive sites. Also, GelMA is polymerized via free-radical initiated photo-polymerization using ultraviolet wavelength of light (365nm ± 40nm). Further, given that the PAm hydrogel layers on the top and bottom surfaces of the microfluidics device are microporous, we hypothesized that with a low concentration of GelMA, this could be exploited to form an inter-penetrating network (IPN) of GelMA-PAm. A low concentration of GelMA would yield a low hydrogel stiffness upon polymerization. Thus, the GelMA hydrogel structure would disintegrate and leave behind a thin, exposed layer of GelMA that forms an inter-penetrated network with the PAm, allowing cells to attach directly to the PAm via the GelMA. Additionally, if incubated with growth media containing fetal bovine serum, proteins from the serum would attach to the GelMA-PAm IPN to further promote cell attachment. This process is outlined in Figure 3.3.

Figure 3.4 illustrates the entire device fabrication, GelMA protein patterning, and cell-seeding process. A PDMS-based silicone device containing two PAm hydrogel layers on the top and bottom of the central chamber was created (Figure 3.4A). Following this, we used a previously-described 3D photopatterning method to generate PAm hydrogel pillars between the top and bottom PAm hydrogel layers (Figure 3.4B-C).[31] With these structural components in place, we next formed a GelMA-PAm IPN via photo-patterning (Figure 3.4D-E). A low concentration of 4.5% GelMA was infused into the device and polymerized in the shape of a large capsule surrounding two PAm hydrogel pillars, then washed with PBS to leave behind a thin coating of GelMA as an IPN with the PAm. The sample was perfused with standard growth media in a heated incubator for 24 hours to fully remove any chunky remnants of GelMA hydrogel and allow for protein attachment to the GelMA layer (Figure 3.4F). Finally, hiPSC-myogenic progenitors in myogenic growth media were perfused into the device

(Figure 3.4G). These cells attached to the GelMA pattern and formed a two-dimensional layer of cells within 30 minutes and began forming a 3D tissue strip by day 1 (Figure 3.2B).

Formation of 3D hiPSC-based skeletal muscle micro tissues

Human-specific skeletal muscle microtissues were formed using the hiPSC-derived myogenic precursors discussed previously. Following formation of the GelMA-PAm IPN, acellular samples were perfused with growth media for 24 hours, after which hiPSC-myogenic progenitors were seeded onto the patterns and cultured for 24 hours in 20% KOSR myogenic growth media. Finally, tissues were maintained for 7 days in myogenic differentiation media containing 2% horse serum and ITS to induce cell differentiation, cell fusion, alignment, and maturation (Figure 3.5A). Up to 10 tissues were formed in each microfluidic chip, spatially separated from one another by a minimum of 800μm in all directions. The 2D pattern of hiPSC-myogenic precursors was monitored for tissue formation for up to 8 days (Figure 3.5B). Brightfield images at day 0, 1, 4, and 8 in Figure 3.5B show that the individual cells that initially created a 2D layer around two hydrogel pillars formed cell-cell attachments and quickly evolved into a 3D muscle strip by day 1, and further maintained this structure until the end of culture at day 8.

Characterization of hiPSC-SMOC tissue morphology and differentiation

Engineered human skeletal muscle microtissues were characterized for myogenic protein expression. Samples cultured for 8 days were immunostained for myosin heavy chain, a marker for differentiated muscle cells, desmin, an intermediate filament found in muscle cells, myogenin, a nuclear marker specific to skeletal muscle, PAX7, a marker for skeletal

muscle stem cells known as satellite cells, and sarcomeric α-actinin, a microfilament protein that attaches actin filaments to the Z-lines of sarcomeres in muscle cells, and counterstained for cell nuclei. Images of a projection of all z-slices obtained from a spinning disk confocal microscope show multiple horizontally-aligned myotubes parallel to one another, and nuclei elongated along the major axis of the sample, two hallmarks of skeletal muscle tissue (Figure 3.6A). Further, we observe the presence of a stem-cell niche in PAX7 satellite cells, and the expression of late myogenic marker myogenin as well, suggesting the formation of a muscle tissue consisting of a heterogeneous population of myoblasts, myotubes, and satellite cells. Finally, the expression of α-actinin clearly depicts the formation of sarcomeres, indicating that tissue alignment may play a role in hiPSC-muscle tissue formation and differentiation (Figure 3.6D). Further, we can clearly observe the three-dimensional nature of the engineered hiPSC-muscle tissues by viewing X-Z and Y-Z cross sectional images of a representative skeletal muscle tissue. Figure 3.6B depicts the X-Z view, showing independent elongated MF20+ myotubes in various z-planes. This is reaffirmed by Figure 3.6C, which illustrates the Y-Z view, showing multiple densely clustered MF20+ myotubes in multiple Y and Z planes. The myotubes range from 4-12μm in diameter, and nuclei lie within the center or around the periphery of the myotubes. Although the myotubes are smaller in diameter than those formed from C2C12 or primary mouse myoblasts, the engineered hiPSC-skeletal muscle microtissues closely mimic the morphology and structure of native human skeletal muscle tissue.[41] An opacity rendering of the hiPSC muscle microtissue further illustrates the 3D structure and aligned arrangement of myofibers surrounded by nuclei (Figure 3.6E).

Assessment of hiPSC-SMOC function via acetylcholine-mediated contraction

Besides characterizing the structure and morphology of the engineered human skeletal muscle microtissues, we wanted to prove that the tissues are also functional, as for any studies involving skeletal muscle, function is of paramount importance. Skeletal muscle function can be assessed by observing an active muscle contraction in response to various stimuli, which can include electrical, optical, or chemical stimulation. For the hiPSC-SMOC microtissues, we sought to emulate the conditions at the neuromuscular junction in the human body. At this junction, the action potential that travels down the motor neuron stimulates the release of the neurotransmitter acetylcholine (ACh) at the motor end plate, which then binds to ACh receptors on the muscle fibers that initiates further intracellular signaling that ultimately activates the contractile machinery. We subjected our hiPSC-muscle microtissues to 10mM of ACh and observed a contraction of the muscle strip inwards from the two pillars, as seen in Figure 3.7. The dotted lines and arrows clearly illustrate the change in length of the muscle tissue after administration of ACh, indicating that the tissue has contracted. Thus, the myotubes comprising the hiPSC-derived muscle microtissue were sufficiently mature and connected with adjacent myotubes, and thus able to generate enough force to contract the tissue against the pillars. Therefore, the hiPSC-derived human muscle microtissue was functional, and could potentially contract in response to electrical or optical stimulation in future iterations of this platform.

Microfluidic-controlled mechanical stimulation of hiPSC-SMOC

In the human body, skeletal muscle is subjected to several stimuli under normal use, including lengthening and shortening during motion and exercise, and compression and shear during massage. To emulate this *in vitro*, previous studies have shown that cyclical stretch or

compression of tissue-engineered skeletal muscle tissues made from primary myoblasts leads to myofiber hypertrophy, formation of striations in myofibers, and stronger contractile response *in vitro*, as well as decreased inflammation *in vivo*.[27, 28, 42] In our experience, hiPSC-derived myogenic progenitors were more representative of nascent cells and created immature myofibers as compared to primary cells or cell lines. Therefore, it was important to explore ways to further mature the hiPSC-derived muscle microtissues to bring them closer to and adult-like state. Similar to cyclical stretch or compression, we used the microfluidic device to apply a cyclical load to the tissues through dynamic, pulsatile fluid flow. From a baseline rate of 40μL/hr, flow rate was pulsed to 100mL/hr for 1 second every 30 seconds for a 20-minute period (Figure 3.8A). These settings were arbitrarily chosen based on constraints such as the frequency of media-refilling and the rotor speed of the syringe pump. The loading schedule was varied and based on the interval between loading cycles, where control conditions involved no loading, long-interval conditions involved applying pulsatile flow ever 6 hours, and short-interval conditions involved applying pulsatile flow every 2 hours (Figure 3.8B). For the experiment, mechanical loading began on day 1, after the initial 3D tissue formation, and stopped on day 4, after which samples were analyzed (Figure 3.8C).

To better understand the stresses being generated by the pulsatile flow, we used finite element analysis to model the skeletal muscle tissue as a muscle strip inside of a chamber exposed to laminar fluid flow. The model was compared at the two flow rates - 40μL/hr and 100mL/hr. The theoretical velocity field, pressure, and shear stress of the fluid, as well as stresses on the tissue, are shown as heat maps in Figure 3.9. We see that at the lower flow rate, the velocity field, pressure, and fluid shear stress maps are uniform, and stresses on the tissue are negligible. However, at the high flow rate subjected to the tissue during pulsatile

flow, the fluid pressure is drastically higher near the inlet port than the outlet port (Figure 3.10). Note that the heat map shows a pressure spike at the first pillar closest to the fluid inlet, likely due to interference to fluid flow by the pillar. The velocity field reflects the higher flow rate, and fluid shear stress is significant. At both flow rates, stresses within the tissue in the *x*- and *y*- directions are negligible. However, the pattern suggests that under the 100mL/hr flow condition, shear stresses within the tissue are noticeably higher than those at the lower flow rate, presumably due to the shear stresses incurred at the tissue boundary during rapid fluid flow. Specifically, the shear stresses within the tissue at 40μL/hr are on the order of 0-0.5 Pa, whereas the same shear stresses within the tissue at 100mL/hr are on the order of 0-50 Pa. Therefore, the model confirms that the pulsatile flow mechanically-loads the tissue by producing shear stresses within the muscle microtissue.

Samples were immunostained for MyoG, a late-stage skeletal muscle differentiation marker indicative of muscle cell maturity. Interestingly, cyclical mechanical loading via pulsatile flow led to higher expression of MyoG across all samples (Figure 3.11A). In fact, increasing the number of loading cycles also led to a greater number of MyoG+ cells. This was confirmed by quantifying the MyoG score, which we have defined as the total number of MyoG+ cells with respect to the total number of cells in the sample (Figure 3.11B). Nuclear elongation, another traditional characteristic of skeletal muscle nuclei, was assessed by quantifying the ratio of the major axis to the minor axis of each nuclei. We saw that samples that were cyclically-loaded had a higher nuclear elongation ratio as compared to control samples (Figure 3.11C). Therefore, mechanical loading through pulsatile flow, a unique characteristic of a microfluidic-based system, led to increased maturation of hiPSC-derived skeletal muscle microtissues.

3.5 Discussion

Human induced pluripotent stem cells (hiPSCs) have immense potential to accurately model human disease on a patient-specific level. These cells are isolated from adult patients and reprogrammed to pluripotency, after which they can be differentiated to a specific cellular lineage. When combined with the organ-on-a-chip, we can create human tissue analogs in a unique microfluidic system, in which nutrients are supplied to the tissues and wastes are removed via constant perfusion, circumventing mass transport limitations associated with traditional static tissue cultures. Further, the organ-on-a-chip incorporates analysis of tissue morphology, structure, gene expression, and tissue function over time, thus multiple aspects of tissue response to drug treatment can be analyzed in real-time without destroying the tissue sample. In this study, we have created entirely human-specific, three-dimensional, functional skeletal muscle microtissues in a microfluidics device using hiPSC-derived myogenic progenitor cells.

To create human tissues, various skeletal muscle cell sources could have been used, including primary cells from patient biopsies or cells derived from human pluripotent stem cells such as embryonic stem cells and induced pluripotent stem cells. Each cell source is associated with its own benefits and challenges. Human primary cells maintain human adult muscle phenotype, but they are taken from donor tissue, and thus are limited in supply and variable from patient-to-patient. Embryonic stem cells must be harvested from early-stage embryos, thus they are both ethically-challenging and in short supply. However, once obtained, these cells can be expanded indefinitely and differentiated to the intended specific cell lineage. Further, these cells are often used to study human development and associated developmental disorders, but are less useful in disease modeling since the exact disease of

the unborn patient is unknown. Induced pluripotent stem cells theoretically solve several of these key issues. The hiPSCs are obtained from somatic cells of any adult human, such as peripheral blood mononuclear cells or dermal fibroblasts, and returned to pluripotency through genetic reprogramming. Therefore, these cells are infinite in supply, retain unlimited proliferation potential, have no associated ethical issues, retain pathological phenotypes, and can be differentiated to any cell lineage of interest. Further, since hiPSCs can be isolated from adults, they are valuable cells for disease modeling and, eventually, personalized medicine. Therefore, in our study, we have developed a functional skeletal muscle microtissue platform using hiPSC-derived cells. In the future, this can be used to model muscular diseases including Duchenne muscular dystrophy, an X-linked condition in which the dystrophin gene carries a mutation that prohibits the normal formation of the protein, preventing muscle development, restricting motion and activity and ultimately leading to muscle degeneration.

Differentiation of hiPSC to the skeletal muscle lineage also poses challenges. It has traditionally been a challenge to generate high-purity hiPSC-derived myogenic progenitors. The most common method has been direct reprogramming of hiPSC, which is accomplished by the overexpression of myogenic transcription factors such as PAX7 or MYOD1 by viral gene delivery.[43, 44] Direct reprogramming can result in a highly-pure myogenic cell population, and also creates Pax7 satellite cells that can be expanded *in vitro* to retain a stem cell-like population of proliferative myogenic progenitors for future use in *in vivo* transplantation studies or further *in vitro* studies. However, the random injection of viral DNA could interfere with the host DNA and eventually mask the disease phenotype or create other mutations that alter the cell's intended phenotype. Alternatively, we have developed 3D microtissues from hiPSC-myogenic progenitors generated from chemically-mediated cell

differentiation. In this method, the cells progress from pluripotency to the myogenic lineage by modulating various signaling pathways to induce paraxial mesoderm fate using a variety of growth factors and small molecules, similar to the natural development of skeletal muscle in our bodies.[45] Therefore, it is believed these cell may more accurately reflect native skeletal muscle cells and disease phenotypes due to the natural progression of the cell fate and lack of DNA manipulation. However, this process yields a heterogeneous cell population of myoblasts, satellite cells, and other unknown cell types. For use in large-scale applications and drug development or screening, more efficient differentiation protocols will need to be developed that yield a high-purity (>90%) myogenic cells and functional myotubes, similar to the high-purity resulting from differentiation protocols for cardiomyocyte production.[46] Our differentiation created a relatively pure population of myogenic cells as well as satellite cells to repopulate the stem cell niche, thus allowing us to create a 3D microtissue consisting of multinucleated myofibers and satellite cells.

There are additional challenges associated with using hiPSC-derived myogenic cells in preclinical drug screening and disease modeling. The hiPSC-myogenic progenitors created thin myotubes indicative of immature muscle tissue, rather than the thick myotubes that result from primary cells from mice or humans. Thus, it will be necessary to explore methods to further mature the tissues and induce myofiber hypertrophy, via further chemical differentiation or various stimulation methods, to better represent adult human skeletal muscle tissue. Further, we found that the hiPSC-derived cells, having been reprogrammed to a pluripotent state and then differentiated to the myogenic lineage, were extremely sensitive to sudden environmental changes during cell culture as compared to primary cells or cell lines. These cells required maintenance at 37°C and in fresh media for the majority of culture

time, or else the cells often died. Thus, the microfluidic platform may be an ideal bioreactor for hiPSC-myogenic progenitors due to the constant perfusion of fresh media.

The immunofluorescence images show the three-dimensional nature of the engineered skeletal muscle microtissue. Notably, as in Figure 3.6B, we see multiple planes containing MF20+ myotubes, and in Figure 3.6C, we see clusters of MF20+ myotubes surrounded by nuclei. Interestingly, our method of UV-light initiated photo-patterning of GelMA to spatially-confine the hiPSC-myogenic progenitors in a two-dimensional monolayer ultimately led to the formation of a multi-layered 3D tissue. We hypothesized several reasons for this phenomenon. First, GelMA is a small molecule in solution that, when injected into the microfluidic device, diffuses into the PAm hydrogel layer due to the molecular miscibility of monomers. Thus, during photo-polymerization, the GelMA at the interfaces forms an interpenetrating network with the PAm, while the GelMA in the region between the top and bottom PAm forms a hydrogel block. At low concentrations of GelMA, the stiffness of the hydrogel is insufficient to retain its hydrogel form, and it dissolves away with flow over time, leaving behind only the GelMA IPN at the PAm surface, as described in Figure 3.3. Therefore, cell-adhesive sites on the GelMA were available for cell attachment during cell seeding, leaving the cells attached to the GelMA surface in a capsule geometry as intended. Second, the hiPSC-myogenic progenitors form cell-cell attachments with neighboring cells in the pattern, and as they secrete proteases to degrade the GelMA hydrogel, the cells condense around the two PAm hydrogel pillars to form a 3D microtissue construct. Finally, it is likely that the cells secrete their own extracellular matrix proteins such as laminin and collagen to maintain 3D tissue structure during extended periods of culture.

The PAm hydrogel plays a key role in this process as well. PAm is a bio-inert, non-degrading hydrogel that prevents cell attachment. Thus, upon cell-mediated degradation of the GelMA IPN, the hiPSC-myogenic progenitors detach from the unfavorable, non-adhesive underlying PAm hydrogel and favorably attach to adjacent cells, ultimately leading to 3D tissue formation. Further, the miscibility of monomers also allows for the attachment of PAm hydrogel pillars to the top and bottom PAm hydrogel layers. These pillars were essential in maintaining tissue structure for the duration of culture and inducing uniaxial tissue alignment that ultimately led to myotube formation. Interestingly, despite the bio-inert properties of PAm, the muscle microtissue remain attached to the underlying PAm. This may be a result of secreted ECM proteins that also form entanglements with the PAm and serve as cell attachment points.

Using the microfluidic system, we applied a novel mechanical load in the form of pulsatile fluid flow. We observed the upregulation of myogenin, a late-stage skeletal muscle marker, in response to the fluidic-based stimuli. While it is difficult to pinpoint the exact mechanisms that led to this result, we believe it can be attributed to mechanotransduction due to shear stresses created in the tissue construct as a result of the high flow rate. In fact, the shear stresses under pulsatile flow were two orders of magnitude greater than those under control flow conditions. Further, the stresses created by the pulsatile flow were highest on the thin layers of tissue surrounding the two pillars. This may explain microtissue rupture which was observed during the course of experimentation. In future analyses, we will need to study additional indications of maturation, such as multinucleation of myofibers, myofiber hypertrophy, and functional maturation in terms of muscle force generation.

Functional response to the neurotransmitter acetylcholine was observed at a concentration of 10mM. Thus, the hiPSC-SMOC microtissues had clustering of acetylcholine receptors, a common phenomenon of a neuromuscular junction in a human. While acetylcholine is a molecular supplement to induce contraction, future studies may include electrical or optical stimulation to rhythmically contract the tissue multiple times. Perhaps, we could study tissue response to repeated stimulation, simulating exercise *in vitro* to assess changes in contractile response, nuclear fusion, and myofiber diameter.

We have demonstrated the formation of 3D human muscle strips from chemically-differentiated hiPSC-derived myogenic progenitors through a novel UV light-mediated protein patterning method. Further, we have demonstrated that the tissues are functional and have a contractile response to acetylcholine. Finally, we have utilized microfluidics to cyclically-apply a mechanical load to the tissues and have shown an increase in myogenic maturation markers in response. Our platform is completely amenable to all forms of microscopy for real-time, non-destructive, long-term analysis. At this time, one limitation is the inability to quantify contractile force generated by the tissue. Perhaps in the future, a force transducer can be incorporated to measure the magnitude of contractile forces.

3.6 Conclusion

In summary, we have developed a 3D skeletal muscle-on-a-chip platform utilizing human induced-pluripotent stem cell-derived myogenic progenitors. Our approach utilizes a novel multilayered hydrogel system composed of a bio-inert PAm hydrogel layer, bio-inert PAm hydrogel pillars to induce tissue alignment, and a cell-adhesive GelMA surface patterning to provide initial cell-attachment sites. We have demonstrated that this system supports tissue formation and cell differentiation over an eight-day culture period, and we have characterized tissue morphology and structure. Further, we have qualitatively verified contractile function. We found increased expression of myogenic maturation markers in response to cyclical mechanical loading applied through pulsatile fluid flow. Thus, the hiPSC-skeletal muscle-on-a-chip here provides a platform to study changes in skeletal muscle differentiation, morphology, and function in response to various stimuli. In the future, hiPSC from healthy and diseased patients could be isolated and used to develop 3D microtissue analogs as human disease models. These platforms could be extremely valuable in preclinical drug screening and personalized medicine. It could also be used to study molecular or cell-based treatments for muscle injury *in vitro*, given the presence of satellite cells in the hiPSC muscle microtissues. Ultimately, we hope to create hiPSC-based organ-on-a-chip models of various tissue types, such as liver, heart, intestine, and brain, and integrate these together with the skeletal muscle-on-a-chip to study drug response in an integrated, multi-organ human-based *in vitro* platform.

3.7 Acknowledgments

We would like to acknowledge all members of the Varghese Lab for their support and fruitful discussions that led to the culmination of this work. We are thankful that this research was supported by the California Institute for Regenerative Medicine (CIRM) under grant number RT3-07907. In particular, I would like to thank Priya Nayak for her perseverance to successfully differentiate hiPSCs to skeletal muscle progenitors.

Chapter 3, in full, is currently being prepared for submission to publish the material. Gaurav Agrawal, Priya Nayak, Shyni Varghese, "Human induced-pluripotent stem cell-derived myoblasts produce functional skeletal muscle microtissues: an hiPSC-organ-on-a-chip". The dissertation author is the primary investigator and lead author of this material.

3.8 Figures

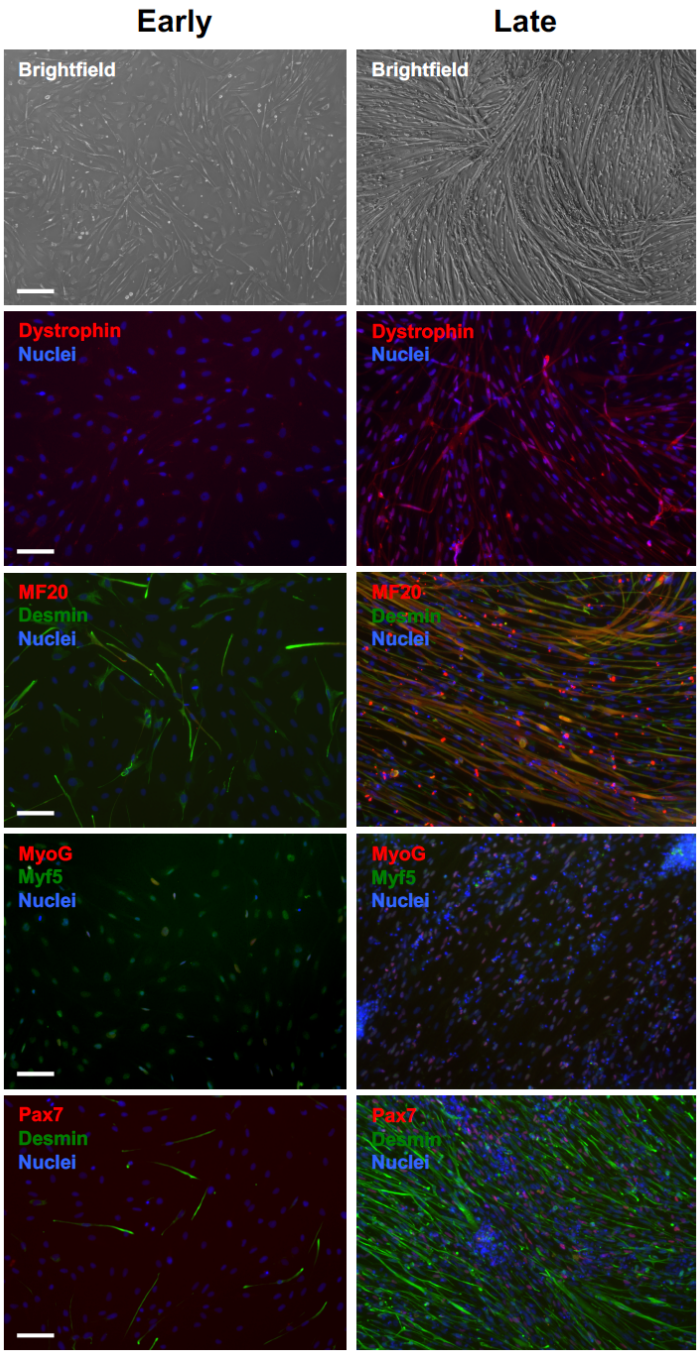

Figure 3.1: Characterization of hiPSC-derived myogenic progenitors at early- and late-stage timepoints

Immunofluorescent staining of myogenic markers dystrophin, MF20, desmin, MyoG, Myf5, and Pax7. Scale bars of brightfield images: 200µm. All other scale bars: 100µm

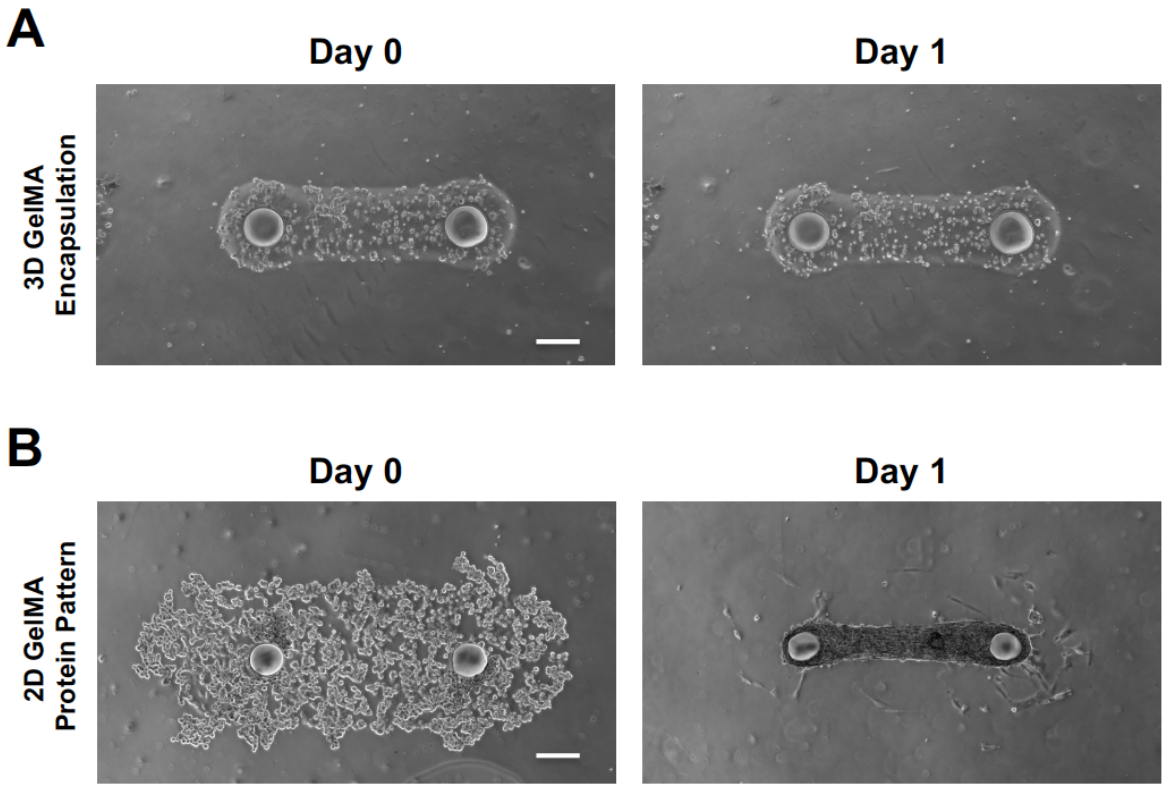

Figure 3.2: Direct encapsulation of hiPSC-myogenic progenitors in GelMA versus seeding cells on GelMA protein patterns

(A) hiPSC-myogenic progenitors directly encapsulated in GelMA failed to spread within the matrix and ultimately died. (B) hiPSC-myogenic progenitors seeded onto a 2D pattern of GelMA attach and form a 3D muscle microtissue. All scale bars: 100μm

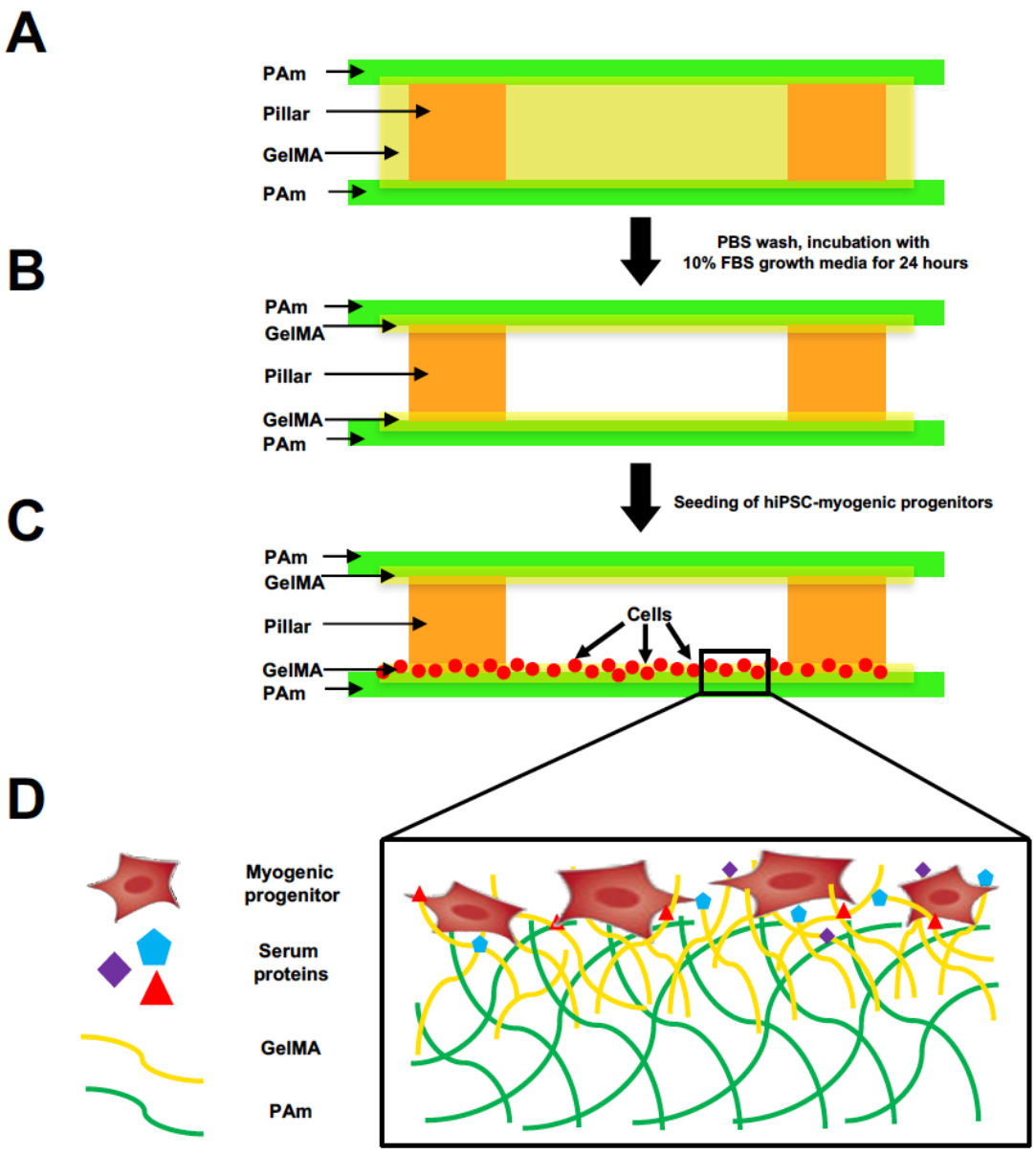

Figure 3.3: Schematic of GelMA protein patterning and subsequent cell attachment

(A) GelMA at 4.5% (wt/v) initially forms a hydrogel block that spans from the top to the bottom PAm hydrogel layers. (B) Following a PBS wash and continuous perfusion of growth media in a heated incubator, the GelMA block disintegrates away, leaving behind GelMA physically entangled with the PAm hydrogel layers as an inter-penetrating network (IPN) (C) Cells seeded into the device attach to the GelMA pattern in its original shape. (D) Magnified schematic illustrating the PAm-GelMA IPN, random attachment of various serum proteins, and myoblast attachment to the GelMA upon initial cell seeding.

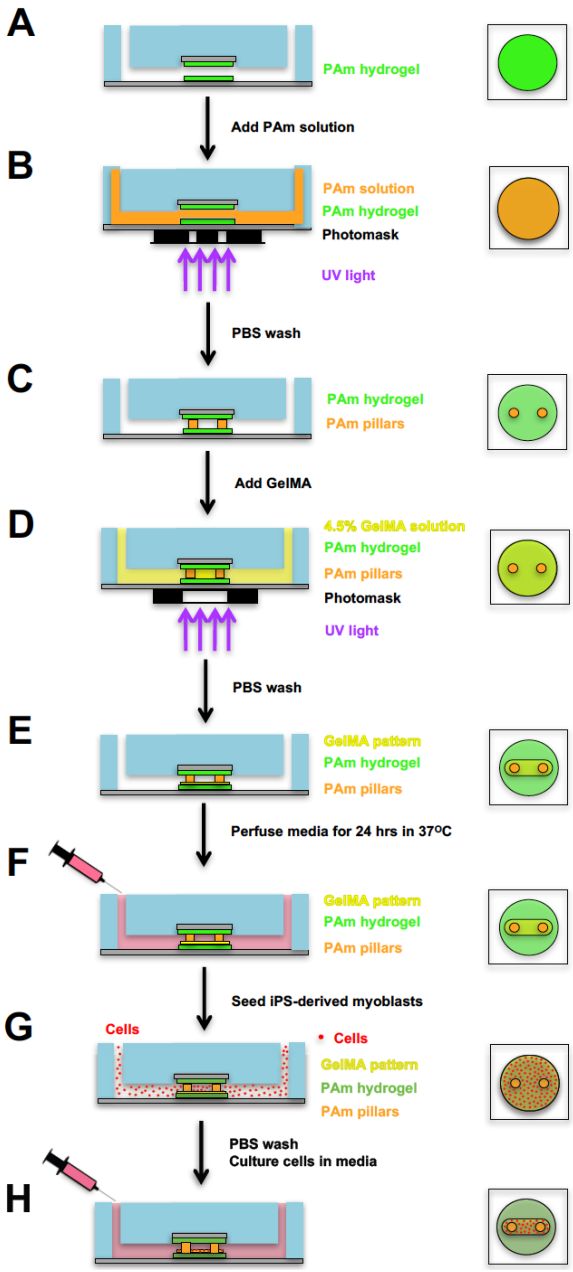

Figure 3.4: Schematic of device fabrication, GelMA patterning, and cell seeding

(A) Following device fabrication, 5% Am, 0.225% BisAm solution is infused into the device. (B) A photomask and collimated UV light is used to photopolymerize round pillars that span the height of the microfluidic chamber. (C),(D) Following PBS wash, 4.5% GelMA is infused into the device and photopolymerized in a capsule shape around the two pillars. (E), (F) After a PBS wash, the device is connected to a syringe pump and supplied media in an incubator overnight for GelMA disintegration and serum protein attachment to the GelMA entangled at the PAm surface. (G) hiPSC-myoblasts are seeded into the device, and upon attachment, supplied culture media via syringe pump (H).

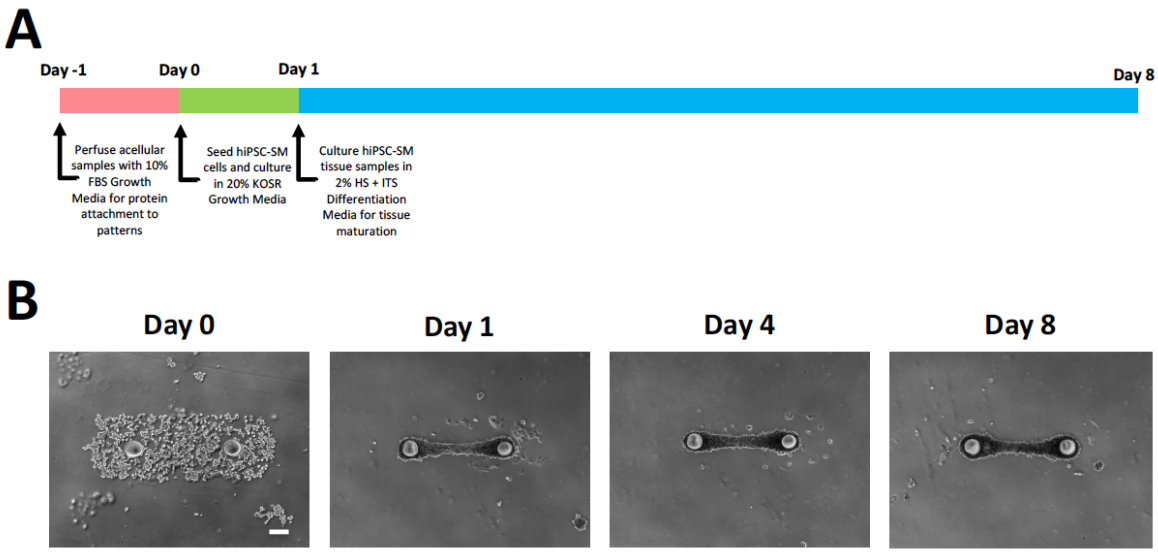

Figure 3.5: hiPSC-SMOC muscle microtissue formation

(A) Experimental setup illustrating the timing of various media formulations (B) Brightfield images depicting cell attachment to the GelMA pattern and subsequent condensation into an aligned, 3D skeletal muscle microtissue. Scale bar: 100μm

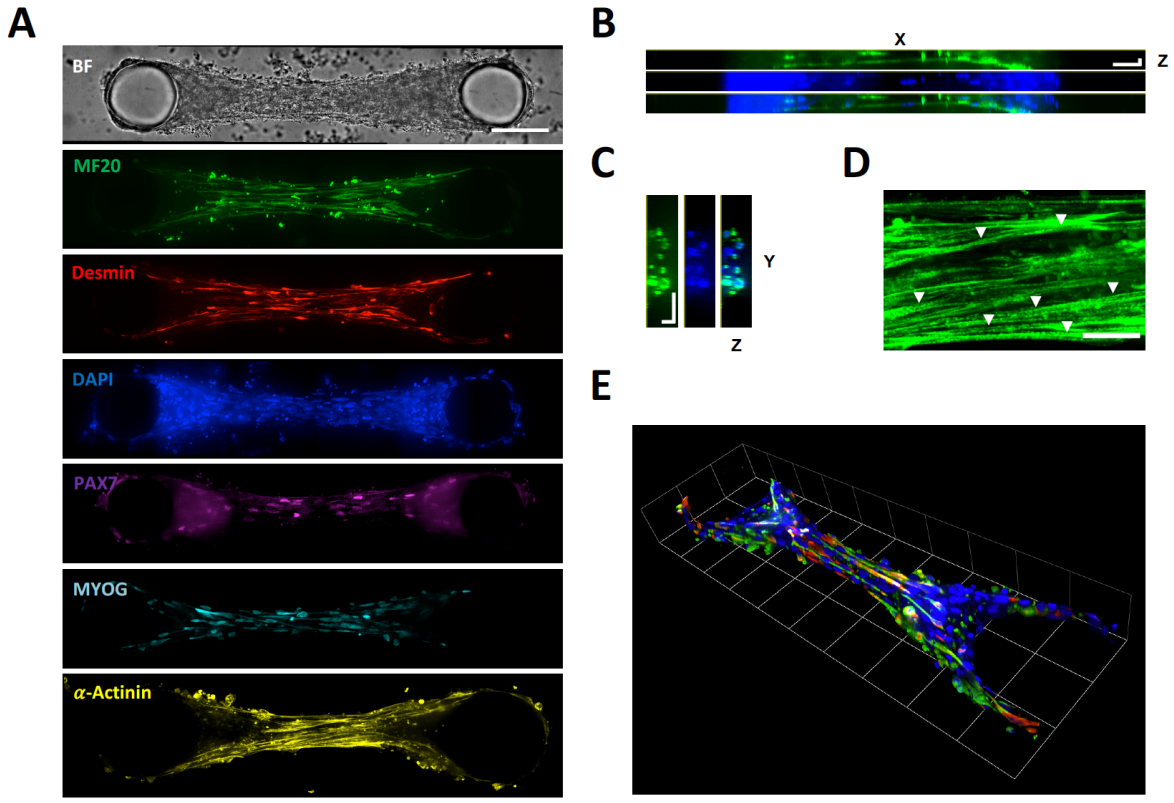

Figure 3.6: Characterization of 3D hiPSC-SMOC muscle microtissues

(A) Immunofluorescent staining of Day 8 hiPSC-SMOC microtissues shows samples express all myogenic markers – MF20, desmin, Pax7, MyoG, and α-actinin. Scale bar: 100μm (B) X-Z cross-sectional image of MF20 and nuclei show multiple layers of myotubes, indicating a 3D tissue structure. Scale bars: x-direction: 50μm, z-direction: 25μm. (C) Y-Z cross-sectional image of MF20 and nuclei show dense clusters of myotubes arranged in a 3D structure. Scale bars: y-direction: 50μm, z-direction: 25μm. (D) Staining for sarcomeric α-actinin illustrates that aligned tissue structure leads to formation of muscle sarcomeres (arrows). Scale bar: 25μm. (E) 3D opacity rendering illustrate three-dimensional structure of engineering hiPSC muscle micro-tissue. Each unit: 75μm.

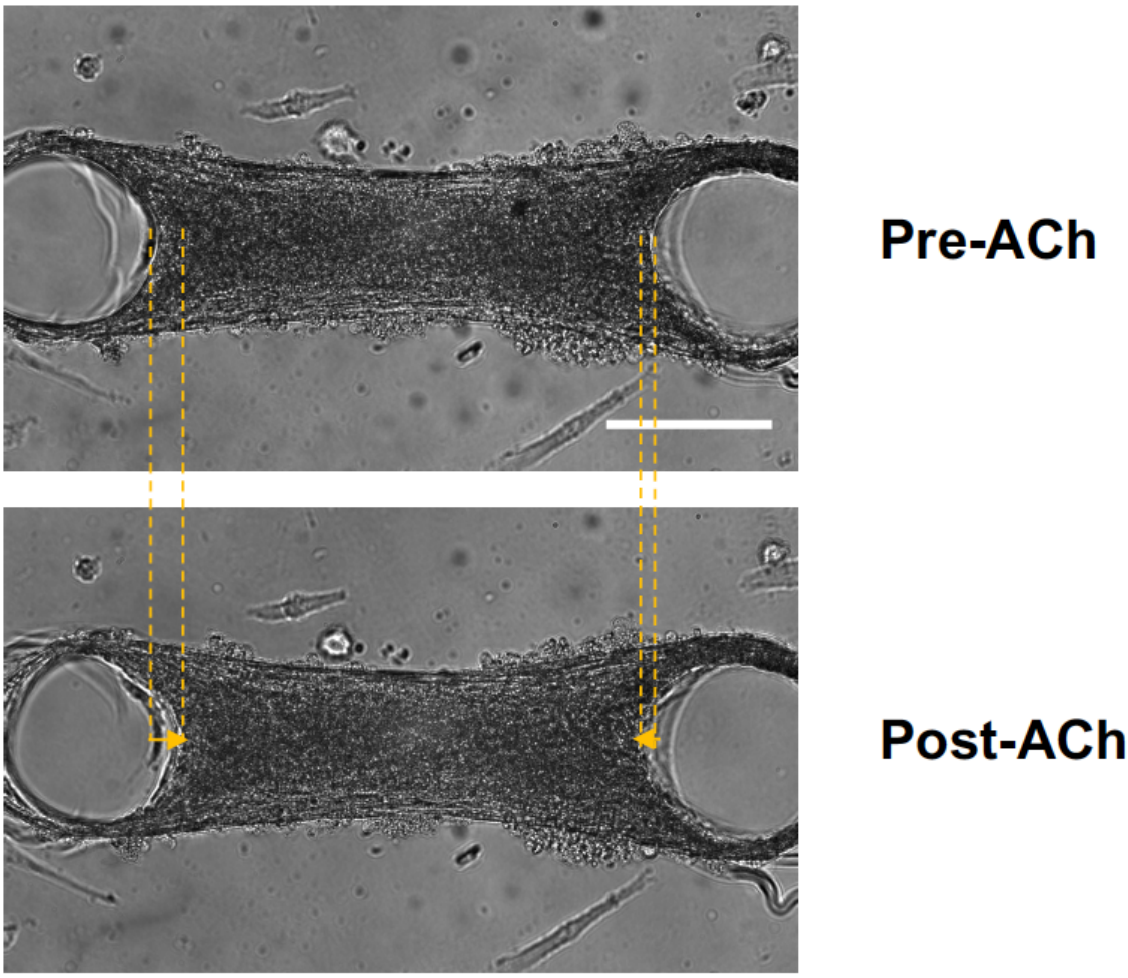

Figure 3.7: Acetylcholine-mediated hiPSC-SMOC muscle microtissue contraction

hiPSC-SMOC microtissues treated with 10mM of the neurotransmitter acetylcholine respond by contracting inwards. Yellow lines compare the pre- and post-ACh images to illustrate the contraction. Scale bar: 100μm.

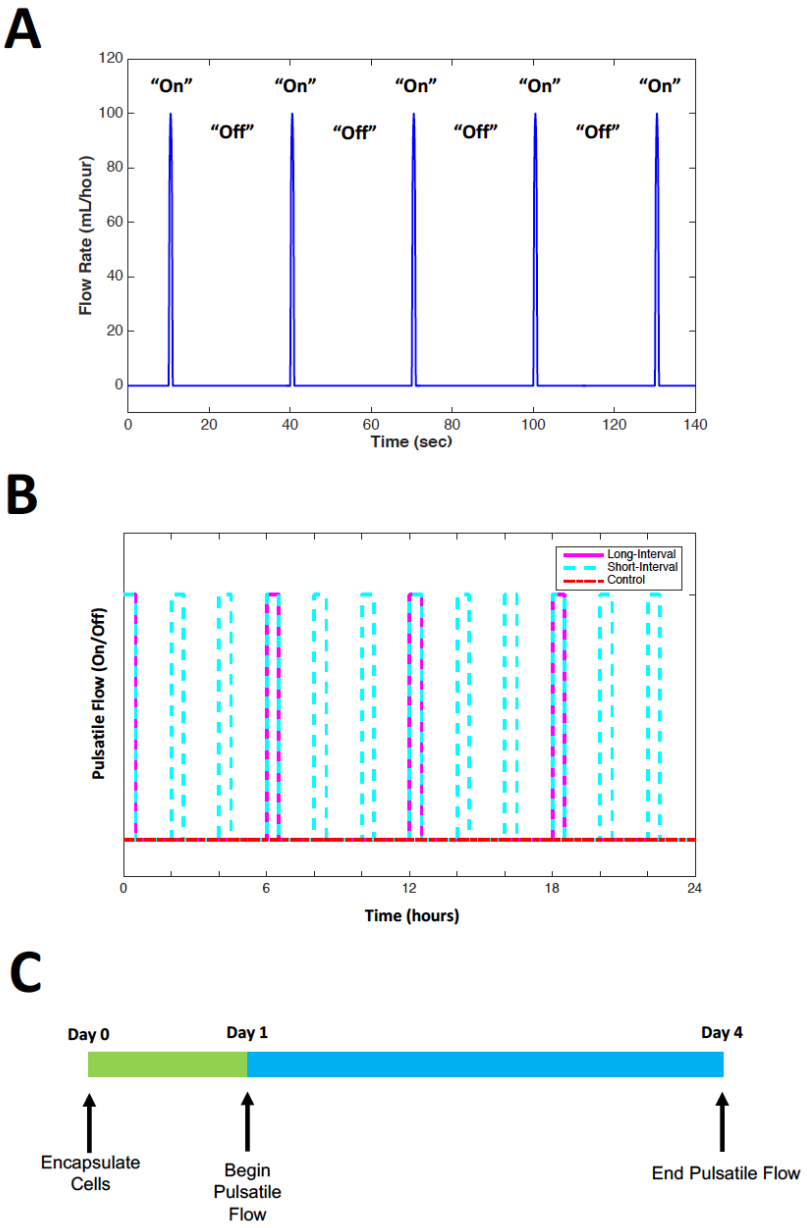

Figure 3.8: Settings and Timeline of pulsatile flow application

(A) Representation of the pulsatile flow application to the hiPSC-SMOC. Samples were pulsed at 100mL/hr flow rate for 1 second every 30 seconds. Between pulses, no flow was applied. (B) Representation of the three experimental conditions: long-interval pulsatile flow was initiated every 6 hours, short-interval pulsatile flow was initiated every 2 hours, and control conditions had no pulsatile flow. (C) Experimental timeline for mechanical stimulation via pulsatile flow, initiating on day 1 of hiPSC-SMOC culture and ending at day 4.

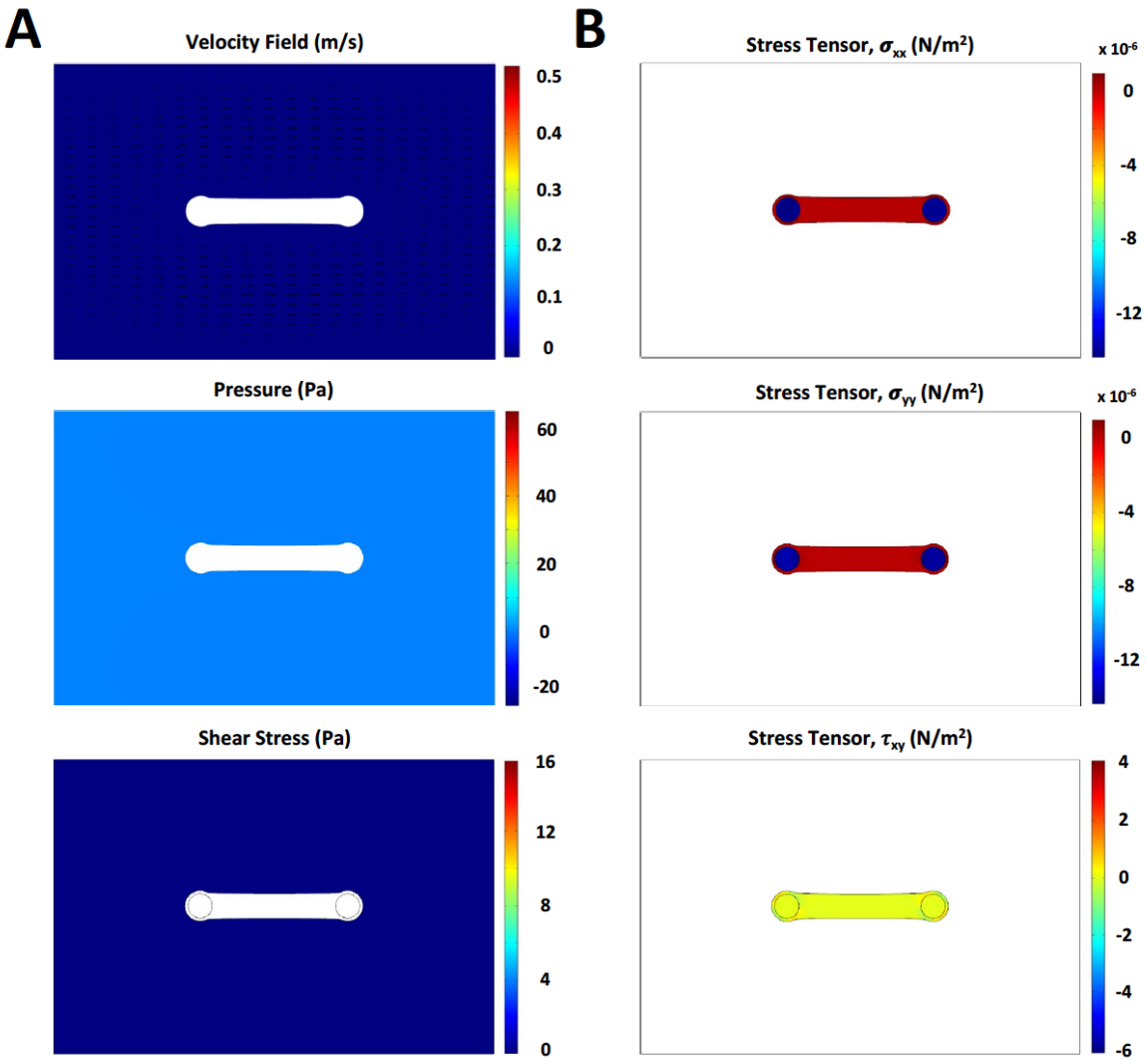

Figure 3.9: Heat maps depicting a model of fluid-generated stresses at 40µL/hr flow rate using COMSOL

(A) Fluid flow is left-to-right. Velocity field, pressure, and fluidic shear stresses are negligible at the low flow rate. (B) Stresses in the *x*- and *y*-directions are negligible, and shear stresses are low, on the order of 0-0.5 Pa.

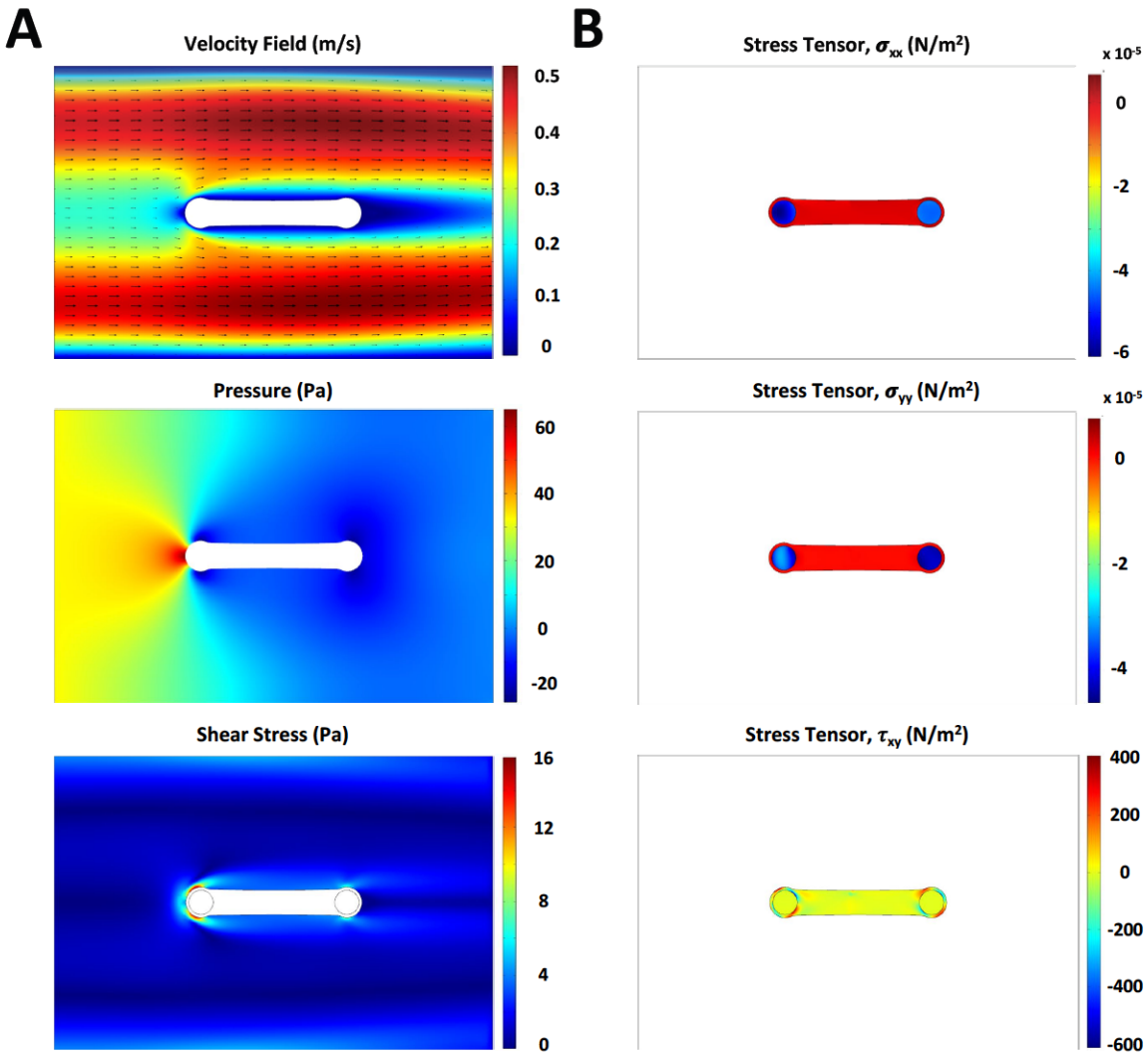

Figure 3.10: Heat maps depicting a model of fluid-generated stresses at 100mL/hr flow rate using COMSOL

(A) Fluid flow is left-to-right. Velocity field is significantly higher away from the tissue, but due to no-slip boundary condition, velocity minimizes adjacent to the tissue. Pressure is highest upon contact with the first pillar, before dramatically dropping. A similar trend is seen for fluidic shear stresses. (B) Stresses in the *x*- and *y*-directions are negligible, however shear stresses are on the order of 0-50 Pa, almost 100x greater than in the case of the low 40μL/hr flow rate, likely due to the shear stresses caused by no-slip (zero velocity) at the fluid-solid boundary.

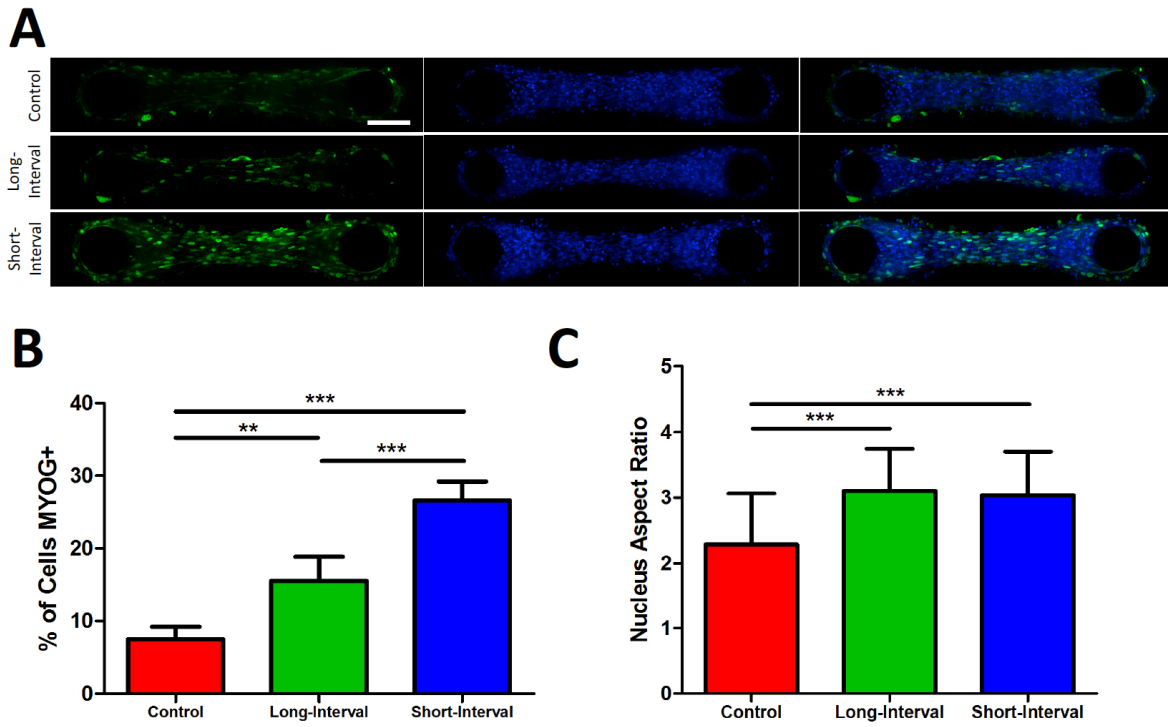

Figure 3.11: Maturation of hiPSC-SMOC muscle microtissues in response to various pulsatile flow regimes

(A) Immunofluorescent staining of day 4 mechanically-stimulated samples illustrates higher expression of myogenic marker MyoG in samples put through cyclical loading. (B) MyoG score reflects the same trend, calculated as total number of MyoG+ cells divided by total number of nuclei per sample. 4 samples from multiple experiments were used per group. Each group is plotted as the mean value along with standard deviation. (C) Nuclear elongation, quantified as the ratio of the nuclear major axis to its minor axis, is higher in cyclically-loaded samples than in the control sample. Four samples from multiple experiments were used per group. Each group is plotted as the mean value along with standard deviation. One-way ANOVA with Tukey's multiple comparison test was used to assess statistical significance (*$p < 0.1$, **$p < 0.01$, ***$p < 0.001$). Scale bar: 100μm

3.9 References

1. K. H. Benam, S. Dauth, B. Hassell, A. Herland, A. Jain, K. J. Jang, K. Karalis, H. J. Kim, L. MacQueen, R. Mahmoodian, S. Musah, Y. S. Torisawa, A. D. van der Meer, R. Villenave, M. Yadid, K. K. Parker and D. E. Ingber, *Annual review of pathology*, 2015, **10**, 195-262.

2. A. K. Capulli, K. Tian, N. Mehandru, A. Bukhta, S. F. Choudhury, M. Suchyta and K. K. Parker, *Lab on a chip*, 2014, **14**, 3181-3186.

3. S. N. Bhatia and D. E. Ingber, *Nature biotechnology*, 2014, **32**, 760-772.

4. D. Huh, B. Matthews, A. Mammoto, A. Montoya-Zavala, H. Y. Hsin and D. E. Ingber, *Science*, 2010, **328**, 1662-1669.

5. H. J. Kim, D. Huh, G. Hamilton and D. E. Ingber, *Lab on a chip*, 2012, **12**, 2165-2174.

6. H. J. Kim, H. Li, J. J. Collins and D. E. Ingber, *Proceedings of the National Academy of Sciences of the United States of America*, 2016, **113**, E7-15.

7. A. Agarwal, J. A. Goss, A. Cho, M. L. McCain and K. K. Parker, *Lab on a chip*, 2013, **13**, 3599-3608.

8. A. Grosberg, P. W. Alford, M. L. McCain and K. K. Parker, *Lab on a chip*, 2011, **11**, 4165-4173.

9. J. A. Brown, V. Pensabene, D. A. Markov, V. Allwardt, M. D. Neely, M. Shi, C. M. Britt, O. S. Hoilett, Q. Yang, B. M. Brewer, P. C. Samson, L. J. McCawley, J. M. May, D. J. Webb, D. Li, A. B. Bowman, R. S. Reiserer and J. P. Wikswo, *Biomicrofluidics*, 2015, **9**, 054124.

10. A. Herland, A. D. van der Meer, E. A. FitzGerald, T. E. Park, J. J. Sleeboom and D. E. Ingber, *PloS one*, 2016, **11**, e0150360.

11. A. Mathur, P. Loskill, K. Shao, N. Huebsch, S. Hong, S. G. Marcus, N. Marks, M. Mandegar, B. R. Conklin, L. P. Lee and K. E. Healy, *Scientific reports*, 2015, **5**, 8883.

12. A. Aung, I. S. Bhullar, J. Theprungsirikul, S. K. Davey, H. L. Lim, Y. J. Chiu, X. Ma, S. Dewan, Y. H. Lo, A. McCulloch and S. Varghese, *Lab on a chip*, 2016, **16**, 153-162.

13. K. H. Benam, R. Villenave, C. Lucchesi, A. Varone, C. Hubeau, H. H. Lee, S. E. Alves, M. Salmon, T. C. Ferrante, J. C. Weaver, A. Bahinski, G. A. Hamilton and D. E. Ingber, *Nature methods*, 2016, **13**, 151-157.

14. G. Wang, M. L. McCain, L. Yang, A. He, F. S. Pasqualini, A. Agarwal, H. Yuan, D. Jiang, D. Zhang, L. Zangi, J. Geva, A. E. Roberts, Q. Ma, J. Ding, J. Chen, D. Z. Wang, K. Li, J. Wang, R. J. Wanders, W. Kulik, F. M. Vaz, M. A. Laflamme, C. E. Murry, K. R. Chien, R. I. Kelley, G. M. Church, K. K. Parker and W. T. Pu, *Nat Med*, 2014, **20**, 616-623.

15. M. J. Workman, J. P. Gleeson, E. J. Troisi, H. Q. Estrada, S. J. Kerns, C. D. Hinojosa, G. A. Hamilton, S. R. Targan, C. N. Svendsen and R. J. Barrett, *Cellular and Molecular Gastroenterology and Hepatology*, 2018, **5**, 669-677.e662.

16. K. Takahashi and S. Yamanaka, *Cell*, 2006, **126**, 663-676.

17. Y. Shi, H. Inoue, J. C. Wu and S. Yamanaka, *Nat Rev Drug Discov*, 2017, **16**, 115-130.

18. I. Janssen, S. B. Heymsfield and R. Ross, *JAGS*, 2002, **50**, 889-896.

19. H. H. Vandenburgh, J. Chromiak, J. Shansky, M. Del Tatto and J. Lemaire, *FASEB*, 1999, **13**, 1031-1038.

20. M. Hicks and A. Pyle, *Cell stem cell*, 2015, **17**, 255-257.

21. T. A. Jarvinen, T. L. Jarvinen, M. Kaariainen, V. Aarimaa, S. Vaittinen, H. Kalimo and M. Jarvinen, *Best practice & research. Clinical rheumatology*, 2007, **21**, 317-331.

22. L. Rao, Y. Qian, A. Khodabukus, T. Ribar and N. Bursac, *Nature communications*, 2018, **9**, 126.

23. S. M. Maffioletti, S. Sarcar, A. B. H. Henderson, I. Mannhardt, L. Pinton, L. A. Moyle, H. Steele-Stallard, O. Cappellari, K. E. Wells, G. Ferrari, J. S. Mitchell, G. E. Tyzack, V. N. Kotiadis, M. Khedr, M. Ragazzi, W. X. Wang, M. R. Duchen, R. Patani, P. S. Zammit, D. J. Wells, T. Eschenhagen and F. S. Tedesco, *Cell Rep*, 2018, **23**, 899-908.

24. K. Shimizu, H. Araki, K. Sakata, W. Tonomura, M. Hashida and S. Konishi, *Journal of bioscience and bioengineering*, 2015, **119**, 212-216.

25. C. G. Anene-Nzelu, K. Y. Peh, A. Fraiszudeen, Y. H. Kuan, S. H. Ng, Y. C. Toh, H. L. Leo and H. Yu, *Lab on a chip*, 2013, **13**, 4124-4133.

26. G. Agrawal, A. Aung and S. Varghese, *Lab on a chip*, 2017, **17**, 3447-3461.

27. G. Moon du, G. Christ, J. D. Stitzel, A. Atala and J. J. Yoo, *Tissue engineering. Part A*, 2008, **14**, 473-482.

28. C. A. Powell, B. L. Smiley, J. Mills and H. H. Vandenburgh, *American journal of physiology. Cell physiology*, 2002, **283**, C1557-1565.

29. P. Heher, B. Maleiner, J. Pruller, A. H. Teuschl, J. Kollmitzer, X. Monforte, S. Wolbank, H. Redl, D. Runzler and C. Fuchs, *Acta biomaterialia*, 2015, **24**, 251-265.

30. J. W. Nichol, S. T. Koshy, H. Bae, C. M. Hwang, S. Yamanlar and A. Khademhosseini, *Biomaterials*, 2010, **31**, 5536-5544.

31. S. K. Davey, A. Aung, G. Agrawal, H. L. Lim, M. Kar and S. Varghese, *Tissue engineering. Part C, Methods*, 2015, **21**, 1188-1196.

32. T. Majima and W. Schnabel, *Macromol. Chem.*, 1991, **192**, 2307-2315.

33. A. Aung, J. Theprungsirikul, H. L. Lim and S. Varghese, *Lab on a chip*, 2016, **16**, 1886-1898.

34. Y. Tamura, N. Suzuki and K. Mihashi, *Biophysical journal*, 1993, **65**, 1899-1905.

35. I. V. O'gneva and I. B. Ushakov, *Atomic Force Microscopy Investigations into Biology - From Cell to Protein*, 2012, 325-354.

36. A. M. Zollner, O. J. Abilez, M. Bol and E. Kuhl, *PloS one*, 2012, **7**.

37. L. Madden, M. Juhas, W. E. Kraus, G. A. Truskey and N. Bursac, *eLife*, 2015, **4**, e04885.

38. Y. Hwang, T. Seo, S. Hariri, C. Choi and S. Varghese, *Polymers-Basel*, 2017, **9**.

39. J. Chal, M. Oginuma, Z. Al Tanoury, B. Gobert, O. Sumara, A. Hick, F. Bousson, Y. Zidouni, C. Mursch, P. Moncuquet, O. Tassy, S. Vincent, A. Miyanari, A. Bera, J. M. Garnier, G. Guevara, M. Hestin, L. Kennedy, S. Hayashi, B. Drayton, T. Cherrier, B. Gayraud-Morel, E. Gussoni, F. Relaix, S. Tajbakhsh and O. Pourquie, *Nature biotechnology*, 2015, **33**, 962-969.

40. X. Tang, M. Y. Ali and M. T. Saif, *Soft matter*, 2012, **8**, 7197-7206.

41. R. L. Lieber, *Skeletal muscle structure, function and plasticity: the physiological basis of rehabilitation*, Lippincott Williams & Wilkins, 2002.

42. C. A. Cezar, E. T. Roche, H. H. Vandenburgh, G. N. Duda, C. J. Walsh and D. J. Mooney, *Proceedings of the National Academy of Sciences of the United States of America*, 2016, **113**, 1534-1539.

43. R. Abujarour, M. Bennett, B. Valamehr, T. T. Lee, M. Robinson, D. Robbins, T. Le, K. Lai and P. Flynn, *Stem Cell Transl Med*, 2014, **3**, 149-160.

44. E. Shoji, H. Sakurai, T. Nishino, T. Nakahata, T. Heike, T. Awaya, N. Fujii, Y. Manabe, M. Matsuo and A. Sehara-Fujisawa, *Scientific reports*, 2015, **5**, 12831.

45. B. Borchin, J. Chen and T. Barberi, *Stem cell reports*, 2013, **1**, 620-631.

46. P. W. Burridge, E. Matsa, P. Shukla, Z. C. Lin, J. M. Churko, A. D. Ebert, F. Lan, S. Diecke, B. Huber, N. M. Mordwinkin, J. R. Plews, O. J. Abilez, B. Cui, J. D. Gold and J. C. Wu, *Nature methods*, 2014, **11**, 855-860.

CHAPTER 4:

Multi-organ 'body-on-a-chip' platform as a model system to assess cancer drug efficacy and toxicity

Gaurav Agrawal[1†], Han Liang Lim [1†], Shyni Varghese[1,2*]

[1] Department of Bioengineering, University of California, San Diego, La Jolla, California, USA

[2] Department of Biomedical Engineering, Duke University, Durham, North Carolina, USA

4.1 Abstract

In recent years, organ-on-a-chip technology has gained attention for its potential to model human tissues and disease pathophysiology *in vitro*. These microphysiological systems can mimic human tissue architecture, cell-cell and tissue-tissue interfaces, physical, chemical, and mechanical microenvironments, and the delivery of nutrients and removal of wastes through fluid similar to the function of blood in the body. Thus, by producing advanced levels of tissue functionality not possible in standard 2D cell culture systems, and providing a human-based alternative to animal models, organs-on-chips may help facilitate pharmaceutical drug development and expedite the drug testing process. Finally, multiple organs-on-chips can be linked together into a single system, effectively creating an *in vitro* human analog that consists of the critical tissue components essential to testing any novel drug compound. Herein, we describe the development of a multi-organ integrated 'human-on-a-chip' platform consisting of three-dimensional (3D) organ-on-chip models of liver, heart, skeletal muscle, and cancer tissues. Using a variety of approaches to pattern cells into specific geometries that mimic tissue architecture and function, we demonstrate the ability to link all four models into one system powered by a recirculating fluid pump. We show the viability of each of the organ-on-chip models in the integrated system over a 7-day period of culture, and further have characterized the tissue morphologies, tissue-specific protein expression, and tissue function by using a combination of microscopy and computational tools. Finally, to illustrate the utility of such a system in preclinical drug development, we perform a proof-of-concept drug compound test using known small molecule oncology drugs, Fluorouracil (5-FU) and Tegafur, a pro-drug of 5-FU. Using the integrated organ-on-a-chip system, we assess both drug efficacy against cancer as well as drug toxicity to the heart. Our

results demonstrate the function of the liver-on-chip module in first metabolizing the drug candidates to an active molecule that moves downstream to ultimately disrupt cardiac rhythm and destroy cancer tissue. This platform may be further expanded to include additional organs-on-chips by creating additional model systems of the bone, gut, lung, brain, pancreas, and more. Using patient-specific cells, we could ultimately create a truly unique, *in vitro*, multi-organ 'human-on-a-chip' platform that recreates a patient's own physiology, a powerful tool for personalized medicine.

4.2 Introduction

Over the past several years, there has been a stimulus towards the development of advanced *in vitro* biological platforms that mimic human physiology and function to provide an alternative model to antiquated cellular and non-human mammalian systems. In fact, researchers and scientists have worked at the interface of biological science, materials science, and biomedical engineering to develop promising multi-cellular and three-dimensional (3D) tissue systems that are akin to human tissue, thus providing a possible next-generation test system for preclinical drug development and testing.[1-12] Furthermore, when combined with human-sourced, and more specifically, patient-sourced cells, these systems provide an avenue for patient-specific disease models and personalized drug screening.[13, 14]

Aside from advancements in monolayer cultures and multicellular 3D organoid models, current research has focused on the development of organ-on-a-chip microtissue systems, which continue to model the complexity of human physiology while providing a dynamic continuous fluid perfusion system, circumventing mass transport limitations associated with stagnant cell culture practices.[15-17] Microfluidic systems can also minimize the use and wastage of reagents and drug compounds, which may be valuable and in short supply. In fact, organ-on-chip models of the heart, liver, lungs, gut, bone marrow, blood-brain barrier, skeletal muscle, and cancer have already been developed.[18-37] These microphysiological systems may also be engineered under the mechanical, chemical, and physical cues typically experienced by native human tissues. As an example, Ingber and colleagues developed a lung-on-a-chip in which alveolar epithelial cells are mechanically stretched and relaxed to mimic the cyclic expansion of the lung during breathing.[25] Similarly, cyclic stretching of intestinal epithelial cells to mimic the peristaltic motion of food through

the gut led to the formation of intestinal microvilli representative of the human gut in a gut-on-a-chip model.[27]

More recent research has demonstrated the potential of organs-on-chips to recapitulate human disease pathophysiology and serve as human-specific preclinical drug screening models. The aforementioned lung-on-a-chip was used to demonstrate the lung inflammatory response seen in COPD patients *in vitro*, and further showed its reversal after treatment with an experimental anti-inflammatory drug.[38] The gut-on-a-chip was further developed to demonstrate the harmful effects of radiation exposure on the gut lining, and the ability to reverse these effects with a radioprotective drug.[39] A human airway musculature-on-a-chip model was used to demonstrate asthmatic inflammation and bronchoconstriction when exposed to inflammatory cytokines, which was subsequently reversed using a β-agonist such as albuterol, the standard of treatment for asthma.[40] Additionally, these organ-on-a-chip platforms can be tailored to individual human patients or patient-specific diseases using human-derived induced pluripotent stem cells (hiPSCs). Functioning hiPSC-based organ-on-a-chip platforms of the liver, heart, and intestine have already been developed.[20, 23, 41-43] These could prove valuable in personalized medicine, where cells could be taken from an individual patient to create different organs-on-chips that possess the same genetic background as the patient, allowing us to determine optimal drug regiments and dosages to maximize efficacy from patient-to-patient.

From a drug development perspective, the ultimate goal of the organ-on-a-chip is to link together models of all the relevant tissues found in the body, such as liver, heart, lung, stomach, gut, skeletal muscle, brain, bone, bone marrow, pancreas, kidney, and more, to create an *in vitro* "body-on-a-chip" model that may replace the animal models. Multi-organ-

on-a-chip systems could be more accurate predictors of drug toxicity and efficacy due to the tissue-tissue cross-talk that is possible with recirculating microfluidics. However, despite the widespread development of individual organs-on-chips, only a few groups have integrated multiple of these systems together, partially because of the challenges associated with culturing multiple different types of tissues under a single culture media condition while maintaining their intended structure and function.[44-50] Shuler and colleagues recently developed one such multi-tissue system by creating monolayers of liver, heart, skeletal muscle, and neurons, and demonstrating cytotoxicity in response to various common drugs.[51] The research group has also devised a micro-cell culture analog model containing liver, bone marrow, and cancer cells, and further showed the ability to reproduce the metabolism of Tegafur to its active form, 5-Fluorouracil, and its consequent cytotoxic effect on cancer cells.[52] Thus, the multiple cell types were cultured under the same conditions and cross-talk was also observed between liver and cancer.

Herein, we describe the development of a modular multi-organ 3D "body-on-a-chip" system and its application in studying organ cross-talk via drug metabolism and the associated cancer cytotoxicity and cardiac toxicity. An orally-taken drug typically does a first-pass through the liver, where it is metabolized, after which it is taken to the heart, from where it is pumped to the rest of the body, eventually reaching cancerous and non-cancerous tissues (Figure 4.1). Therefore, we have combined 3D organ-on-a-chip platforms of the liver, heart, skeletal muscle, and cancer into one cohesive system supplied by a single culture media that sustains the structure and function of each tissue over a 7-day period. Furthermore, we show that within the integrated system, each tissue retains its characteristic function, such as metabolism and albumin secretion by the liver, spontaneous rhtythmic contractions by the

heart, multinucleated myotube formation by the skeletal muscle, and growth by the cancer mass. We also perform a proof-of-concept cancer drug test using a cancer pro-drug, Tegafur, to demonstrate metabolism of the drug by the liver to its activated form 5-FU, which leads to destruction of the tumor mass and toxicity to cardiac contraction, illustrating the potential utility of this platform as a drug screening tool as additional organ-on-a-chips are developed and integrated together in the future.

4.3 Materials and Methods

Cell culture of MCF7, Huh7, and C2C12

Growth medium was composed of Dulbecco's Modified Eagle high glucose medium with L-glutamine (Hyclone) supplemented with 10% fetal bovine serum (FBS, Gibco) and 1% penicillin/streptomycin. For the LOC, the Huh7 human hepatocarcinoma cell line was obtained and cultured in growth medium. For the MOC, the C2C12 mouse murine myoblast cell line was obtained from ATCC and cultured in growth medium. For the COC, the MCF7 human breast adenocarcinoma cells were obtained from ATCC and cultured in growth medium. In all cases, the cells were grown to 70% confluency and passaged at least three times prior to usage in the experiments.

Cell culture of human induced pluripotent stem cells

Human induced-pluripotent stem cell (hiPSC) line SCVI15 was generously provided by Dr. Joseph Wu and the Stanford Cardiovascular Institute. Cells were initially thawed and plated at low confluency on Matrigel (Corning)-coated 6-well plates, and maintained in mTeSR-1 stem cell media (Stem Cell Technologies), a feeder-free maintenance media. The hiPSCs were passaged using ReLeSR (Stem Cell Technologies) cell dissociation solution at 70% confluency a minimal of three times prior to differentiating into cardiomyocytes, to ensure the cells retained pluripotency prior to differentiation.

Differentiation of hiPSC to Cardiomyocytes

For the HOC, hiPSCs were differentiated into spontaneously-contracting cardiomyocytes according to a modification of the protocol defined by Burridge, et al.[53]

Briefly, hiPSCs were dissociated using Versene (Gibco) cell dissociation solution for 15 minutes. The hiPSCs were plated as single cells at a cell density of 150,000 cells/well into a 12-well plate. The cells were plated in mTeSR-1 media supplemented with 2μM Thiazovivin (Selleck Chemicals) for 24 hours, and maintained in mTeSR-1 media thereafter. Upon reaching 95% confluency, cardiac differentiation was initiated. CDM3 (cardiac differentiation media) was prepared as a basal media composed of RPMI 1640 (Gibco) supplemented with AlbuMAX I Lipid-rich BSA (Gibco) at 500μg/mL, L-ascorbic acid-2-phosphate (Sigma-Aldrich) at 213μg/mL, and 1% antibiotic-antimycotic (Gibco). Media was changed every 48 hours, within 1 hour deviation from the time of media change of the previous step. From day 0 – day 2, CDM3 media was supplemented with 6μM CHIR99021 (Selleck Chemicals). From day 2 – day 4, CDM3 media was supplemented with 2μM Wnt-C59 (Selleck Chemicals). From day 4 onwards, media was changed to CDM3 media. Spontaneously-contracting cardiomyocytes were first observed between day 7-8, and robustly beating sheets of cardiomyocytes were seen by day 12. Cells were typically used in the HOC between day 12 – day 18 of differentiation.

Synthesis of gelatin methacrylate (GelMA)

The synthesis of gelatin methacrylate (GelMA) followed a protocol described previously.[54, 55] Briefly, 10g of bovine gelatin (Sigma Aldrich) was dissolved in 100 mL of PBS and heated to 60°C for 60 minutes, with stirring, until the gelatin was fully dissolved. Next, the temperature was reduced to 50°C, and 8 mL of methacrylic anhydride (Sigma Aldrich) was added drop-by-drop to the dissolved gelatin. The solution was then stirred at a high speed for 60 minutes. PBS was warmed and added to the mixed solution, which was

dialyzed against Milli-Q ultrapure water using a 12-14 kDa cutoff dialysis tubing (Spectrum Laboratories) for seven days at 40°C, changing water three times per day. This was meant to remove contaminants, excess small molecules, and unreacted methacrylic anhydride from the solution. Lastly, the dialyzed GelMA solution was then flash frozen in liquid nitrogen and lyophilized in a freeze dryer for 4 days until it became a lightweight white cake-like solid, and stored at -20°C until use.

Synthesis of lithium phenyl-2,4,6-trimethylbenzoylphosphinate (LAP) photoinitiator

The photoinitiator used in this study, LAP, was synthesized as described elsewhere.[56] Briefly, 2,4,6-trimethylbenzoyl chloride (Sigma Aldrich) was added dropwise to an equal molar solution of dimethyl phenylphosphonite (Sigma Aldrich) under argon, while stirring at 25°C. The temperature was changed to 50°C after 18 hours of reaction time, and 4M excess lithium bromide (Sigma Aldrich) with 2-butanone was added to the reaction mixture. A white precipitate was formed within 10 minutes, after which the temperature was reduced to 25°C for 4 hours. The precipitate was isolated via filtration, then washed three times using 2-butanone to ensure complete removal of excess lithium bromide. The excess 2-butanone was removed by drying the product under vacuum, yielding LAP as a white crystalline powder.

Fabrication of silicon mold

Micro-patterned silicon wafers were fabricated as described previously.[21] Briefly, a photomask of the desired microfluidic device design was developed in AutoCAD and printed by CAD/Art Services, Inc. Next, a 5-inch diameter silicon wafer was spun-coat with NR9-1500PY negative photoresist (Futurrex). The microfluidic design was lithographically-

defined via UV light. The Si wafer was etched using the deep reactive ion etching (DRIE) process, which entails flowing SF6 gas at 100 sccm for 11 seconds of reaction time, followed by flowing C4F8 gas at 80 sccm for a 7-second passivation cycle. An etching depth of 75μm was achieved using an etch rate of 0.7μm per cycle. After etching, the photoresist was removed by immersing the silicon wafer in acetone for 4 hours before rinsing with methanol, isopropanol, and deionized water. Finally, the Si mold was dried with compressed nitrogen gas and silanized by vapor deposition of trichlorosilane (TCI Inc.) to allow casting and removal of PDMS.

Methacrylation of Glass Coverslips

To tether polyacrylamide (PAm) hydrogels within the microfluidic device, cover-glass was chemically-methacrylated as described previously.[37, 55] Briefly, round glass coverslips (12mm round, #1 thickness, Fisher) and rectangular glass coverslips (24mm x 50mm, #1 thickness, Fisher) were washed with 200 proof ethanol for 15 minutes, then treated with a methacrylate solution composed of 97.7% (v/v) of ethanol, 0.3% (v/v) glacial acetic acid, and 2% (v/v) 3-(trimethoxysilyl)propyl methacrylate (Sigma Aldrich) for 5 minutes. The glass was washed several times with 200 proof ethanol under agitation, then dried under heat at 60°C for 2 hours prior to use.

Fabrication of microfluidics device with PAm hydrogel layers

The LOC, MOC, and COC were created in devices that contained a flat PAm hydrogel layer on the top and bottom of the central chamber of the microfluidic device as described previously, with slight modifications.[36] To create the hydrogels, a polyacrylamide (PAm)

precursor solution composed of 5% (wt/v) acrylamide (UltraPure Acrylamide, ThermoFisher Scientific), 0.225% (wt/v) *N,N'*-methylenebis(acrylamide) (Sigma Aldrich), and 0.12% (wt/v) ammonium persulfate (APS, Sigma Aldrich) in phosphate buffered saline (PBS) was made. For imaging purposes, 200nm fluorescent far red microparticles (ThermoFisher Scientific) were added to the precursor solution at a 1:100 dilution. Quickly, 0.6μL of a 10% (wt/v) *N,N,N',N'*-tetramethylethylenediamine (TEMED, Sigma Aldrich) in PBS was mixed into the precursor solution. Immediately, 3μL of the solution was dropped onto the center of a methacrylated 24 x 50mm coverslip and covered with a non-methacrylated 12mm round coverslip to create a 12mm round PAm hydrogel layer. A similar process was followed to make an equal PAm hydrogel layer on a 12mm round coverglass, in which 3μL of PAm solution was dropped onto a non-methacrylated 24 x 50mm coverglass and covered with a methacrylated 12mm round coverglass. After 30 minutes to allow for polymerization, the samples were immersed in DI water before cleaving off the non-methacrylated glass with a razor blade, leaving behind a 12mm round PAm hydrogel tethered to the 24 x 50mm rectangular coverglass and 12mm round coverglass. These would form the bottom and top surfaces of the microfluidic device.

To create the device, 5μL of DI water was dropped onto the circular central chamber of the micropatterned silicon wafer, before covering it with the 12mm round PAm-tethered coverglass (facedown), to keep the PAm hydrated throughout the fabrication process. Next, polydimethylsiloxane (PDMS) (Sylgard 184, Dow Corning) was prepared by mixing base and curing agent together in a 10:1 ratio by mass for 5 minutes. After bubbles were removed by vacuum, the PDMS was cast onto the micropatterned silicon wafer containing 12mm round glass with PAm hydrogel, then baked at 60°C for 2 hours to cure the PDMS. The

PDMS was separated from the silicon wafer with the 12mm round glass and PAm hydrogel still attached. To provide access points for inlet and outlet tubing, 0.5mm round holes were punched into the PDMS at the two ends of the microfluidics pattern. Next, the PDMS was bonded to the PAm-tethered rectangular glass after UV-Ozone treatment, attachment, and baking at 60°C for a minimum of 2 hours. This resulted in a microfluidics device, in which the central chamber is flanked by PAm hydrogels on the top and bottom surfaces of the device. PBS was perfused into the device to allow the PAm hydrogels to equilibrate prior to use.

Fabrication of microfluidics device without PAm hydrogel layers

The HOC was created in a device that lacked the aforementioned PAm hydrogel layers on the top and bottom of the central chambers. The same procedure was followed to create this device, except after glass methacrylation, no PAm hydrogel was formed on the 24 x 50mm rectangular glass or the 12mm round glass. The methacrylated round glass was placed on the central chamber of the micropatterned silicon wafer, and PDMS was cast, cured, removed, and bonded to the rectangular glass under UV-Ozone, as described previously. This resulted in a microfluidics device in which the central chamber has methacrylated glass on both the top and bottom. PBS was perfused into the device to allow the PAm hydrogels to equilibrate prior to use.

Liver-on-chip formation via Huh7 encapsulation

A 10% (wt/v) GelMA solution in PBS was prepared by dissolving the GelMA precipitate in PBS at 60°C for 30 minutes. The solution was sterilized by syringe filtration

with a 0.22μm filter to remove contaminants and any insoluble components. Huh7 human hepatic cells were trypsinized and mixed into the sterilized GelMA solution at a cell density of 20 million cells/mL. Finally, 0.01% ascorbic acid (Sigma Aldrich), a free-radical quencher, and 2mM LAP, a photoinitiator, were added to prepare the GelMA solution for photo-polymerization.

The cell-laden hydrogel suspension was infused into the microfluidic device using a syringe. A transparency photomask containing an array of ellipse patterns (500μm-by-150μm ellipses) was placed on the fluorescence microscope, with the patterns positioned over an open turret of the microscope. The device was mounted on the photomask, and oriented so that the ellipse patterns fit within the bounds of the central chamber of the device. The region was exposed to UV light (365nm ± 40nm excitation wavelength) for 15 seconds to photo-polymerize the GelMA solution containing Huh7 cells, effectively immobilizing the cells in a collection of ellipse-shaped hydrogel networks. Unreacted monomer solution and cells were washed away with sterile PBS, leaving each device with up to 40 liver organoids. The samples were supplied with growth media for the duration of single-chip culture (3 days), through a syringe pump (Harvard Apparatus) at a constant flow rate of 40μL/hr in an incubator set to 37°C and 10% CO_2. These settings were chosen based on previous studies.[21, 36, 37] Thus, the liver-on-a-chip with 3D organoids was created, and ready for integration with the remaining organ-on-chip systems by day 3.

Formation of PEG-DA walls for heart-on-a-chip

The heart-on-a-chip was made using the microfluidics device without PAm hydrogel layers. To create directionally-aligned cardiac sheets, polyethylene glycol diacrylate (PEG-

DA) was used to create linear walls that would serve as boundaries guiding cardiomyocyte alignment. A precursor solutions composed of 10% PEG-DA (Polysciences Inc.), 0.01% ascorbic acid, and 2mM LAP, in PBS, was prepared and infused into the device. For linear walls, a transparency photomask with line patterns of 200μm width and 500μm separation was mounted onto the stage of a fluorescence microscope stage as described. The central chamber of the device was positioned over the line patterns of the photomask, and exposed to UV light for 30 seconds to photo-polymerize the PEG-DA solution into a collection of hydrogel "walls". Due to the presence of two methacrylated glass components on the bottom and top of the device, the photo-polymerized hydrogel walls spanned from the bottom to the top of the device, effectively confining the cells that would be seeded between these wall patterns. Unreacted monomer solution was washed away with PBS solution, and the device was sterilized under UV light for 2 hours prior to cell seeding.

Heart-on-a-chip formation via hiPSC-CM seeding

The microfluidic device with PEG-DA walls was perfused with Matrigel solution (Corning) according to manufacturer's instructions, and incubated for 2 hours to allow for homogeneous coating in order to prepare the glass for cell attachment. Differentiated hiPSC-cardiomyocytes (hiPSC-CM) between day 12-18 of differentiation were dissociated into single-cells with TrypLE Express (Gibco) for 20 minutes, then collected and strained through a 70μm cell strainer to remove excess extracellular matrix and clumps of cells. A cell solution composed of hiPSC-CM at a density of 40 million cells/mL along with 2μM Thiazovivin in CDM3 media was perfused into the Matrigel-coated device. The device was incubated at 37°C for 1 hour to allow for hiPSC-CM attachment to the glass, after which unattached cells

were washed away with repeated PBS washes. The result was sheets of hiPSC-CM confined between PEG-DA walls. Samples were cultured in CMD3 media supplemented with 2μM Thiazovivin and 30% knock-out serum replacement (Gibco) for the first 48 hours, then switched over to basal CDM3 media from day 2 onwards for the remaining 5 days of single-chip culture. Media was supplied to the cells through a syringe pump at a rate of 40μL/hour in an incubator set at 37°C and 10% CO_2 as before. Contracting myocytes in the HOC were observed around day 3, and thus the heart-on-chip with 2D aligned cardiac sheets was created and ready for integration with the remaining organ-on-chip systems by day 7.

Formation of PAm pillars for skeletal muscle-on-a-chip

To create uniaxially-aligned skeletal muscle microtissues, anchoring pillars were first formed in the microfluidic device, as described previously.[36] Briefly, a precursor solution composed of 5% acrylamide, 0.225% bis-acrylamide, and 2mM LAP in PBS was prepared and perfused into the device. A transparency photomask with an array of circular patterns of 100μm diameter and 500μm pillar-to-pillar distance was placed onto the microscope stage, and the central chamber of the microfluidic device was centered over the pattern. The device was exposed to UV light for 1 minute to initiate photo-polymerization, resulting in circular hydrogel pillars sandwiched between the bottom and top PAm hydrogel layers within the device. Unreacted monomer solution wash washed away with repeated PBS washes, and the device was sterilized under UV light for 2 hours prior to encapsulation of cells.

Skeletal muscle-on-a-chip formation via C2C12 encapsulation

The skeletal muscle-on-a-chip was created as described previously.[36] Briefly, a 7% (wt/v) GelMA solution was prepared by dissolving the GelMA precipitate in PBS at 60°C for 30 minutes. The solution was sterilized as described for the LOC. A cell-hydrogel suspension composed of C2C12 myoblasts at a cell density of 12.5 million cells/mL, 0.01% ascorbic acid, and 2mM LAP was prepared and perfused into the microfluidic device containing PAm hydrogel pillars. A transparency photomask containing a capsule pattern (200μm width and 800μm length) was mounted on the microscope, and the device containing the cell-hydrogel solution was manually positioned using the microscope eyepiece under brightfield illumination to locate two pillars within the capsule pattern. This region was then exposed to collimated UV light for 15 seconds to photopolymerize the GelMA solution into a capsule shape. This process was repeated several times to obtain up to 10 samples within each device. Unreacted monomer solution and cells were washed away with several sterile PBS washes, resulting in cell-laden hydrogels strategically-positioned around two PAm pillars. Samples were cultured in growth media for the first 24 hours, then switched over to differentiation media composed of Dulbecco's Modified Eagle high-glucose medium (Hyclone) supplemented with 2% horse serum (Omega Scientific) and 2% penicillin-streptomycin (Gibco) to induce cell differentiation and fusion for the remaining 2 days of single-chip culture. Media was supplied through a syringe pump as before. Thus, the skeletal muscle-on-a-chip with 3D aligned microtissues was created, and ready for integration with the remaining organ-on-chip systems by day 3.

Formation of spheroids from MCF7 cells

To form spherical masses of cancer cells, known as cancer spheroids, MCF7 cells were trypsinized and plated into a 10cm non-cell adherent petri dish (Fisher Brand) at a cell density of 100,000 cells/mL. The dish was immediately placed onto an orbital shaker with a rotation speed of 57 rpm in an incubator maintained at 37 °C and 5% CO_2. By day 3, suspended cancer spheroids had formed and could be obtained for formation of the cancer-on-a-chip.

Cancer-on-a-chip formation via MCF7 spheroid encapsulation

The cancer-on-a-chip was created as described previously, with modifications.[37] Briefly, cancer spheroids cultured for 3 days on the orbital shaker were obtained using cell strainers to retain the spheroids that ranged between 40-100μm in diameter. The spheroids were suspended in 10% (wt/v) GelMA solution containing 0.01% ascorbic acid and 2mM LAP. This solution was infused into the microfluidic device. A transparency photomask containing a single circle pattern (320μm diameter) was mounted onto the microscope, and the device containing the spheroid-hydrogel solution was placed on top of the circle pattern. The microscope was used to visualize a spheroid through the circle pattern using brightfield illumination, and the device was manually positioned such that a spheroid lay in the center of the pattern. This region was then exposed to collimated UV light for 12 seconds to photopolymerize the GelMA solution into a circle shape. The process was repeated several times to obtain up to 10 samples in each device. Unreacted monomer solution and excess spheroids were washed away with several sterile PBS washes, resulting in spheroid-laden hydrogels, mimicking a tumor mass within an extracellular matrix environment. The samples were supplied with growth media for the duration of single-chip culture (1 day), through a

syringe pump (Harvard Apparatus) at a constant flow rate of 40μL/hr in an incubator set to 37°C and 10% CO_2, as with the previously discussed chips. Thus, the cancer-on-a-chip with 3D cancer micro-tumors was created, and ready for integration with the remaining organ-on-chip systems by day 1.

Integrating LOC, HOC, MOC, and COC with a peristaltic pump

An 8mm diameter PDMS disk with two 1mm holes punched through, a 1.7mL microcentrifuge tube, a 3-inch segment of elastic silicone tubing (ID 0.025", cat. No: 51845K67, McMaster-Carr) and various segments of 26-gauge PTFE tubing, were autoclaved for sterility. A 1-mL media reservoir was made to provide a continuous supply of nutrients to the various constituents of the 'human-on-a-chip' system. The 8mm PDMS disk was fit to the opening of the microcentrifuge tube to seal off any contaminants from entering the reservoir, and to provide inlet and outlet media access ports. Next, two short segments of PTFE tubing were inserted into either end of the elastic silicone tubing to connect the two segments, and the junctions were further sealed using Parafilm laboratory film (Bemis). The elastic silicone tubing was looped tightly around the wheel of the peristaltic pump (Cole-Parmer). The outlet end would connect to a series of 'organ-on-a-chip' modules, while the inlet end would connect to a reservoir containing media for the tissues. Due to the elastic nature of the silicone tubing, as the peristaltic pump cycles it draws up media from the reservoir to deliver it to the organ-on-a-chip modules. After passing through all organs-on-chips, the media empties back into the original reservoir, thus keeping its volume constant. Several organs-on-chips were connected to one another via sterilized 26 gauge PTFE tubing in the order of liver-on-a-chip, heart-on-a-chip, cancer-on-a-chip, and skeletal muscle-on-a-

chip (Figure 4.3). During 'body-on-a-chip' culture, CDM3 cardiac media was chosen to supply media to all tissues due to the sensitivity of the hiPSC-CM within the HOC. Since CDM3 contain albumin, it was sufficient media to sustain the growth, development, and function of all four organ-on-a-chip platforms. The integrated setup was cultured at 37°C and 10% CO_2, and fresh media was replenished every day and supplied to the samples under peristaltic flow.

Characterization of fluid flow through the integrated system

To determine the bulk flow rate through a varying number of chips, we created various multi-organ setups (2, 3, 4, and 5 chips linked together) and mounted them on the peristaltic pump. The settings were varied at five intervals from low to high (5rpm to 99rpm), and for each instance, we measured the volume of fluid exiting the system after 10 minutes, thus yielding an average flow rate in μL/min.

Analysis of peristaltic flow

To characterize the peristaltic nature of the flow in each chip, we perfused fluorescent microparticles (FluoSpheres, Invitrogen) at 1% (v/v) in PBS through an integrated system containing 5 acellular microfluidic devices. Each device was sequentially mounted onto a microscope with time-lapse capabilities (Keyence BZ-X710), and a video was obtained to capture fluid flow.

The flow was characterized by tracking the 2D displacement of microparticles suspended in the fluid using a custom-written MATLAB script. First, the time-lapse video was compiled into stack of images before being converted to a binary image. by thresholding

to 2.5 times the average intensity of each pixel in each image. All pixels below the threshold were assigned a value of 0, and all pixels above the threshold were assigned a value of 1. To determine the displacement of the microparticles between each image, the MATLAB 2D cross-correlation function, *xcorr2*, was used to compare the current image to the next image in the stack. The resulting x-y shift between subsequent images was used to obtain displacements between each image in the stack. This displacement, when divided by the period of time between each frame from the video acquisition, yielded the velocity profile of the microparticles in flow. Furthermore, we were able to obtain the total displacement of the fluid flow over time by summing the frame-by-frame displacements across the time of acquisition.

Albumin secretion assay

To assess liver function in the integrated system, sandwich enzyme-linked immunosorbent assay (ELISA) was performed to measure albumin secretion from the LOC over a 7-day period. Every 24 hours, the 1-mL of media found in the media reservoir was collected and frozen at -80°C until time of analysis. At the end of 7 days, human albumin levels were measured using the Human Albumin ELISA Quantitation Set (Bethyl Labs) according to the manufacturer's protocol.

Cardiac beating frequency and analysis

To characterize beating frequency of cardiac sheets in the integrated system, a video of hiPSC-CM sheet contraction was captured at 30 fps using an open-source video-capture software, CamStudio, and analyzed via a custom MATLAB script. The video was converted

to a stack of images. A reference frame was selected based on an instance where the cardiac sheets were in a maximally relaxed state. Every other frame in the stack was correlated against the reference frame, and the difference was plotted for the time span of the video to yield the contraction curve. Frequency was calculated as the number of peaks within a 60-second period, yielding frequency in hertz. Average frequency over time was obtained by averaging the frequency of 5 different samples each day over a 7-day period.

Cancer spheroid growth analysis

To quantify the size of the cancer spheroids in the integrated system, brightfield images of each cancer spheroid in the COC device were captured on a microscope (Zeiss AxioVision, Leica DMi8) at 24-hour intervals from day 0 – day 7. The cross-sectional area of the spheroid was measured using ImageJ. The area was normalized to day 0 to yield normalized spheroid size over time.

Immunofluorescence staining of microtissues

To visualize expression of tissue-specific proteins post-integration, LOC, HOC, and MOC tissue were stained for representative tissue-specific markers. At the end of integration culture, samples were washed with PBS three times, fixed with 4% paraformaldehyde (PFA, Sigma Aldrich) for 15 minutes at room temperature, then washed again with PBS to remove excess PFA. A blocking buffer was prepared, composed of 3% bovine serum albumin (BSA, Sigma Aldrich) and 0.25% Triton-X 100 (Fisher Scientific), and added to the samples for 1 hour in 4°C, to prevent non-specific binding of antibodies. Next, primary antibodies diluted at 1:100 in blocking buffer were prepared and added to the samples overnight at 4°C. For the

liver-on-a-chip, human albumin (goat polyclonal, Bethyl Labs), CYP3A4 (mouse monoclonal, ThermoFisher Scientific), and CYP2A6 (mouse monoclonal, ThermoFisher Scientific) antibodies were used. For the heart-on-a-chip, connexin-43 (rabbit polyclonal, ThermoFisher Scientific), and sarcomeric α-actinin (mouse monoclonal, Sigma-Aldrich) were used. For the skeletal muscle-on-a-chip, myosin heavy chain (MF20 mouse monoclonal, Developmental Studies Hybridoma Bank) was used. After 24 hours, stains were washed away with several PBS washes. Next, a solution consisting of fluorescently-labeled secondary antibody diluted 1:100 in blocking buffer along with Hoechst 33342 dye diluted to 1x to view nuclei, was added to the samples overnight at 4°C, then washed away with excess PBS prior to imaging. The secondary antibodies were some combination of AlexaFluor 488 goat anti-mouse secondary antibody (ThermoFisher Scientific), AlexaFluor 488 goat anti-rabbit secondary antibody (ThermoFisher Scientific), and AlexaFluor 568 goat anti-mouse secondary antibody (ThermoFisher Scientific), depending on the primary antibodies added to each respective sample. Samples were imaged with either a conventional epifluorescence microscope (Keyence BZ-X710) or a spinning disk confocal microscope (Perkin Elmer UltraView) at various magnifications.

Live/Dead viability assay

To demonstrate the viability of every tissue type at the end of the integrated culture period, a live/dead assay for mammalian cells (ThermoFisher Scientific) was performed. Live/dead solution containing 1μL of calcein AM stock solution and 0.25μL of EthD-1 stock solution diluted in 500μL of Opti-Mem was prepared according to the manufacturer's protocol. After a brief PBS wash to rinse away media, the live/dead solution was added

individually to the LOC, HOC, MOC, and COC modules and incubated for 15 minutes at 37°C. Samples were washed with multiple PBS washes before imaging immediately on a fluorescence microscope (Zeiss AxioVision, Leica DMi8). Care was taken to image quickly to avoid photobleaching.

Drug screens with 5-Fluorouracil and Tegafur

As a proof-of-concept validation of the potential utility of the integrated multi-organ platform as a screening tool, we examined the effect of two anti-cancer small molecule drugs on the cancer-on-a-chip tissues. To this end, an integrated system consisting of liver-on-a-chip + cancer-on-a-chip (LOC+COC) versus cancer-on-a-chip only (COC only) was constructed and prepared for drug screen. Solutions of 5-Fluorouracil (5FU, Sigma Aldrich) and Tegafur (Sigma Aldrich) at 10mg/mL in DMSO were prepared. 5FU and Tegafur were each diluted to 10µg/mL in CDM3 media for the initial drug comparison study. For the dose-dependence study, Tegafur was diluted to concentrations of 0.1µg/mL, 1.0µg/mL, and 10µg/mL. The drug solutions were added to the media reservoir of the respective integrated setups, and replenished every day to reset the drug concentration. The integrated setup was cultured at 37°C and 10% CO_2, and the drug solution was supplied to tissues under peristaltic flow, as mentioned previously. Brightfield images of spheroids were captured every day from day 0 to the end of the culture period. Cancer spheroids were analyzed to evaluate growth rate $\left(\frac{D_X - D_0}{D_0} \times 100\right)$ and normalized spheroid size at the end of the culture period $\left(\frac{D_7}{D_0}\right)$. At day 7, spheroids were also incubated in live/dead solution as described previously, to assess viability under the various drug conditions. For both spheroid growth rate and normalized

spheroid size, data is presented as mean ± standard deviation. For spheroid growth rate, the comparison between the groups was carried out by using two-way ANOVA with Bonferonni's multiple comparison test, where P-values < 0.05 were considered statistically significant. For normalized spheroid size, the comparison between the groups was carried out by using one-way ANOVA with Tukey's multiple comparison test, where P-values < 0.1 were considered statistically significant. Data is presented using GraphPad Prism software.

To evaluate cardiotoxicity, cardiac beating frequency was determined for control and drug conditions at day 0, 1, 3, 5, and 7. Normalized cardiac contraction frequency was taken for each day with respect to day 0 and graphed to determine the trend over time. The toxicity was determined by evaluating the overall percentage decrease in contraction frequency at the end of the experimental period, day 7, with respect to day 0.

4.4 Results

System setup and acellular flow characterization

To develop a multi-organ 'human-on-chip' platform that, as a proof-of-concept, recreates several aspects of whole human physiology *in vitro*, we attempted to create a system where nutrients and drugs would be forcibly passed through various target "organs" via continuously recirculating media, similar to the recirculation of blood in our bodies (Figure 4.2). To accomplish this, we linked together liver, heart, cancer, and skeletal muscle organoid models and supplied nutrients continuously via a peristaltic pump, effectively mimicking the systemic circulation of blood through the tissues of the human body. Specifically, to make the organoid models, we created a single microfluidic device containing a central chamber capable of housing multiple acellular and cell-laden hydrogel layers. This microfluidic device was designed with the versatility to be purposed for several 'organ-on-chip' applications – liver-on-chip, heart-on-chip, muscle-on-chip, and cancer-on-chip – by tweaking the geometry and architecture of the hydrogel layers and varying the respective cell sources. Several individual 'organ-on-chip' modules could then be linked together in a sequential manner, to demonstrate a multi-tissue 'human-on-chip' platform. A single, universal media, containing nutrients for survival and drug compounds for pharmaceutical testing, would be pumped through the entire system via a peristaltic pump that operated 24 hours a day for the duration of the studies. A depiction of the entire setup, including the order of the chips and reservoir containing culture media, is given in Figure 4.3.

In order to determine the appropriate peristaltic pump settings to ensure even, non-turbulent flow to all 'organ-on-chip' modules and to determine the feasibility of sustaining up to four 'organ-on-chip' modules in a single fluidic circuit, flow was first characterized in

acellular samples. First, bulk flow rate through all integrated chips was characterized by varying the number of chips from 1-5 and varying the pump settings from 5 (lowest) to 99 (highest), and quantifying the total amount of fluid exiting the system in a 10-minute period. Bulk flow rate was determined to range from 1 – 15 μL/min (60 – 900 μL/hr), depending on the number of chips and pump setting (data not shown). Generally, as the number of chips was increased, the flow rate was observed to decrease. This is likely attributable to the increased resistance in the fluidic channels as a result of additional length, especially at the low-to-medium pump settings. At the highest pump setting of 99, the pressure was large enough to mitigate any decrease in flow rate; thus, there is no difference in flow rates at this setting regardless of the number of chips. Given that our aim was to have at least four 'organ-on-chip' modules, and previous 'organ-on-chip' studies by our lab and others have used flow rates in the range of 40 μL/hr, we chose the peristaltic pump setting of 5 (lowest), corresponding to a flow rate of 1 μL/min, or 60 μL/hr.[20, 21]

To characterize the fluid displacement and flow velocity within each chip at the chosen pump setting, the motion of fluorescent microparticles mixed in with solution was tracked over time during pumping. The first chip displayed the greatest inhomogeneity in flow, as evident in observing both the fluid displacement and flow velocity patterns (Figure 4.4). Here, the flow velocity would spike at regular intervals to 90 μm/s before dropping to 0 μm/s, likely due to the wave-like flow patterns indicative of peristalsis. However, from the second chip onwards, the fluid displacement curves become consistent and flow velocity patterns smoothen. The oscillatory-nature of flow seen in chip 1 dampens to a more constant flow velocity between 15-30 μm/s, especially between the 3rd, 4th, and 5th chips in the sequence (Figure 4.4). As such, in ensuing experiments, to develop the multi-organ 'human-

on-chip' platform we integrated together 5 chips, where chip 1 acted purely as a "flow buffer" to dampen the flow patterns that would eventually reach chips 2-5, the four 'organs-on-chip' of interest.

Fabrication of individual organs-on-chips

Having determined the overall setup of the integrated multi-organ 'human-on-chip' systems from an acellular perspective, we next developed each individual 'organ-on-chip' module by varying the cell sources and spatial geometry of the hydrogel components. For the liver, skeletal muscle, and cancer microtissues, gelatin methacrylate, or GelMA, was used as the cell-encapsulating hydrogel. Gelatin is a collagen-derived matrix possessing cell-adhesive sites, and the methacrylate-groups allow for UV-light-initiated free-radical polymerization. Each individual 'organ-on-a-chip' was first fabricated and cultured for a defined period of time prior to integration into the multi-organ 'body-on-a-chip' system.

To create the liver-on-a-chip (LOC), liver organoids were formed using human hepatocarcinoma cells, specifically Huh7 hepatocytes, encapsulated in a GelMA hydrogel (Figure 4.5A). Liver organoids were created in an ellipse shape for three reasons: (1) to minimize resistance and preserve laminar fluid flow, (2) to circumvent potential diffusion limitations and ensure nutrients in the culture media efficiently diffuse throughout the organoid, and (3) to confine Huh7 cells to a small area to promote cell aggregation, which is known to preserve liver function. Each LOC was able to contain and sustain up to 40 liver organoids. Following encapsulation, LOC organoids were cultured for 1 day in growth medium to allow the cells to equilibrate and grow in their new environment, prior to integrating with the remaining 'organ-on-chip' modules (Figure 4.6A).

To create the heart-on-chip (HOC), laminar sheets of cardiomyocytes were formed using human induced-pluripotent stem-cell-derived cardiomyocytes (hiPSC-CM) seeded between hydrogel "walls" (Figure 4.5B). The hiPSC-CM are patient-specific cells that possess an identical genetic make-up to the individual from whom the cells were isolated. Thus, a HOC platform utilizing these cells demonstrates the capability of creating a 'human-on-chip' tailored to each individual patient, a powerful tool for drug screening and optimizing drug regiments. The hydrogel "walls", formed from photo-polymerized PAm, served the purpose of confining the cells during initial cell seeding, and guiding the formation of laminar sheets of heart tissue. Cardiac sheets would emulate the native anisotropic architecture of the heart's myocardium, and ensure unidirectional contraction of spontaneously beating cardiomyocytes. Each HOC was able to contain up to 10 independently-contracting cell sheets. Following cell seeding, HOC cardiac sheets were cultured for 7 days in CDM3 cardiomyocyte medium, prior to integrating with the remaining 'organ-on-chip' modules, to allow the cardiomyocytes to regain a robust beating phenotype (Figure 4.6B).

To create the cancer-on-chip (COC), tumor masses were formed using spheroids of MCF7 human breast adenocarcinoma cells encapsulated in a GelMA hydrogel. Cancer organoids were formed in circular patterns of GelMA to allow for even radial growth of the spherical tumor mass in all directions (Figure 4.5C). Each COC device contained up to 5 tumor masses. Following encapsulation, COC organoids were cultured for 1 day in growth medium to allow the cells to equilibrate in their new environment, prior to integrating with the LOC, HOC, and MOC modules (Figure 4.6C).

To create the skeletal muscle-on-chip (MOC), microtissue strips of skeletal muscle were formed from C2C12 murine myoblasts encapsulated in a GelMA hydrogel around two

PAm hydrogel pillars (Figure 4.5D). The hydrogel pillars acted as anchoring sites to induce uniaxial alignment of the cells as they grow and mature into a muscle tissue strip over time. This process was further facilitated by the fusion of myoblasts into multinucleated myotubes and cell-mediated degradation of the GelMA hydrogel. Each MOC device contained up to 10 skeletal muscle microtissue strips. Following encapsulation, MOC organoids were cultured for 1 day in growth medium to equilibrate with the new environment, followed by 2 days in low-serum differentiation medium to induce cell differentiation and fusion. After day 3 of culture, the MOC module was integrated and cultured with the remaining 'organ-on-chip' modules (Figure 4.6D).

Characterization of cell viability and tissue functionality within the integrated system

The viability and functionality of each 'organ-on-chip' module was assessed after 7 days of integrated co-culture. Due to the sensitive nature of the hiPSC-CM, CDM3 cardiomyocyte maintenance medium was used as the single culture medium for the entire integrated system. As a low-serum medium itself, we hypothesized that CDM3 was sufficient to sustain the survival and differentiation of C2C12 muscle microtissue strips in the MOC. We further assumed that CDM3 was sufficient to support the proliferation of Huh7 liver cells in the LOC and MCF7 cancer cells in the COC.

Evaluation of liver tissue formation, viability, and function

In the first several days of integration, the Huh7 cells proliferated from individual cells to small clusters of cells within the GelMA hydrogel, and eventually amassed into larger, dense spheroids of hepatocytes (Figure 4.5A). The structural integrity of the GelMA hydrogel

was visibly weakened, likely in response to degradation by the Huh7 cells as they proliferate and migrate. The LOC organoids had ~95% viability at the end of the 7-day experimental period of integration, with few dead cells interspersed throughout each construct (Figure 4.5A). Liver function was preserved throughout the integration co-culture period. LOC organoids stained positive for human albumin, a protein synthesized by hepatocytes (Figure 4.7A). Further, albumin secretion by the liver was detected over the 7-day culture period via ELISA. Our LOC module yielded steadily increasing levels of albumin, a positive indication of normal liver function (Figure 4.7B). Thus, it was concluded that the LOC organoids were able to survive and function normally despite the choice of CDM3 media, which is atypical of Huh7 culture conditions, in the recirculating integration co-culture setup. Further, liver function was preserved despite potential interference from wastes and by-products secreted by the other 'organ-on-chip' modules.

Evaluation of cardiac tissue formation, viability, and function

The cardiac sheets within the HOC module displayed a consistent spontaneous contraction phenotype prior to integrating with the LOC, MOC, and COC. Over the 7-day integration co-culture period, the hiPSC-derived cardiomyocytes underwent some tissue compaction but overall retained their cardiac sheet-like morphology (Figure 4.5B). The hiPSC-CM have limited proliferation capacity, and the cardiac sheets were confluent upon initial cell seeding. As such, it was assumed that cell growth in the integrated system was negligible. Further, the HOC had approximately ~90% cell viability at the end of the integration co-culture, with few dead cells distributed throughout each sheet (Figure 4.5B). We assessed the differentiation persistence of the hiPSC-CM comprising the HOC cardiac

sheets by immunofluorescent staining of cardiac markers after 7 days of integrated co-culture. The HOC was characterized for expression of connexin-43 and α-actinin, markers for cardiac gap junction proteins and sarcomeric microfilament proteins, respectively, and counterstained for cell nuclei. Gap junctions allow for the intercellular communication of electrical activity through the movement of ions, which facilitates coordinated cardiac contraction. Sarcomeric α-actinin is an actin-binding protein critical in cross-linking adjacent sarcomeres within and between cells, and plays a role in maintaining the structure of the cardiac cytoskeleton. This is necessary for the coordinated contraction of the millions of cardiomyocytes functioning as one organ. Images of a representative HOC cardiac sheet show positive expression of both gap junctions and sarcomeric proteins (Figure 4.8A). The corresponding high-magnification image of α-actinin clearly depicts sarcomeres that are uniaxially-aligned with the major axis of orientation (Figure 4.8B). Thus, the HOC cardiac sheets mimicked the native structure and morphology of myocardial tissue, despite integration with LOC, MOC, and COC.

In addition to characterizing the structure and morphology of the cardiac sheets, we assessed their function. Spontaneous contraction of the cardiac sheet was observed during the 7-day integrated co-culture period (Video 1 not provided). To evaluate cardiac sheet function in the HOC, we examined contraction patterns and beating frequency. Contraction was characterized in terms of average deviation from the relaxed, or reference, state. A representative trace depicting contraction over a 20-second time interval illustrates the consistency of contractions, both in terms of amplitude (peak height) and interval (peak-to-peak distance) (Figure 4.8C). The beating frequency was also obtained each day for the 7-day period of integration co-culture (data not shown). Immediately after integration of the

HOC with the other 'organ-on-chips', the measured beating frequency dropped to 0.3 Hz after 24 hours, and was undetectable after 48 hours. However, from day 3 onwards, the HOC cardiac sheets resumed their spontaneous contraction and stabilized around 0.5 Hz. It is possible that the integration process itself had an initial adverse effect on the contraction phenotype. This may be a result of the cardiomyocytes adjusting to changes in the media composition caused by various factors secreted by the LOC, MOC, and COC. However, ultimately the HOC cardiac sheets equilibrated to their new environment, and the integration of the HOC with the LOC, MOC, and COC had no apparent negative effect on the structural or functional phenotypes of the differentiated cardiac sheets.

Evaluation of skeletal muscle tissue formation and viability

Prior to linking the MOC to the integrated 'human-on-chip' system, the microtissue strips were first differentiated for 3-days. During this period, myoblast expansion was followed by cell-cell attachment, remodeling of the GelMA hydrogel, and compaction of the skeletal muscle microtissue (Figure 4.5D). Following this initial differentiation phase, the MOC was integrated with the LOC, HOC, and COC, and during 7-days of integration co-culture, the MOC displayed similar tissue compaction. The muscle microtissue strips displayed ~95% cell viability at the end of the culture period, indicating that the CDM3 media, which is not a commonly-used differentiation media for C2C12 myoblasts, did not negatively impact tissue survival (data not shown). To characterize the structure of the skeletal muscle microtissues, the MOC was immunofluorescently stained for desmin, a marker for myoblasts, and myosin heavy chain, a marker for differentiated muscle cells, and counterstained for the nuclei. As seen in Figure 4.9, the presence of several elongated cells

expressing myosin heavy chain indicates the formation of multinucleated myotubes. Further, the majority of myotubes observed are horizontally-aligned, with only slight deviations in the direction of the major axis. Thus, the MOC skeletal muscle cells successfully survived and differentiated into a microtissue strip within the integrated multi-organ system.

Evaluation of cancer tissue viability and growth

The tumor spheroids within the COC module displayed constant continual growth even after integration with the LOC, HOC, and MOC (Figure 4.5C). Cell viability in the COC was close to 100% across all samples – thus the COC organoids retained the highest viability as compared with other 'organ-on-chip' modules (Figure 4.5C). Thus, as expected, the cancer organoids survived irrespective of the multi-organ integration setup, the unconventional culture medium, or of any potential secreted factors from the connected LOC, HOC, and MOC modules.

Proof-of-concept drug screen for cancer efficacy and cardiac toxicity

To demonstrate the utility of a multi-organ 'body-on-a-chip' platform, we performed a proof-of-concept drug screen using known small molecule cancer therapeutics, Fluorouracil and Tegafur. Fluorouracil, known as 5-FU, is a cytotoxic chemotherapeutic of the class fluoropyrimidine, commonly used to treat cancers of the breast, colorectal, and more.[57] Tegafur, a chemotherapeutic oral pro-drug of 5-FU, is used to treat gastric, colon, breast, and other cancers after a cancer surgery to destroy remaining tumor cells and prevent recurrence.[58] As a pro-drug, Tegafur is inactive in the human body until it is metabolized by cytochrome P450 enzymes found in the liver, and thus has a much longer bioavailability as

compared to 5-FU, which rapidly degrades.[52] In order to observe an efficacy against the tumor mass, Tegafur must be metabolized by the liver. Additionally, while fluoropyrimidines like 5-FU are linked to much lower occurrences of cardiotoxicity than anthracyclines like doxorubicin, they have been shown to lead to pectoral angina, myocardial ischemia, arrhythmias, myocardial infarctions, and even sudden death.[59, 60] In fact, in patients who develop severe cardiotoxic responses to 5-FU, Tegafur is often used as a substitute as it is known to be associated with significantly reduced occurrences of cardiac toxicity.[61] Thus, we probed whether we could emulate the cardiotoxic effect of a fluoropyrimidine such as 5-FU or Tegafur in the 'body-on-a-chip' system. Since we were most interested in evaluating the LOC, as the site of drug metabolism, the COC, as the site of the target tissue, and the HOC, as the site of potential cardiac toxicity, the MOC was excluded from the proof-of-concept drug screen experiment.

Cancer pro-drug metabolism and cytotoxicity within integrated system

To demonstrate the difference in response of 5-FU and Tegafur against the tumor spheroids in the COC, we varied the configuration of the setup by testing the drugs in the HOC + COC versus in the LOC + HOC + COC. A concentration of 10 μg/mL was chosen based on known IC50 values for 5-FU against MCF7 cancer cells.[62] When 10 μg/mL of 5-FU was supplemented in the culture medium to both experimental setups, the tumor mass ceased to grow, and the majority of cancer cells died (Figure 4.10). Thus, as expected, by day 7 of the experiment, 5-FU universally destroys the cancer, with or without the LOC. When 10 μg/mL pf Tegafur was supplemented in the culture medium to the HOC + COC, the tumor mass continued to grow and the majority of cells remained viable at day 7. However, when

the same concentration of Tegafur was administered to the LOC + HOC + COC setup, tumor growth ceased and many cells died at day 7 (Figure 4.10). This indicates that in the 'body-on-a-chip', liver organoids in the LOC function to mimic first-pass metabolism of Tegafur to its active form 5-FU before it proceeds to destroy the tumor mass downstream, whereas without the LOC, Tegafur remains inactive and the tumor growth continues. These results are further corroborated by the analysis of spheroid growth rate as a function of time, where growth rate of the cancers that received Tegafur in the HOC + COC rises up to 25%, whereas the growth rate is essentially zero in all other cases, ranging between -2% and 2% (Figure 4.11A). Furthermore, the normalized spheroid size of the tumors that received Tegafur in the HOC + COC is the greatest at ~1.2, while the normalized spheroid size is <1.0 for all other cases (Figure 4.11B). Thus, as expected of the pro-drug, Tegafur does not attack the tumor mass until it is metabolized by liver organoids.

We studied the capability of the multi-organ 'body-on-a-chip' to discern variations in tissue response to different dosages of Tegafur. Using 10 μg/mL as an upper limit, owing to the fact that it previously resulted in cancer cell death, we screened Tegafur in the LOC+COC integrated setup at 0.1, 1.0, and 10 μg/mL. As seen in Figure 4.12, there is a dose-dependent effect on spheroid growth and cancer cell survival. At both 0.1 μg/mL and 1.0 μg/mL, the tumor spheroid grows between day 0 and day 7, and most cells appear alive, while at 10 μg/mL, the tumor spheroid shows no growth and many cells are clearly dead. Further, there is a dose-dependent difference in spheroid growth rate and normalized spheroid size post-treatment (Figure 4.13). Tumor spheroids exposed to 0.1 μg/mL Tegafur grow most rapidly, and multiply in size by ~2.7x, while those exposed to 1.0 μg/mL Tegafur double in size. Thus, although growth rate is positive, it is hindered by the drug at 1.0 μg/mL as compared

to 0.1 μg/mL. The tumor masses exposed to the highest concentration of 10 μg/mL Tegafur exhibit negligible growth due to the high number of cells that die once the LOC metabolizes the drug. Therefore, the multi-organ 'human-on-chip' system elicits data clearly differentiating tissue response to varying dosages of medication, which is important in not only in developing a drug-screening platform but also in determining optimal dosage ranges for patient-specific or population-specific applications.

Drug-induced liver CYP450 protein expression and cardiac toxicity in integrated system

Liver organoids were further examined to verify the activity of cytochrome interactions are due to the CYP3A4 isoform, it has been shown previously that Tegafur is metabolized primarily by CYP2A6 isoforms in liver microsomes.[63, 64] 'Body-on-a-chip' samples containing a LOC + HOC + COC were subjected to 10 μg/mL Tegafur for 7 days, then stained for cytochrome P450 protein isoforms CYP3A4 and CYP2A6. Immunofluorescence images illustrate that there is expression of CYP2A6 whereas there is no expression of CYP3A4, demonstrating the specificity of protein metabolic activity in response to Tegafur in the 'body-on-a-chip' system (Figure 4.14).

Cardiac toxicity was assessed in terms of changes in beating frequency over time. 'Body-on-a-chip' systems consisting of LOC + HOC + COC were subjected to 0.1, 1.0, and 10 μg/mL Tegafur, 10 μg/mL 5-FU, or a control of no drug, and compared to a 'body-on-a-chip' system consisting of HOC + COC (no liver module) subjected to 10 μg/mL Tegafur. Beating frequency was recorded and analyzed over 7 days (Figure 4.15). The results indicate that the no-drug control and 10 μg/mL Tegafur without liver mostly maintain a steady contraction phenotype over time. This is expected as without liver organoids, the Tegafur

should not form active 5-FU and therefore it should not lead to any cardiotoxicity. In the condition of the 10 μg/mL 5-FU, there is a precipitous decrease in contraction presumably due to direct contact of the 5-FU with cardiomyocytes, leading to arrhythmias and cell death. In the condition of 0.1, 1.0, and 10 μg/mL Tegafur in the fully-integrated system, the magnitude of decrease in beating frequency mirrors the drug concentration increase (Figure 4.15A). Thus, the presence of liver organoids leads to metabolism of Tegafur to 5-FU, which appears to cause cardiotoxicity. These results are further corroborated by Figure 4.15B, which uses a percentage decrease in beating frequency at day 7 with respect to day 0 to assess cardiotoxicity. We see that the 10 μg/mL Tegafur in the fully-integrated system causes the greatest cardiotoxicity as compared to lower concentrations of the drug; however, this cardiotoxicity is lesser than that caused by native 5-FU itself. These results emulate those seen in patients receiving Tegafur clinically, and further exemplifies the utility of multi-organ 'body-on-a-chip' platforms for pharmaceutical screening of similar therapeutics, as compared to the standard multi-well culture plate used for *in vitro* testing.

4.5 Discussion

Organ-on-a-chip systems have immense potential in serving as *in vitro* human tissue surrogates for preclinical applications. These platforms may provide the key to next-generation human disease modeling and pharmaceutical drug screening to aid in the development of promising new medications. When combined with patient-derived cells, including those from individuals with rare diseases, organ-on-a-chip systems may be valuable in expediting the development of medications for lesser studied orphan diseases. When combined with multiple organs-on-chips together, researchers and scientists can perform more comprehensive studies on a systemic level. Previous studies utilizing cells from various tissue types have demonstrated a linear path of drug metabolism for breakdown to an active form, followed by toxicity of the active drug molecule on the target and a series of off-target sites.[52] Multi-organ systems can provide greater reproducibility across samples than animals, which vary amongst each other. Further, these systems are inexpensive to produce, do not require large animal facilities for breeding and care, and require small amounts of drug compounds and reagents due to the micro-scale of the fluidic system. Thus, operation of the organ-on-a-chip is extremely low-cost and versatile. In this study, we have utilized previously-developed organs-on-chips for skeletal muscle and cancer, while using similar methods to develop two new organs-on-chips for liver and heart, to create a multi-organ 3D 'body-on-a-chip' system to demonstrate cell viability, tissue function, and response to cancer drugs.[36, 37]

Multi-organ *in vitro* platforms have immense downstream applications ranging from basic research of tissue-tissue cross-talk to preclinical pharmaceutical drug development and screening. For relevance in these applications, it can be reasoned that a 'body-on-a-chip'

system recreate the following tissues and organs – liver, heart, skeletal muscle, and cancer. The proper function of these tissues is critical to the survival and well-being of any individual. The liver is responsible for breaking down toxic substances and metabolizing drug compounds, as well as synthesizing critical proteins such as albumin. In fact, all drugs that are ingested into the human body, after reabsorption by the gut, will first pass through the liver for appropriate metabolic breakdown. The heart is responsible for pumping blood carrying oxygen, nutrients, and drug compounds, including those from the previous liver step, to all tissues in the human body. Proper contractile function of the heart, in terms of contraction frequency and contractility, is essential for normal bodily function. Skeletal muscle, the largest tissue by mass in the human body, provides motion for everyday function and activity.[65] Skeletal muscle has been shown to atrophy as an adverse side effect to the oxidative stress that results from various drug treatments, including cancer drug therapies.[66] Toxicities to any of these three tissues can have severely detrimental effects on a patient, and thus these must be actively monitored. Finally, cancer tissue is an abnormal tumor mass that can be destroyed, at least in part, by cancer therapeutics. However, existing cancer therapeutics, especially the small molecules that are the majority in chemotherapy treatment, have side effects ranging from hair loss, nausea, and vomiting to toxicity that causes improper tissue function and disease. Integrating each of these tissues into a singular platform opens the potential to simultaneously obtain two pieces of information during an oncology drug screen – efficacy against the tumor, and toxicity to the liver, heart, or muscle. This has immense potential in the grand scheme of preclinical drug development, where mice are the standard model of choice despite the known differences between mice and humans.

One of the critical issues with multi-organ systems is the choice of culture media to sustain normal cellular and tissue function of all the different organs-on-chips, since only one media can be used in a continuous flow system as described in this study. Given that the cardiac sheets, composed of hiPSC-derived cardiomyocytes, were the most sensitive tissues in our system, any variation from the CDM3 media was likely to cause issues in the normal function of these tissues. The liver, skeletal muscle, and cancer were all created from cells derived from immortalized cell lines, and as such, were hypothesized to be resistant to variations in their typical culture media compositions. Further, the CDM3 media contains bovine serum albumin, which is a major component of fetal bovine serum typically used in growth media for Huh7, MCF7, and C2C12 cells. Thus, our media choice of CDM3 cardiac differentiation media proved to be sufficient in sustaining the structure and function of all the organs-on-chips. The immunofluorescence images of the liver, heart, and skeletal muscle depict the presence of classic protein markers in each tissue type. Further, the functional measurements of each tissue confirm the continuation of normal activity following integration into a 'body-on-a-chip'. The liver, in which the cells grow in clusters, expresses albumin, one of the most abundant proteins in the human body, and continues to function normally and secrete albumin over the course of the experiment. The cardiac sheets, which form aligned sheets of cells, express classic cardiac markers for gap junctions, essential for intercellular propagation of the cardiac action potential, and sarcomeric proteins, which allow for coordinated contractions within a cell and between adjacent cells. Further, the cardiac contraction was characterized to demonstrate consistent contraction frequency over time. The skeletal muscle microtissues formed long muscle strips with multinucleated myofibers and elongated nuclei on the myotubes, indicating muscle maturation from single cells to unified

muscle bundles. Finally, the cancer tissues exhibited continued growth over the course of the experimental period, confirming normal function.

Future studies with multi-organ 'body-on-a-chip' systems will aim to integrate additional tissue types, such as gut, brain, bone, bone marrow, and more, as well as continuing to use sensitive primary cells or patient-specific hiPSC-derived cells in lieu of cell lines. Therefore, additional work will be required to optimize media conditions that sustain normal structure and function of these tissue types. Perhaps, new organ-on-a-chip designs will need to be developed that allow for different media types to be used for each individual tissue module, while maintaining the tissue-tissue cross-talk that makes the 'body-on-a-chip' unique.

The 'body-on-a-chip' system was powered by a peristaltic pump to continuously recirculate media throughout all tissues. However, the peristalsis caused irregular flow patterns in the first chip closest to the rotor (Figure 4.4). This could be exacerbated by the microfluidic chip design, which consists of thin glass irreversibly bonded to PDMS elastomer. It is possible that the bolus of fluid entering the first chip causes the central chamber to expand, and upon reaching its expansion limit it recoils, pushing fluid through and causing a sharp spike in flow velocity. The irregular flow pattern is further reflected in the stepwise pattern of displacement seen in Figure 4.4A. However, the irregularities are attenuated from chips 2 onwards, resulting in linear displacement and constant velocity profiles. Thus, it was necessary to use the first chip to buffer the flow, in order to mitigate unwanted effects of shear stress or fluid pressure on the tissues. Further, if additional organs-on-chips were to be added to this system, the peristaltic rotational settings may need to be re-evaluated. An increasing number of chips creates additional resistance to flow and,

theoretically, reduces flow rate, therefore it is possible that the bulk flow rate may change. Perhaps this would necessitate a variation in the design of the microfluidic chip itself, with wider channels and higher gauge tubing to reduce the overall resistance to flow and allow a greater number of chips.

The liver, skeletal muscle, and cancer spheroid tissues consisted of cells encapsulated in a GelMA matrix, which supports cell attachment through cell-adhesive sites. GelMA is also degradable, allowing cell growth, as in the case of liver and cancer, and remodeling during tissue development, as in the case of skeletal muscle. Further, these tissues were grown between PAm hydrogels, which are a non-adherent surface to prevent cell growth and attachment outside of the defined GelMA hydrogel. Photo-polymerization via 3D photopatterning also provides versatility to choose a defined geometry for each tissue. To observe and quantify spheroid growth, a circular geometry was chosen, while in the case of skeletal muscle, a capsule shape that surrounded two pillars was chosen to allow for remodeling and tissue condensation to a muscle strip. For the liver, an ellipse shape was chosen to minimize resistance to fluid flow and streamline flow patterns given that the liver would be the first chip in the setup, which contained some turbulent velocity patterns as compared to the remaining downstream chips. Furthermore, the ellipse would be sufficient to minimize diffusion limitations and ensure all of the nutrients or drug compounds reach the cells and are metabolized accordingly. Interestingly, in the case of the liver, it was observed that many cells migrated to the periphery of the GelMA construct and the majority of cell proliferation and clustering accumulated at the edges. It has been shown previously that this may be due to the abundance of nutrients in the media flow, which attracts cells to the periphery and leads to rapid cell growth.[37] A corollary to this is that the cells on the periphery

may consume nutrients or drugs before ever reaching cells in the interior, thus it is conceivable that there is a difference in function of the liver cells at the periphery versus those in the interior of the construct. To mitigate this, the minor axis of the liver organoids was 150μm, well within expected diffusion limit of 200μm. A similar diffusion-based gradient could exist in the cancer-on-a-chip. In this case, the organoids are 320μm and surpass the aforementioned diffusion limit. However, the spheroids themselves ranged from 40-100μm, and GelMA is inherently porous to nutrients and molecular compounds. Taken together, these should pose a minimal barrier to diffusion.

On the other hand, the cardiac sheet was composed of a high-density of cells plated directly onto glass. A small fraction of cardiomyocytes was observed to die upon encapsulation in the GelMA matrix, likely due to the sensitivity of hiPSC-derived cells to minute concentrations of small molecules used in the GelMA synthesis protocol. Direct cell seeding to the glass between hydrogel walls ensured that the cells attached and spread to form cell-cell contacts, which is critical to the onset of cardiac contraction. Further, over time, the surviving cells clustered together and in some cases, detached from the glass in the center of the sample, forming a suspended, contracting cardiac sheet anchored on the left and right ends of the sample.

An inherent limitation of the multi-organ 'body-on-a-chip' was the inability to extensively diversify the quantification of tissue function. This limitation largely stemmed from a need to analyze samples, obtain relevant data, and draw conclusions on tissue function non-destructively, in order to track the tissues continuously over 7 days of culture. The vast majority of analysis was based on image analysis of optically-acquired data, since the microfluidic device can be imaged on any inverted microscope. In all cases, it would not be

possible to stain the samples for tissue-specific protein markers at any point in the middle of the culture period without sacrificing the sample altogether.

For the liver, only albumin secretion was measured; however, during drug intake, liver damage can occur and be assessed by measuring the amounts of common liver proteins including alanine aminotransferase (ALT), aspartate aminotransferase (AST), and alkaline phosphatase (ALP), enzymes commonly residing in the liver but released into the bloodstream during liver damage.[67] With respect to cardiac tissue, beating frequency was characterized by imaging videos of contraction each day. However, while beating frequency was characterized, contractile force is a key metric missing from this 'body-on-a-chip' system. Prior heart-on-a-chip studies have demonstrated an ability to measure contractile force within their systems.[18] However, given that our more sensitive hiPSC-derived cardiomyocytes required plating directly onto glass, quantification of contractile force was not possible. In future iterations of the 'body-on-a-chip', encapsulation of these cells within a purified hydrogel matrix may allow quantification of contractile force using 'far-field' traction force microscopy approaches as described previously.[21] Similarly, for the skeletal muscle-on-a-chip model, we will need to integrate methods to quantify contractile function of the engineered muscle strip, since motion and strength is a primary function of this tissue. Perhaps, this force can be quantified by inducing active contraction of the muscle strip with electrical, chemical, or optical stimulation. Further, for both the cardiac and the skeletal muscle models, certain enzymes known to be secreted during tissue damage should also be measured, such as troponin, creatine kinase, and lactate dehydrogenase.[68] With respect to the cancer spheroids, given that the only cell type is the cancer cell itself, our quantification was limited to spheroid growth rate, overall size, and viability. In future studies, evaluating cancer

migration and metastasis would be valuable additions to this system.

Interestingly, the contraction of the 'heart-on-a-chip' samples ceased on day 2 of the integration, before recovering on day 3 and contracting at a rate of approximately 0.5 Hz. It is likely that the integration process led to an equilibration period for the cardiac samples, where the cardiac strips may initially be negatively impacted by secreted factors from the liver, skeletal muscle, and cancer tissues. We also hypothesize that the integrated co-culture might have led to a severe nutrient depletion due to media consumption by metabolically-active cancer, liver, and muscle cells. This may have shocked the cardiomyocytes, resulting in lower beating frequency immediately after integration.

While each individual organ-on-a-chip module consisted of its core cell type (e.g. hepatocytes, cardiomyocytes, myoblasts, and carcinoma cells), incorporation of additional cell types such as endothelial cells, fibroblasts, and immune cells, amongst others, would allow the 'body-on-a-chip' to better mimic native human physiology. Future studies can also incorporate inflammatory cues to examine the effect of inflammation on tissue function. Furthermore, the current system is best suited to screening cancer small molecule therapeutics. However, addition of certain immune cells such as regulatory T cells and cytotoxic T cells to the cancer-on-a-chip would allow for a more diverse range of pharmaceutical drug testing to bring the 'body-on-a-chip' to a new era of cancer immunotherapeutic research, a field that has limited and insufficient pre-clinical models for drug development.

Our results illustrate that while 5-FU destroys the cancer immediately, its pro-drug form Tegafur must first be catalyzed by liver enzymes in liver cells before it is converted to active 5-FU, at which point it destroys the cancer (Figure 4.10 and 4.11). A target

concentration of 10 μg/mL was chosen for 5-FU and Tegafur based on the known IC50 of 5-FU against MCF7 cancer cells of 10 μM, which converts to ~1.3 μg/mL.[62] Based on this, we dosed Tegafur at concentrations of 0.1, 1.0, and 10 μg/mL. Interestingly, characterization of spheroid size between the integrated and non-integrated samples shows only a marginal difference, but characterization of cell viability very clearly illustrates a drastic difference, showing the effect of including the liver metabolism step in the 'body-on-a-chip' (Figure 4.10). Thus, spheroid size alone is insufficient to assess drug effect on the cancer spheroids. Further, we have characterized changes in the contraction patterns of the 'heart-on-a-chip' cardiac sheets to assess cardiotoxicity in response to the various drugs. Since hiPSC-derived cardiomyocytes contract spontaneously, samples may contract at varying rates and, therefore, it was necessary to normalize beating frequency. Interestingly, the contraction frequency decreased even at lower concentrations of Tegafur, albeit to a lower magnitude. Thus, while at both 0.1 μg/mL and 1.0 μg/mL of Tegafur there is no apparent cancer cytotoxicity, there appears to be a cardiac toxicity (Figure 4.15). While these low concentrations of Tegafur are below the IC50 of Tegafur against MCF7 cancer cells, it is unknown if Tegafur is toxic to all human cardiomyocytes at all concentrations or if these concentrations are simply at inherently toxic levels for specifically hiPSC-derived cardiomyocytes. Therefore, the 'body-on-a-chip' system may help elucidate dangerous drug side effects prior to ever entering patients in clinical trials.

As the 3D 'body-on-a-chip' further develops, patient-specific cells will allow accurate recreation of a target patient's tissue pathophysiology. These patient-specific cells can come from primary cells from a human tissue biopsy, embryonic stem cells (hESCs), or human induced pluripotent stem cells (hiPSCs). Primary cells are limited in number, contain various

excess cell types and extracellular matrix proteins, may carry various other contaminants, and are difficult to acquire due to limited supply. The hESCs are taken from human embryos and thus are limited in numbers and pose ethical dilemmas. The hiPSCs come from adult somatic cells, taken from fibroblasts, keratinocytes, or peripheral blood of live patients. These are then reprogrammed to a pluripotent state, which can be expanded infinitely, prior to differentiating into the target tissue of choice. Thus, these cells are theoretically unlimited in supply, and possess the same genetic make-up as the host from which they were derived. Prior hiPSCs have been taken from patients with disorders including long QT syndrome, Alzheimer's disease, and Duchenne's muscular dystrophy, and have genetically and phenotypically replicated these diseases in a laboratory setting.[69, 70] As a proof-of-concept, our 'body-on-a-chip' system demonstrated the ability to use patient-specific hiPSCs to develop cardiac tissues. Future studies will need to include various hiPSC-derived cells to replicate a specific patient's disease state, to help screen drugs and determine optimal combination drug therapy regiments to most effectively treat the patient.

4.6 Conclusion

In summary, we have created a multi-organ 'body-on-a-chip' platform using four different tissues – liver, heart, skeletal muscle, and cancer – and demonstrated viability under a uniform media condition for 7 days. Each tissue is engineered, using a combination of biomaterials and cells to create 3D tissue constructs, within a microfluidic device. Our approach utilizes four microfluidic chips linked in series to a peristaltic pump, which drives flow continuously through the system. The system is entirely modular – organs-on-chips can be removed or added to the system with ease. Each organ-on-a-chip continues to maintain its tissue-specific phenotype throughout the duration of culture, and displays characteristic protein markers at the end of culture. Our proof-of-concept oncology drug test further illustrates the importance of the 'body-on-a-chip' approach which allows for inter-organ communication. In this case, the presence of a liver-on-a-chip was necessary to first metabolize a drug, Tegafur, into its active form 5-Fluorouracil, after which the 5-FU in media proceeded on to destroy the cancer. Without the liver component, the Tegafur had no effect on the cancer, indicating that our system maintains molecular cross-talk between organs through the fluidic circuit. This was further validated by evaluating drug-induced cardiac toxicity in response to Tegafur. Moving forward, using both healthy and disease-specific hiPSCs will allow us to create human-specific and, more importantly, patient-specific 'body-on-a-chip' platforms that may revolutionize personalized medicine. These systems could be used to further study cell migration, cancer metastasis to a distal secondary site, or cellular cross-talk for studies of systemic inflammation, cell differentiation, and more. By recreating key features of the human body, the 'body-on-a-chip' may also be a valuable tool in pre-clinical drug screening, and will hopefully reduce the reliance on animal models.

4.7 Acknowledgments

The authors acknowledge all members of the Varghese research group for their support and fruitful discussions that led to the culmination of this work. We are thankful that this study was supported by the California Institute for Regenerative Medicine (CIRM) under grant number RT3-07907. We thank the NIH National Heart Lung and Blood Institute for a Ruth L. Kirschstein National Research Service Award NIH/NHLBI T32 HL 105373 which supported Gaurav Agrawal in his pre-doctoral studies. We thank Dr. Prashant Mali for generously allowing us to use his lab space and equipment to collect data for this study. In particular, I would like to thank Dr. Han Liang Lim for initially setting up the integrated system with the peristaltic pump, and for his continued support in conducting the drug-screening experiments, without which this thesis chapter would not have been possible.

Chapter 4, in full, is currently prepared and in submission for publication of the material. Gaurav Agrawal, Han Liang Lim, Shyni Varghese, “Multi-organ ‘body-on-a-chip’ platform as a model system to assess cancer drug efficacy and toxicity”. The dissertation author is the primary investigator and a co-author of this material.

4.8 Figures

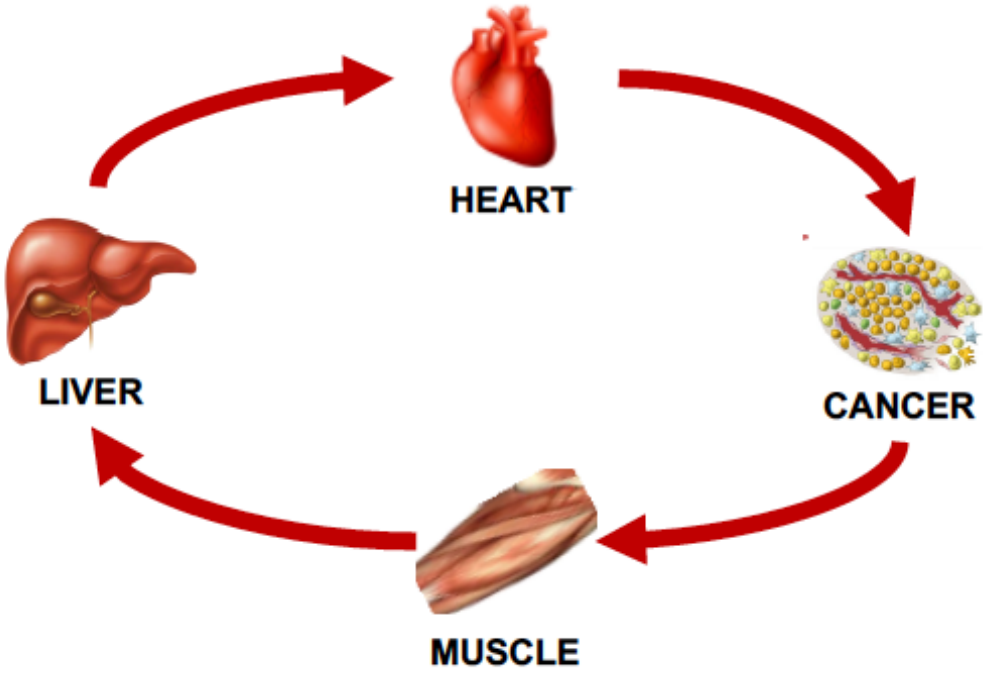

Figure 4.1: Overview of key organs and tissues involved in cancer drug screening.

Drugs are metabolized by the liver, pumped to the rest of the body by the heart, attack cancer masses, and exhibit potential side effects to non-cancer tissues including skeletal muscle, liver, and heart. Blood carrying nutrients, wastes, toxins, and drug compounds is continuously recirculated throughout our body.

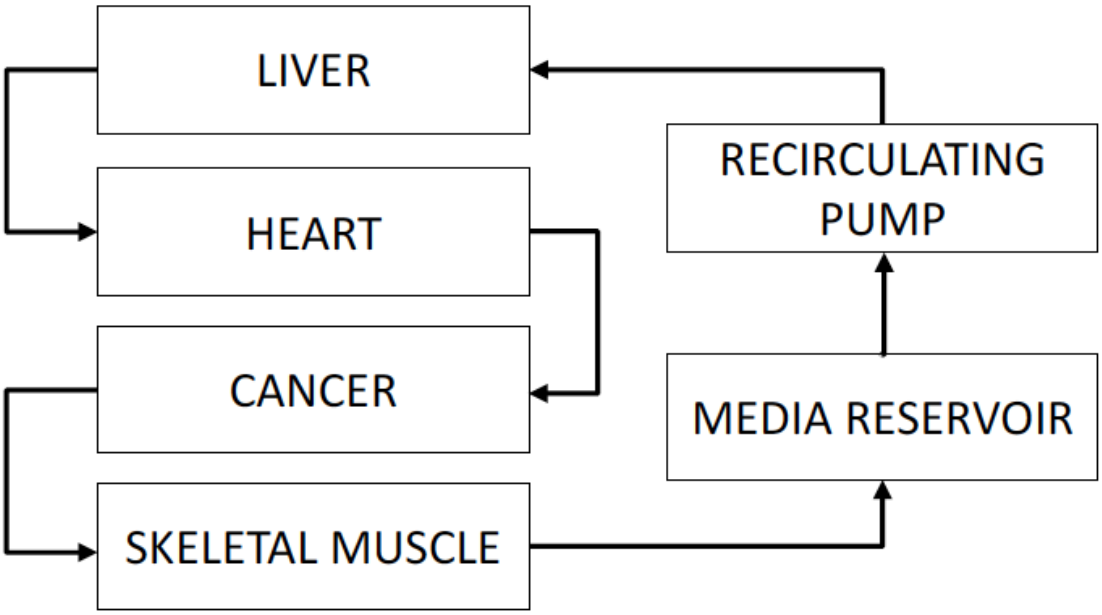

Figure 4.2: Schematic of proposed 'body-on-a-chip' experimental setup.

A liver, heart, cancer, and skeletal muscle are fed nutrients via continuous circulation achieved by a peristaltic pump

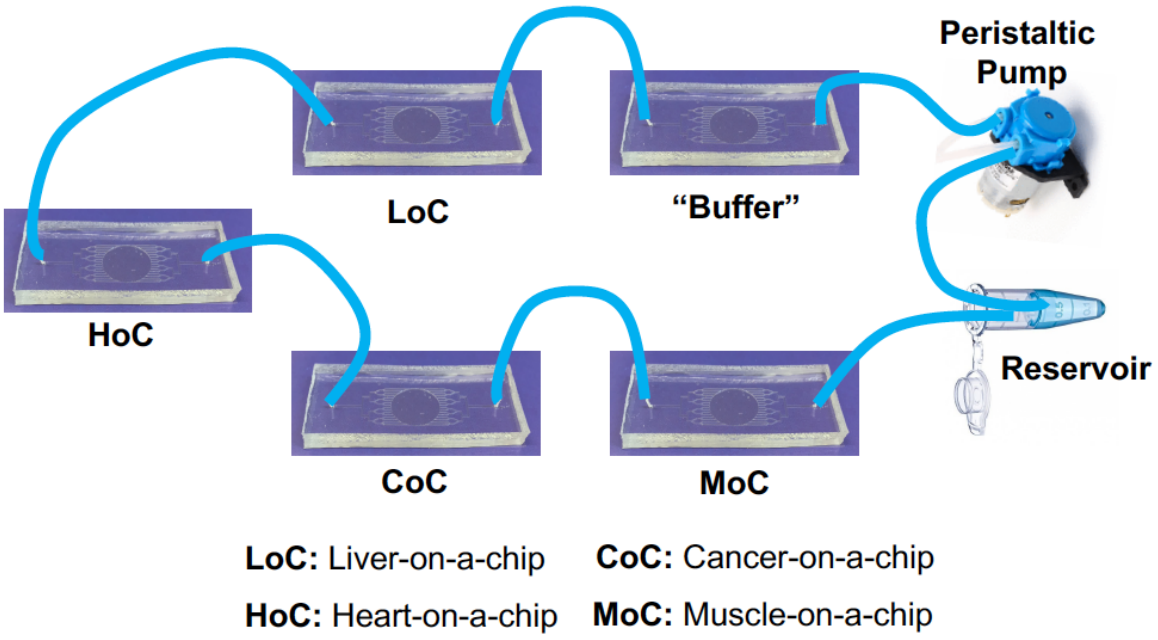

Figure 4.3: Actual 'body-on-a-chip' setup.

Tissues are developed in microfluidics devices that allow for continuous fluid flow. The final experimental setup includes an extra microfluidics device before the liver-on-a-chip to buffer turbulent flow coming from the peristaltic pump.

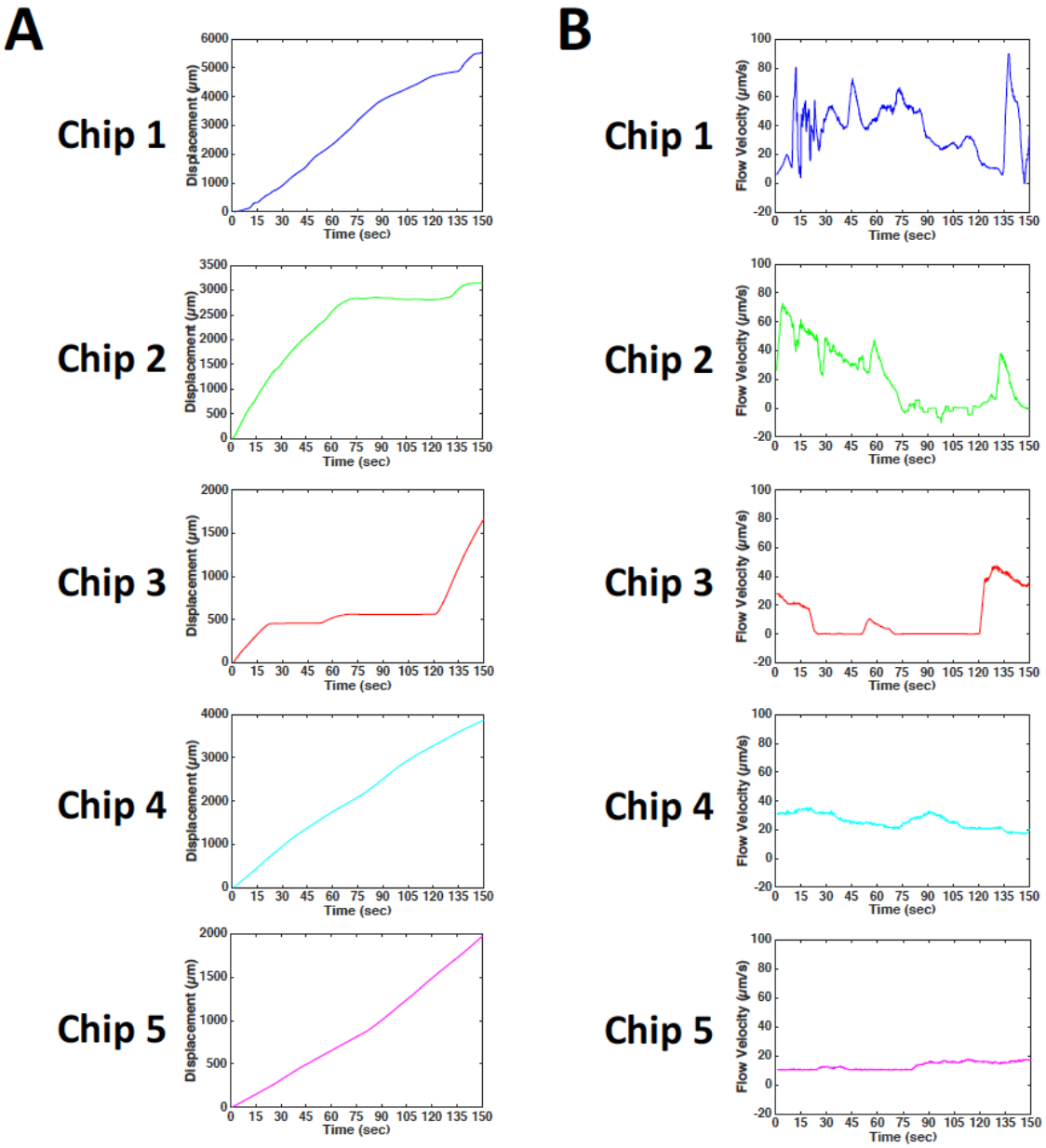

Figure 4.4: Fluid profiles in each chip of the 5-chip 'body-on-a-chip' system.

(A) Fluid displacement profile and (B) fluid velocity profiles. Chip 1 has a step-wise displacement curve and spikes in velocity, whereas the remaining chips display constant flow conditions. Thus, a buffer chip was inserted before the liver-on-a-chip to attenuate flow patterns.

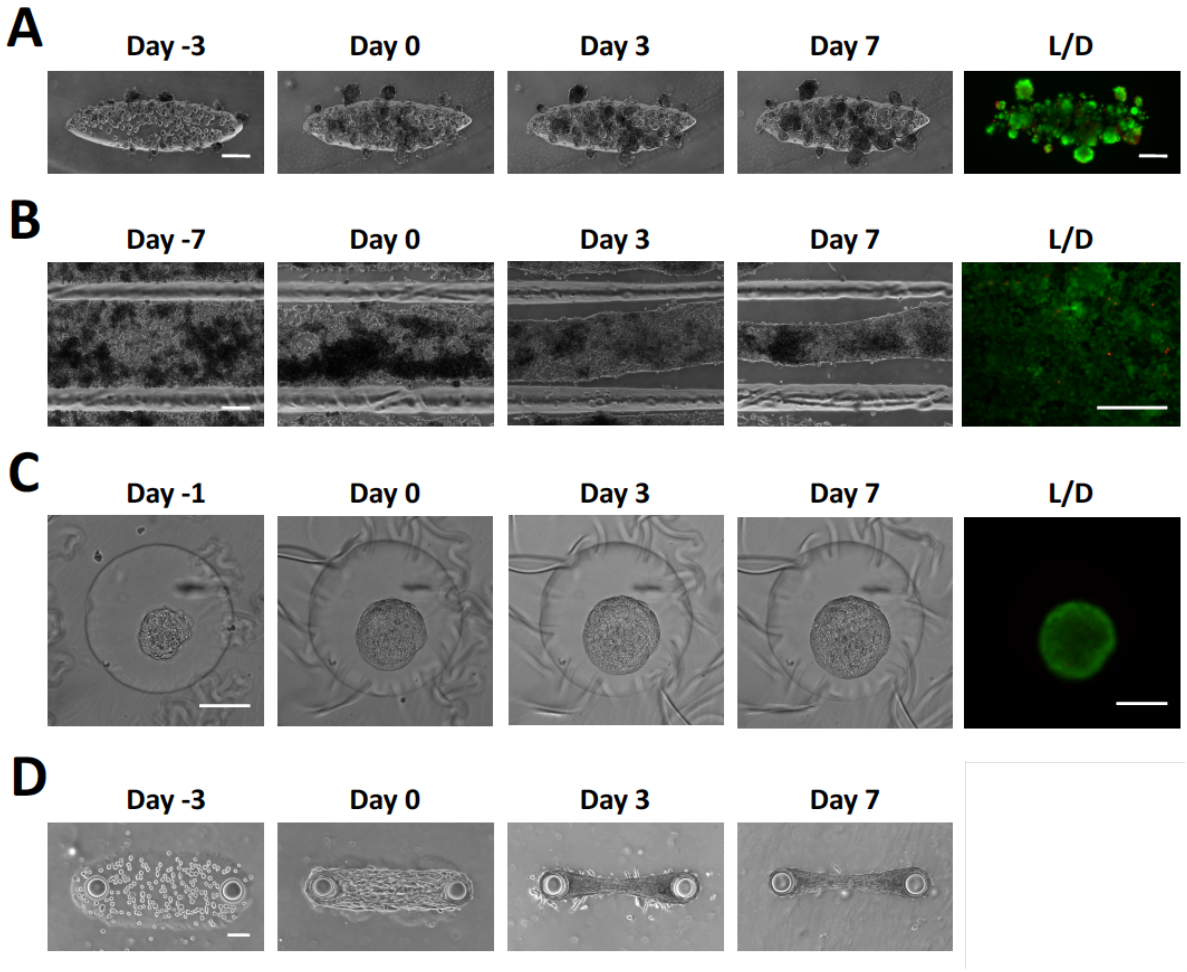

Figure 4.5: Characterization of the formation of various organ-on-a-chip tissues, pre- and post-integration

Brightfield and day 7 cell viability for the (A) liver-on-a-chip, (B) heart-on-a-chip, (C) cancer-on-a-chip, and (D) skeletal muscle-on-a-chip. All scale bars are 100µm.

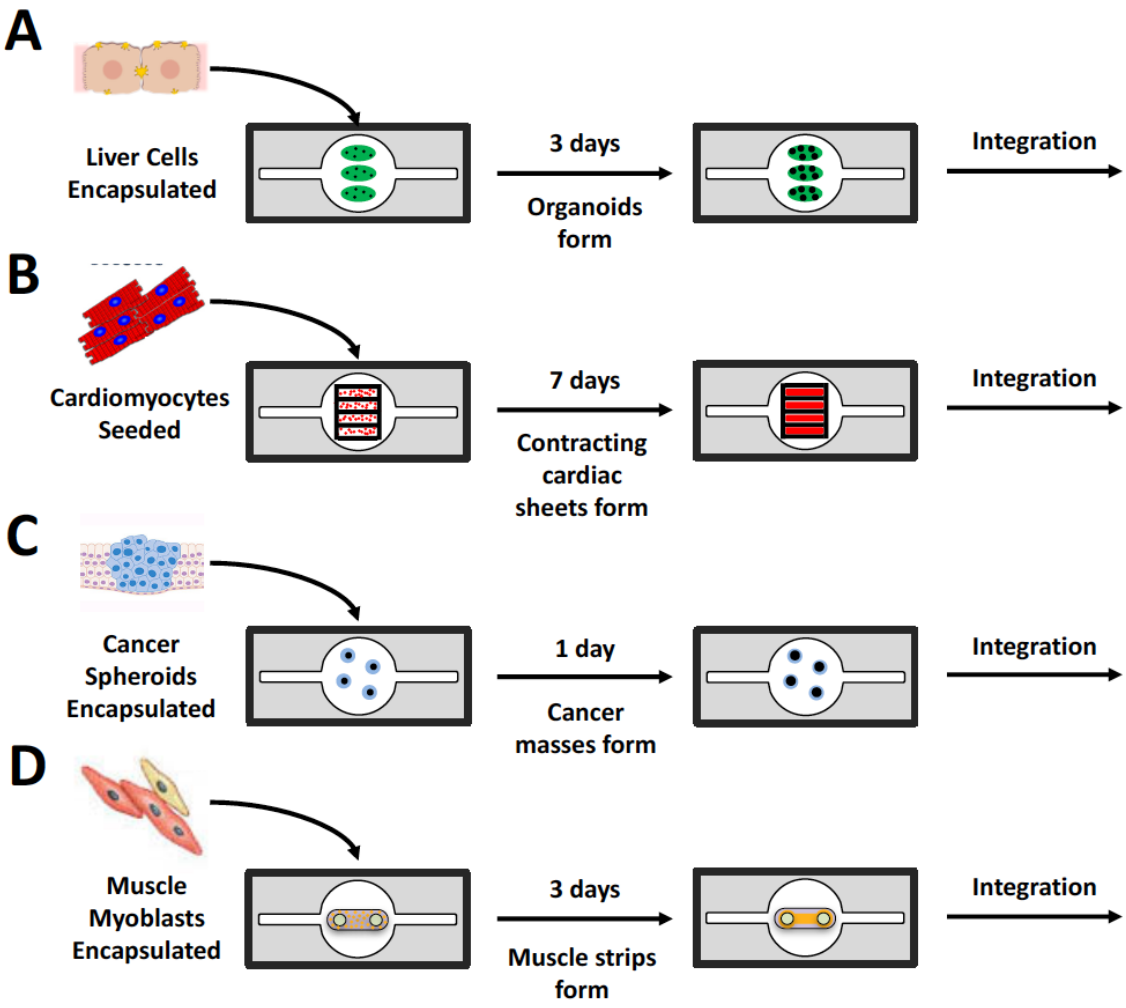

Figure 4.6: Timeline of organ-on-a-chip culture time prior to integration.

(A) Liver-on-a-chip formed from hepatocytes, cultured for 3 days, then integrated, (B) Heart-on-a-chip formed from hiPSC-derived cardiomyocytes, cultured for 7 days, then integrated, (C) Cancer-on-a-chip formed from breast cancer spheroids, cultured for 1 day, then integrated, (D) Skeletal muscle-on-a-chip formed from muscle myoblasts, cultured for 3 days, then integrated.

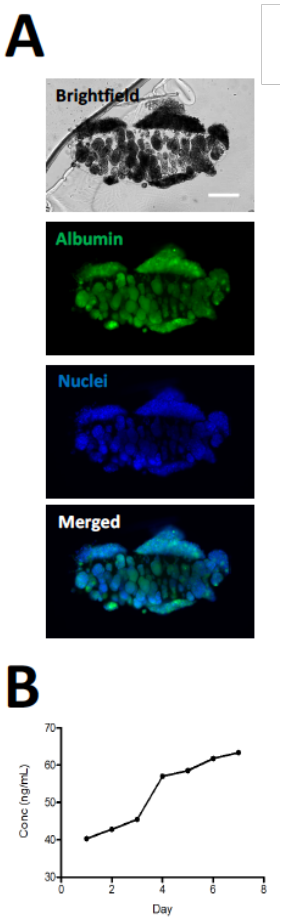

Figure 4.7: Liver-on-a-chip characterization and functional measurements during integration co-culture.

(A) Brightfield and immunofluorescence images of albumin proteins counterstained for nuclei. (B) Continuous human albumin secretion by liver-on-a-chip affirms liver function over time. Scale bar: 100µm.

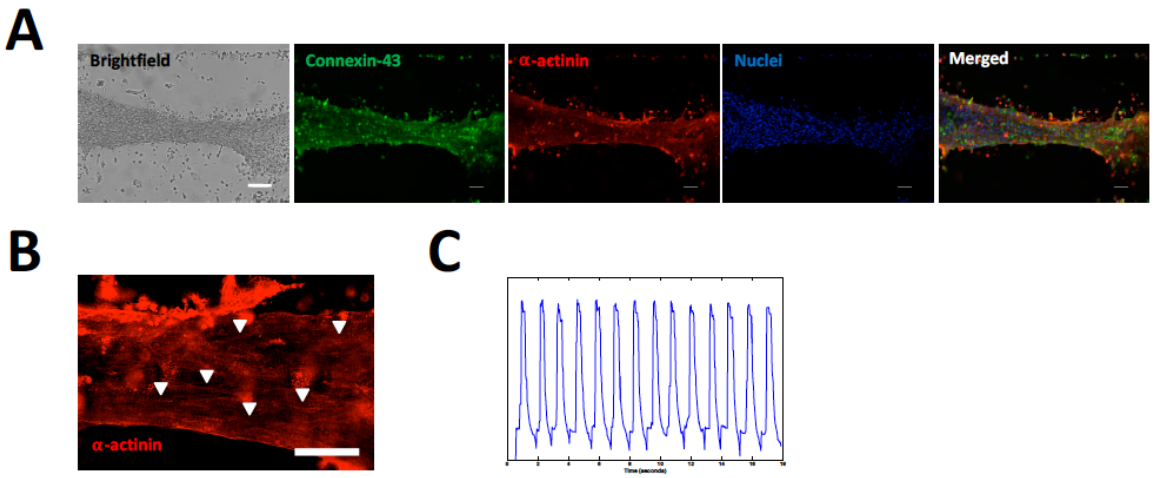

Figure 4.8: Heart-on-a-chip characterization and functional analysis during integration co-culture.

(A) Brightfield and immunofluorescence images of connexin-43 (gap junction proteins) and sarcomeric α-actinin (sarcomeric proteins) counterstained for nuclei. (B) High-magnification image of sarcomeric α-actinin shows sarcomere formation and unidirectional alignment of sarcomeres (C) Characteristic cardiac contraction trace for a cardiac sheet taken at day 7 of integration co-culture. Scale bars: 100μm.

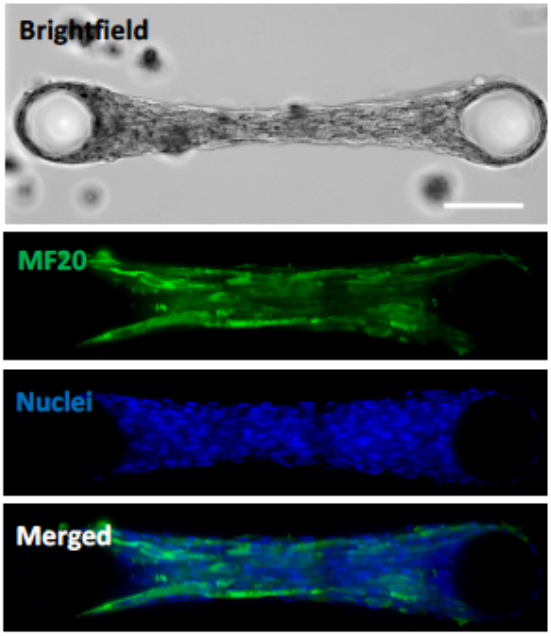

Figure 4.9: Skeletal muscle-on-a-chip characterization

Brightfield and immunofluorescence images of MF20 (myosin heavy chain) counterstained for nuclei indicate the presence of multinucleated myofibers. Scale bar: 100µm.

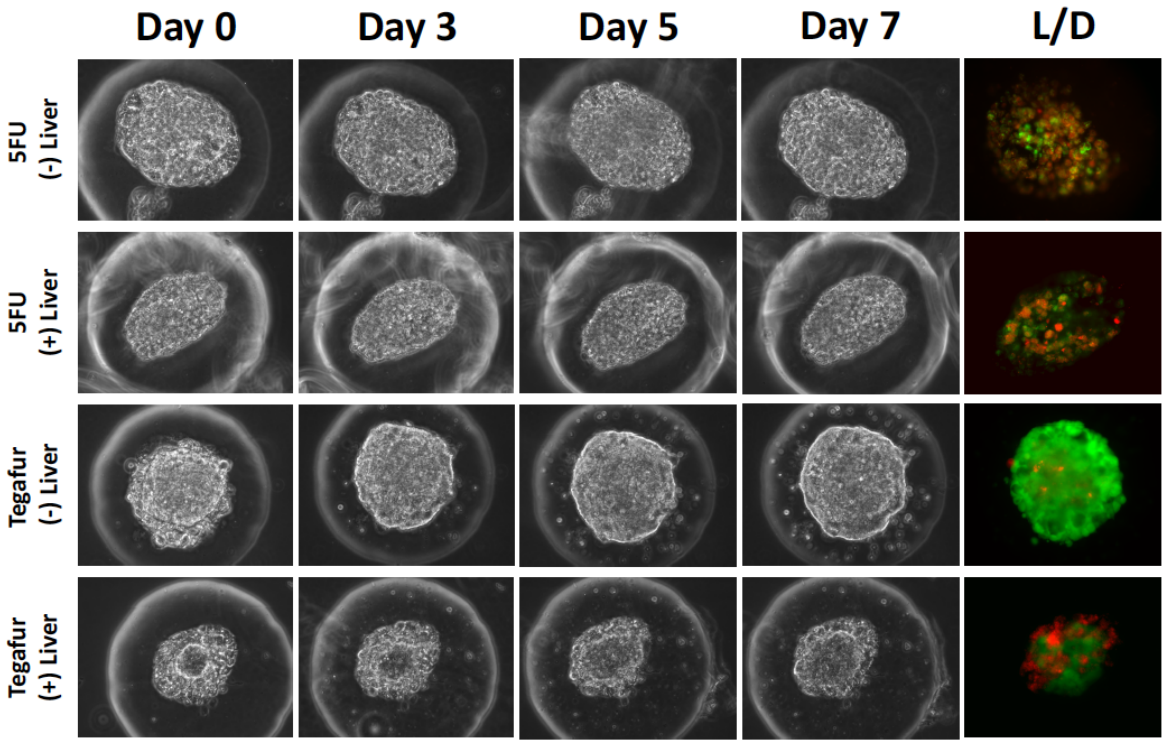

Figure 4.10: Characterization of cancer-on-a-chip tissues subjected to cancer drugs with or without integration with the liver-on-a-chip.

(A) Brightfield images and (B) Day 7 cell viability of cancer spheroids at day 0, 3, 5, and 7 of drug treatment under various integration conditions (+/- LOC). Results confirm that Tegafur fails to destroy cancer without liver metabolic activity to activate Tegafur to 5-FU. All scale bars are 50μm.

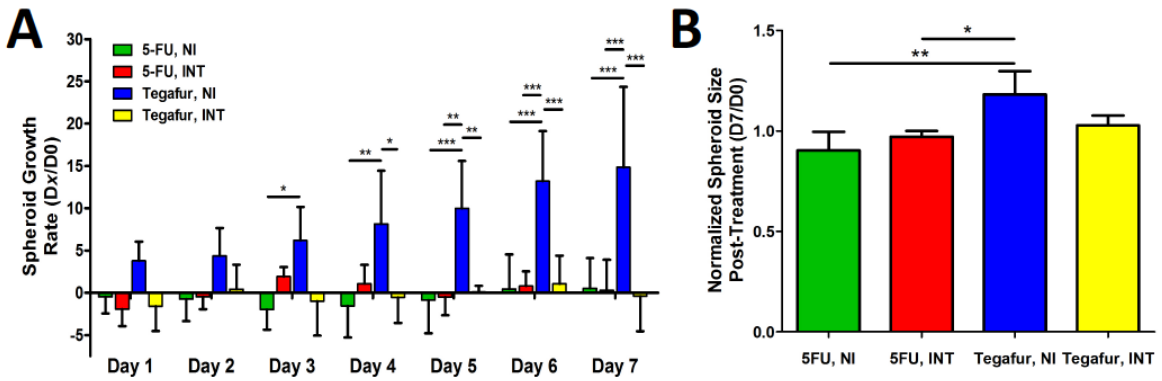

Figure 4.11: Analysis of cancer-on-a-chip tissues subjected to cancer drugs with or without integration with the liver-on-a-chip.

(A) Spheroid growth rate at day 0, 1, 2, 3, 4, 5, 6, 7 of drug treatment under various integration conditions (+/- LOC). Plot shows mean values with standard deviation. Two-way ANOVA with Bonferroni's multiple comparison test was used to assess statistical significance (*p < 0.05, **p < 0.01, ***p < 0.001). (B) Normalized spheroid size of cancer spheroids at day 7 of drug treatment with respect to day 0 under various integration conditions (+/- LOC). Plot shows mean values with standard deviation. One-way ANOVA with Tukey's multiple comparison test was used to assess statistical significance (*p < 0.1, **p < 0.01, ***p < 0.001). Results reaffirm the reliance of Tegafur on liver metabolic activity via the LOC, which would be missing in a standard cell culture dish model.

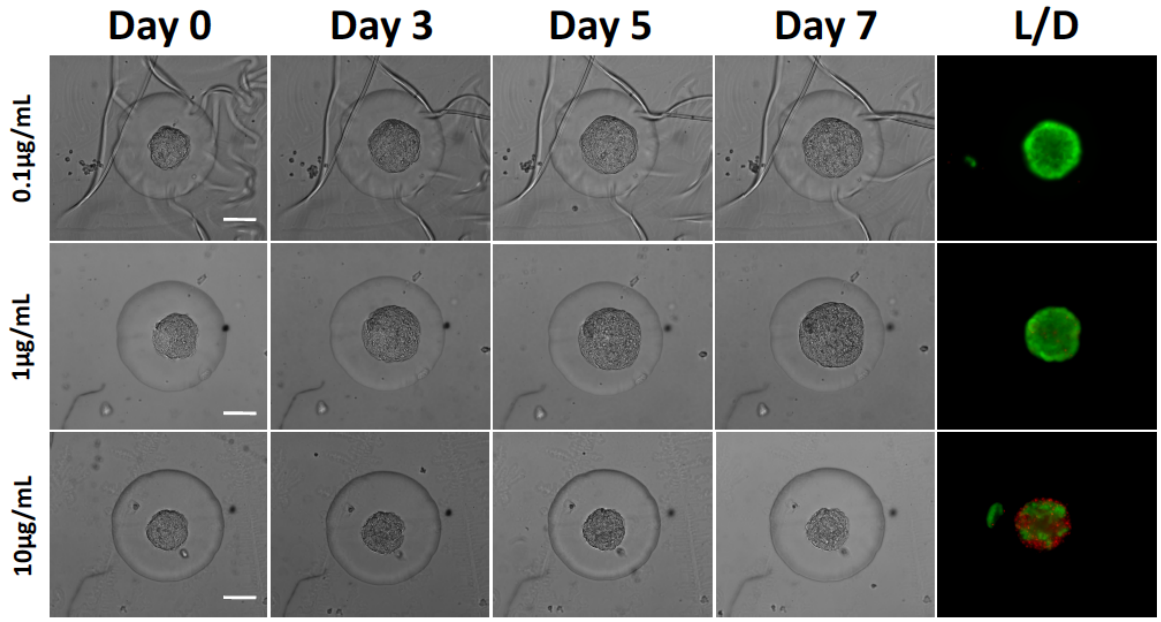

Figure 4.12: Characterization of fully-integrated cancer-on-a-chip tissues subjected to varying dosages of Tegafur

(A) Brightfield images and (B) Day 7 cell viability of cancer spheroids at day 0, 3, 5, and 7 of drug treatment under various dosage conditions. Results illustrate cancer mass death at the highest concentration of Tegafur, 10µg/mL, which is in-line with the IC50 of 5-FU. All scale bars are 100µm.

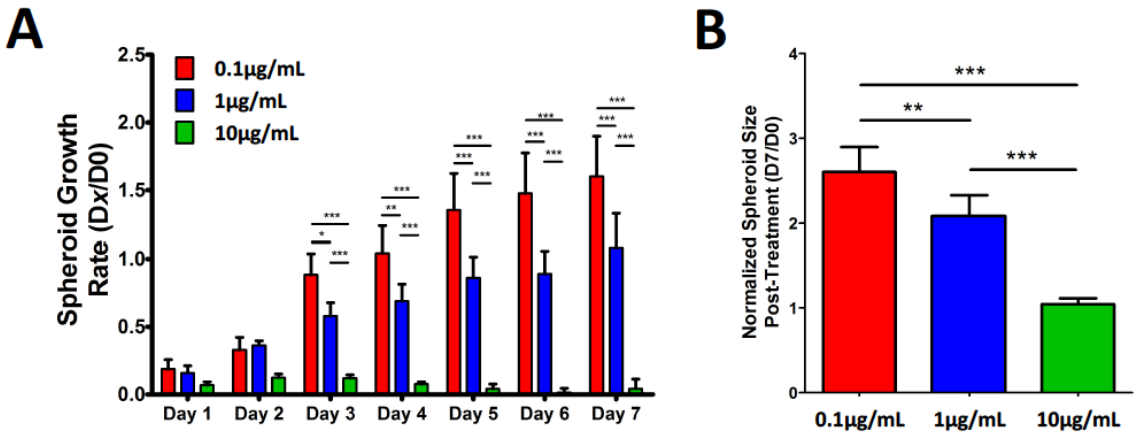

Figure 4.13: Analysis of fully-integrated cancer-on-a-chip tissues exposed to varying dosages of Tegafur

(A) Spheroid growth rate at day 0, 1, 2, 3, 4, 5, 6, 7 of drug treatment under various dosage conditions. Plot shows mean values with standard deviation. Two-way ANOVA with Bonferroni's multiple comparison test was used to assess statistical significance (*$p < 0.05$, **$p < 0.01$, ***$p < 0.001$). (B) Normalized spheroid size of cancer spheroids at day 7 of drug treatment with respect to day 0 under various dosage conditions. Plot shows mean values with standard deviation. One-way ANOVA with Tukey's multiple comparison test was used to assess statistical significance (*$p < 0.1$, **$p < 0.01$, ***$p < 0.001$).

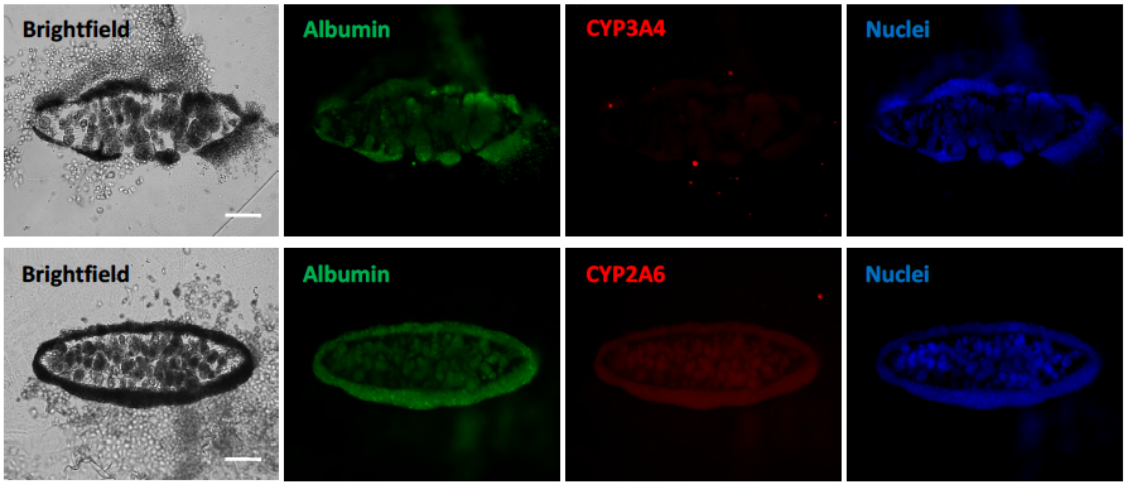

Figure 4.14: Characterization of cytochrome P450 activity in response to Tegafur

Immunofluorescence images of albumin and (A) CYP3A4 or (B) CYP2A6 of liver-on-a-chip samples post-treatment with 10µg/mL Tegafur. Results confirm upregulation of CYP2A6, which is primarily responsible for metabolism of Tegafur. All scale bars are 100µm.

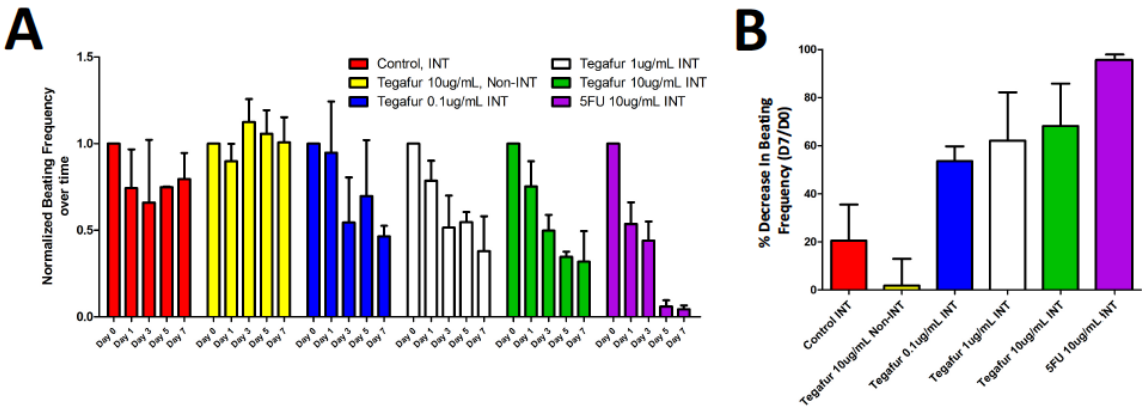

Figure 4.15: Cardiotoxic response of cardiac sheets in heart-on-a-chip subjected to various drugs and conditions.

(A) Normalized beating frequency at day 0, 1, 3, 5, and 7 and (B) Percentage decrease in beating frequency at day 7 with respect to day 0 of cardiac sheets subjected to the following conditions: control (no drug), Tegafur 10µg/mL without liver-on-a-chip, Tegafur 0.1µg/mL fully-integrated, Tegafur 1.0µg/mL fully-integrated, Tegafur 10µg/mL fully-integrated, and 5-FU 10µg/mL fully-integrated. Without the liver-on-a-chip, Tegafur does not exhibit cardiotoxicity against the heart. 5-FU leads to complete cessation of contraction, while all concentrations of Tegafur lead to some decrease in contraction, with toxicity increasing with increasing Tegafur concentration.

4.9 References

1. Y. C. Huang, R. G. Dennis, L. Larkin and K. Baar, *Journal of applied physiology*, 2005, **98**, 706-713.

2. D. Loessner, K. S. Stok, M. P. Lutolf, D. W. Hutmacher, J. A. Clements and S. C. Rizzi, *Biomaterials*, 2010, **31**, 8494-8506.

3. A. S. Kienhuis, H. M. Wortelboer, J. C. Hoflack, E. J. Moonen, J. C. Kleinjans, B. van Ommen, J. H. van Delft and R. H. Stierum, *Drug metabolism and disposition: the biological fate of chemicals*, 2006, **34**, 2083-2090.

4. H. Karlsson, M. Fryknas, R. Larsson and P. Nygren, *Experimental cell research*, 2012, **318**, 1577-1585.

5. H. K. Dhiman, A. R. Ray and A. K. Panda, *Biomaterials*, 2005, **26**, 979-986.

6. F. Xu and K. J. Burg, *Cytotechnology*, 2007, **54**, 135-143.

7. A. Hansen, A. Eder, M. Bonstrup, M. Flato, M. Mewe, S. Schaaf, B. Aksehirlioglu, A. P. Schwoerer, J. Uebeler and T. Eschenhagen, *Circulation research*, 2010, **107**, 35-44.

8. A. A. Chen, D. K. Thomas, L. L. Ong, R. E. Schwartz, T. R. Golub and S. N. Bhatia, *Proceedings of the National Academy of Sciences of the United States of America*, 2011, **108**, 11842-11847.

9. N. Thavandiran, N. Dubois, A. Mikryukov, S. Masse, B. Beca, C. A. Simmons, V. S. Deshpande, J. P. McGarry, C. S. Chen, K. Nanthakumar, G. M. Keller, M. Radisic and P. W. Zandstra, *Proceedings of the National Academy of Sciences of the United States of America*, 2013, **110**, E4698-4707.

10. V. Y. Sidorov, P. C. Samson, T. N. Sidorova, J. M. Davidson, C. C. Lim and J. P. Wikswo, *Acta biomaterialia*, 2017, **48**, 68-78.

11. K. Shimizu, R. Genma, Y. Gotou, S. Nagasaka and H. Honda, *Bioengineering (Basel)*, 2017, **4**.

12. L. Madden, M. Juhas, W. E. Kraus, G. A. Truskey and N. Bursac, *eLife*, 2015, **4**, e04885.

13. I. Mannhardt, K. Breckwoldt, D. Letuffe-Breniere, S. Schaaf, H. Schulz, C. Neuber, A. Benzin, T. Werner, A. Eder, T. Schulze, B. Klampe, T. Christ, M. N. Hirt, N. Huebner, A. Moretti, T. Eschenhagen and A. Hansen, *Stem cell reports*, 2016, **7**, 29-42.

14. L. Rao, Y. Qian, A. Khodabukus, T. Ribar and N. Bursac, *Nature communications*, 2018, **9**, 126.

15. A. K. Capulli, K. Tian, N. Mehandru, A. Bukhta, S. F. Choudhury, M. Suchyta and K. K. Parker, *Lab on a chip*, 2014, **14**, 3181-3186.

16. S. N. Bhatia and D. E. Ingber, *Nature biotechnology*, 2014, **32**, 760-772.

17. K. H. Benam, S. Dauth, B. Hassell, A. Herland, A. Jain, K. J. Jang, K. Karalis, H. J. Kim, L. MacQueen, R. Mahmoodian, S. Musah, Y. S. Torisawa, A. D. van der Meer, R. Villenave, M. Yadid, K. K. Parker and D. E. Ingber, *Annual review of pathology*, 2015, **10**, 195-262.

18. A. Agarwal, J. A. Goss, A. Cho, M. L. McCain and K. K. Parker, *Lab on a chip*, 2013, **13**, 3599-3608.

19. A. Grosberg, P. W. Alford, M. L. McCain and K. K. Parker, *Lab on a chip*, 2011, **11**, 4165-4173.

20. A. Mathur, P. Loskill, K. Shao, N. Huebsch, S. Hong, S. G. Marcus, N. Marks, M. Mandegar, B. R. Conklin, L. P. Lee and K. E. Healy, *Scientific reports*, 2015, **5**, 8883.

21. A. Aung, I. S. Bhullar, J. Theprungsirikul, S. K. Davey, H. L. Lim, Y. J. Chiu, X. Ma, S. Dewan, Y. H. Lo, A. McCulloch and S. Varghese, *Lab on a chip*, 2016, **16**, 153-162.

22. N. S. Bhise, V. Manoharan, S. Massa, A. Tamayol, M. Ghaderi, M. Miscuglio, Q. Lang, Y. Shrike Zhang, S. R. Shin, G. Calzone, N. Annabi, T. D. Shupe, C. E. Bishop, A. Atala, M. R. Dokmeci and A. Khademhosseini, *Biofabrication*, 2016, **8**, 014101.

23. A. Schepers, C. Li, A. Chhabra, B. T. Seney and S. Bhatia, *Lab on a chip*, 2016, **16**, 2644-2653.

24. J. M. Prot, A. Bunescu, B. Elena-Herrmann, C. Aninat, L. C. Snouber, L. Griscom, F. Razan, F. Y. Bois, C. Legallais, C. Brochot, A. Corlu, M. E. Dumas and E. Leclerc, *Toxicol Appl Pharmacol*, 2012, **259**, 270-280.

25. D. Huh, B. Matthews, A. Mammoto, A. Montoya-Zavala, H. Y. Hsin and D. E. Ingber, *Science*, 2010, **328**, 1662-1669.

26. D. D. Huh, *Ann Am Thorac Soc*, 2015, **12 Suppl 1**, S42-44.

27. H. J. Kim, D. Huh, G. Hamilton and D. E. Ingber, *Lab on a chip*, 2012, **12**, 2165-2174.

28. H. J. Kim, H. Li, J. J. Collins and D. E. Ingber, *Proceedings of the National Academy of Sciences of the United States of America*, 2016, **113**, E7-15.

29. M. Kasendra, A. Tovaglieri, A. Sontheimer-Phelps, S. Jalili-Firoozinezhad, A. Bein, A. Chalkiadaki, W. Scholl, C. Zhang, H. Rickner, C. A. Richmond, H. Li, D. T. Breault and D. E. Ingber, *Scientific reports*, 2018, **8**, 2871.

30. K. Y. Shim, D. Lee, J. Han, N. T. Nguyen, S. Park and J. H. Sung, *Biomedical microdevices*, 2017, **19**, 37.

31. Y. S. Torisawa, C. S. Spina, T. Mammoto, A. Mammoto, J. C. Weaver, T. Tat, J. J. Collins and D. E. Ingber, *Nature methods*, 2014, **11**, 663-669.

32. S. Sieber, L. Wirth, N. Cavak, M. Koenigsmark, U. Marx, R. Lauster and M. Rosowski, *J Tissue Eng Regen Med*, 2018, **12**, 479-489.

33. J. A. Brown, V. Pensabene, D. A. Markov, V. Allwardt, M. D. Neely, M. Shi, C. M. Britt, O. S. Hoilett, Q. Yang, B. M. Brewer, P. C. Samson, L. J. McCawley, J. M. May, D. J. Webb, D. Li, A. B. Bowman, R. S. Reiserer and J. P. Wikswo, *Biomicrofluidics*, 2015, **9**, 054124.

34. A. Herland, A. D. van der Meer, E. A. FitzGerald, T. E. Park, J. J. Sleeboom and D. E. Ingber, *PloS one*, 2016, **11**, e0150360.

35. Y. Koo, B. T. Hawkins and Y. Yun, *Scientific reports*, 2018, **8**, 2841.

36. G. Agrawal, A. Aung and S. Varghese, *Lab on a chip*, 2017, **17**, 3447-3461.

37. A. Aung, J. Theprungsirikul, H. L. Lim and S. Varghese, *Lab on a chip*, 2016, **16**, 1886-1898.

38. K. H. Benam, R. Villenave, C. Lucchesi, A. Varone, C. Hubeau, H. H. Lee, S. E. Alves, M. Salmon, T. C. Ferrante, J. C. Weaver, A. Bahinski, G. A. Hamilton and D. E. Ingber, *Nature methods*, 2016, **13**, 151-157.

39. S. Jalili-Firoozinezhad, R. Prantil-Baun, A. Jiang, R. Potla, T. Mammoto, J. C. Weaver, T. C. Ferrante, H. J. Kim, J. M. S. Cabral, O. Levy and D. E. Ingber, *Cell Death Dis*, 2018, **9**, 223.

40. A. P. Nesmith, A. Agarwal, M. L. McCain and K. K. Parker, *Lab on a chip*, 2014, **14**, 3925-3936.

41. G. Wang, M. L. McCain, L. Yang, A. He, F. S. Pasqualini, A. Agarwal, H. Yuan, D. Jiang, D. Zhang, L. Zangi, J. Geva, A. E. Roberts, Q. Ma, J. Ding, J. Chen, D. Z. Wang, K. Li, J. Wang, R. J. Wanders, W. Kulik, F. M. Vaz, M. A. Laflamme, C. E. Murry, K. R. Chien, R. I. Kelley, G. M. Church, K. K. Parker and W. T. Pu, *Nat Med*, 2014, **20**, 616-623.

42. M. Workman, E. Troisi, S. J. Kerns, G. A. Hamilton, C. Svendsen, S. R. Targan and R. J. Barrett, *Gastroenterology*, 2017, **152**, S57-S58.

43. M. J. Workman, J. P. Gleeson, E. J. Troisi, H. Q. Estrada, S. J. Kerns, C. D. Hinojosa, G. A. Hamilton, S. R. Targan, C. N. Svendsen and R. J. Barrett, *Cellular and Molecular Gastroenterology and Hepatology*, 2018, **5**, 669-677.e662.

44. M. B. Esch, A. S. T. Smith, J. M. Prot, C. Oleaga, J. J. Hickman and M. L. Shuler, *Adv Drug Deliver Rev*, 2014, **69**, 158-169.

45. I. Maschmeyer, A. K. Lorenz, K. Schimek, T. Hasenberg, A. P. Ramme, J. Hubner, M. Lindner, C. Drewell, S. Bauer, A. Thomas, N. S. Sambo, F. Sonntag, R. Lauster and U. Marx, *Lab on a chip*, 2015, **15**, 2688-2699.

46. C. Zhang, Z. Zhao, N. A. Abdul Rahim, D. van Noort and H. Yu, *Lab on a chip*, 2009, **9**, 3185-3192.

47. C. D. Edington, W. L. K. Chen, E. Geishecker, T. Kassis, L. R. Soenksen, B. M. Bhushan, D. Freake, J. Kirschner, C. Maass, N. Tsamandouras, J. Valdez, C. D. Cook, T. Parent, S. Snyder, J. J. Yu, E. Suter, M. Shockley, J. Velazquez, J. J. Velazquez, L. Stockdale, J. P. Papps, I. Lee, N. Vann, M. Gamboa, M. E. LaBarge, Z. Zhong, X. Wang, L. A. Boyer, D. A. Lauffenburger, R. L. Carrier, C. Communal, S. R. Tannenbaum, C. L. Stokes, D. J. Hughes, G. Rohatgi, D. L. Trumper, M. Cirit and L. G. Griffith, *Scientific reports*, 2018, **8**.

48. A. Skardal, S. V. Murphy, M. Devarasetty, I. Mead, H. W. Kang, Y. J. Seol, Y. S. Zhang, S. R. Shin, L. Zhao, J. Aleman, A. R. Hall, T. D. Shupe, A. Kleensang, M. R. Dokmeci, S. J. Lee, J. D. Jackson, J. J. Yoo, T. Hartung, A. Khademhosseini, S. Soker, C. E. Bishop and A. Atala, *Scientific reports*, 2017, **7**.

49. M. B. Esch, G. J. Mahler, T. Stokor and M. L. Shuler, *Lab on a chip*, 2014, **14**, 3081-3092.

50. M. B. Esch, H. Ueno, D. R. Applegate and M. L. Shuler, *Lab on a chip*, 2016, **16**, 2719-2729.

51. C. Oleaga, C. Bernabini, A. S. T. Smith, B. Srinivasan, M. Jackson, W. McLamb, V. Platt, R. Bridges, Y. Q. Cai, N. Santhanam, B. Berry, S. Najjar, N. Akanda, X. F.

Guo, C. Martin, G. Ekman, M. B. Esch, J. Langer, G. Ouedraogo, J. Cotovio, L. Breton, M. L. Shuler and J. J. Hickman, *Scientific reports*, 2016, **6**.

52. J. H. Sung and M. L. Shuler, *Lab on a chip*, 2009, **9**, 1385-1394.

53. P. W. Burridge, E. Matsa, P. Shukla, Z. C. Lin, J. M. Churko, A. D. Ebert, F. Lan, S. Diecke, B. Huber, N. M. Mordwinkin, J. R. Plews, O. J. Abilez, B. Cui, J. D. Gold and J. C. Wu, *Nature methods*, 2014, **11**, 855-860.

54. J. W. Nichol, S. T. Koshy, H. Bae, C. M. Hwang, S. Yamanlar and A. Khademhosseini, *Biomaterials*, 2010, **31**, 5536-5544.

55. S. K. Davey, A. Aung, G. Agrawal, H. L. Lim, M. Kar and S. Varghese, *Tissue engineering. Part C, Methods*, 2015, **21**, 1188-1196.

56. T. Majima and W. Schnabel, *Macromol. Chem.*, 1991, **192**, 2307-2315.

57. D. B. Longley, D. P. Harkin and P. G. Johnston, *Nat Rev Cancer*, 2003, **3**, 330-338.

58. T. Nakayama and S. Noguchi, *Oncologist*, 2010, **15**, 26-36.

59. F. Steger, M. G. Hautmann and O. Kolbl, *Radiat Oncol*, 2012, **7**.

60. P. Alter, M. Herzum, M. Soufi, J. R. Schaefer and B. Maisch, *Cardiovascular and Hematological Agents in Medicinal Chemistry*, 2006, **4**, 1-5.

61. J. C. Marsh, P. Catalano, J. Huang, D. L. Graham, M. J. Cornfield, P. J. O'Dwyer and A. B. Benson III, *Clinical Colorectal Cancer*, 2002, **2**, 43-50.

62. H. Hernandez-Vargas, E. Ballestar, P. Carmona-Saez, C. von Kobbe, I. Banon-Rodriguez, M. Esteller, G. Moreno-Bueno and J. Palacios, *Int J Cancer*, 2006, **119**, 1164-1175.

63. C. C. Ogu and J. L. Maxa, *Proc (Bayl Univ Med Cent)*, 2000, **13**, 421-423.

64. K. Ikeda, K. Yoshisue, E. Matsushima, S. Nagayama, K. Kobayashi, C. A. Tyson, K. Chiba and Y. Kawaguchi, *Clin Cancer Res*, 2000, **6**, 4409-4415.

65. I. Janssen, S. B. Heymsfield, Z. Wang and R. Ross, *J Appl Physiol*, 2000, **89**, 81-88.

66. L. A. Gilliam and D. K. St Clair, *Antioxid Redox Signal*, 2011, **15**, 2543-2563.

67. E. Bjornsson and R. Olsson, *Hepatology*, 2005, **42**, 481-489.

68. Y. Tonomura, S. Matsushima, E. Kashiwagi, K. Fujisawa, S. Takagi, Y. Nishimura, R. Fukushima, M. Torii and M. Matsubara, *Toxicology*, 2012, **302**, 179-189.

69. J. Jang, J. E. Yoo, J. A. Lee, D. R. Lee, J. Y. Kim, Y. J. Huh, D. S. Kim, C. Y. Park, D. Y. Hwang, H. S. Kim, H. C. Kang and D. W. Kim, *Exp Mol Med*, 2012, **44**, 202-213.

70. E. Shoji, H. Sakurai, T. Nishino, T. Nakahata, T. Heike, T. Awaya, N. Fujii, Y. Manabe, M. Matsuo and A. Sehara-Fujisawa, *Scientific reports*, 2015, **5**, 12831.